Universität Potsdam

“Synthesis of InP Quantum Dots and their Applications”

Dissertation

Zur Erlangung des akademischen Grades

“doctor rerum naturalium” (Dr. rer. nat.)

in der Wissenschaftdisziplin “Material Science”

eingereicht an der

Mathematisch-Naturwissenschaftlichen Fakultät

Institute für Chemie der Universität Potsdam

von

Jiyong Kim, M.Sc.

Potsdam, 27. 08. 2022

The following research was carried out in the research group of Dr. Armin Wedel from February 1st, 2020, to October 30th, 2022, at the Fraunhofer Institute for Applied Polymer Research IAP under the guidance with Prof. Dr. Andreas Taubert at Institute of Chemistry of the University Potsdam.

1st Reviewer: Prof. Dr. Andreas Taubert
2nd Reviewer: Dr. Armin Wedel
3rd Reviewer: Prof. Dr. Wolfgang Brütting

I certify that the content presented within this report is my own original work based on research that I performed using only the means and source materials as noted therein. This thesis was not submitted to another examination board in this, or other countries were no unsuccessful examination process. Jiyong Kim

Published online on the
Publication Server of the University of Potsdam:
https://doi.org/10.25932/publishup-58535
https://nbn-resolving.org/urn:nbn:de:kobv:517-opus4-585351

Zusammenfassung

Umweltfreundliche InP Quantenpunkte (QDs) sind technologisch relevant und werden typischerweise als grüne und rote Emitter in Bildschirmen verwendet. Nach dem Stand der Technik kann eine sorgfältig hergestellte Kern-Schale-Heterostruktur (ZnSe innen/ZnS außen) zu außergewöhnlich hohen Photolumineszenz-Quantenausbeuten (PL-QYs) von nahezu Eins (95 - 100 %) führen. Dennoch gibt es bisher nur einige wenige industrielle Anwendungen wie QD-Flüssigkristall-Bildschirme (liquid crystal display, QD-LCD), in denen die Anregung durch eine blaue Hintergrundbeleuchtung realisiert wird. Dabei haben QDs aufgrund ihrer Modifizierbarkeit noch viele weitere industrielle Einsatzmöglichkeiten, beispielsweise QD basierte lichtemittierende Dioden (QD-LEDs) und lumineszierende Solarkollektoren (luminescence solar concentrator, LSC).

Vor dem Hauptteil werden in den Kapiteln 1 und 2 die Grundlagen von QDs und die theoretischen Grundlagen basierend auf quantenmechanischer Beschreibung und experimentellen Ergebnissen eingeführt. Zum besseren Verständnis werden: das Konzept der QDs, kolloidale QDs, Kern-Schale-Strukturen vom Typ I, mit Übergangsmetallen dotierte Halbleiter-QDs, die Oberflächenchemie von QDs und ihre Anwendungen (LSC, QD-LEDs und electrohydrodynamic EHD-Jet-Printing), nacheinander eingeführt. Der Schwerpunkt dieser Doktorarbeit liegt hauptsächlich auf der Kombination von QD-Materialien und QD-Bauelementen, basierend auf der Synthese von InP QDs mit einem anorganischen Kern (Kern-Schale-Heterostruktur) und einer organischen Hülle (Oberflächenliganden auf der QD-Oberfläche). In die Kern-Schale-Heterostruktur wird eine ZnCuInS-Mittelschale als Zwischenschicht zwischen einem Cu-dotierten InP Kern und einer ZnS-Schale für LSC-Bauelemente neu eingeführt. Bei den Oberflächenliganden wird der Ligandeneffekt von 1-Oktanthiol und Chloridionen auf die Stabilität von QD-LEDs und die Druckbarkeit mit EHD-Jet-Printing hin untersucht. Dabei erhält der Protonentransfermechanismus auf der QD-Oberfläche ein besonderes Augenmerk.

In Kapitel 3 wird die Eintopfsynthese von hocheffizient emittierenden QDs mit einer Cu:InP/Zn-Cu-In-S (ZCIS)/ZnS Kern/Schale/Schale-Heterostruktur beschrieben. Wenn diese neuartige Kombination einer ZCIS/ZnS-Doppelschalenstruktur mit eine Reihe von Cu:InP-Kerne mit unterschiedlichen Größen kombiniert wird, ergeben die daraus entstehenden Cu:InP/ZCIS/ZnS-QDs die bisher höchsten publizierten PL-QYs von 71,5 – 82,4 % im nahen IR-Bereich von 694 – 850 nm mit einstellbarer PL Wellenlänge. Diese Ergebnisse weisen auf die Wirksamkeit der ZCIS-Zwischenschicht hin, welche die Grenzflächenspannung zwischen Kern und Schale effektiv mildert und damit zu einem solch hohen Emissionsvermögen führt. Diese ZCIS-Zwischenschicht wird durch

vergleichende Größen-, Struktur- und Zusammensetzungsanalysen weiter untersucht. Am Ende des Kapitels wird der aktuellen Stand der Forschung auf dem Gebiet der LSC-Bauelemente aus solchen Cu:InP/ZCIS/ZnS-QDs vorgestellt.

Kapitel 4 befasst sich hauptsächlich mit dem Ligandeneffekt bei der Passivierung mit 1-Oktanthiol von InP/ZnSe/ZnS-QDs im Hinblick auf die unvollständige Oberflächenpassivierung während der Synthese. Es fehlen anionischen Carboxylat-Liganden auf der InP/ZnSe/ZnS-Oberfläche der QDs, an denen Zink Carboxylat Liganden durch Protonentransfer vom 1-Oktanthiol in Carbonsäure-Liganden umgewandelt werden könnten. Die so synthetisierten QDs haben zunächst eine unterkoordinierte Oberfläche mit Leerstellen, die durch Lösungsmittel-Liganden wie Ethanol oder Aceton passiviert werden. Wenn 1-Octanthiol an die QD-Oberfläche bindet bewirkt der Protonentransfer die Bindung von Carboxylat-Liganden (aus Zink-Carboxylat) an die Oberfläche, wobei Ethanol- oder Aceton-Liganden ausgetauscht werden. Systematische Analysen wie Thermogravimetrie (thermogravimetric analysis TGA), Massenspektrometrie (MS) und Protonen-Kernmagnetresonanz (proton nuclear magnetic resonance 1H-NMR) zeigen direkt den Zusammenhang zwischen Oberflächenliganden und QD-LEDs.

Kapitel 5 zeigt den Zusammenhang zwischen der Materialstabilität von QDs und der Bauteilstabilität von QD-LEDs durch Untersuchung der Oberflächenchemie und der Schalendicke. In typischen kolloidalen III-V-InP-QDs wird eine anorganische ZnS-Außenhülle auf den InP Kern aufgetragen, um Stabilität zu gewährleisten. In dieser Arbeit wird jedoch eine schnellere Photodegradation von InP/ZnSe/ZnS-QDs mit einer dickeren statt einer dünneren ZnS-Schale gezeigt, wenn 1-Oktanthiol als Schwefelquelle zur Bildung der äußersten ZnS-Schale verwendet wurde. 1-Oktanthiol induziert die Bildung eines schwach gebundenen Carboxylatliganden durch Protonentransfer auf der QD-Oberfläche, was zu einem schnelleren Abbau unter UV-Licht trotz dickerer ZnS-Schale führt. Detailliertere Einblicke in die Oberflächenchemie werden durch 1H-NMR, TGA und MS gewonnen. Überraschenderweise zeigen jedoch die Lebensdauern der aus InP/ZnSe/ZnS-QDs mit dicken oder dünnen ZnS-Hüllen hergestellten EL-Bauelemente eine gegenteilige Stabilität: Die QD-LEDs mit QDs mit dicker ZnS-Hülle haben eine längere Lebensdauer, als jene mit dünner ZnS-Hülle. Es wird der Degradationsmechanismus der QDs und der QD-Leuchtdioden anhand der Ergebnisse erläutert und der Effekt auf die unterschiedlichen Lebensdauern von Material und Bauteil diskutiert.

In Kapitel 6 wird eine Methode vorgeschlagen, wie die Druckbarkeit von QD-Tintenformulierungen beim EHD-Jet-Druck über die QD-Materialien verbessert werden kann. Dazu werden InP-QDs mit GaP-Zwischenschalen erweitert, um die Oberflächenladung zu beeinflussen.

Darüber hinaus verbessern GaP-Zwischenschalen in III-V kolloidalen InP-QDs deren thermische Stabilität und PL-QY im Falle von Typ-I-Kern/Schale/Schale-Heterostrukturen (InP/GaP/ZnSeS-QDs). Diese stark lumineszierenden InP/GaP/ZnSeS-QDs wurden synthetisiert und für den EHD-Jet-Druck verwendet. Nicht umgesetzte Ga und Cl-Ionen auf der QD-Oberfläche reduzieren die benötigte Betriebsspannung zur Ausbildung eines Taylor-Kegels und eines stabilen Tinten-Jets. Dieses Ergebnis deutet darauf hin, dass die Oberflächenladungen der Quantenpunkte eine wichtige Rolle bei der Ausbildung des Taylor-Kegels spielen. Mittels Zeta-Potenzial-Messung von QD-Tinten wurde eine industriell erprobte und einfache Methode zur Untersuchung der Oberflächenladungen verwendet. Darüber hinaus wurde optische Emissionsspektrometrie mit induktiv gekoppeltem Plasma (inductively coupled plasma-atomic emission spectroscopy ICP-OES) zur Bestimmung der Elementzusammensetzung durchgeführt.

Diese Dissertation beschäftigt sich sowohl mit der Synthese von hocheffizienten InP QDs mit schmalbandiger Emission (full width at half maximum FWHM), als auch den Zusammenhängen zwischen QD-Material und QD-Bauelementen. Die Ergebnisse sind einerseits relevant für die breitere industrielle Anwendung dieser Materialien und andererseits für ein tieferes chemisch-physikalisches, theoretisches und experimentelles Verständnis der Prozesse, die zu langlebigen und stabilen Bauelementen führen.

Schlüsselwörter

Kolloidaler Quantenpunkt, Cu-dotiertes InP, Oberflächenchemie, QD-Stabilität, QD-Gerät.

Abstract

Technologically important, environmentally friendly InP quantum dots (QDs) typically used as green and red emitters in display devices can achieve exceptional photoluminescence quantum yields (PL QYs) of near-unity (95-100%) when the-state-of-the-art core/shell heterostructure of the ZnSe inner/ZnS outer shell is elaborately applied. Nevertheless, it has only led to a few industrial applications as QD liquid crystal display (QD–LCD) which is applied to blue backlight units, even though QDs has a lot of possibilities that able to realize industrially feasible applications, such as QD light-emitting diodes (QD–LEDs) and luminescence solar concentrator (LSC), due to their functionalizable characteristics.

Before introducing the main research, the theoretical basis and fundamentals of QDs are described in detail on the basis of the quantum mechanics and experimental synthetic results, where a concept of QD and colloidal QD, a type-I core/shell structure, a transition metal doped semiconductor QDs, the surface chemistry of QD, and their applications (LSC, QD–LEDs, and EHD jet printing) are sequentially elucidated for better understanding. This doctoral thesis mainly focused on the connectivity between QD materials and QD devices, based on the synthesis of InP QDs that are composed of inorganic core (core/shell heterostructure) and organic shell (surface ligands on the QD surface). In particular, as for the former one (core/shell heterostructure), the ZnCuInS mid-shell as an intermediate layer is newly introduced between a Cu-doped InP core and a ZnS shell for LSC devices. As for the latter one (surface ligands), the ligand effect by 1-octanethiol and chloride ion are investigated for the device stability in QD–LEDs and the printability of electro-hydrodynamic (EHD) jet printing system, in which this research explores the behavior of surface ligands, based on proton transfer mechanism on the QD surface.

Chapter 3 demonstrates the synthesis of strain-engineered highly emissive Cu:InP/Zn–Cu–In–S (ZCIS)/ZnS core/shell/shell heterostructure QDs via a one-pot approach. When this unconventional combination of a ZCIS/ZnS double shelling scheme is introduced to a series of Cu:InP cores with different sizes, the resulting Cu:InP/ZCIS/ZnS QDs with a tunable near-IR PL range of 694–850 nm yield the highest-ever PL QYs of 71.5–82.4%. These outcomes strongly point to the efficacy of the ZCIS interlayer, which makes the core/shell interfacial strain effectively alleviated, toward high emissivity. The presence of such an intermediate ZCIS layer is further examined by comparative size, structural, and compositional analyses. The end of this chapter briefly introduces the research related to the LSC devices, fabricated from Cu:InP/ZCIS/ZnS QDs, currently in progress.

Chapter 4 mainly deals with ligand effect in 1-octanethiol passivation of InP/ZnSe/ZnS QDs in terms of incomplete surface passivation during synthesis. This chapter demonstrates the lack of anionic carboxylate ligands on the surface of InP/ZnSe/ZnS quantum dots (QDs), where zinc carboxylate ligands can be converted to carboxylic acid or carboxylate ligands via proton transfer by 1-octanethiol. The as-synthesized QDs initially have an under-coordinated vacancy surface, which is passivated by solvent ligands such as ethanol and acetone. Upon exposure of 1-octanethiol to the QD surface, 1-octanthiol effectively induces the surface binding of anionic carboxylate ligands (derived from zinc carboxylate ligands) by proton transfer, which consequently exchanges ethanol and acetone ligands that bound on the incomplete QD surface. The systematic chemical analyses, such as thermogravimetric analysis–mass spectrometry and proton nuclear magnetic resonance spectroscopy, directly show the interplay of surface ligands, and it associates with QD light-emitting diodes (QD–LEDs).

Chapter 5 shows the relation between material stability of QDs and device stability of QD–LEDs through the investigation of surface chemistry and shell thickness. In typical III–V colloidal InP quantum dots (QDs), an inorganic ZnS outermost shell is used to provide stability when overcoated onto the InP core. However, this work presents a faster photo-degradation of InP/ZnSe/ZnS QDs with a thicker ZnS shell than that with a thin ZnS shell when 1-octanethiol was applied as a sulfur source to form ZnS outmost shell. Herein, 1-octanethiol induces the form of weakly-bound carboxylate ligand via proton transfer on the QD surface, resulting in a faster degradation at UV light even though a thicker ZnS shell was formed onto InP/ZnSe QDs. Detailed insight into surface chemistry was obtained from proton nuclear magnetic resonance spectroscopy and thermogravimetric analysis–mass spectrometry. However, the lifetimes of the electroluminescence devices fabricated from InP/ZnSe/ZnS QDs with a thick or a thin ZnS shell show surprisingly the opposite result to the material stability of QDs, where the QD light-emitting diodes (QD–LEDs) with a thick ZnS shelled QDs maintained its luminance more stable than that with a thin ZnS shelled QDs. This study elucidates the degradation mechanism of the QDs and the QD light-emitting diodes based on the results and discuss why the material stability of QDs is different from the lifetime of QD–LEDs.

Chapter 6 suggests a method how to improve a printability of EHD jet printing when QD materials are applied to QD ink formulation, where this work introduces the application of GaP mid-shelled InP QDs as a role of surface charge in EHD jet printing technique. In general, GaP intermediate shell has been introduced in III–V colloidal InP quantum dots (QDs) to enhance their thermal stability and quantum efficiency in the case of type-I core/shell/shell heterostructure InP/GaP/ZnSeS QDs. Herein, these highly luminescent InP/GaP/ZnSeS QDs were synthesized and applied to EHD jet

printing, by which this study demonstrates that unreacted Ga and Cl ions on the QD surface induce the operating voltage of cone jet and cone jet formation to be reduced and stabilized, respectively. This result indicates GaP intermediate shell not only improves PL QY and thermal stability of InP QDs but also adjusts the critical flow rate required for cone-jet formation. In other words, surface charges of quantum dots can have a significant role in forming cone apex in the EHD capillary nozzle. For an industrially convenient validation of surface charges on the QD surface, Zeta potential analyses of QD solutions as a simple method were performed, as well as inductively coupled plasma optical emission spectrometry (ICP-OES) for a composition of elements.

Beyond the generation of highly emissive InP QDs with narrow FWHM, these studies talk about the connection between QD material and QD devices not only to make it a vital jumping-off point for industrially feasible applications but also to reveal from chemical and physical standpoints the origin that obstructs the improvement of device performance experimentally and theoretically.

Keywords

Colloidal quantum dot, Cu doped InP, surface chemistry, QD stability, QD device.

Fraunhofer IAP
Geiselbergstr. 69
14476 Potsdam-Golm, Germany

This doctoral thesis originated from collaborating with the Fraunhofer Institute for Applied Polymer Research (IAP) and the University of Potsdam.

Acknowledgments

First of all, I would like to express my deepest gratitude to Dr. Armin Wedel, who is the greatest advisor in my doctoral course and my boss in division director of functional polymer systems at Fraunhofer IAP. He gave me a lot of opportunities to be able to carry out the research projects under excellent conditions with academic freedom and financial supports. Moreover, with an honest attitude rather than words, he always showed us how to harmonize and work with colleagues in our laboratory, and how to organize and proceed with research projects during my doctoral course. These have been a great inspiration to me, as well as my Ph.D. research, and have become great nourishment for the journey of my life.

Above all, I would like to sincerely appreciate Prof. Dr. Andreas Taubert, who is my Doktorvater at the University of Potsdam. Whenever I asked many questions related to academic topics, English writing, and university administration since I started my Ph.D. course, he always gave me thoughtful and detailed answers despite his extremely tough schedule. Publishing papers along with his guidance was a great honor to me, where his teaching became my big primary picture of this doctoral thesis and the basement of my research style.

As working and researching at Fraunhofer, I would like to appreciate Dr. Christine Boeffel since she always gave me thoughtful advice and talks, whenever I had a problem, and discussed paper writing and doctoral thesis despite her busy schedule. Always thoughtful and intelligent, Dr. Manuel Gensler offered sparkling ideas and advised a better way whenever I ran into difficulties during a project. It is undeniable that much of my research has been greatly influenced by his advice and ideas, and I really appreciate him so much. Also, many thanks to Stefan Kröpke, an expert on the instrument in Fraunhofer and an extremely experienced researcher. He is my teacher on the use of the equipment and its theoretical basis, and a good friend. When I first came to Germany, Dr. Yohan Kim and Hyung-Seok Choi, my Korean colleague, helped me to adapt well to Germany. All fabrication of the QD-LEDs in my research was conducted by Dr. Yohan, and the result also made a tremendous contribution to this doctoral thesis. As a faithful Christian, Dr. Yohan Kim is my colleague and good friend, and I would like to thank him again. Hyung-Seok Choi, who did the Ph.D. course with me in Fraunhofer IAP, spent the most time discussing with me in the same office and gave me a lot of inspiration and various perspectives on academic challenges. Many thanks to my friends and colleagues Bert Fisher and Franziska Ebert. When I faced difficult circumstances and many complicated regulations in the office and laboratory, they always actively helped me, and I would never forget their warm help. Not only that, they gave me excellent knowledge about German beer, food, and culture, which allowed me

to adapt and study well at Fraunhofer IAP and Germany. In addition, I would like to thank Dr. Christina Günter (XRD), Kathrin Gessner (TGA MS), Dr. Melanie Bartel (NMR), Minh Thu Tran (TEM), Dr. Andreas Bohn (TEM) for their technical support of the measurements and their technical review. In particular, Kathrin Gessner inspired me a lot in TGA MS analysis to expand the scope of quantum dot analysis. I respect her measuring skills, and I always appreciate her.

Many thanks to the researchers, Dr. Chul-Jong Han, Dr. Kyoungwon Park, Dr. Hong-Joo Song, Jeong-Min Yi, and Dr. Min Seok Oh in Korea Electronics Technology Institute (KETI). In particular, Dr. Chul-Jong Han helped me the most to pursue my Ph.D. at Fraunhofer IAP in Germany, and I really respect his warm personality as well as his outstanding academic brilliance and tremendous industrial knowledge. Also, the genius quantum physicist Dr. Kyoungwon Park helped me to analyze various simulations beyond the scope of chemistry. He stayed for two months at Fraunhofer IAP in Germany as a visiting scientist, and it was a pleasant time for me, and I could feel his warm humanity, and I respect it. Also, I would like to thank researcher Jeong-Min Yi, who helped me in LSC fabrication and transition metal doping research.

Lastly, I would like to express my sincere gratitude to my wife, Hea-Jin, who is by my side and protects me with love. Perhaps if she had not been with me, I would not have successfully completed Ph.D. course in Germany. I would also like to sincerely thank my mother, Mrs. Geum-Young Yoon, who is the greatest supporter in my life, and my younger sister, Jimin Kim. Warm advice and sincere talks from my honorable mother helped me greatly in my studies and living in Germany. Many thank Mr. Frank Andraschko and Mrs. Innes Andraschko as my German family, The time, when we had dinner and BBQ at home, gave me a relaxing break time from my busy Ph.D. course, which allowed me to forward my advanced further research. Finally, I would like to apologize to many people I didn't mention in this acknowledgment, and I sincerely thank everyone.

Thanks again and best regards,

Jiyong Kim

27 October. 2022. Potsdam, Germany

Abbreviation Table

No.	Name	Abbreviation
1	Quantum dots	QDs
2	Light emitting diode	LED
3	1-octadencene	ODE
4	Indium acetate	In(Ac)3
5	Zinc acetate	Zn(Ac)2
6	Tri-n-octylphosphine	TOP
7	1-octanoic acid	HOA
8	1-octanoate	OA
9	Zinc stearate	ZnSA
10	1-octanethiol	OTT
11	Selenium	Se
12	Sulfur	S
13	Acetone	AC
14	Ethanol	EtOH
15	Tri(trimethylsilyl)phosphine	TMSP
16	Zinc octanoate	ZnOA
17	Tri-octylphosphine selenide	TOP–Se
18	Tri-octylphosphine sulfide	TOP–S
19	4,4',4"-tris(carbazol-9-yl)triphenylamine	TCTA

20	Molybdenum oxide	MoO3
21	Silver	Ag
22	Photoluminescence	PL
23	Photoluminescence quantum yields	PL QYs
24	Photoluminescence peak wavelength	PL WL
25	X-ray diffraction	XRD
26	Transmission Electron Microscopy	TEM
27	Nuclear magnetic resonance	NMR
28	Fourier Transform Infrared spectroscopy	FT–IR
29	Time–resolved photoluminescence	TR–PL
30	Ultraviolet-visible	UV-vis
31	Thermal Gravimetric Analysis	TGA
32	Mass spectrometry	MS
33	Near-infrared	NIR
34	Magic sized clusters	MSCs

List of Table

Table of Contents

1. INTRODUCTION

1.1. Quantum Dot

For the past two decades, "nanoscale science and technology," broadly defined as a new direction of modern research, have emerged and become a field of critical study in the modern high-tech industry.[1] These studies involve the functionality to characterize, design, and control artificially created nanostructures, the trends of which are manipulated and controlled under the nanoscale. More detailed, such boundary of trends embraces the range of research as various as material engineering, chemistry, physics, and biology. Moreover, such trend is a field that is evolving a very fast pace, and it is driven by the desire to manipulate nanomaterials with characteristic and enhanced properties, such as electrical and thermal conductivity, and optical response.[2] This research is currently evolving towards nanomaterials that can fabricate to perform versatile and complex roles, including functional materials with a highly selective and sensitive response, a conversion of current to visible light, or efficient energy storage and production systems.[2]

Nanomaterials are mentioned as an intermediate behavior between macroscopic solid and atomic systems, where inorganic compounds are composed of very few atoms, the properties of which are distinguished from that of a bulk solid and a single atom; that is, the properties of nanoscopic objects are not belonged to the range of their larger (bulk solid) or smaller (a single atom) counterpart.[3] Furthermore, this system has additional unique characteristics, many of which are not readily identified by a simple inference. These can be explained by the quantum mechanics, and it is the particle-wave duality (suggested by De Broglie), where any particle or quantum entity may be described as either a particle or a wave, the wavelength of which is inversely proportional to the particle's linear momentum.[3] In other words, when the size of physical system become comparable to the wavelength of the particles, the behavior of particle is well explained by the rules of quantum mechanics.[4] However, this quantum mechanics is not applied to the macroscopic materials, because the wavelength of which are much smaller than their size, and it can be well derived from the principles of classical mechanics. Therefore, the concept of particle-wave duality makes it possible to readily explain the behavior of carriers (electrons and holes) in a semiconductor nanocrystal.[3] On the other hands, a bulk inorganic semiconductor possesses conduction band electrons and valence band holes which are free to move inside the crystal, so their motion may be well matched to a linear combination of plane waves (with wavelength in the order of nanoscales).[3] In the case that the size of the semiconductor solid becomes comparable to corresponding wavelengths, a free carrier has constrained in this structure, behaving as a particle in a potential box.[5] The Schrödinger equation's solutions indicate the waves

confined in the potential well, and the energies from two district wave functions are, in principle, not continuous. That is, the system of the particles shows a discrete energy level spectrum, for which this behavior is usually called as “quantum-confined.” As a result, the more shrunk down a semiconductor crystal is to a few nanometers, the stronger the quantum-confinement effect is.[3] Therefore, the consequent system is referred to as a "quantum dot" (QD).

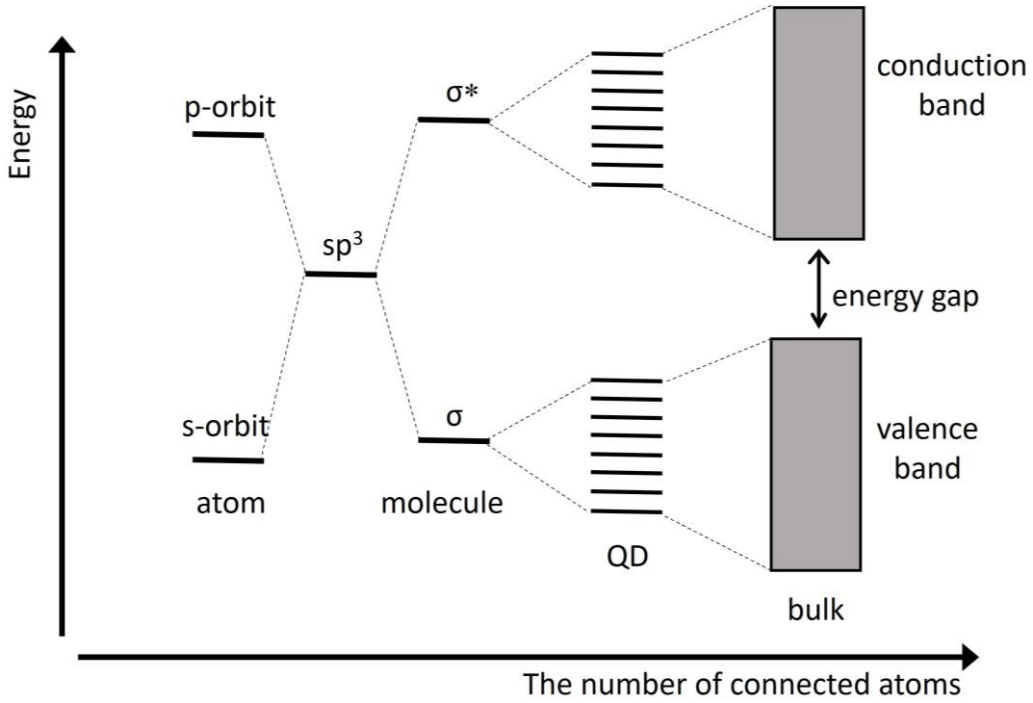

Figure 1. Electronic energy levels depending on the number of bound atoms.[6]

From the chemist's standpoint, the basic unit of an object is an atom composed of electrons and nuclei, where each chemical element has a certain number of electrons that orbits surrounding a single nucleus. However, the elements with more electrons than hydrogen atoms make it complicated to calculate the energy levels because the interaction between electron-electron should be considered, as well as that between nucleus and electron.[3] In this case, each electron is involved in the atomic orbital with a discrete energy level. The atomic orbitals are designated as spherical s-orbital, cubic-like p-orbitals, and a more complex d- or f- orbitals, which follow the Octet rule and the Pauli beta principle, the former one being the tendency of atoms to prefer to have eight electrons in the valence shell, the latter one being the rule about orbital with one spin up and one spin down.[6] In the case of methane (CH_4), the sp^3 hybridized carbon linearly forms a sigma (σ) bonding with s- orbitals of neighboring hydrogen atoms, where these orbitals share their electrons which are delocalized throughout a

molecule. Different from atoms and molecules, the energy structure of bulk solids is no longer discrete energy levels but consists of broad bands of energy.[6] Figure 1. illustrates the merge of the discrete energy levels of the atomic orbitals with increasing the binding atoms, where it becomes merged into energy bands; thus, QDs can be classified as a hybrid state between a single molecule and a bulk material. Therefore, these systems of QD are hard to explain with the same model used for bulk material, the electronic structure of which can be regarded as an intermediate between an atomic system and the band structure of a bulk solid. Thus, the energy levels of QDs are discrete with a larger density and a smaller spacing than the corresponding levels of an atom or a small atomic cluster. With the concepts in bulk solid such as energy bands and band gap, The highest and lowest atomic levels interact and combine to form the valence and the conduction bands of QD, respectively. Accordingly, the energy gap between the valence and conduction bands indicates the band gap of QD.

1.2. Quantum Confinement Effects

Size-dependent optical properties of colloidal semiconductor particles have been reported since the early twentieth century[7], even though this phenomenon was defined in terms of "size quantization" during 1980s.[2, 8-9] The most impacting effect in semiconductor nanoparticles is the widening of the band gap of them between the highest occupied electronic levels and the lowest occupied hole levels by varying their size,[10] where minimum energy to create an electron-hole pair in a QD is defined by its band gap.[11] These optical properties are mainly distinguished from the corresponding bulk material. This effect can be interpreted by "quantum confinement effect" using particle in a box model, the mathematical equations of which are obtained for the confinement energy and energy gap of QDs.[12] As for theoretical study of the quantum confinement effects on QDs, Onyia, Al et al., showed that discrete electronic states, which paly a fundamental role in optical and electronic properties, arose at conduction and valence bands of QDs, where they demonstrated their energy gap can be tuned by varying the size of QDs.[12]

Particle in a box model is described as a free particle moving in a limited space surrounded by impassable barrier. The basic model of that is a one-dimensional system where a single particle of mass (m) is confined in a box of length, L, where the Schrödinger equation is applied to obtain the wavefunction and energy levels of a particles in one dimensional box.[13-14] The confinement energy of a particle in the one dimensional box is as below (Equation 1):

$$E_n = \frac{n^2 h^2}{8mL^2} \quad (1)$$

The above equation demonstrates that the particle's energy is quantized in the lowest amount of energy of the particle at n=1, not zero as below (Equation 2).

$$E_n = \frac{h^2}{8mL^2} \tag{2}$$

However, two particles (the electron and hole) are strongly confined inside QD rather than one particle, and they cannot escape from QD but move freely within the dot, according to the particle in a box model. Therefore, Onyia et al. suggested some adjustments to compensate for their resultant mis-interpretation, in which the factor that QDs are geometrically spherical in shape rather than square; that is, the length of the box L is replaced to radius R and the masses of the electron and hole are changed by their effective masses.[12] Thus, the below equation corresponds to the equation of the ground state confinement energy of the electrons in QDs (Equation 3):

$$E_n = \frac{h^2}{8m_eR^2} + \frac{h^2}{8m_hR^2} \tag{3}$$

However, this Eq. 3 indicates the model of electrons in QDs that freely move in a vacuum state. Indeed, the electrons are present inside bulk semiconductor crystals with constant movement, so the energy band gap of the bulk counterpart describes the baseline energy of the QD system; thus, the energy gap of QD is expressed by the sum of the energy gap of bulk semiconductor and the confinement energy of QD (the electrons and holes), as like below.[12]

$$E_{g\ (QD)} = E_{g\ (bulk)} + \frac{h^2}{8R^2}\left(\frac{1}{m_e} + \frac{1}{m_h}\right) \tag{4}$$

Eg (bulk) is the energy band gap of the bulk counterpart, h is the Planck's constant, R is the radius of the QD, m_e is the effective mass of electrons and m_h is effective mass of hole. In this equation, the electrons and holes are considered independently because the coulomb interaction between them is not that strong to make a bound exciton at nano scales.[8, 12] This equation shows the discrete electronic states arisen at conduction and valence bands in QDs, which become larger when QD size decreases due to the increase of the confinement of electrons and holes within the QDs. This is referred as to "quantum confinement effect" that observed when the size of QD is close to the exciton Bohr radius.[12]

In principle, the exciton Bohr radius is the separation between electron and hole in an electron-hole pair, where the excited state of semiconductor QD is called as an "exciton", the meaning of which can be simply considered as an analogon to as a hydrogen atom, where the hole is proton.[3] Thus, the classic Bohr model can utilize to calculate the average distance between the electron and hole in semiconductor QDs as below:

$$a_{exc} = \left(\frac{1}{m_e} + \frac{1}{m_h}\right) \cdot m_0 \varepsilon a_H \tag{5}$$

Where a_{exc} is the exciton Bohr radius, m_0 = 9.11 * 10^{-31} kg is the electron mass, a_H = 52.9 pm is the hydrogen Bohr radius, and ε is the dielectric constant of semiconductor QDs. For example, the exciton Bohr radius of InP indicates 10.2 nm (Table 1), so that the particle size below that exciton Bohr radius (10.2 nm) exhibits size-dependent optical properties.

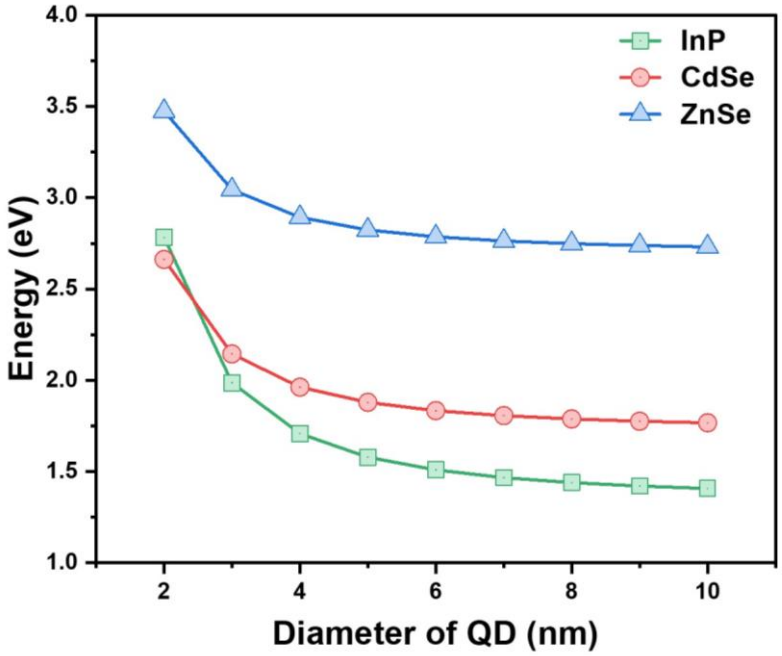

Figure 2. Confinement energy *versus* diameter of QD for CdSe, ZnSe, and InP QDs.

Table 1. Material constants for semiconductor nanoparticles.[15-16]

QD	m_e / m_0	m_h / m_0	Dielectric constant	E_g (bulk)	exciton Bohr radius
CdS	0.19	0.8	5.7	2.58 eV	2.0 nm
CdSe	0.13	0.45	5.8	1.73 eV	3.0 nm
InP	0.073	0.65	12.6	1.35 eV	10.2 nm
PbS	0.105	0.105	17.2	0.41 eV	17.3 nm
ZnSe	0.145	0.75	8.6	2.7 eV	3.7 nm
ZnS	0.23	0.184	8.3	3.6 eV	4.3 nm

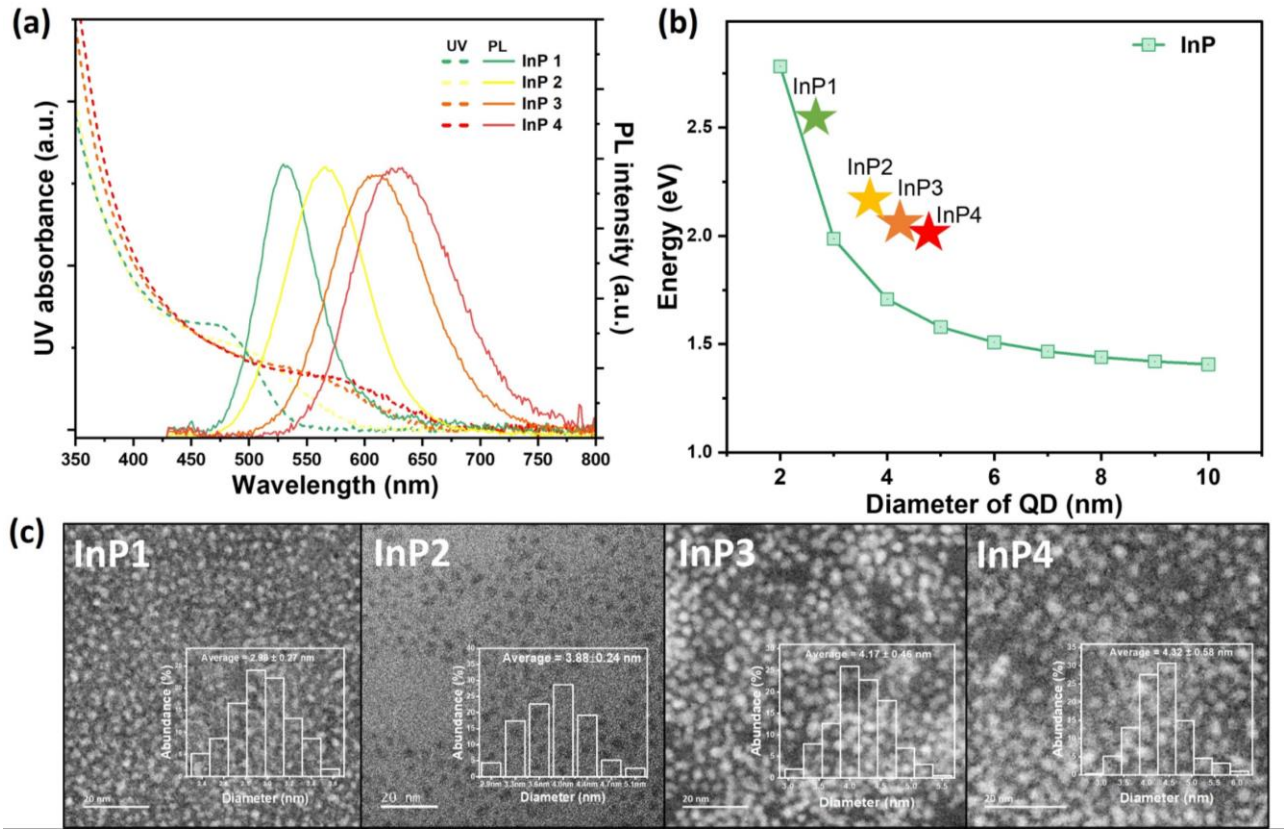

Figure 3. (a) PL and UV spectra of InP QDs according to their size distributions, and the corresponding (b) confinement energy and (c) TEM images from InP1 to InP4 QDs, all data of which are synthesized and measured in Fraunhofer IAP.

1.3. Transition Metal Doped QDs

Transition metal ion (Cu^+, Mn^{2+})-doped semiconductor QDs have shown unique photo-physical properties such as strong thermal stability, large Stokes shift, broad emission bandwidth, and long excited state lifetime.[17-21] Cu doping in conventional II–VI or III–V QDs creates intra-gap sates above the valence band, by which energy down-shifted photoluminescence (PL) appears (Figure 4). In the case of Mn doping, the exciton energy of the host QD is transferred to the dopant, which also generates phosphorescence with a lower energy than the host exciton energy.[22]

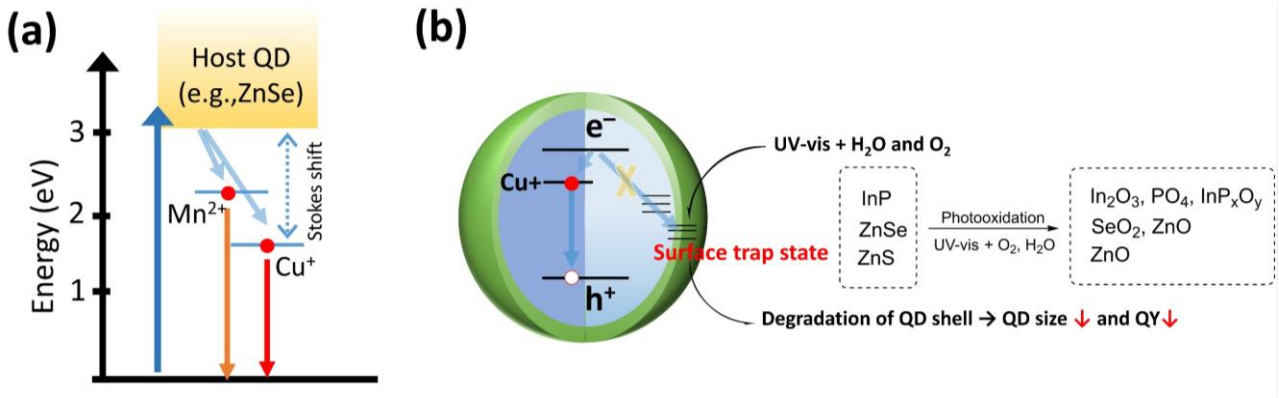

Figure 4. Illustrated (a) band gap of Cu^+ and Mn^{2+} doped QDs (e.g., Cu^+, Mn^{2+} doped ZnSe) and (b) the surface degradation model of Cu^+ doped QD.

Such non-excitonic transitions of doped QDs naturally entail appreciable Stokes shifts that beneficially lead to the suppression of inter-QD self-absorption, which is highly required particulary in the fields of color conversion-based light-emitting diodes (LEDs) and luminescent solar concentrator (LSCs). A principal disparity of Cu *versus* Mn doping is not largely dependent on the type of host QD due to the d orbital intrashell electronic transition ($^4T_1$–$^6A_1$), Cu-doped counterparts can exhibit a wide PL tunability typically in the range of blue-to-near-infrared (NIR) by varying the band gap (i.e., composition and size) of the host QD (Figure 4).

Cu-containing metal chalcogenide I–III–VI QDs with the representative compositions such as (Zn)$CuInS_2$ and (Zn)$CuIn(Se,S)_2$ are regarded as promising candidates for non-toxic (i.e., Cd-, Pb-free) emitters that can produce not only large Stokes shifts (e.g.,4300 meV) due to the defect-associated radiative recombination but also widely tunable emissivity in the green-to-NIR range and high PL quantum yields (QYs) greater than 80%.[23-29] By taking advantage of these beneficial attributes, they have been successfully explored as effective energy down-shifted emitters for applications in high-efficiency white LEDs,[24-25] LSC devices,[28-29] and the biofield.[30] Meanwhile, recently, Klimov's group

revealed that in $CuInS_2$ (CIS) QDs, the origin of the smearing of the absorption edge into the longer wavelength (also called 'tailing') was due to the energy level of Cu^+, and not of Cu^{2+}.[31] This absorption smearing of $CuInS_2$ QDs in turn makes Stokes shift somewhat limited.

In this respect, Cu-doped QDs particularly with environmentally benign host compositions such as ZnSe and InP may exhibit an even larger Stokes shift compared to the above-mentioned I–III–VI counterparts. When Cu ions are properly doped into ZnSe QDs that are capable of emitting in the near-UV region, the resulting color usually ranges from blue to green, depending on the size of the host QD.[32-35] The highest PL QY of Cu-doped ZnSe (ZnSe:Cu) QDs reported to date is still as low as 20% even after ZnS shelling presumably due to the synthetically immature shelling.[32] Meanwhile, compared to ZnSe:Cu QDs, InP:Cu QDs can exhibit longer emission wavelengths due to a lower band gap of InP versus ZnSe host QDs. Typical emission coverage of InP:Cu QDs ranges from red to near-IR by virtue of the variation of the size (or band gap) of the InP host.[36-39] Single shell-based InP:Cu/ZnSe[36] and InP:Cu/ZnS QDs[37] possessed similar PL QYs of ca. 40% from the sole dopant PL. Although a much higher PL QY of 66.4% was reported by Guo's group, their InP:Cu/ZnS QDs consisted of the simultaneous emissions of excitonic and dopant transitions.[38] Such dual PL likely alludes to the incomplete Cu doping to individual InP host QDs, resulting in the unintended mixture of undoped and doped QDs in the ensemble. To attain more efficient InP:Cu QDs, Kim et al. recently adopted the double shell scheme of ZnSe inner and ZnS outer shells from the state-of-the-art undoped InP QD heterostructure, where the ZnSe layer functions as an effective lattice intermediator between the considerably lattice-mismatched InP core and ZnS shell, allowing for the mitigation of core/shell interfacial strain toward higher emissivity.[40-41] The resulting InP:Cu/ZnSe/ZnS QDs with a dopant PL only peaking at 652–676 nm produced the highest-ever PL QY of 57–58%.[39]

1.3.1. Transition Metal Doping Mechanism in QD

Doping all colloidal QDs, such as InP, ZnSe, and CdSe, is still open to challenge due to the extremely small volume of them. To overcome this challenge, Pradhan et al. proposed methods to decouple the doping process via the steps of nucleation and growth, which allows us how to establish the transition metal doping strategy for nearly all colloidal QDs.[18] Basically, a surface area of QD is relatively large at over 35% compared to its bulk counterpart, and wet chemical synthesis of colloidal QDs offers the possibility for transition metal ions to be doped inside the host QDs. Despite this natural advantage of QD, the host QDs are passivated by surface ligands that are included in the strongly binding species, like anionic carboxylate and thiolate ligands. Different from a doping system on bulk

material, these strongly bound ligands on QD surface often disturb a diffusion of transition metal ions into nanocrystal lattice, resulting in the status of cation adsorption on QD surface.

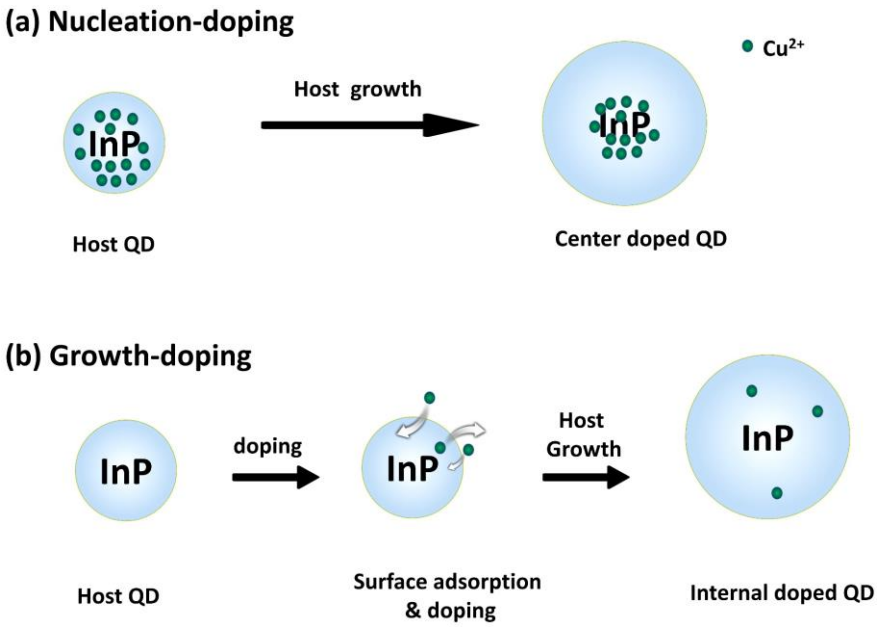

Figure 5. Illustrated schematic (a) nucleation- and (b) growth doping.[18]

Figure 6 shows two different strategies that are nucleation-doping and growth-doping, respectively. In nucleation doping, dopant metal ions are introduced into the reactor simultaneously when host precursors form small host QDs, where dopant metal ions are deeply incorporated inside the host QD and can form inorganic compounds with host anion precursors.[18] After nucleation, additional host precursors are then introduced for further growth of the host QDs. Then a reaction temperature increases to a high temperature of over 240°C to induce a thermal decomposition of host precursors. This process has a similarity with core/shell heterostructure QDs, where the center doped QD and the pure host layers without dopants resemble core and shell, respectively.[18] However, growth-doping strategy utilize a diffusion of dopant metal ion from liquid phase into nanocrystal lattice. At first, small host QDs are independently prepared for transition metal doping, and dopant ion precursors are introduced into the reactor with high temperature. Herein, we can visually observe the whole process of metal ion doping via a comparison of host PL emissions with dopant PL emissions, where the dopant PL emissions increase with decreasing the host PL emission due to the formation of dopant level inside the band gap of the host QD. However, in the case of nucleation-doping, dopant metal ions are deeply located inside the host lattice, so that dopant PL emissions are early quenched in the step of nucleation-doping, different from growth-doping.[18]

1.3.2. Diffusion Barrier

As mentioned in 1.3.1. Transition Metal Doping Mechanism in QD, growth-doping requires a diffusion process of dopant metal ions to form the dopant level inside the band gap of QD. However, this diffusion is bidirectional toward both the inner and outer of QDs, so that penetration of dopant ions into the interior is quite limited due to the cation-cation repulsion with QDs (Figure 8).[18]

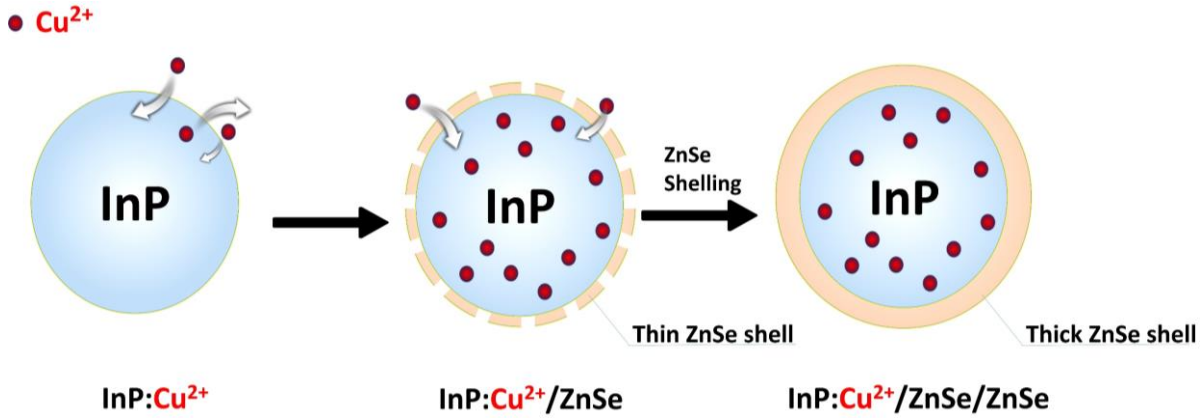

Figure 6. Illustrated schematic Cu-doping on the surface InP QD with ZnSe diffusion barrier.

Therefore, this bidirectional characteristic of dopant diffusion can be overcome by using diffusion barriers, such as ZnSe and ZnS shells. Previously, Xie et al. demonstrated that Cu-doped InP QDs emitters were synthesized by epitaxial growth of a ZnSe diffusion barrier for the dopant ions.[42] In particular, upon forming the ZnSe diffusion barrier on Cu-doped InP QDs, the host PL emissions of InP QDs were rapidly suppressed and quenched with increasing Cu-related dopant PL emissions. In other words, this ZnSe diffusion barrier not only suppresses the loss of dopant ions that spread out of QD but also improves the quantum efficiency due to the enhanced quantum confinement by type- I core/shell heterostructure.[18] In addition, based on Hard-Soft Acid-Base Theory (ref),[43] Mn^{2+} is a harder Lewis acid compared to In^{3+} which is located in borderline Lewis acid. Thus, the Mn^{2+} precursor should be significantly less reactive than In^{3+} if they both have the same anion complex. However, Cu^{2+} and Cu^{+} are classified as borderline and softer Lewis acids, so that in many cases, Cu doping onto InP QD is more reactive than Mn^{2+} doping onto it. As a result, both a utilization of diffusion barrier and reactivity of dopant ions should be considered before synthesis of transition metal doped QDs.

1.4. Surface Chemistry of QD

Ligand stabilized quantum dots (QDs) are composed of a crystalline inorganic core and organic molecules on the surface. It is a similar relationship between metal ions and ligands in inorganic metal compounds. That is why organic molecules present in QD surface are called as a "surface ligand." In particular, the surface area of a QD is relatively large, with an exposure atom ratio of above 35%.[44] Thus, the role of surface ligands is considerably critical in the aspect of electrical and physical properties.

Scheme 1. Nanocrystal ligand binding motif according to covalent bond classification concept.[45-48]

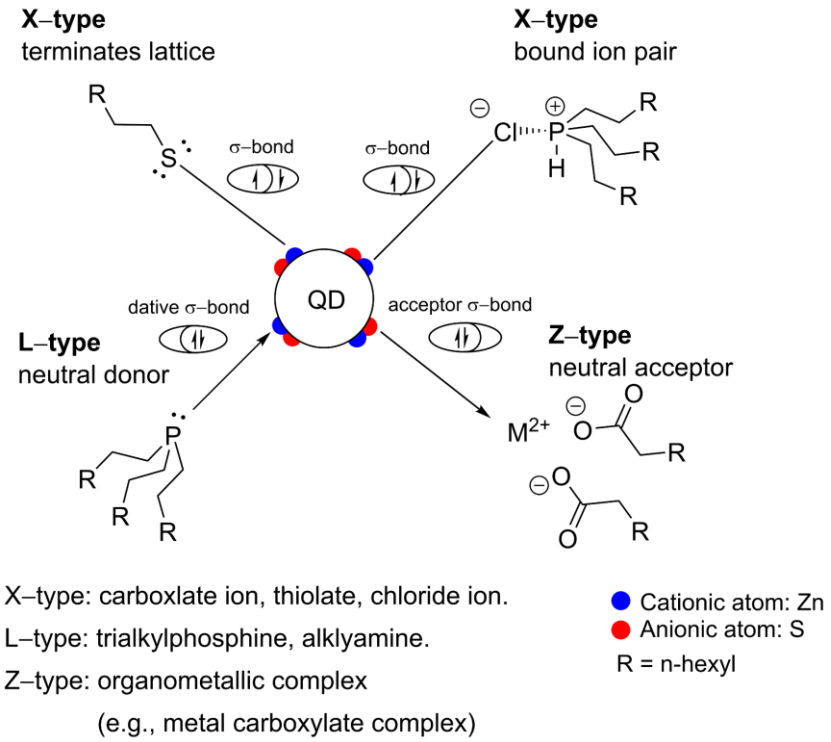

Ligands coordinating with the inorganic QD core are classified as X–ligands (anionic, one-electron donor), L–ligands (neutral Lewis bases, two-electron donor), and Z–ligands (Lewis acid, two-electron acceptor) (Scheme 1).[45-48] This covalent bond classification concept is based on their interaction as an electron donor or an acceptor with the surface charge, and introduces the concept of valency number and ligand bond number instead of the fundamental concepts of formal oxidation state and coordination number.[45, 48] Basically, this method is concerned only with those compounds which are well described by the covalent model, including the infinite lattice compounds, and it can be applied to the covalent compounds of all elements. More detailed, not only be the concept of formal oxidation

state not used for the organization of compounds, but the coordination number is also replaced as the number of attached ligand atoms to the central metal atom.[45] That is why this concept is useful to describe the relationship between the inorganic core and organic shell of colloidal QD due to the relative simplicity of interpretation, as well as organometallic compounds.

Different from organometallic compounds, QD can include at least a few inorganic compounds in a dot and extend its size until 10–15 nm at the largest, so it has a lot of ligand-binding sites on the surface were exposed cation or anion atoms predominantly.[3] In the process of wet chemistry, various organic and inorganic chemicals, as precursors and solvents, are in general introduced to form inorganic seed complexes from monomers and grow particles, many of which are classified as coordinating ligands to bind to the QD surface or non-coordinating ligands to be eliminated after the purification step. Therefore, a mixture of precursors and solvents is directly attached to the QD surface mainly according to their cationic or anionic functionality, mainly based on Le Chatelier's principle; thus, it makes it difficult to verify individual binding properties of the surface ligand through concepts of formal oxidation state and coordination number.

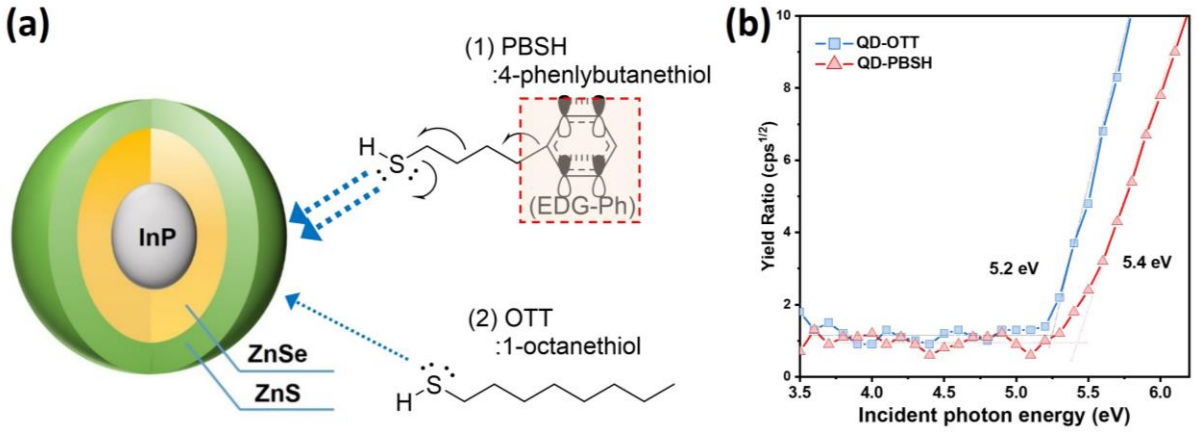

Figure 7. (a) InP/ZnSe/ZnS QDs with PBSH or 1-octanethiol (OTT) ligands, and (b) their valence band maxima measured by photoelectron spectroscopy in (AC-2), respectively.[49]

In general, wet chemical QD synthesis often induces metal enrichment on the QD surface at smaller particle sizes.[50-51] This surface charge is compensated by anionic X-type ligands like aliphatic carboxylates. Charge compensation can also be associated with proton transfer[47, 52-54] or trimethylsilyl transfer to drive ligand exchange.[47, 55] This makes it difficult for researchers to study the role of surface ligands due to their proton transfer with other ligands. Moreover, the dipole moments of the surface ligands may tune the QD bandgap according to the structure of the molecules, and the functional group

of the ligand affects surface trap states.[49, 56-57] Considering colloidal stability, ligands like alkanoates with branched alkyl chains can provide further stabilization and processability by preventing chain-chain interdigitation.[58]

Figure 7 shows the valence band maxima of QD-PBSH and QD-OTT (OTT, 1-octanethiol) measured by photoelectron spectroscopy (AC–2), and the resulting values represented 5.2 and 5.4 eV, respectively.[49] These results are consistent with the tendency from previous reports, which indicates the negative dipole moment of the ligands tunes the energy level of QDs.[59] For example, Moon et al. demonstrated that the energy level of QD can be affected by thiol ligands with electron donating group (EDG) like phenyl group, where the negative dipole moment of the ligand was one of the influencing factors that change the level of valence band maximum.[56]

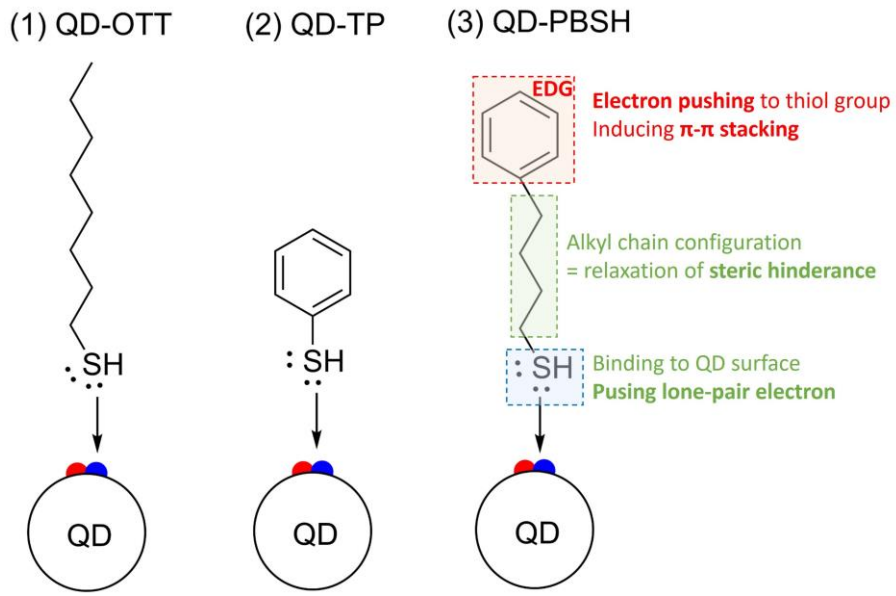

Figure 8. The comparison of surface ligands, (1) OTT, (2) thiophenol, and (3) PBSH, present on QD surface.

Figure 8 shows the QDs with OTT, TP, and PBSH as surface ligands. As mentioned above, the surface ligands can make differences in electronic property, such as the charge transport property in QD devices. In particular, the fully conjugated TP molecule is a hexagonal planner structure with sp^2-hybridized carbon (i.e., a resonance form); thus, it makes a crystalline-like form that induces the overlap of perpendicular p orbitals. This leads the better charge transporting through the overlapped π-electron clouds between neighboring ligand molecules than QDs with aliphatic alkylthiol ligands. However, this ligand modification impacts the QD surface not only electronically but also physically because it usually accompanies the structural transformation of ligand molecules, for example, with

additional phenyl groups like the electron donating group. Without spacing-freedom by alkyl chain configuration, the fully conjugated ligand molecule like TP often reveals poor solubility and self-aggregation in an organic solvent system, so that the elongated alkyl chain is usually applied in between functional groups (i.e., a QD binding site) and a phenyl group to improve their solubility and the feasibility with QD devices. Basically, the elongated alkyl chain is sp^3 hybridized carbon without perpendicular p orbital, so it is rational to have low charge transporting properties compared to the ligands with sp^2 hybridized carbon (e.g., QD-TP in Figure 6). Nevertheless, this ligand design, which considers both an electronic and a steric effect, is one of the most useful and reasonable tactics for the structure of the surface ligand. Consequently, the electron abundance due to electron-pushing by EDG (e.g., phenyl group) affects the dipole moment of colloidal QD, resulting in the manipulation of quantum confinement of QDs.

InP QDs are a potential candidate to replace the Cd–based QDs because of the Restrictions of the Hazardous Substances (RoHS) directive.[60] The addition of ZnSe/ZnS multi-layer on InP core leads to near-unity optical efficiency, but is challenging.[41, 61] For successful commercial application in QD electroluminescent (EL) devices, controlling the surface properties and the corresponding optical and electronic properties is critical.[62-63] However, the surface chemistry of commercially useful III–V colloidal InP type QDs like InP/ZnSe/ZnS is still rather unclear. This is in stark contrast to II–VI colloidal Cd–based QDs, with much better-known surface properties.[57, 64-67] Most studies have focused on Cd–based QD using ^1H, ^{12}C, and ^{12}P NMR (diffusion–ordered spectroscopy (DOSY) and nuclear Overhauser effect spectroscopy (NOESY)) to elucidate the binding status of surface ligands.[48, 53-55, 68-69] For a definite validation of the surface layer on a QD surface, methods like NMR, infrared (IR), ultraviolet-visible (UV-vis) spectroscopy, and mass spectroscopy (MS) should be combined. This is because a closely binding of ligands to the QD surface gives rise to peak broadening and shift. Besides the interaction of the ligand with the QD surface, this is also due to intermolecular interactions between individual ligands. In consequence, these interactions and resulting peak broadenings significantly complicate the analysis.

1.5. Stability of QD material and QD–LEDs

InP QDs are unstable in photoluminescence (PL) films and electroluminescent (EL) devices like QD–LEDs under ambient conditions without an inorganic barrier matrix as a film or overcoated layer, which obstructs the industrially feasible manufacturing process.[70] In general, QDs can degrade by oxidation, thermal decomposition, hydration, and UV exposure, causing the performance and lifetimes of QD–based LEDs to correlate with photo-, chemical, and thermal stability of QDs (Figure 9).

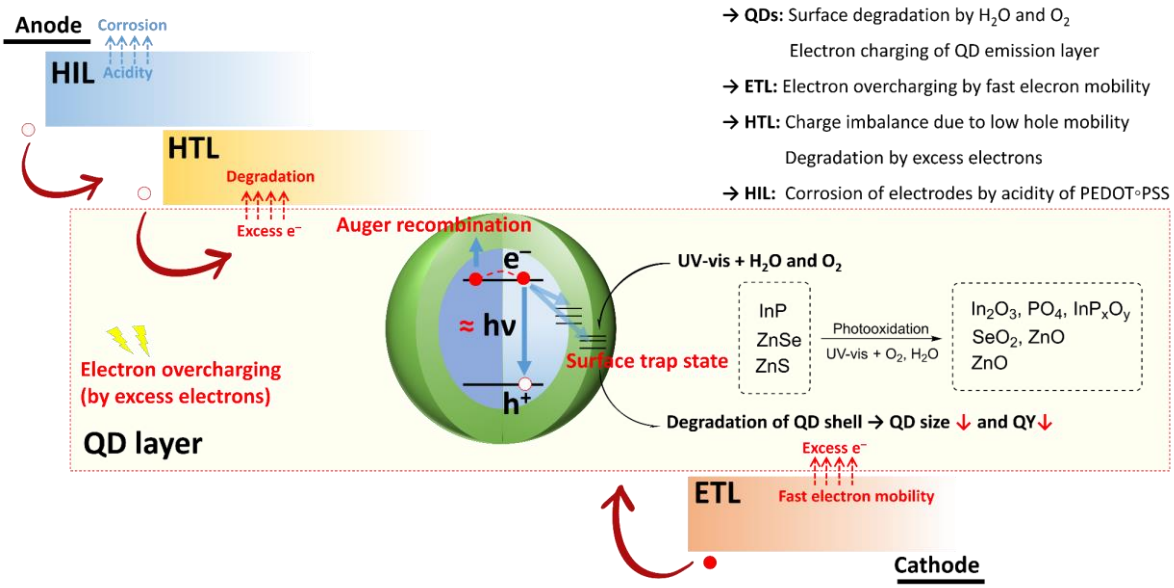

Figure 9. Schematic illustration of degradation of QD and QD–LED, which is organized from the previous report.[71]

Regarding the degradation mechanism of QDs: the surface oxidation by water and oxygen mainly affects photostability when QDs are photo-excited, inducing the generation of metal oxide compounds, like CdO, InO_x, and ZnO, onto the inorganic outmost shell.[70, 72] With this photo-oxidation on the QD surface, continuous exposure of oxygen and water induces the surface defect sites, giving rise to an irreversible decay of PL QY since this photo-corrosion dissociates cation and anion from QDs even though the core is overcoated by an inorganic shell.[73]

To improve the material stability of QDs, well-manipulated core/shell structures are suggested to protect the core from surface degradation and reduce surface defect sites by dangling bonds because type-I core/shell heterostructure induces excitons to be strongly confined in the core.[74] In particular, a formation of the intermediate shell, such as ZnSe and GaP, between the InP core and ZnS shell has led

to the remarkable enhancement of chemical and thermal stability and optical properties such as high PL QY of over 80% and narrow FWHM.[75-76] This is because the intermediate shell effectively alleviates the interfacial traps and lattice strain between core and shell.[77] Furthermore, increasing the shell thickness also provides better stability to the core, for which some works of the previous literature showed that thicker ZnS shelled QDs enhance both PL QY and photostability compared to QDs with thin ZnS shell overcoated on the surface of InP and CdSe cores.[78-79]

Moreover, thicker shelled QDs suppress energy transfer with closely packed neighboring QDs and alleviate an electron overcharging of the QD layer in QD–LED, leading to higher device efficiency via the suppression of nonradiative Auger recombination.[80-81] For example, Lim et al. synthesized CdSe/$Zn_{1-X}Cd_XS$ QDs with varying shell thickness when the CdSe core radius was fixed at 2.0 nm and fabricated QD–LEDs using them, in which the thicker-shelled QDs represented higher current efficiencies in the QD–LEDs despite the nearly identical PL QYs and PL decay times of the QDs in solution-based analyses.[82] As shown in Figure 3, negatively overcharged electrons in the QD layer (not recombined with holes) leak into HTL and induce the degradation of HTL materials due to their conjugated structure being vulnerable to decomposing, resulting in the main origin of short lifetimes in QD–LEDs.[71]

Among surface ligands, alkylthiol is one of the strongest surface binding species; thus, it offers better thermal stability than other ligands, such as carboxylic acid and tertiary alkylamine. For example, T. Kim et al. demonstrated that CdSe/ZnS QDs passivated by 1-dodecanethiol ligands enhance thermal stability compared to that passivated by oleic acid ligands.[83] However, the role of alkylthiol still remains controversial due to its concentration- and PH-dependencies. It has been reported that a high concentration of OTTs provokes low PL QY by hole trapping, which is known to be ascribed to a thiolate form of alkylthiols.[84-85] Furthermore, alkylthiols have other roles as sulfur donors to form sulfide compound with cationic metal ions, such as Zn and Pb, when reaction temperature reaches around 200°C, where the thermal decomposition of thiol groups is usually taking place. However, the role of not only a surface ligand but also a sulfur donor obstructs observing the ligand effect caused by alkylthiols, so that needs elaborate temperature control, maintaining a low temperature under 150°C to independently investigate the ligand effect.[86]

2. FUNDAMENTALS

2.1. Synthesis of Colloidal QDs

Colloidal QDs are chemically produced through wet chemical synthesis, in which nanoparticles are independently grown in the reaction solvent, basically different from the QD system.[14] In other words, colloidal QDs are classified as a subgroup of nanomaterial, most of which can be synthesized using wet chemical synthesis. In general, the reaction flask contains precursors dissolved in a liquid solvent mixture, which controls the seed nucleation and particle growth.[3] Sequentially, the precursors with atomic species are introduced into the reaction flask, forming nanocrystal building blocks. After introducing precursors, as molecules or chemical complexes, into the reaction flask, the precursors decompose to form the monomers that induce, in turn, the steps of seed nucleation and particle growth, where the activation energy of decomposition is supplied by thermal collisions or by a certain chemical reaction between precursors via the liquid medium.[14] In these processes, including seed nucleation and particle growth, "surfactant" is one of the critical parameter that adsorbs to the surface of inorganic QDs, affords the addition of monomers to access close to QD surface, and prevent self-aggregation with neighboring nanoparticles; that is, an suitable binding surfactant species is necessary for the growth of QDs because too strong binding suppresses seed nucleation and particle growth and too weak binding induces the broadening of particle size distributions with self-aggregation with QDs in the middle of reaction.[3] In addition, the thermal decomposition temperature of organic surfactants is formed at the range from 250 to 400°C, where is generally matched to steps of seed nucleation and particle growth. Thus, the selection of thermally stable surfactant should be considered beforehand despite an increasing trend of thermal decomposition energy of surfactant when bound to the QD surface.[3] After the wet chemical synthesis of QDs, various surfactants, including alkyl phosphine, phosphine oxide, aliphatic alkyl thiol, alkyl amines, and alkyl carboxylic acid, bind strongly to the surface and enable to be soluble in hydrophilic and hydrophobic organic solvents with different polarity and solubility, which also offers the flexibility that can be exchanged for other type surfactants with different functional groups, leading to various applications towards bio- and display industrial materials.[3] On the other hand, controlling the surfactant component ratio makes a difference in the size distribution and shape of QDs during seed nucleation and particle growth due to the role of surfactants that differently binds to the QD surface according to the binding properties of their functional groups.[87-89]

2.1.1. Seed Nucleation and Growth of QDs

InP is the most influencing and widely studied semiconductor nanocrystal as a colloidal QDs, PL emissions of which can cover from blue (~ 470 nm) to near infrared (near IR) (~ 850 nm) according to their size distribution due to strong quantum confinement regime.[3] However, II-VI and IV-VI QDs, such as CdSe and PbS QDs, have more ionic bonding characteristics as semiconductors than III-V semiconductors, such as InP QDs. Thus, this covalent bond formation of III-V InP QDs usually requires a high reaction temperature of over 300°C, a long reaction time to form their seeds and particles, and highly reactive precursors like tris(trimethylsilyl)phosphine (TMSP).[90]

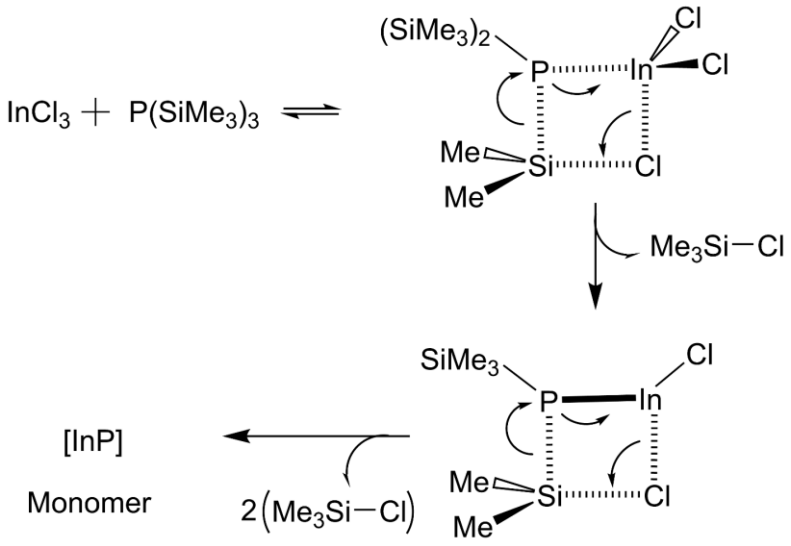

Figure 10. Schematic mechanism motif of Wells' dehalosilylation reaction between Indium (III) chloride and tris(trimethylsilyl)phosphine. It has been suggested that the intermediated II exists in oligomer from $[Cl_2InP(SiMe_3)_2]x$. Reproduced from ref.[91-92]

Figure 10 shows Well's dehalosilylation reaction using TMSP precursors as a common followed route to synthesize InP QDs.[91, 93-94] In this mechanism, trimethylsilyl groups are one of the powerful leaving group as a strong Lewis acid, which enhances the reactivity of TMSP when it reacts with Indium complex precursor. Besides, other candidates that can replace TMSP are suggested through the study of Allen & Bawendi to compensate for air-disposable properties, high cost, and toxicity of TMS3P,[95] for which PCl_3,[96] Na_3P,[97] gaseous phosphine (PH_3),[98] and $In(tBu_2P)_3$[99] are investigated whether they can overcome the resultant InP QD synthesized form TMSP.[3] Even though it showed the possibility partially in optical properties, such as PL QY and FWHM, these candidates

could not overcome the feasibility of TMSP toward industry material due to easily aggregated particles after synthesis and the difficulty of controlling the particle size distribution.

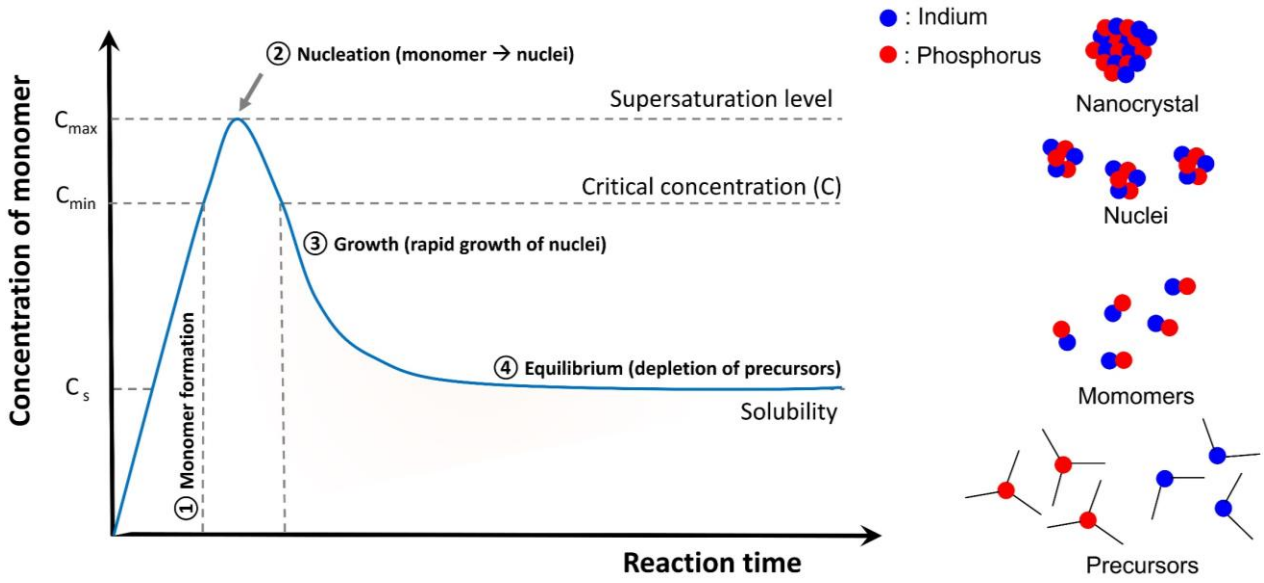

Figure 11. LaMer plot for the formation of monomer, nucleation, and resultant growth of nuclei. Reproduced from ref.[92, 100]

Figure 11 shows the formation of nanocrystals from precursors in wet chemical colloidal QD synthesis, which is governed by the two steps of nucleation and growth. The first stage (1) is the formation of monomer, where precursors' concentration rapidly decreases with dissociating their cation and anion counterparts from precursors and forming free monomers, that is, this stage is defined by a gradual increase in supersaturation of monomers with decreasing the concentration of precursors, with mostly increasing reaction temperature in the heating-up reaction of InP.[100] The second stage (2) is called a nucleation rate which climbs from an infinitesimal rate to a maximum, where we observe a rapid increase in nuclei concentration with decreasing the concentration of monomer. Thus, these nuclei gradually grow up to an appropriate size above the size of the monomer with maximizing the standard deviation of their particle size distribution.[100] The third stage (3) is the decline of the nucleation rate rapidly after the maximum point of supersaturation, which arises from the rapid growth of the nuclei present in a reactor.[100] In addition, a small amount of Early Time Ripening (ETR) is observed in this stage as dissolving some of the nucleated clusters back into a reactor solution,[101] resulting in nanoparticles with narrow FWHM and maximum average size. In the final fourth stage (4), the reaction is usually quenched with cooling down the reaction temperature for the isolation of nanoparticles *via* purification, but prolonged reaction at high temperature without cooling down would eventually induce the classical Ostwald ripening.[3]

In particular, the wet chemical colloidal synthesis of InP QDs indicate that separation of nucleation and growth is more difficult to be obtained compared to CdSe QDs due to the more covalent nature of the III-V precursors[90] and the fast depletion of monomers and precursors at high temperature.[92, 95] Due to this the more covalent nature of the III-V precursors, the chemist often obtains InP QDs with wider full widths at half maxima (FWHM) at around 35–40 nm, whereas in the case of the CdSe based QDs, the values of FWHM often shows below 25 nm at the same wavelength in InP QDs; that is, these high values of FWHM in InP QDs via wet chemical colloidal synthesis originate from their larger inhomogeneity in size, not from an intrinsic material's properties between CdSe and InP.[92]

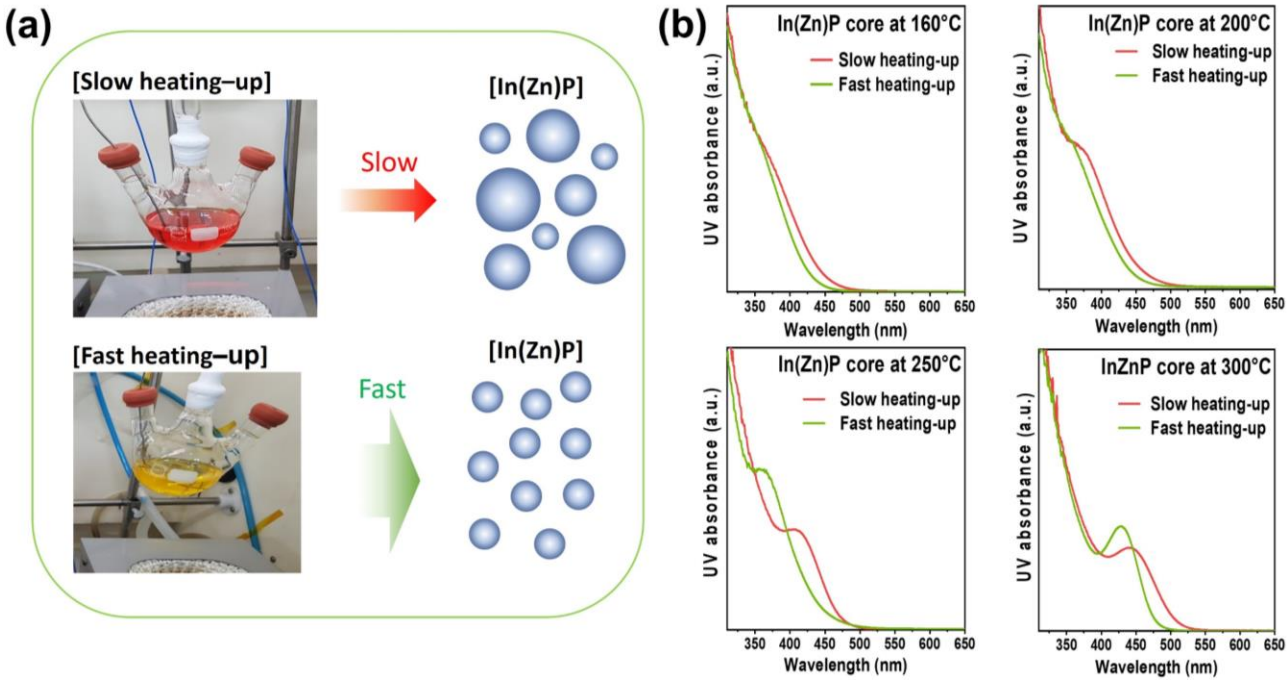

Figure 12. (a) The illustrated synthesis of In(Zn)P green core with slow and fast heating-up process, and (b) their UV-vis spectra at 160, 200, 250, and 300°C

Figures 12a and b show the synthesis of In(Zn)P green core with the fast and the slow heating-up rate, where in slow heating-up system, the growth of In(Zn)P nuclei emerged at lower temperature around 250°C compared to that with faster heating-up rate. These data indicate that nucleation at low temperature gives rise to the wider particle size distribution as represented to the corresponding 1st excitonic peaks in UV-vis spectra (i.e., peak broadening of 1st excitonic peak). Compared to the as-synthesized In(Zn)P QDs with a faster heating-up rate, In(Zn)P QDs with a slow heating-up rate

represented further growth of the core, which apparently indicates that core growth at low temperature has a negative effect on the QD size distribution.

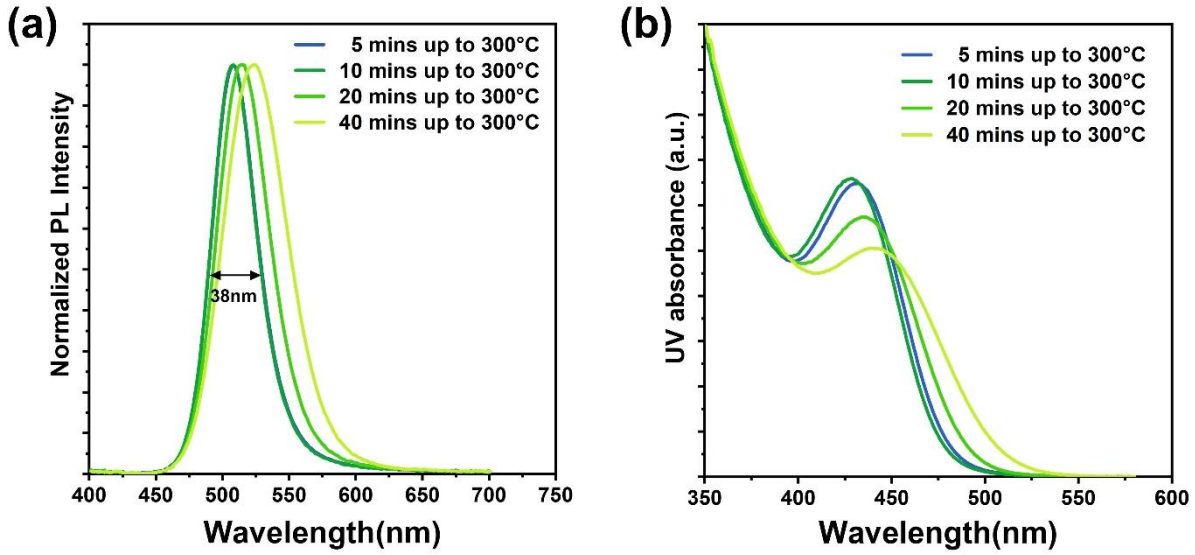

Figure 13. (a) PL and (b) UV-vis spectra of InP/ZnS green QDs by varying the heating up rate from 5 to 40 min / 300°C.

Figures 13a and b show PL and UV-vis spectra of InP/ZnS QDs with different heating-up rates from 5 to 40 min / 300°C, where the shallow ZnS shelling was performed to observe the resulting PL spectra. These data matched well with the synthesis of In(Zn)P QDs with the fast and the slow heating-up rate (Figure 12), indicating a linear correlation of the resultant particle size distribution with increasing the heating-up rate.

Basically, the heat-up synthesis has a relatively long period of nucleation compared to hot-injection synthesis because, in heat-up synthesis, a monomer is progressively produced by increasing the reaction temperature; that is, once nucleation is first triggered at a high temperature from monomers in solution, a few created nuclei can maintain a high supersaturation for an extended period of time.[100] However, slow heating-up rate induces the slow conversion of precursor to monomer, and the nascent nuclei begin to grow with consuming monomers , resulting in a decrease in supersaturation due to slow precursor conversion rate. As a consequence, this low concentration of monomer quenches the nucleation, by which the excess monomer, which does not form the nuclei, enable to continuously grow up the nanoparticles as offering itself as a resource. Therefore, a rapid heating-up rate progresses the production of monomers much quicker than the rate at those nuclei grow from monomers.[3] Under this condition, monomers can predominantly produce nucleation in a high concentration of monomer

at a high temperature without the growth of particles. As a result, a relatively small amount of monomer than the case of slow heating-up rate is fed to a much larger number of nuclei, sequentially leading to the reduced particle size.[100]

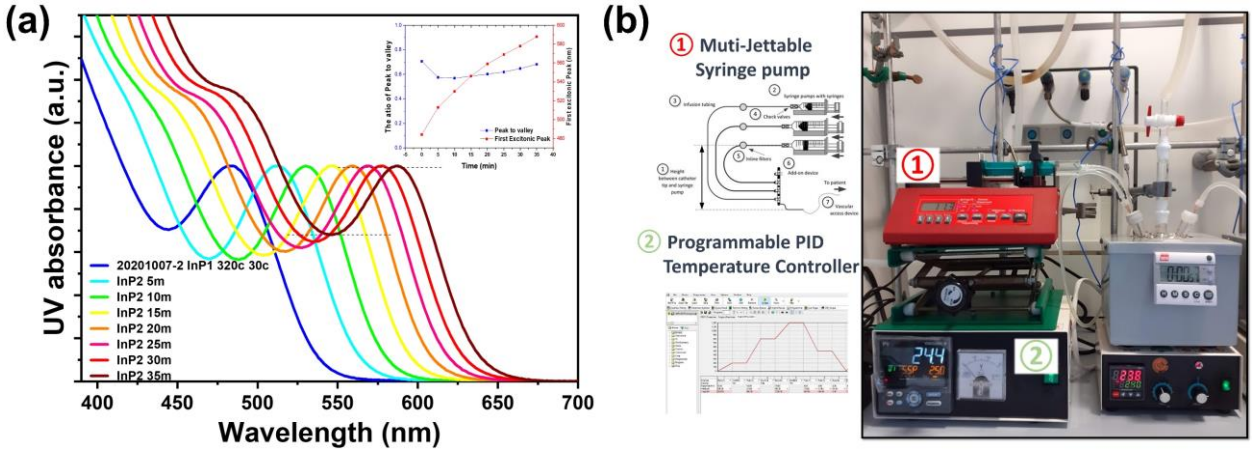

Figure 14. Spectral evolution of absorption of different-sized InP cores, which increase from small size (blue line) to big size (red line), and their actual synthetic equipment including multi-jetting syringe pump and programmable proportional integral derivative (PID) temperature controller.

Due to the more covalent nature of the III-V precursors, the low reactivity of indium precursors requires highly reactive phosphorus precursors with a long reaction time and high reaction temperature to initiate nucleation and sequential growth of nanoparticles, which make it difficult to induce LaMer type growth.[90] In addition, Allen et al. demonstrated that TMS_3P precursors are thermally decomposed at high reaction temperature without forming monomers in the growth step that is proceeded through Ostwald ripening.[95, 102] This fast decomposition of phosphorus precursors disturbs the growth of large-sized InP QDs that cover the range of over red and NIR (> 650 nm). That is why multiple injections, such as dropwise reactions, are necessary to realize high-quality InP red QDs as shown in Figure 14b. Figure 14a and b show spectral evolution of InP QDs by dropwise of TMSP precursors at a high temperature to induce Ostwald ripening. Although slow dropwise (0.1 mmol / 1 hour) with a syringe pump for 6 hours, the valley-to-peak ratio became wider by increasing reaction time, even though a key point of this reaction is to maintain their particle size distribution in growth of InP core.

2.1.2. Magic-size cluster

Nearly all of the synthesis of QDs, based on TMSP and Indium carboxylate precursors, use a non-coordinating solvent like 1-octadencene with surfactants, such as fatty acid,[103] amines,[104] and

alkylphosphine,[105] to stabilize and charge compensate surface.[3] However, the particle size distribution of InP QDs is still poor compared to II-VI or IV-VI QDs with a narrow FWHM and high-quality crystallinity. This means that inducing the separation between nucleation and growth is insufficient to reach the level of quality in II-VI CdSe QDs.[3]

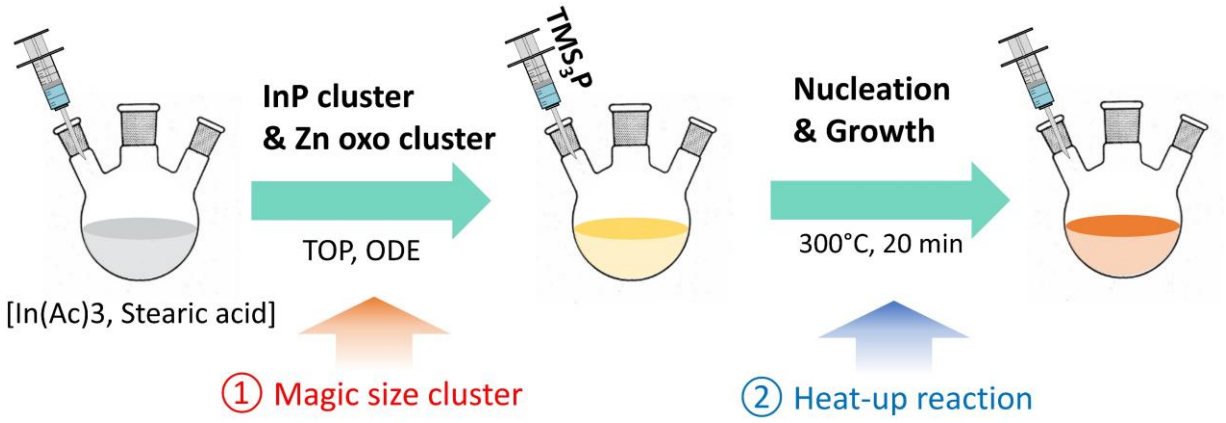

Figure 15. Illustrated reaction scheme of InP QDs via MSCs.

Recently, Gary, D. C. et al. reported on the role of "magic sized clusters (MSCs)" as a key intermediates cluster in nucleation stage besides growth of nanoparticles.[106] MSCs can be regarded as inorganic clusters with a higher thermodynamic stability compared to original inorganic or organic precursors. For the highest level of optical properties, such as PL QY and FWHM, the wet chemical synthesis of the high-quality InP QDs generally depends on how to separate the seed nucleation from the growth after the injection of highly reactive TMSP precursors (Figure 15). However, the rapid consumption of TMSP precursors obstructs this separation between nucleation and size-growth, as mentioned above, giving a rise to the deteriorated size distribution through Ostwald ripening process.[100] As for this issue, the growth kinetics of InP QDs has been known to be affected by Zinc carboxylate precursors. In particular, Kim et al. reported that Zn oxo cluster, produced by the thermal decomposition of Zn carboxylate over 300°C, can effectively suppress the reactivity of the highly reactive phosphorus precursors (e.g., TMSP), because it affords Zn-phosphine complex between In precursors and TMS_3P during the synthesis of InP core.[107] This investigation offered further insight that can realize high-quality InP QDs, because a lot of efforts to control nucleation and growth by tuning precursor reactivity have already reached a limitation. Thus, MSC intermediates were applied to our synthesis process to satisfy our target values toward high quality III-V InP QDs with a narrow FWHM.

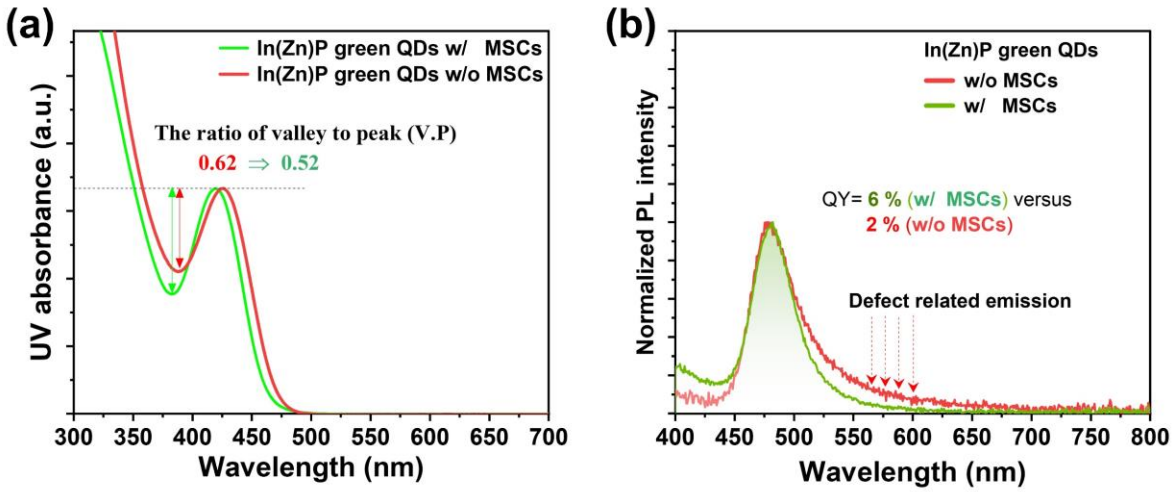

Figure 16. (a) PL and (b) UV-vis spectra of In(Zn)P core with or without Zn oxo clusters as MSCs.

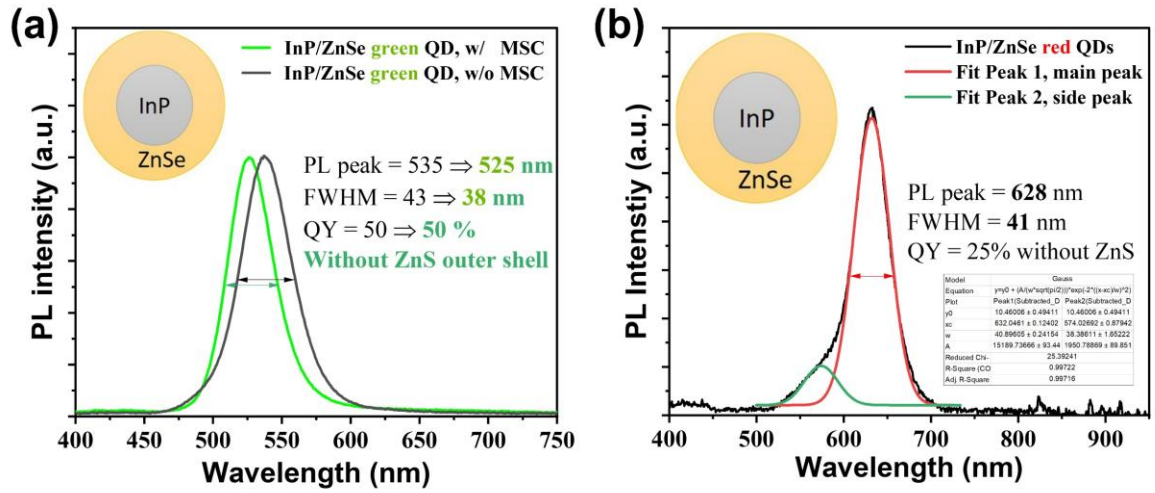

Figure 17. PL spectra of InP/ZnSe QDs as (a) a green and (b) a red emitter, where the pre-synthesized InP cores were applied to the process of ZnSe shelling.

Figures 16a and b show the synthesis of InP green and red cores when Zn oxo clusters were applied as intermediate clusters during the synthesis process, where the valley-to-peak ratio of InP green and red cores with MSCs apparently demonstrate somewhat improvement in their particle size distributions. These data indicate that MSCs suppress high reactivity and fast depletion of TMSP precursors. Herein, significantly important is the data that MSCs, such as InP clusters and Zn oxo clusters, are attributed to the improvement of color purity, by which this technique should be

continuously researched to realize an industrially feasible display material. In addition, PL spectra of InP QDs synthesized using MSCs indicate that the formation of Zn oxo-complex allows the kinetics of growth to be suppressed, and it results in the alleviation of defect-related emission at 550 nm to 800 nm compared to the use of Zn alkanoate as cation precursors (Figure 16b). This result may imply that thermodynamically stable Zn oxo clusters induce Zn cations to be incorporated more inside the lattice structure of InP QDs and stabilize their system, leading to the narrow FWHM and higher PL QY compared to InP without MCSs.

Figures 17a and b show the PL spectra of InP/ZnSe QDs as a green and a red emitter, where the pre-synthesized InP QD cores were applied to the process of ZnSe shelling. Upon shelling the ZnSe layer on top of InP QDs, the band-edge emission gradually emerges as PL intensities with a narrow FWHM due to strongly confined electrons in a conduction band level of QD band gap. The optical properties (FWHM and PL wavelength (PL WL)) of InP green core were all reflected in InP/ZnSe core/shell QDs after the ZnSe shelling as keeping their narrow color purity. In addition, the comparison of InP/ZnSe green QDs with or without MSCs definitely revealed that the application of MSCs during synthesis induces (1) a blue-shifted PL WL and (2) a narrow FWHM. Accordingly, it is evidence that the existence of MSCs during the synthesis of InP QDs is ascribed to the separation between nucleation and growth effectively, resulting in reduced QD size and better particle size distribution.

2.1.3. Core/Shell heterostructure

InP QDs without inorganic or organic shell generate low PL emissions, PL QYs of which are generally less than 1–2% and easily degraded by oxygen, water, and UV-visible light on the surface. Upon overshelling the InP core with inorganic semiconductors, such as ZnSe and ZnS, PL QY and chemical stability are rapidly enhanced due to strengthening quantum confinement and removal of phosphorus dangling bonds.[3] A selection of outer shell material is one of the critical factors in realizing industrially feasible type- I core/shell heterostructure QD material, and these factors are as followed: (1) the band gap of inorganic shell material should be larger than that of the InP core because it acts as a quantum well that induce efficient charge carrier confinement in the core; (2) the conduction band minimum and valence band maximum should not include core's conduction and valence band edges for band alignment that induces type-1 core/shell structure; (3) the crystal structure and lattice parameters between the core and shell materials should be similar since it makes shell materials facilitate epitaxial-like growth on the core.[92] The lattice parameters of inorganic compounds used in semiconductor materials are represented in Table 2, while a detailed information depicting the band alignment of these semiconductor materials can be found in previous literature.[92, 108]

Table 2. Lattice parameters of inorganic semiconductor materials in bulk.[109]

Material	Structure	E_g (eV)	Lattice constants (Å)
InP	Zinc blende	1.35	5.869
InAs	Zinc blende	0.35	6.058
ZnSe	Zinc blende	2.69	5.668
ZnS	Zinc blende	3.61	5.41
CdS	Wurtzite	2.58	4.136 / 6.714
CdSe	Wurtzite	1.73	4.30 / 7.01
CdTe	Zinc blende	1.43	6.482
PbSe	Rock salt	0.28	6.117
PbS	Rock salt	0.41	5.936

Most display materials belong to type-I core/multi-shell heterostructure QD, such as InP/ZnS,[110] InP/ZnSe,[111] and InP/ZnSe/ZnS QDs,[41] where the hole and electron in the core are strongly confined inside the band gap of the core surrounded by the larger band gap of shell materials that have the higher conduction band energy and lower valence band energy. In contrast to type-I QDs, type-II QDs have unbalanced band alignment with the band gap of shell material, in which the valence and conduction band edges in the core are situated below or above the corresponding band edges of the shell.[92] Thus, either electron or hole is strongly confined in the core, but the other is delocalized throughout the core/shell structure, resulting in weak quantum confinement and the red-shifted PL emission as an indirect recombination between core and shell. Consequently, these type- I core/multi-shell heterostructure InP QDs shows higher PL QY and better stability due to strongly confined electrons and holes in the core.

Table 2 also shows lattice constants of diverse inorganic semiconductors, the minimization of crystallographic strain between core and shell is significant to determine the resultant optical properties and maximum shell thickness. However, general assumption that small lattice mismatch between core and shell is not equally applied to core/shell heterostructure QD. Although the lattice mismatch of CdSe/ZnS QDs is 10–11% larger than that of InP/ZnS QDs (7.7%), the thicker ZnS shells up to 3–4 monolayers are grown successfully on the surface of CdSe QDs as compared to the thin ZnS shell up to 1–2 monolayers on the surface of InP QDs.[112-113] This can be originated from a difference of intrinsic material's physical properties, but a specific incomplete surface passivation (e.g., phosphorus dangling bonds) during synthesis may disturb epitaxial growth of shell material on top of the core.[114-115] In the

previous report of InP/ZnS core/shell QDs, the ZnS has been known to form the thin shell up to 0.5 nm on the InP core due to a large lattice mismatch (7.7%), but the resulting PL QY only increased by 20% despite the thin ZnS shell.[112] This data indicates that a shell thickness without modification of lattice mismatch between core and shell is not a critical impact in improving optical properties of core/shell QDs, even though it attributes pho-, thermal-, and chemical stability. To improve the optical properties (e.g., PL QY) as well as the material stability of QDs, a formation of the intermediate shell, such as ZnSe and GaP, between the InP core and ZnS shell has led to the remarkable enhancement of chemical and thermal stability and optical properties such as high PL QY of over 80% and narrow FWHM (Figure 18 and Table 3).[75-76] This is because the intermediate shell effectively alleviates the interfacial traps and lattice strain between core and shell.[77]

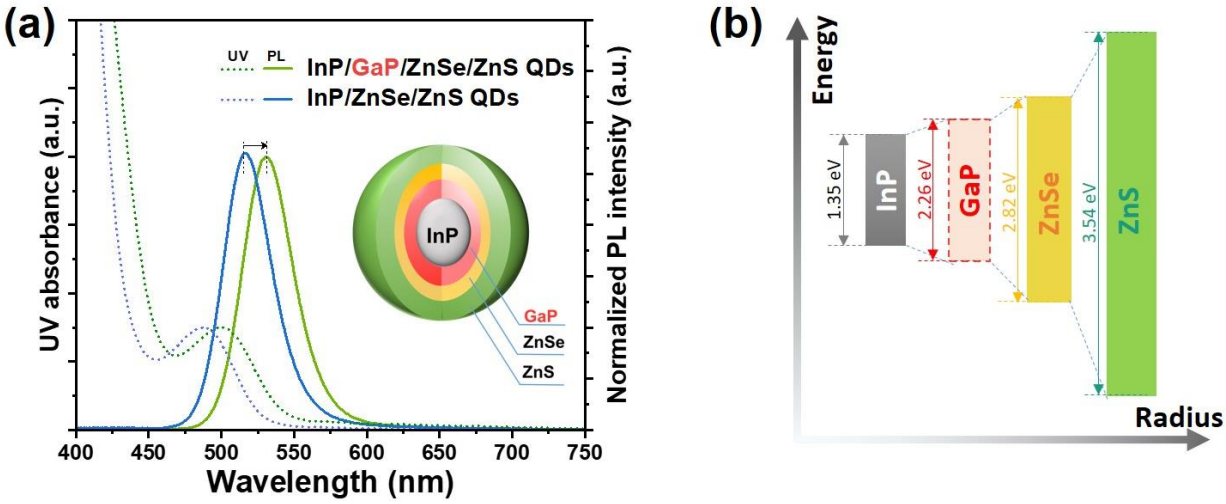

Figure 18. (a) PL and UV spectra of InP/ZnSe/ZnS QDs with or without GaP intermediate layer, and (b) their illustrated energy band diagram.

Table 3. Optical properties of InP/ZnSe/ZnS green QDs with or without GaP intermediate layer.

Structure	PL WL (nm)	FWHM (nm)	PL QY (%)
InP/GaP/ZnSe/ZnS	529.6	41.8	82.2
	530.5	40.8	78.4
InP/ZnSe/ZnS	517.2	39.1	56.8
	533.3	38.1	73.0
InP/ZnSe/ZnS/ZnS	530.5	40.1	77.5

For example, ZnSe (3.3%) has a lower lattice mismatch with InP compared to that of ZnS (7.7%), the shallow overshelling of which on top of InP QDs lead to the formation of a thicker ZnS shell than the case of solely ZnS applied InP QDs (i.e., InP/ZnS QDs), resulting in relatively high PL QYs of over 40%.[116-117] In contrast, the GaP mid-shell between InP and ZnS layer has been focused on as one of the effective intermediate shells that can remarkably improve PL QY by up to 85% even though its lattice mismatch (7%) with InP is almost the same with that of ZnS, where GaP has been known to induce indirect shelling via the cation exchange In with Ga on the surface of InP QD.[118] Moreover, the formation of the shallow intermediate shells, such as ZnSe and GaP, induces ZnS outmost shell to be grown thicker than the case without an intermediate shell due to the alleviated lattice mismatch between them, thereby the resulting thicker ZnS shell consequently provides better stability to the core, for which some works of the previous literature showed that thicker ZnS shelled QDs enhance both PL QY and photostability compared to QDs with thin ZnS shell overcoated on the surface of InP and CdSe cores.[79] Based on the experimental results, Figure 18 and Table 3 show the PL and UV spectra of InP/ZnSe/ZnS QDs with or without GaP mid-shell, and their corresponding optical properties, including maximum PL WL, FWHM, and PL QY. In general, to enhance PL QY and QD stability of QDs, the well-modified core/shell hetero-structured InP QDs are strongly recommended to alleviate a lattice strain between core and shell, to protect core from surface degradation, and to reduce surface defect sites by dangling bonds, because type-I core/shell hetero-structures induce their excitons to be strongly confined in core, as mentioned above. As a result, these data show the high-quality InP green QDs with PL QY of over 80% and narrow FWHM close to 40 nm, but still, the resulting optical properties do not fully satisfy our target values toward world best class. Nevertheless, InP/ZnSe green QDs show the possibility of the narrower FWHM of near 38 nm before the ZnS outmost shelling process. Therefore, if the ZnS outmost shelling is well modified to control the synthesis condition, such as various precursors and reaction temperature, these results imply that InP green QDs can soon reach the highest target optical values.

In addition, throughout nucleation and growth, the reactivity of monomer should be considered as a means of controlling the final QD size, composition, and morphology[119] Kelly. L et al. organized well about the impact of reactivity according to electronic and steric effects of precursors in the previous review paper,[119] the detailed information of which could be found for a better understanding of the role of precursors, where they classified ligand effects of precursors on monomers as follows: (1) strongly bound ligands to the monomer (e.g. ZnSe or InP monomer), which decrease monomer reactivity to disturb the access with neighboring monomers; (2) sterically bulk ligands, which physically limits the probability of contact with neighboring monomers, resulting in low reactivity of

monomer by steric hindrance; (3) high concentration of ligands, which increase the ligand coverage around monomers, inhibiting monomer reactivity via steric hindrance and the ligand-ligand repulsion between monomers.[119]

Scheme 2. Chemical equation of metal precursor formation, from metal oxide and carboxylic acid, and chalcogenide precursor formation, from trialkylphosphine and chalcogens. Reproduced from ref.[119]

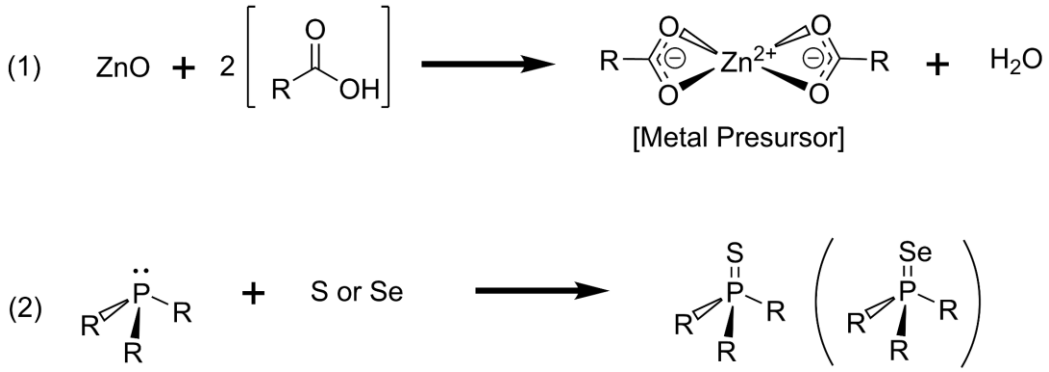

Universally, metal carboxylates have become one of the main precursors that can form colloidal QD formation.[119] Metal oxide, such as ZnO and CdO, react with two molar equivalents of an elongated alkyl chain carboxylic acid like stearic acid and oleic acid for balanced steric hindrance during nucleation and growth (Scheme 2).[120-121] Also, these metal oxide precursors can be replaced with metal acetates, such as Zn acetate and Cd acetate as usual, which thereby makes acetic acid, as a side product, to be easily evaporated faster than water that is produced in the case that metal oxide precursors are used instead of metal acetate. This is because water has strong hydrogen bonds with neighboring molecules as well as binds strongly to monomers, resulting in negative effects on nucleation and growth.[122-123] In the case of chalcogenide source, tertiary alky phosphine chalcogenides universally used as primary selection for synthesis of colloidal QDs,[119] where the structure of tertiary alky phosphine can be modified as manipulating alkyl groups to short or long chain (e.g., n-butyl and n-octyl), secondary alkyl or aryl phosphines,[124] aryl phosphites,[121] phosphorus amides.[125] This transformation of main structure in tertiary phosphine provokes electronically and sterically its reactivity with cation counterpart, metal carboxylate precursors. Moreover, their relatively simple synthesis made it possible to be a versatile chalcogenide precursor because dissolving molar equivalents of the chalcogenide metal into neat phosphine under an inert atmosphere or vacuum condition at around 50°C for reducing activation energy, which then becomes a clear solution as the chalcogenides coordinate with the phosphorus of tertiary phosphine.[119]

Scheme 3. Schematic reaction mechanism of ZnSe monomer from Zn carboxylate complex and trioctylphosphine selenide. Modified and reproduced on the basis of ref.[124]

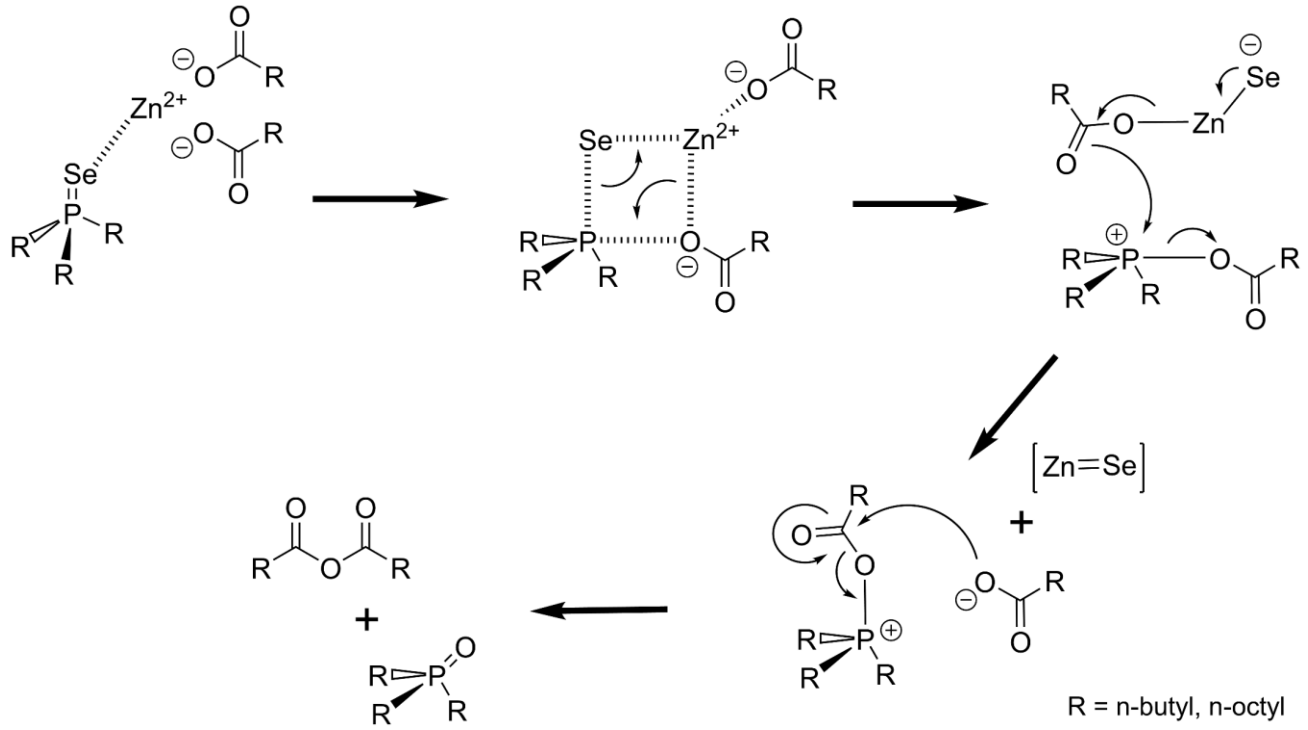

In Scheme 3, the synthesis mechanism of II−VI QDs suggests that electron-rich selenide of trioctyphosphine selenide (TOP–S) coordinates with metal carboxylate precursor, forming a transition state given by a Lewis acid–base complex.[55, 121, 126] This leads to metal chalcogenide bonds via a nucleophilic attack by alkyl carboxylate.[127] Consequently, the general assumption is this resultant monomer, produced by metal carboxylate and chalcogenide precursors, coalesces to form nuclei, and then, the QDs via nucleation and growth. Nevertheless, this reaction mechanism is still controversial regarding which oxidation state of metal includes in forming monomer units. In particular, whether a reactive M^{2+} state directly induces monomer units or a reduced M^0 state, as an intermediate state, produces monomer units can provoke much debate because these make the pathway of mechanism and interpretation differently, the detailed information of which can be found in the previous ref.[119] Nevertheless, significantly important is the fact that the structures of alkyl carboxylate in metal carboxylate precursors and tertiary phosphines affect the precursor's reactivity in forming monomer units. Therefore, the selection of precursors for QD synthesis should be considered systematically.

2.2 Applications of Colloidal QDs

2.2.1. QD–Light emitting diodes (QD–LEDs)

Beyond the Cd based QDs regulated by the Restrictions of Hazardous Substances (RoHS) directive, limiting the concentration of hazardous materials in electrical equipment, InP QDs have been noted as a potent candidate to replace it. Furthermore, they are worthy of further research due to their intriguing optical properties, such as outstanding quantum yield, tunable emission spectrum and elevated color purity.[41, 92] Especially, the cutting-edge optical efficiency of over 90% of InP QDs as green and red emitters has led to great success of QD enhanced film that is employed on top of the blue-back light unit in the display market.[62]

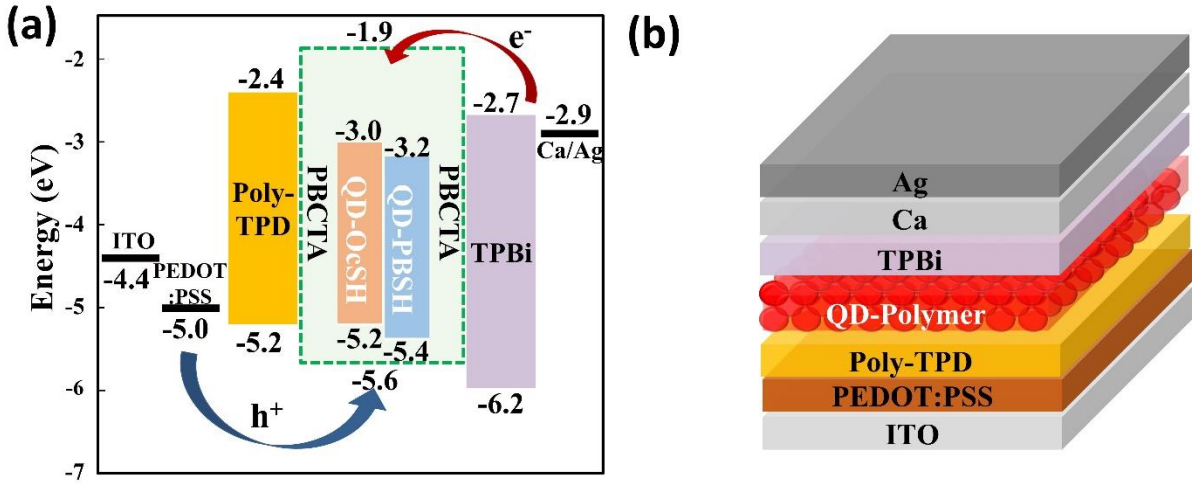

Figure 19. (a) Band structure of inverted QD-LEDs, and (b) its illustrated EL device.

Recently, Jang et al. reported highly performing electrolumicescence (EL) devices having an incredibly high external quantum efficacy (EQE) of over 20% when the state-of-the-art InP QDs was applied, where the active layer, composed of surface treated QDs by hexanoic acid, was sandwiched in between an organic hole transport layer (HTL) and ZnMgO as an inorganic electron transport layer (ETL).[61] To achieve a commercially feasible EL device, the surface modification and band alignment of QD in terms of a charge carrier injection balance have been steadily studied to date.[128] In the progress of QLED, the active layer gets generally affected by a complex combination of charging and the electric field across the device. The injected charge for operation of an EL device can induce a net charge on the active layer, where these charges can induce the quenched state of QD as absorbing exciton energy by non–radiative Auger processes.[129] Like this, the electron overcharge by excess

electrons in the active layer can give rise to non–emissive exciton recombination, resulting in a decay of optical efficacy in QLED. From QD material perspectives, core/shell-based QDs with an elaborately modified outer shell, such as a gradient or giant shell, can alleviate nonradiative Auger processes and eliminate the excess electrons in some measure.[130] Dai et al. showed experimentally that a Poly(methyl methacrylate) (PMMA) interlayer, functioning as an electron blocking layer (EBL) between the active layer and the ETL, is implemented to relatively high stability and device performance when compared to that of without PMMA layer.[131] They reported that the electron mobility of ZnO films ($1.8 \times 10^{-3} cm^2V^{-1}s^{-1}$), examined through current density–voltage (J–V) characteristics, was much faster than the hole mobility of Poly(N,N'–bis–4–butylphenyl–N,N'–bisphenyl)benzidine (Poly–TPD, $1 \times 10^{-4} cm^2V^{-1}s^{-1}$), causing the accumulation of electrons in the QD active layer.[131] Furthermore, the commonly known ETL material, 2,2',2''–(1,3,5–Benzinetriyl)–tris(1–phenyl–1–H–benzimidazole) (TPBi), was revealed to provoke the accumulated electrons of QD layer even though it has a lower electron mobility ($3.8–8.0 \times 10^{-3} cm^2V^{-1}s^{-1}$)[132] than ZnO, causing luminescence quenching, investigated through impedance spectroscopy.[133] In spite of the affirmative aspect of EBMs that able to induce charge carrier balance through the suppression of injected excess electrons, these electron blocking materials, such as 4,4',4''–Tris(carbazol–9–yl)–triphenylamine[134] and above-mentioned PMMA, should be not only thin layer (e.g., 6 nm of the PMMA layer) but also spin-coated, therefore it can be relatively difficult to obtain experimentally reproducible results because the non-uniform or thick EBL causes suppression of charge carrier injection, which rather causes a decrease in device efficiency. It is not considered beneficial from an industrial point of view because it needs an additional spin-coating process of EBL on top of active layer. Despite this, the aforementioned PMMA and TCTA as EBLs were still employed in the territory of Cd–based QLED because of their improved efficiency. This indicates that it is necessary to utilize to InP QDs regime not containing heavy metals, actively applied in the display market.

Consequently, charge transport properties of the QD emission layer, HTL, and ETL inside QD–LEDs are key factors that determine device efficiency. However, organic ligands surrounded by inorganic QD are basically insulators to obstruct the charge transport inside QD–LEDs; thereby, removing the organic shell is significantly reasonable, but those are necessary to realize wet chemical synthesis and all-solution process. Thus, today researchers focus on how to manipulate surface ligands toward better charge transport properties by exploiting the structure of ligand molecules.[49]

2.2.2. Luminescence Solar Concentrators (LSCs)

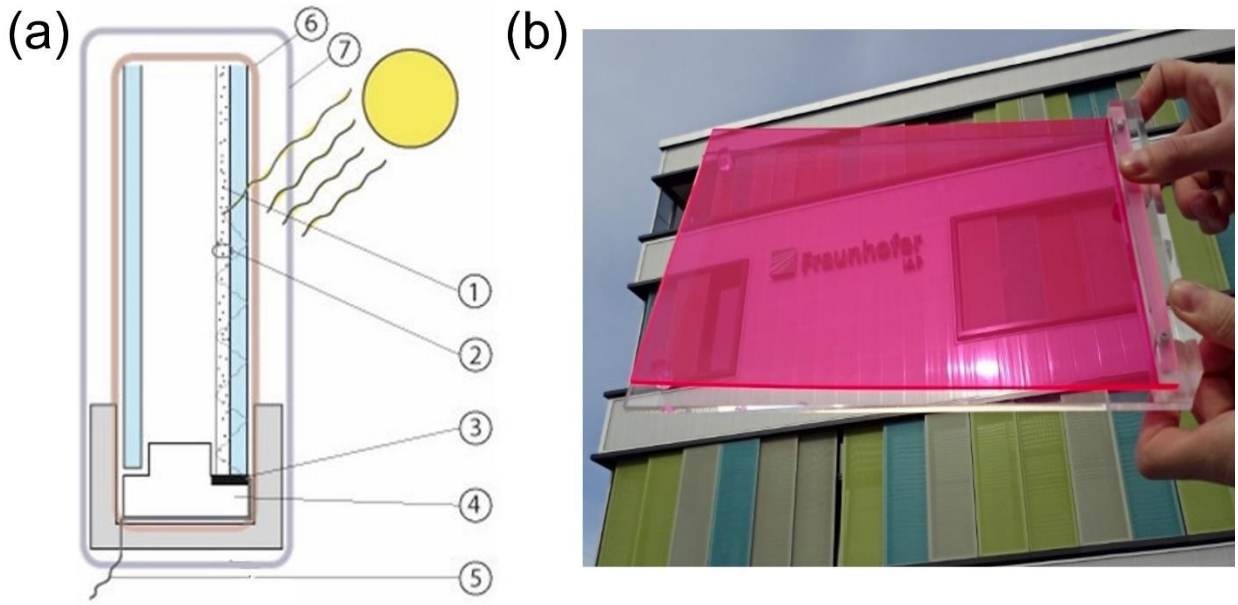

Figure 20. (a) Illustrated LSC module, including (1) PL emitter, (2) resin matrix, (3) PV cell, (4) stationary form, (5) unified electrical line, (6) waveguiding glass, and (7) box cover for ambient condition, and (b) a fabricated demonstrator using organic dye.

Luminescent solar concentrators (LSCs) can be regarded as cost-effective large-area sunlight collectors for space-based photovoltaics, the demonstrator of which are fabricated between transparent glass panels that can realize applicable devices as a window in real life (Figure 20). Also, the LSC module does not require a specific space to be installed differently from silicon-based solar cells; thereby, it can be used in many applications such as car windows, smart window, electronic devices, or fiber optics[135], photon transport for passive daylighting[136-137]. Basically, LSCs are composed of a transparent material having highly emissive fluorophores, which are then sandwiched by glass panels. Thus, sunlight emits photons of fluorophores on a large-area device face, and their emitted photons are waveguided by total internal reflection to the device edge, where they all are collected by photovoltaic cells.[138] Despite this reasonable design of LSCs, LSCs generally rely on photon transport over macroscopic distances and therefore are susceptible to various loss mechanisms.[138] In many cases, a waveguide is made of glass or plastic, which all have approximately 1.5 reflex index, where 25% of emitted photons escape out of the waveguide, and have not reached to PV cell on the edge side.[139] Furthermore, Even though photons are captured by total internal reflection inside the waveguide, their photon energy becomes weakened through scattering from the waveguide surface, internal defects,

scattering with neighboring luminophores themselves, and self-absorption by the luminophores, where the massive self-absorption between luminophores historically make it challenging to realize the practical implementation of large-area LSCs (Figure 21).[135, 140-141]

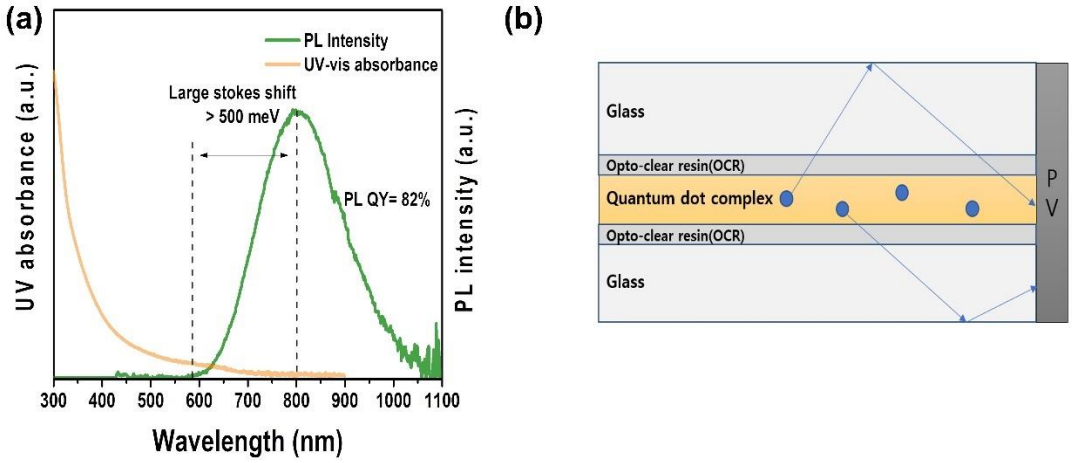

Figure 21. Stokes shift of InP:Cu QDs, and their behaviors in LSCs.

Recently, huge advances in wet chemical synthesis of relatively stable transition metal doped QDs and CIS QDs with high PL QYs and tunability of absorption range have attracted a lot of interest in QD material for LSC technologies.[142-144] One strategy for minimalizing self-absorption between QDs is type-2 heterostructure, for example, CdSe/CdS QDs, the PL emissions of which are red-shifted via indirect transition across the heterointerface, in which the thicker shelling induce an increase in absorption, but it provokes large volume arising from the limitation of QD packing inside resin matrix.[145-148] To implement nearly zero self-absorption, Mn^{2+} doped ZnSe has been suggested for two decades, where the host ZnSe efficiently sensitizes excitation of Mn^{2+} dopant ions to their $^4T_1$ ligand-field excited state, inducing the emission with relatively low PL QY of over 50% and extremely large effective stokes shift.[148]

2.2.3. Electrohydrodynamic (EHD) Jet Printing

Electrohydrodynamic (EHD) printing is known as an electronically, physically complex process, where the charge of fluid, induced by the electric field, influences the momentum flux of the fluid.[149] The gap between the capillary tip and the counter electrode (e.g., indium tin oxide substrate) is situated under high electrical potential by high voltage, where an electrostatic force is formed on the fluid (e.g., solution ink formulation), inducing the electric tangential force for the formation of a Taylor cone.[149] Typically, the EHD jet printing realizes higher resolution (i.e., submicrometer) than piezo-type inkjet printing because the former makes the jet diameter smaller than the nozzle diameter, but the latter makes droplet size almost twice of nozzle size.[150-151] In particular, the nozzle clogging of EHD jet printing can be minimized since the charged particle becomes self-dispersed, which allows the solid percentage of EHD ink formulation to be higher than that of conventional ink and suppresses flow-induced aggregation that often occurs in a piezo-type inkjet printing system.[152-153] Therefore, the range of application in EHD jet printing system has become wider throughout the various fields such as solar cells,[154-156] electronics,[157-158] food,[159] and biological system.[160-161]

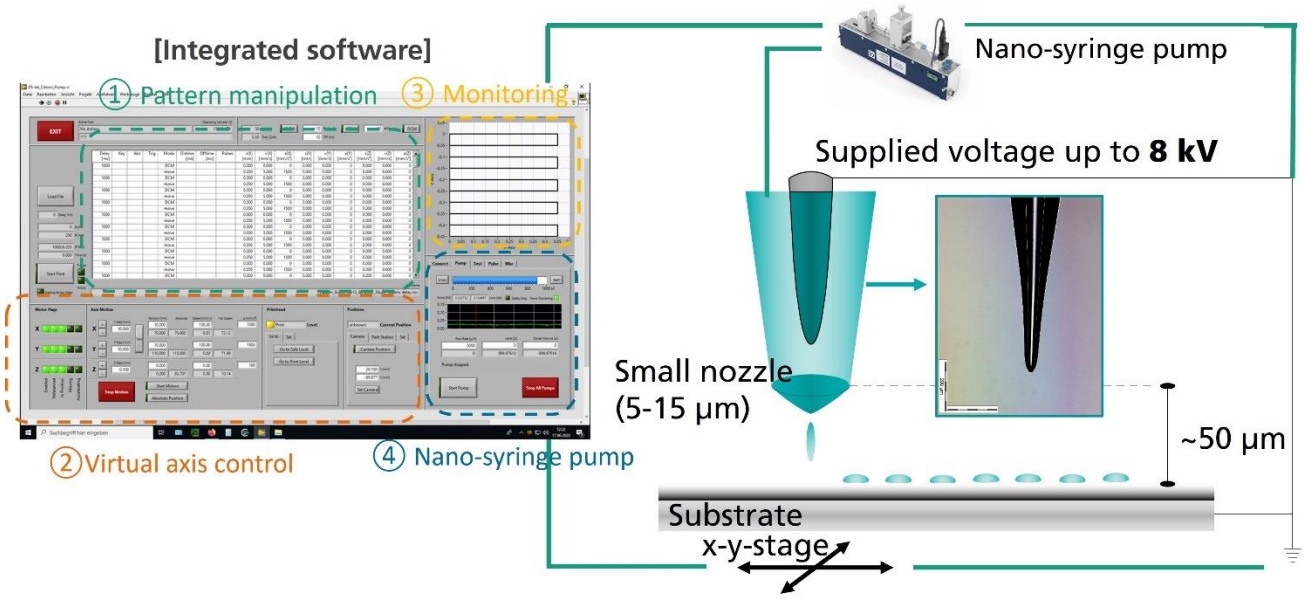

Figure 22. illustrated EHD jet printing system controlled by integrated software.

Figure 22 shows illustrated EHD jet printing system controlled by integrated software, where a nano-syringe pump finely manipulates physical flow rate besides electrical force. Also, the printed ink component should be significantly considered with the printing method in producing on-demand droplets, where EHD jetting properties of ink material are predominantly determined by the

rheological properties of the fluid in the EHD system; that is, intrinsic electronic and physical properties of the fluid should be taken into account as well as their rheological properties even though the electrical force triggers the EHD jetting droplet.[149] In addition to material's intrinsic properties, in a practical experiment in the EHD jet printing system, the electrical and mechanical properties should be essential factors that influence the printing quality, where the shape and material of the print head mainly is one of the significant selections to determine jetting performance.[162]

Historically, Zeleny and Taylor have reported a lot of pioneering research about the droplet in EHD jet printing system and its formation by physical and electronical factors, where the detailed analytical studies could be found in previous ref.[163-165] Had it been introduced briefly, the size of droplet after EHD jetting is affected by the fluid viscosity,[166] the effect of permittivity on the droplet size under a specific emitted current,[167] the deposition of the polymer precursor,[168] and the deposition of the particles with different sizes and functionalities,[169-170] most of which are experimentally studied and reported; thus, these previous researches during one hundred years offer the current researcher a lot of detailed insight for EHD jet printing toward the industrially feasible device. Nevertheless, these studies are often limited within the range in the simple comparison of resulting output; thereby, the optimization of the EHD printing system is still required even though, for example, A. Lee et al. systematically studied the experimental relation of the Taylor cone and the experimental jetting mode for its stable jetting condition.[149] As a result, the EHD jet printing system includes a lot of factors related to all materials and the installed equipment, so every experimental condition should be organized in detail from practical standpoints to realize the stable con-jet mode.

3. Cu-DOPED InP QDs WITH A Zn–Cu–In–S/ZnS DOUBLE SHELL SCHEME

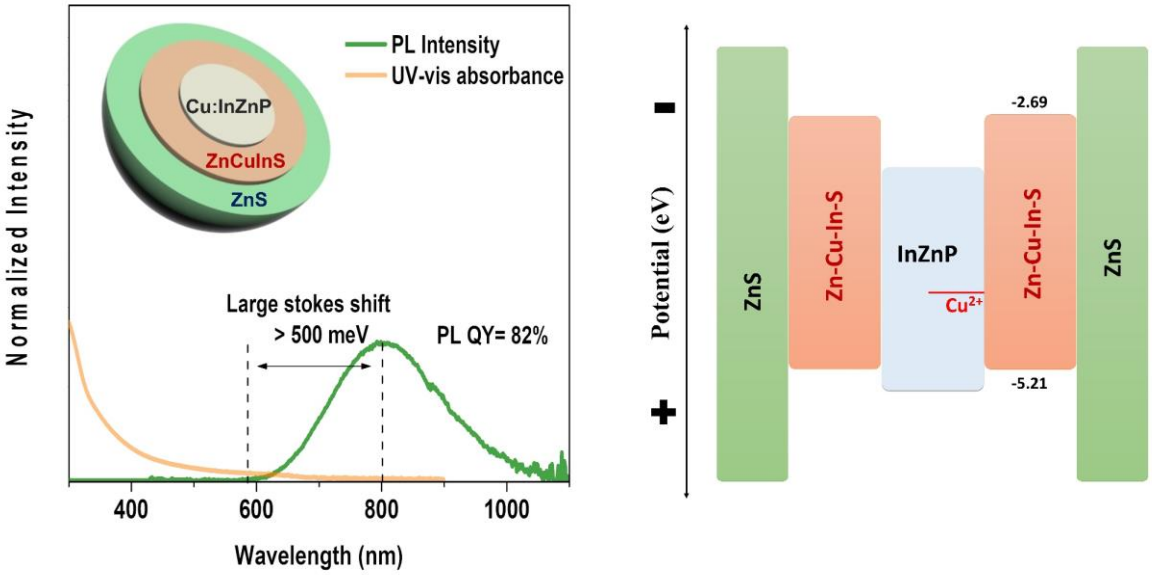

This section is based on the published manuscript, J. Kim et al. Journal of Materials Chemistry C 2021, 9, 4330-4337 (manuscript entitled "Highly luminescent near-infrared Cu-doped InP quantum dots with a Zn–Cu–In–S/ZnS double shell scheme").

3.1. Introduction

In this work, with an aim to considerably improve the PL QY of InP:Cu QDs, we examine a new strain-relieved heterostructure with a combination of Zn–Cu–In–S (ZCIS) inner and ZnS outer shells. ZCIS can be an energetically suitable interlayer between InP and ZnS with the respective band gaps of 1.55 and 3.67 eV, given the experimental band gaps of ZCIS between 1.8 and 2.5 eV.[171] Energetic alignment between the InP core and ZCIS inner shell is simulated to a type-II heterostructure. To demonstrate the emission tunability in the near-IR region, a series of InP cores with different sizes are adopted for Cu doping. The resulting near-IR-emitting InP:Cu/ZCIS/ZnS QDs yield excellent PL QYs up to 82.4% along with considerable Stokes shifts larger than 450 meV.

3.2. Experimental Details

3.2.1. Materials

Technical grade octadecene (ODE, 90%), indium acetate ($In(Ac)_3$, 99.99%), tri-n-octylphosphine (TOP, 97%), zinc acetate ($Zn(Ac)_2$, 99.99%), octanoic acid (OA, >99%), myristic acid (MA, >99%), 1-dodecanethiol (DDT, >98.0%), copper(II) chloride ($CuCl_2$, 99.999%), copper(I) chloride (CuCl, 99.99%), toluene (anhydrous, 99.8%) and acetone (AC, >99.9%) were purchased from Sigma-Aldrich Co. Zinc octanoate (ZnOA) was prepared beforehand. Tri(trimethylsilyl)phosphine (TMSP, 99.5%) was purchased from SK chemicals. All the chemicals were used without further purification.

3.2.2. One-pot synthesis of InP:Cu/ZCIS/ZnS core/shell/shell QDs

Four different-sized InP cores emitting at a peak wavelength of 532, 567, 610, and 628 nm were synthesized. For a typical synthesis of 532 nm-emitting InP cores, 1 mmol of $In(Ac)_3$, 3 mmol of $Zn(OA)_2$, and 10 ml of ODE were placed in a 100 ml three-neck round-bottom flask connected to a reflux condenser and equipped with rubber septa and a thermocouple. The mixture was heated to 150°C and degassed under a reduced pressure (≤150 mTorr) at 150°C for 10 h with vigorous stirring to remove water and oxygen species. After backfilling the reactor with N_2 atmosphere, 1 mmol of TMSP dissolved in ODE was rapidly injected into the flask at 150°C and the solution was heated up to 300°C for 20 min during vigorous stirring, and the growth solution was cooled down to room temperature. For Cu doping, 0.25 mmol of $CuCl_2$ (or CuCl) and 0.5 mmol of DDT were added into the reaction solution. After degassing at 80°C for 2 h and N2-backfilling, the reaction mixture was further heated to 200°C at a heating rate of ~2°C min–1 and maintained at that temperature up to 80 min. The temporal doping process was monitored through PL and UV-visible absorption measurements by taking aliquots from the reaction mixture at a given time/temperature. For the synthesis of the other three InP cores emitting at 567, 610, and 628 nm, 3, 4.5, and 6 mmol of MA, respectively, were additionally introduced along with 1 mmol of $In(Ac)_3$, 3 mmol of $Zn(OA)_2$, and 10 ml of ODE, while the other following synthetic details were kept the same.

For the following ZCIS inner shelling, the above growth solution was cooled down to room temperature and then 2 mmol of $In(Ac)_3$ and 6.3 mmol of 1-DDT were added into the reaction flask. After degassing at 120°C for 1 h and N2-backfilling again, the reaction mixture was heated to 230°C and then reacted for 180 min. For the consecutive ZnS outer shelling, the solution was cooled back to room temperature and 4 mmol of $Zn(Ac)_2$ was added into the reaction flask. After the same degassing at 120°C and backfilling, this mixture was heated to and kept at 230°C for 1 h. 15mmol of DDT was

rapidly injected into the flask at that temperature, followed by the reaction for 2 h. Then, the whole reaction was terminated by cooling to room temperature and adding an excess amount of toluene. The as-synthesized InP:Cu/ZCIS/ZnS QDs were isolated by adding an excess amount of acetone and then purified by repeated rounds of precipitation/redispersion with an acetone/toluene combination using centrifugation (6000 rpm, 10 min).

3.2.3. Characterization

The absorption spectra of QDs dispersed in toluene were recorded by UV-visible spectroscopy (Thermo Evolution 60S). The PL spectra and absolute PL QYs of QDs in toluene were recorded using an integrating hemisphere with an absolute PL QY measurement system (QE-2000, Otsuka) with excitation wavelengths of 365 nm for InP cores and 400 nm for InP:Cu, InP:Cu/ZCIS, and InP:Cu/ZCIS/ZnS QDs. Particle images of QDs were obtained using a high-resolution transmission electron microscope (TEM, JEOL JEM-F200) and annular dark-field scanning transmission electron microscope (STEM) with a semi convergence angle of 25 mrad and a detector annular semi-angle range from 33 to 125 mrad. X-ray diffraction (XRD) patterns and actual elemental compositions of a series of QDs with different shelling stages were obtained using a Bruker AXS GmbH D8 ADVANCE X-ray diffractometer and an inductively coupled plasma-optical emission spectrometer (ICP-OES, Agilent Tech. 5100), respectively. TEM energy dispersive X-ray spectroscopy (EDS) measurements were performed on a double-Cs-corrected JEOL JEM-ARM200F, equipped with a cold field emission gun and a JED-2300 energy-dispersive X-ray detector. X-ray photoelectron spectroscopy (XPS) spectra of QDs were obtained with a Thermo Fisher Scientific K-ALPHA operating at 12 kV and 6 mA. The spectral binding energies were calibrated with the C 1s peak of 284.5 eV as an internal standard.

3.3. Result and Discussion

Doping optically active elements such as transition metal ions into the host QD should in principle lead to the sole appearance of energy down-shifted PL, with the band-edge (BE)-PL quenched fully, since the rate of charge carrier trapping at or exciton energy transfer to the dopant site is much faster than that of exciton recombination.[172-173] In many cases of doped QDs, however, both BE-PL and dopant-PL (D-PL) emerge simultaneously, which may limit their utilization as energy down-shifted emitters. Accordingly, with an aim to more effectively produce the D-PL of InP:Cu QDs, we first screened Cu dopant precursors and then introduced a hole-withdrawing agent that may completely suppress BE-PL with the sole D-PL rising. As reported earlier in Cu-doped InP thin films,[174-175] the origin of D-PL is associated with the recombination of charge carriers from the conduction band of the host InP to the 3d level of the Cu dopant. Work by Peng et al. demonstrated that the PL of InP:Cu QDs was quite widely tunable from 630 to 1100 nm through the variation of QD size.[42] Gamelin and other groups proved that the Cu dopant has +1 oxidation state on the basis of magneto-optical experiments,[176] even though the oxidation state of +1[176-177] versus +2[178-179] is still controversial.

3.3.1. Cu^{+} or Cu^{2+} doped InP QDs

Herein, to examine the effects of the oxidation state of the Cu precursor, the present InP:Cu QDs were synthesized using either Cu(I)Cl or Cu(II)Cl_2. The adsorption of Cu ions onto the surface of QDs leads to the quenching of BE-PL of a host QD, and D-PL emerges instead when Cu ions are further incorporated into the lattice,[180-181] which was well reproduced in the following experiments. Without the purification step of the as-grown InP QDs, either CuCl or $CuCl_2$ was added at room temperature and then the temperature was gradually increased to 200°C. The evolution of Cu^{+} or Cu^{2+} ions during the doping process may be indirectly revealed by monitoring the PL and absorption spectra of aliquots taken at different reaction temperatures and times (Figure 23). In the case of Cu^{+} doping, the original BE-PL of InP QDs became gradually quenched in the course of heating. Upon reaching 200°C, D-PL became dominant with a trace of BE-PL detectable (Figure 23a). Compared to Cu^{+} doping, the use of Cu^{2+} led to a faster quenching of BE-PL and a more negligible BE-PL, albeit still seen, at 200°C (Fig. 1b). In zinc blende InP QDs, the (001) surface is electron-rich with undercoordinated negative ions (i.e., P^{3-}) exposed.[182] This can promote the surface adsorption, attracting and binding Cu ions onto (001) surfaces.[44, 47, 183] The P^{3-} anion, a hard base, of InP QDs likely possesses a higher binding affinity to Cu^{2+} over Cu^{+} ions on the basis of a harder acid nature of the former (chemical hardness, Z = 8.27 eV) relative to the latter (Z = 6.28 eV). This disparity in the reactivity of Cu ions with surface P^{3-} of InP QDs likely results in different quenching rates and degrees of BE-PL. When further annealed at

200°C for prolonged periods of time up to 80 min, we observed persistently remnant BE-PL (Figure 23a) and notably revived BE-PL (Figure 23b) for Cu^{+} and Cu^{2+} doping, respectively. Also note that both BE-PLs obtained from such annealed QDs became blue-shifted from their original ones.

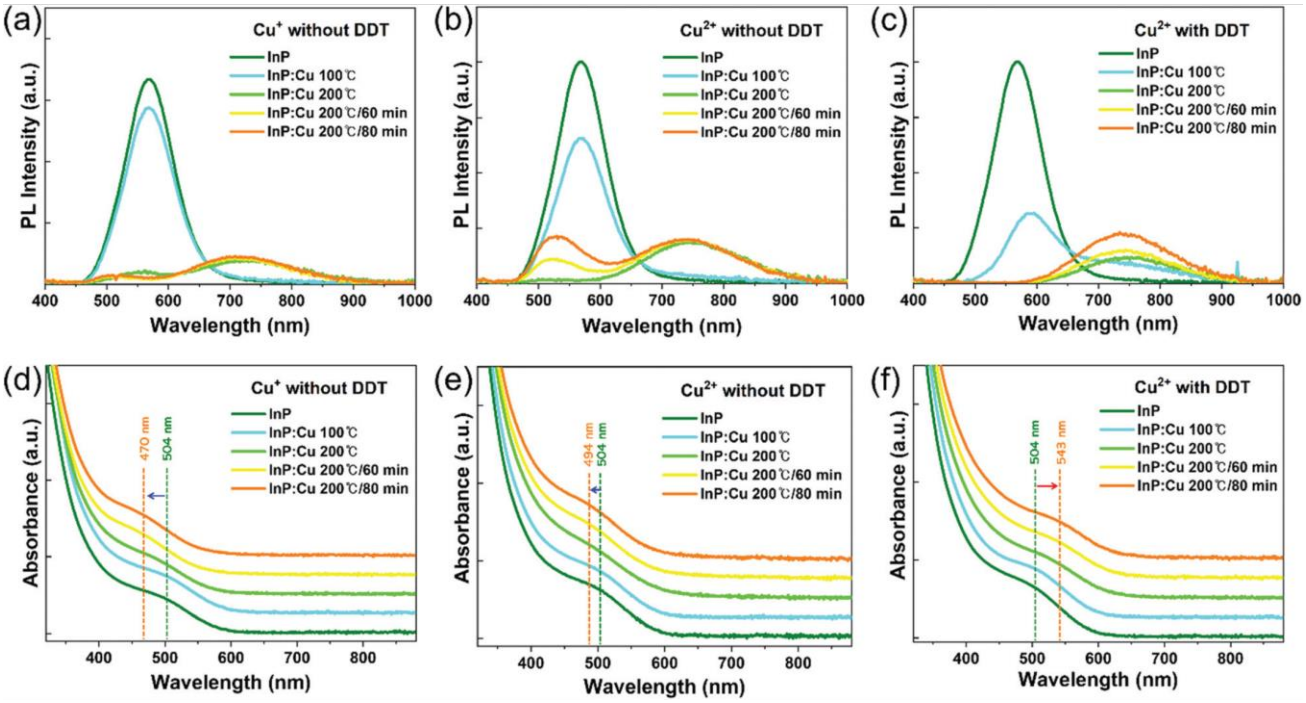

Figure 23. (a–c) PL and (d–f) absorption spectral evolutions with different synthetic temperatures and annealing times. Cu doping was performed by using (a and d) CuCl without DDT, (b and e) CuCl2 without DDT, and (c and f) CuCl2 with DDT. Verticadotted lines in (d–f) indicate the spectral shifts of 1S peaks from initial InP to final InP:Cu QDs.

This was also in line with the absorption spectral outcomes, showing blue-shifts of the first excitonic (1s) peaks (as marked in dotted lines) in Figure 23d and e for Cu^{+} and Cu^{2+} doping, respectively. Since the band gap widening is the direct result of increasing the quantum confinement effect, the above blue-shifts in both absorption and BE-PL apparently point to the reduction of the QD size via the etching of the surface atoms of InP QDs during the annealing. The detailed chemistry for the etching reaction is not clearly revealed at present, however, some by-products such as acetic acid and hydrochloric acid that can be released from the reaction mixture likely provoke such unintended etching. This QD surface etching will naturally entail the detachment of some fraction of surface-anchoring Cu ions as BE-PL quenchers, by which blue-shifted BE-PL persistently existed or even revived, depending on the oxidation state of Cu ions used.

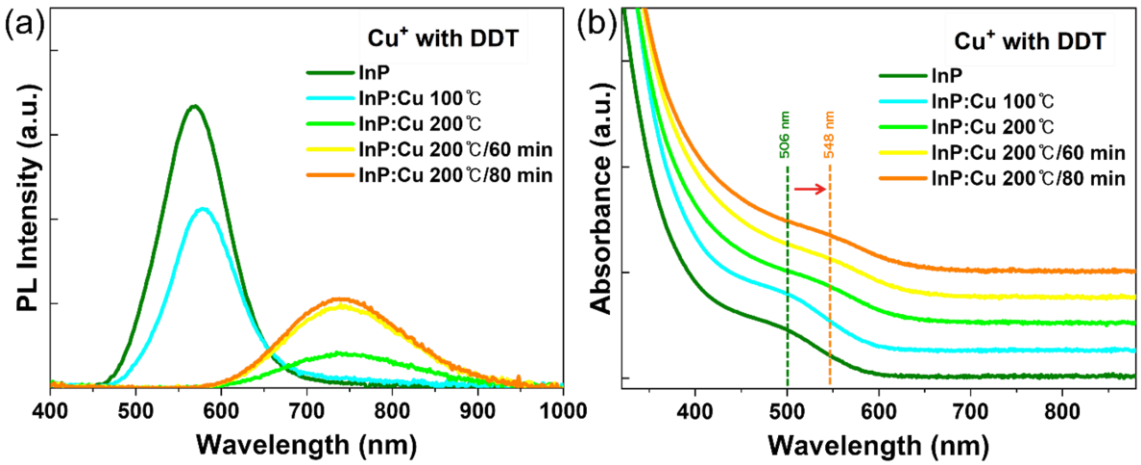

Figure 24. (a) PL and (b) absorption spectral evolutions with different synthetic temperatures and annealing times when Cu doping was performed by using CuCl with DDT. Vertical dotted lines in (b) show the red-shift of 1S peaks from initial InP to final InP:Cu QDs.

Table 4. Absolute PL QYs of InP:Cu QDs synthesized from Cu^{2+} and Cu^{+} with/without DDT.

QD	Absolute PL QY (%)			
	Cu^{2+} (With DDT)	Cu^{2+}	Cu^{+} (with DDT)	Cu^{+}
InP:Cu	26.7	17.2	21.5	9.4

With an intent to fully suppress BE-PL, a small amount (0.5 mmol) of DDT that may function as a hole-withdrawing agent[179, 184] was added together with $CuCl_2$ in the synthesis of InP:Cu QDs. As shown in Figure 23c, BE-PL was completely quenched at 200°C along with the emergence of the sole D-PL, and furthermore the BE-PL did not appear again throughout the annealing process up to 80 min. The replacement of $CuCl_2$ by CuCl in the presence of DDT by and large gave the same PL results, even though the quenching of BE-PL became somewhat tardy (Figure 24). More importantly, gradual red-shifts in BE-PL and absorption were clearly seen in the course of heating and subsequent annealing (Figure 23c and f), being contrary to both blue-shifts from the cases of Cu doping without DDT addition (Figure 23a, b, d and e). This may allude to the formation of the ZCIS shell, albeit primitive, through the reaction from unreacted In, Zn, and Cu species (available in the mixture) together with a sulfur-feeding DDT. Due to this incidental ZCIS shell growth, InP:Cu QDs with DDT overall possessed higher PL QYs than ones without DDT (Table 4).

3.3.2. Theoretical energetic positions of the ZCIS shell

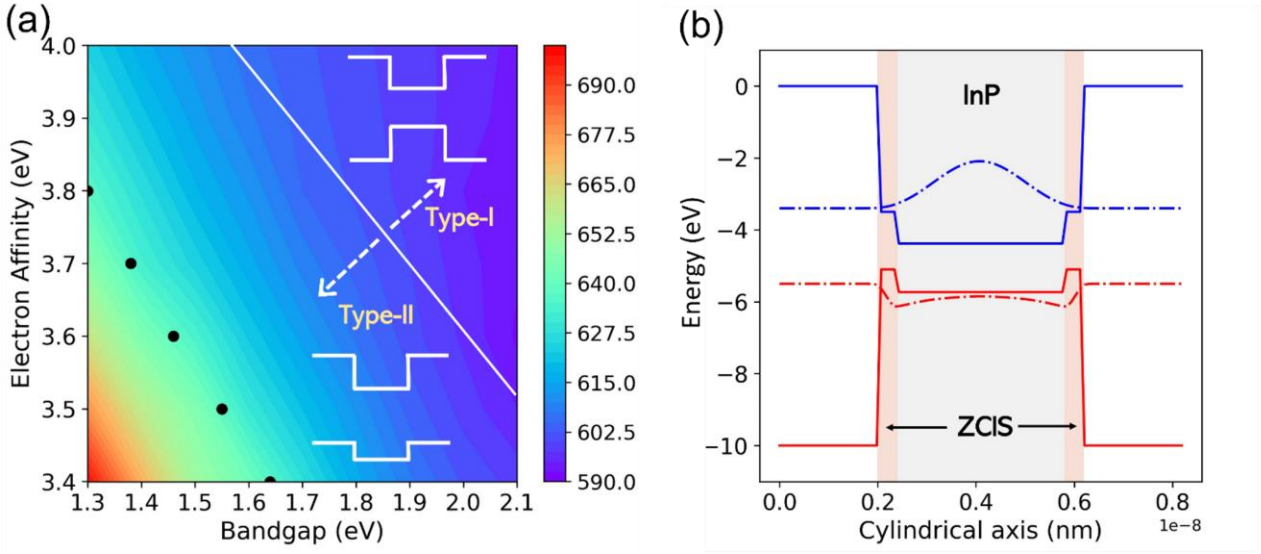

Figure 25. (a) Estimated BE-PL wavelength with the variations of $q\chi$ and E_g. The black dots are the positions that QDs show a PL wavelength of 638 nm. The white solid line indicates the borderline between type-I and type-II energetic structure. (b) Energy band diagram (solid) and wavefunctions (dash-dot) of the QD having a qw of 4.3 eV and an Eg of 0.96 eV. For this simulation, the effect of Cu doping was ignored.

Theoretical energetic positions of the ZCIS shell relative to the InP core were simulated based on the two-band K·P model (Kane method) and iteration with the Poisson equation.[184-185] Since we apply the cylindrical symmetry on the 2D geometry where all material parameters of QDs are allocated, the full 3D simulation is achieved. The parameters used for this calculation were obtained from the literature.[186] Using those, we evaluated the optical band gap (E_g) while varying the electron affinity ($q\chi$) and E_g of the ZCIS (Figure 25a). As indicated by the dotted lines in Figure 23f, we observed a red-shift of the 1s peak by 0.24 meV after annealing at 200°C for 80 min. Based on this band-edge's movement, the corresponding BE-PL wavelength could be estimated to be 638 nm, albeit unseen. In given $q\chi$ (3.4–4.0 eV) and Eg (1.3–2.1 eV) ranges of ZCIS, we searched the energy eigenvalues that correspond to 638 nm and marked them as black dots in Figure 25a. If a type-I heterojunction forms, a shorter BE-PL wavelength than 638 nm will be obtainable due to the limited leakage of charge carriers to the ZCIS shell. That is, the longest BE-PL wavelength from type-I alignment is expected to be < 625 nm (Figure 25a). On the other hand, when a type-II energy alignment forms at the heterointerface, its BE-PL wavelength can reach 638 nm or even longer. A white solid line marked in Figure 25a is the borderline between the type-I and type-II heterostructure, which was estimated from the bulk band alignment with $q\chi$ and E_g. Therefore, we may conclude that the best model that accounts for such considerably red-shifted BE-PL is the formation of the ZCIS shell on the InP core with a type-II heterostructure. And the $q\chi$ and E_g of ZCIS can be estimated to be at or near the black dots or their

interpolation (Figure 25a). Figure 25b shows the representative energy structure and wavefunction distributions of type-II InP/ZCIS QDs having a $q\chi$ of 4.3 eV and an E_g of 0.96 eV.

3.3.3. Optical properties of InP:Cu/ZCIS/ZnS QD, and their component analysis.

After the formation of such a primitive ZCIS shell, more $In(Ac)_3$ and excess DDT were replenished and then the reaction proceeded at 230°C for 3 h in order to grow a thicker ZCIS shell. In this experiment, the amount of $In(Ac)_3$ was varied to examine its effect on the PL QY, resulting in the highest PL QY of 64.8% at a nominal In/Cu molar ratio of 8 (Figure 27). Following such an additional ZCIS inner shell growth, ZnS shelling was consecutively carried out to further improve the PL QY. Besides, the size of InP cores for Cu doping was varied to tune the emission of D-PL. For this, smaller and larger InP cores relative to the reference ones (termed as QD2 in Figure 26) showing a BE-PL of 567 nm (Figure 23) were synthesized, followed by the identical consecutive ZCIS/ZnSmulti-shelling. The entire spectral evolutions of absorption and PL from undoped InP throughout multishelled InP:Cu/ZCIS/ZnS QDs are presented in Figure 26. Increasing the average size of InP cores from 2.98 ± 0.27 nm (QD1) to 4.32 ± 0.58 nm (QD4) (Fig. 28 and 30a) led to a systematic red-shift in BE-PL from 532 (QD1) to 628 nm (QD4) due to the gradual reduction of quantum confinement effects. Accordingly, the peak wavelength of D-PL spanned from 694 nm for the smallest QD1 to 850 nm for the largest QD4 after ZCIS/ZnS multi-shelling was completed. The Stokes shift, the energy difference between D-PL (Figure 26a) and absorption (determined from its second derivative, Figure 29) of InP:Cu/ZCIS/ZnS QDs, was overall large in the range of 451–463 meV (Figures 26b and 29). As summarized in Table 5, the PL QY of InP:Cu QDs was considerably enhanced after the ZCIS inner shelling, followed by a further improvement after the outer ZnS shelling, resulting in the final PL QYs of 71.5–82.4% (Figure 26b). In particular, InP:Cu/ZCIS/ZnS QDs from QD2 having a peak D-PL of 735 nm exhibited the record PL QY of 82.4%, which was much higher than those (40–58%) from the earlier core/shell heterostructured InP:Cu ones having either single ZnS[37-38] or double ZnSe/ZnS shells,[39] indeed proving that the presence of the novel ZCIS interlayer is highly conducive to the effective alleviation of interfacial strain necessary for high emissivity.

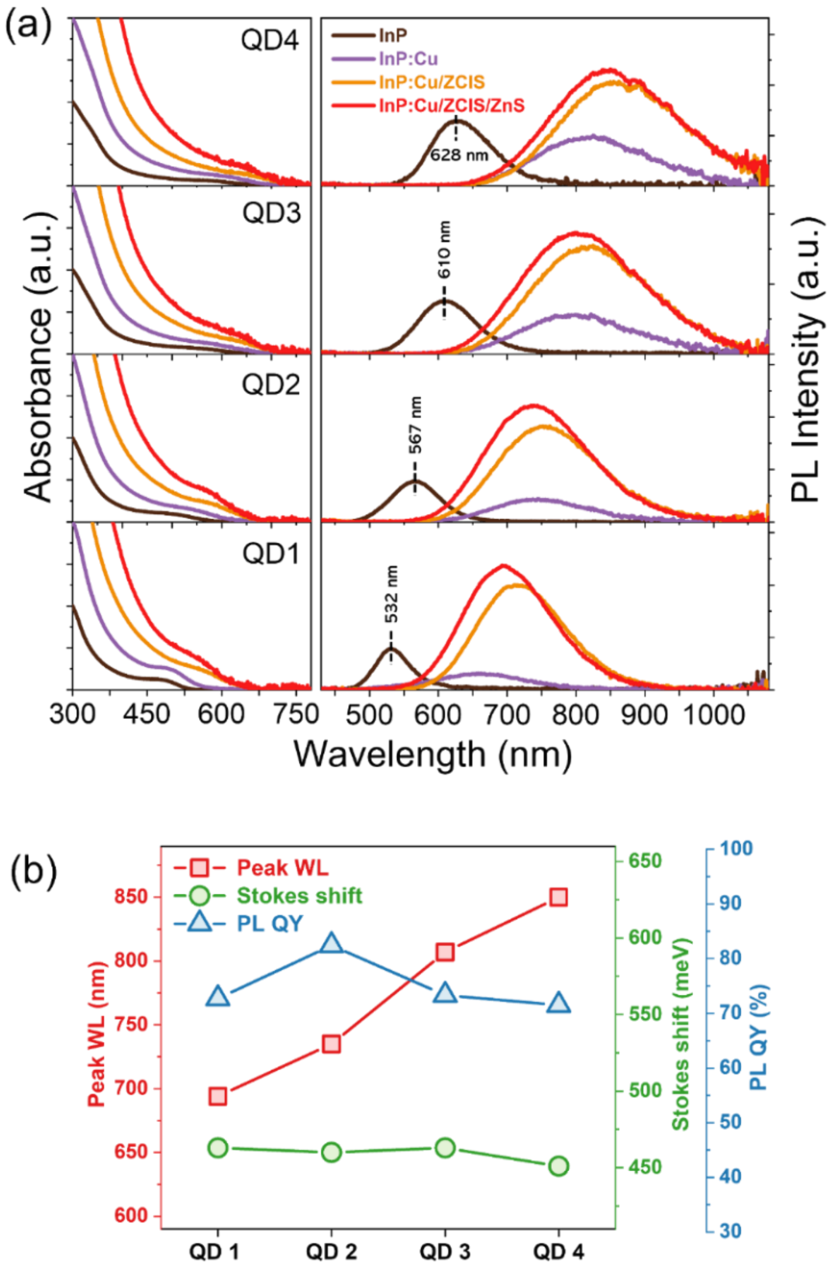

Figure 26. (a) Spectral evolutions of absorption (left panel) and PL (right panel)of InP, InP:Cu, InP:Cu/ZCIS, and InP:Cu/ZCIS/ZnS QDs and (b) variations of PL peak wavelength, Stokes shift, and PL QY of a series of double-shelled InP:Cu/ZCIS/ZnS QDs. Different-sized InP cores emitting at a peak wavelength of 532, 567, 610, and 628 nm were used for Cu doping, being denoted as QD1, QD2 (reference shown in Figure 23), QD3, and QD4, respectively.

Table 5. Absolute PL QYs of InP, InP:Cu, InP:Cu/ZCIS, and InP:Cu/ZCIS/ZnS QDs produced from different-sized InP cores used for Cu doping.

QD	Absolute PL QY (%)			
	532 nm (QD1)	567 nm (QD2)	610 nm (QD3)	632 nm (QD4)
InP	7.5	13.2	12.1	10.5
InP:Cu	20.5	26.7	25.5	24.8
InP:Cu/ZCIS	60.8	64.8	61.5	60.4
InP:Cu/ZCIS/ZnS	72.7	82.4	73.3	71.5

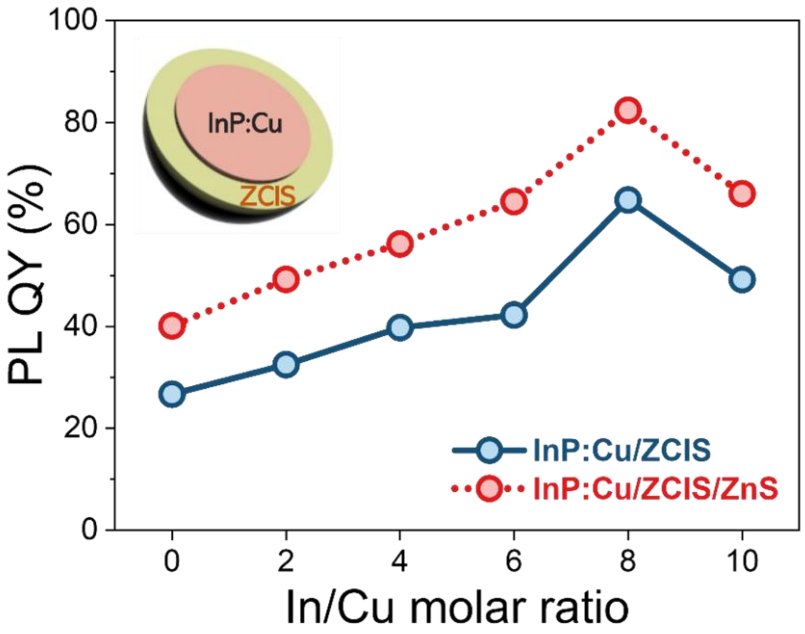

Figure 27. Changes of PL QY of InP:Cu/ZCIS and InP:Cu/ZCIS/ZnS QDs as a function ofnominal In/Cu molar ratio used in ZCIS shelling step.

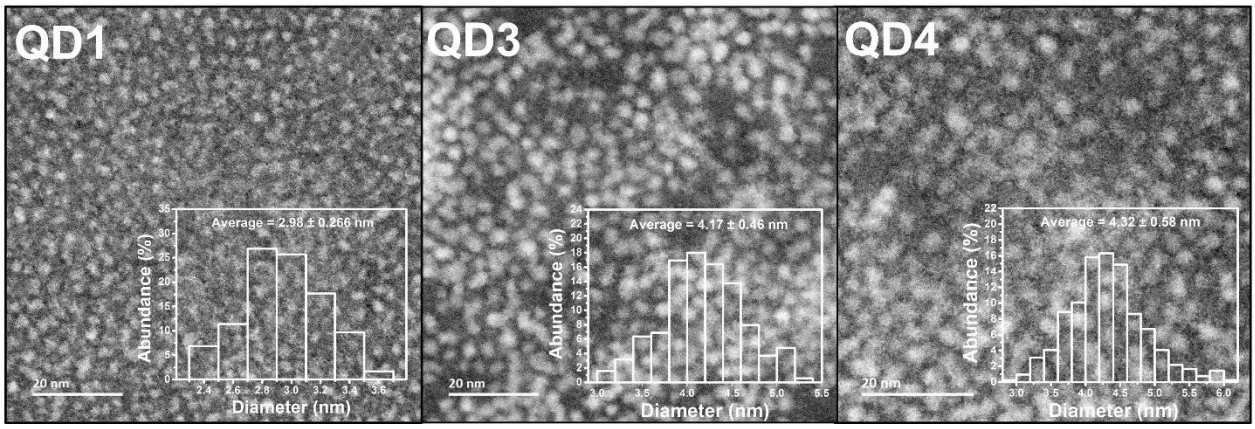

Figure 28. Annular dark-field scanning transmission electron microscopy (ADF-STEM) images and size histograms of QD1 (532 nm), QD3 (610 nm), and QD4 (628 nm), showing average sizes of 2.98 ± 0.27, 4.17 ± 0.46, and 4.32 ± 0.58 nm, respectively.

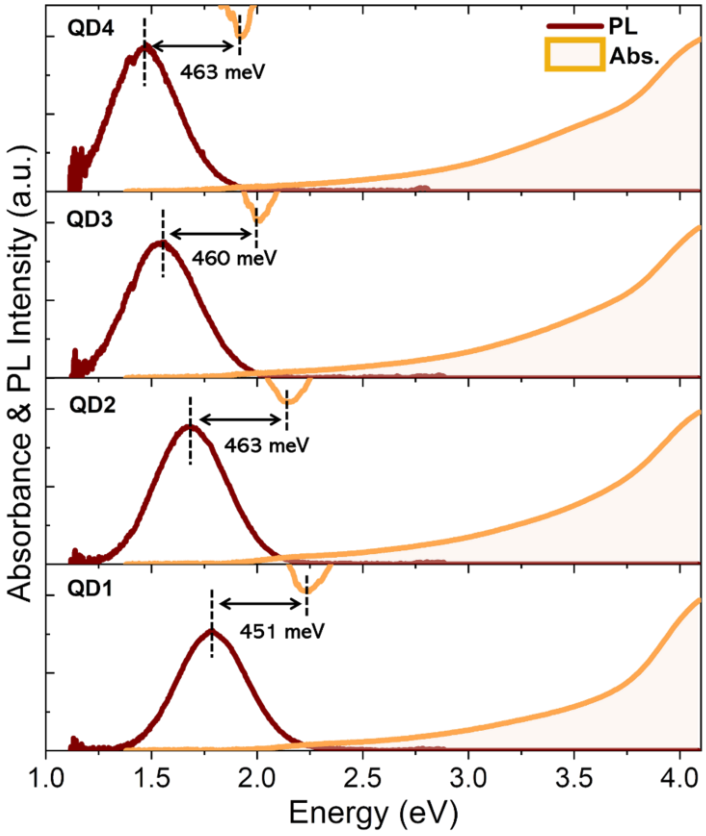

Figure 29. PL versus original and its second derivative absorption spectra of a series of InP:Cu/ZCIS/ZnS QDs synthesized from QD1–4, resulting in overall large Stokes shifts of 451–463 meV.

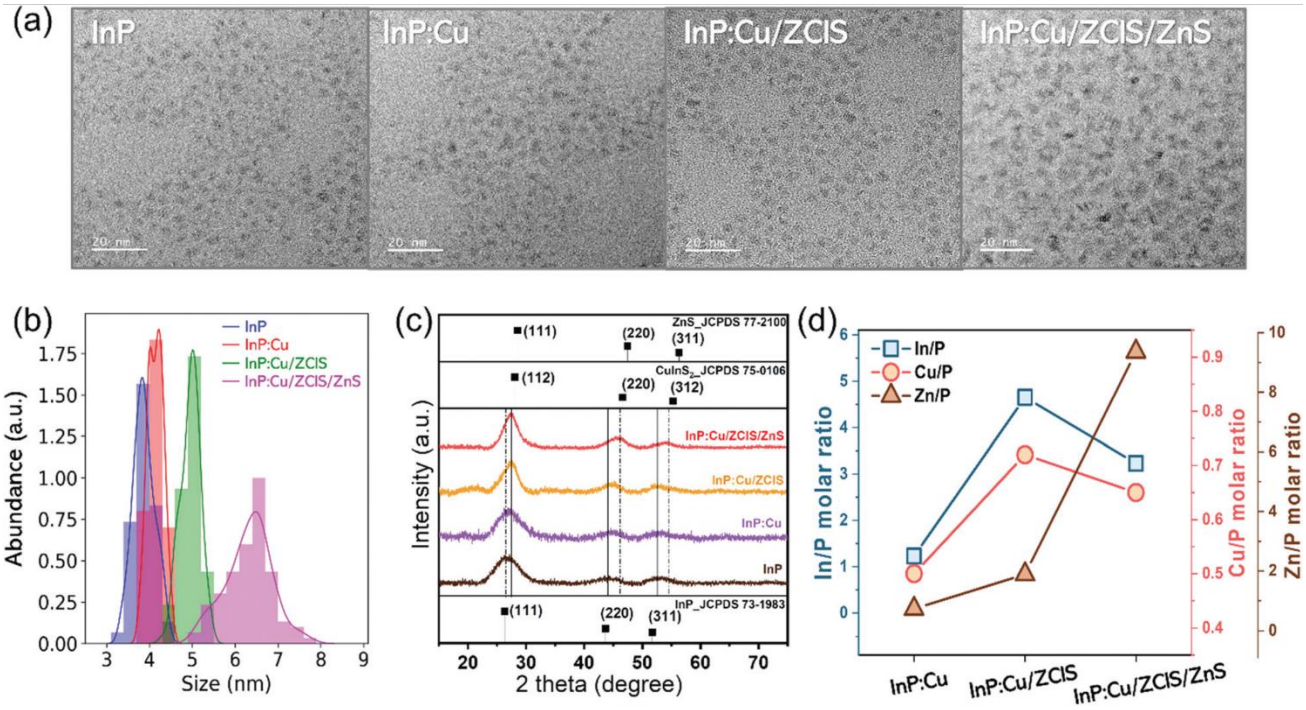

Figure 30. (a) TEM images, (b) corresponding histograms of particle size distribution, and (c) XRD patterns of InP, InP:Cu, InP:Cu/ZCIS, and InP:Cu/ZCIS/ZnS QDs. The scale bars in (a) are 20 nm for all. (d) ICP-OES-based actual elemental compositions of In/P, Cu/P, and Zn/P molar ratios of InP:Cu, InP : Cu/ZCIS, and InP: Cu/ZCIS/ZnS QDs.

Taking a representative sample of QD2 in Figure 26, the size and morphological evolutions of QDs at each step were examined by high-resolution TEM (Figure 30). The overall QD size gradually increased with the synthetic step. The size uniformity was relatively well maintained having small standard deviations ($\sigma \leq 4.4\%$), though the final ZnS shelling step induced a size dispersion to a certain degree (Figure 30b). Specifically, the average diameters of InP and InP:Cu were 3.88 ± 0.18 nm and 4.14 ± 0.24 nm, respectively. This size disparity is physical evidence that the ZCIS shell was indeed formed, albeit nascent, by the presence of a sulfur-feeding DDT added along with $CuCl_2$, as mentioned above. And the intermediate ZCIS and final ZnS shelling led to further increased diameters of 4.94 ± 0.22 nm and 6.32 ± 0.60 nm, respectively. Based on the size difference between InP and InP:Cu/ZCIS QDs, the thickness of the ZCIS inner shell was estimated to be ca. 0.53 nm. As compared in XRD patterns (Figure 30c), three reflection peaks of (111), (220), and (311) planes of zinc blende InP cores slightly shifted to higher 2θ (i.e., toward chalcopyrite $CuInS_2$ phase) indicative of the deposition of the nascent ZCIS shell. The following growth of thicker ZCIS inner and then ZnS outer shells resulted in further peak shifts in the same direction, consistent with the generation of the intended core/shell heterostructure without the adjunctive formation of secondary phases.

Table 6. ICP-OES results of QDs for each synthetic step.

QD	Element			
	In^P	S^P	Zn^P	Cu^P
InP:Cu	1.23	0.34	0.73	0.5
InP:Cu/ZCIS	4.65	3.07	1.89	0.72
InP:Cu/ZCIS/ZnS	3.23	7.92	9.36	0.65

P = the mole ratio calculated based on phosphine atom

Table 7. TEM-EDS-based elemental composition results on InP:Cu/ZCIS/ZnS QDs.

QD	Element				
	In	S	Zn	Cu	P
InP:Cu/ZCIS/ZnS	12.5	27.8	39.3	2.5	3.6

With QD2-based samples the compositional variation at each synthetic step was analyzed by ICP-OES. The relative elemental ratios normalized to phosphorus (P) are shown in Figure 30d and Table 6. Compared to InP:Cu, notable elemental increments of In, Cu, and Zn from InP:Cu/ZCIS are another sign that support the nontrivial inner shell growth, being also in line with TEM and XRD results above. According to the ICP-OES elemental molar ratios of InP:Cu and InP:Cu/ZCIS QDs (Table 6), a stoichiometric ratio of the ZICS inner shell was estimated to be Zn (1.16): Cu (0.22): In (3.42): S (2.73). After the growth of the ZnS outer shell, the relative In/P and Cu/P molar ratios were reduced by 30.5 and 9.7%, respectively, as compared to those of InP:Cu/ZCIS. This likely points to the occurrence of the partial cation exchange between In^{3+} and Cu^{+} of the ZCIS shell and Zn^{2+} in the course of ZnS shelling. Such cation exchange is known to be favorable at the CIS/ZnS interface, since not only are CIS and ZnS highly similar in crystal structures, lattice constants, and Gibbs formation enthalpy but also In^{3+}, Cu^{+}, and Zn^{2+} are similar in ionic radius.[187-188] This partial cation exchange will naturally make the preexisting ZCIS inner shell thinner, in turn inducing a stronger quantum confinement. This scenario is also consistent with the blue shifts of PL and absorption after ZnS shelling (Figures 26 and 31). In addition, to further provide analytical reliability in elemental composition, composition measurements of InP:Cu/ZCIS/ZnS QDs were performed by TEM-EDS, showing very similar results (Figure 32 and Table 7) to those from ICP-OES (Figure 30d).

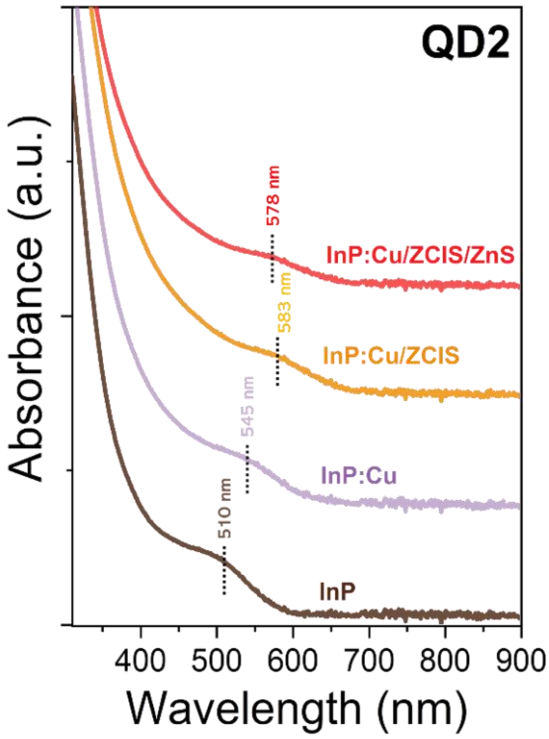

Figure 31. Absorption spectra of InP, InP:Cu, InP:Cu/ZCIS, and InP:Cu/ZCIS/ZnS QDs, showing a slight blue-shift from InP:Cu/ZCIS (583 nm) to InP:Cu/ZCIS/ZnS QDs (578 nm).

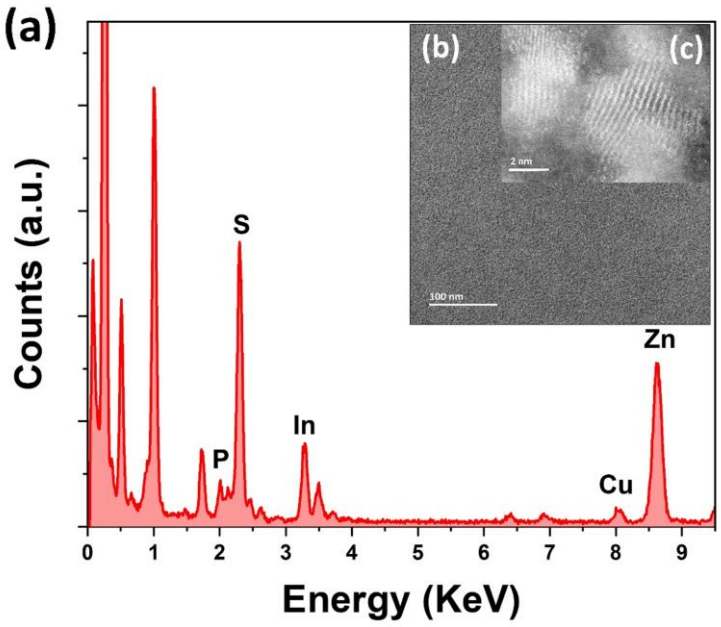

Figure 32. (a) EDS spectrum of InP:Cu/ZCIS/ZnS QDs acquired in (b) TEM image averaged over the broad area, and (c) STEM-ADF image of InP:Cu/ZCIS/ZnS QDs in one spot of (b).

3.3.4. XPS analysis

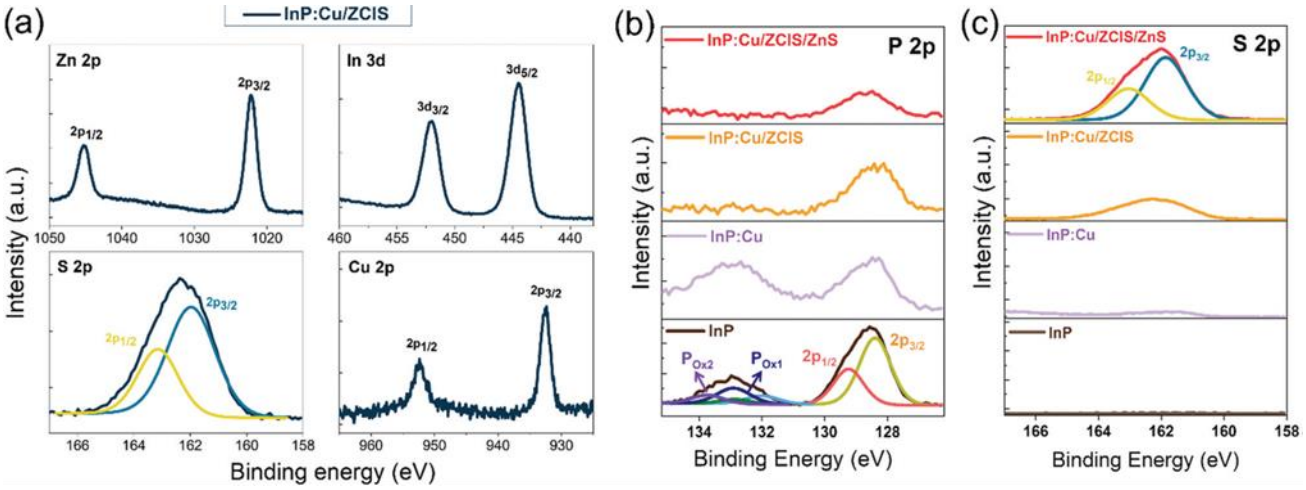

Figure 33. High-resolution XPS spectra of (a) InP:Cu/ZCIS QDs and (b) P 2p and (c) S 2p of InP, InP:Cu, InP:Cu/ZCIS, and InP:Cu/ZCIS/ZnS QDs. All QD samples were derived from QD2.

XPS analysis was implemented to further support the double-shelled heterostructure. As shown in high-resolution XPS scans from InP:Cu/ZCIS QDs (Figure 33a), distinct photoelectron signals from Zn 2p, In 3d, S 2p, and Cu 2p, commonly consisting of doublet peaks with an approximately 2 : 1 ratio in intensity due to their degeneracies, were detected. Both the InP:Cu core and the ZCIS inner shell concertedly contributed to Zn, In, and Cu signals, while the S one originated solely from the ZICS inner shell. A split of Cu 2p photoelectrons only to 2p3/2 (932.52 eV) and 2p1/2 (952.32 eV) points to the +1 oxidation state, although the Cu^{2+} precursor ($CuCl_2$) was used, likely attributable to the reduction of Cu^{2+} to Cu^{+} by excess DDT.[31, 189-190] The relative intensities of P 2p and S 2p of InP, InP:Cu, InP:Cu/ZCIS and InP:Cu/ZCIS/ZnS QDs are compared as shown in Figures 33b and c, respectively. Note that in the case of InP and InP:Cu QDs, the phosphorous oxide (PO_x), peaking at around 133 eV, is attributable to the atmospheric exposure during XPS sample preparation, while no detectable PO_x signal was found in InP:Cu/ZCIS and InP:Cu/ZCIS/ZnS QDs due to the prevention of such an oxidation by the shell. As the synthetic step proceeded sequentially from InP throughout InP:Cu/ZCIS/ZnS, the intensities of P 2p became gradually attenuated, and simultaneously, those of S 2p were escalated, again validating that the ZCIS/ZnS doubles-shelled heterostructure was successfully generated.

3.3.5. Luminescence Solar Concentrators (LSCs)

This section briefly introduces LSC fabrication using as-synthesized InP:Cu/ZCIS/ZnS QDs, most studies of which are cooperated with the display material group in Korea Electronics Technology Institute (KETI). Still, this work, including surface modification and device structure manipulation, is proceeding to implement an industrially feasible LSC module. We hope this work will overcome significant huddles of LSC commercialization.

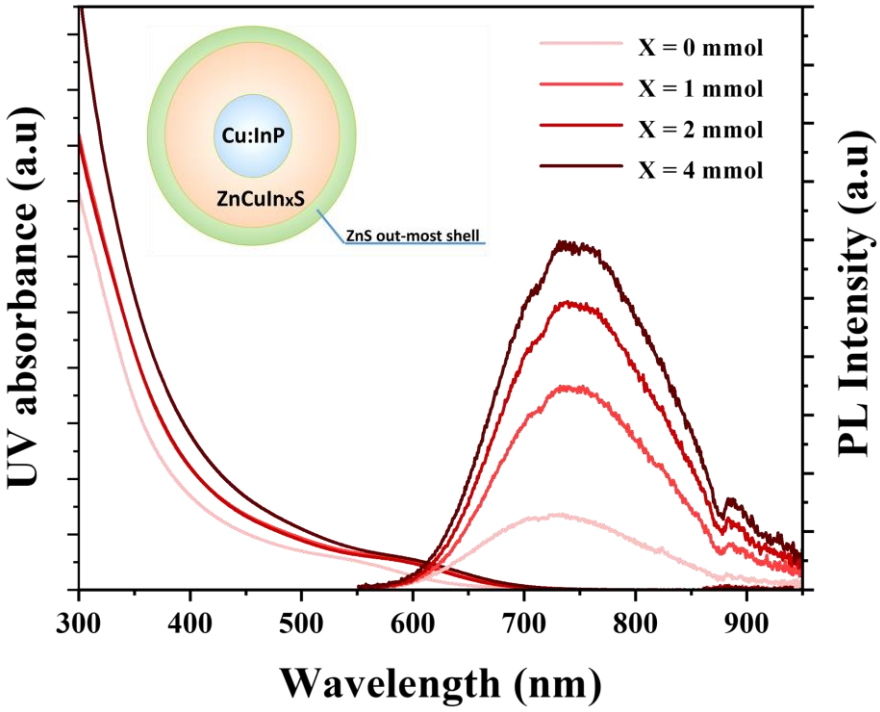

Figure 34. PL and UV spectra of InP:Cu/ZCIS/ZnS QDs by varying indium content in the ZCIS mid-shell.

Table 8. Optical properties of InP:Cu/ZCIS/ZnS QDs by varying indium content in the ZCIS mid-shell.

QD		Optical properties		
Sample	Composition	PL WL (nm)	FWHM (nm)	PL QY (%)
JKS3001	QD (x = 0 mmol)	731.5	164.7	34.3
JKS3002	QD (x = 1 mmol)	743.6	168.7	54.1
JKS3003	QD (x = 2 mmol)	746.0	169.9	62.1
JKS3004	QD (x = 4 mmol)	748.3	175.8	75.6

Figure 34 and Table 8 shows InP:Cu/ZCIS/ZnS QDs by varying indium content in the ZCIS mid-shell, the purpose of which is the research on how indium content in the ZCIS mid-shell affects the optical properties of QD material and the fabricated LSCs. However, both PL QY and UV absorption were changed together, so understanding the effect of the material's optical properties on the LSC module would be ambiguous and difficult. Nevertheless, we synthesized these QDs for LSC demonstrators to see their tendency in devices. Also, without TEM images of those QDs, the red-shifted PL emissions of as-synthesized QDs imply the growth of thicker shell according to the increase of indium precursors. UV absorption of QDs increased with increasing indium content in the ZCIS mid-shell, which supports the formation of thicker ZCIS shell.

Figure 35. External quantum efficiency of LSCs fabricated from InP:Cu/ZCIS/ZnS QDs varying indium contents, the data of which are measured in an absolute sphere with a blue LED light source (450 nm).

Figures 35 and 36 show the external quantum efficiency of LSCs fabricated from InP:Cu/ZCIS/ZnS QDs varying indium contents, where only edge-waveguided emissions were collected and calculated for efficiency in devices. In the LSC module, PL emissions are quenched by scattering and self-absorbing with neighboring particles and additional loss by the reflection index of sandwiched glasses. Of course, this is not reflected in absolute efficiency when exposed to sunlight having a full UV-vis spectrum, but it directly indicates how much PL emissions are lost due to internal negative factors of LSCs. As a result, with increasing in mid-shell thickness, the external QY increased, and the thickest ZCIS shelled InP:Cu QDs showed the maximum external QY of over 14% when

exposed to blue LED light. This data matched well the increasing trend of PL QY and UV absorption in QDs, which indicates that the optical properties of QD material are significant factors in fabricating LSCs.

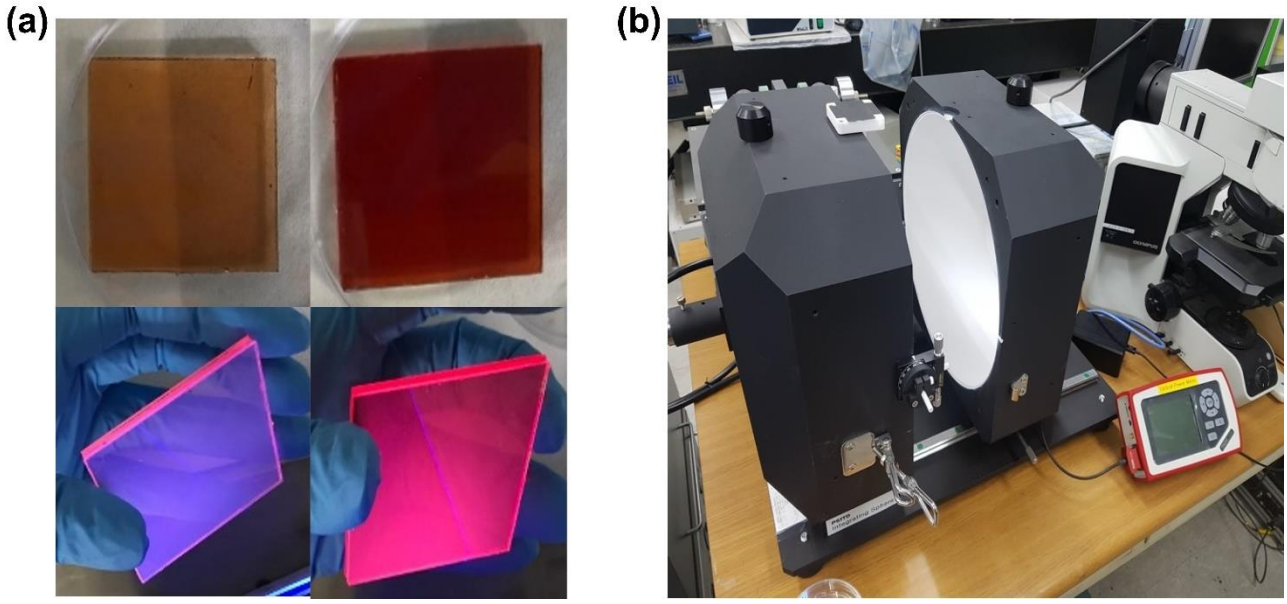

Figure 36. LSCs fabricated from InP:Cu/ZCIS/ZnS QDs, and their external QY measurement system.

3.4. Conclusion

This work mainly focused one-pot synthesis of highly emissive InP:Cu QDs with a novel combination of a ZCIS/ZnS double shelling scheme. After the InP host QDs were synthesized, a small amount of DDT as a hole-withdrawing agent that allowed for the complete suppression of BE-PL was added together with CuCl2, leading to the formation of the primitive ZCIS shell as well as the incorporation of Cu ions into the InP host. Energetic alignment of the ZCIS shell relative to the InP core was simulated to be a type-II heterostructure. Following an additional ZCIS growth for a thicker inner shell, ZnS outer shelling was consecutively implemented, resulting in substantial stepwise increments in the PL QY for each shelling step. Using different-sized InP cores emitting from 532 to 628 nm, identical Cu doping and ZCIS/ZnS double shelling were applied. The resulting InP:Cu/ZCIS/ZnS QDs with the tunable near-IR PL of 694–850 nm displayed unprecedentedly high PL QYs up to 82.4% and substantial Stokes shifts larger than 450 meV. These exceptional PL QYs were attributable to the suitable formation. In addition, InP:Cu/ZCIS/ZnS QDs were applied for LSC fabrication, which shows the possibility that this new structured NIR-emitted QDs can be utilized.

4. LIGAND EFFECT IN 1-OCTANETHIOL PASSIVATION OF InP/ZnSe/ZnS QDs

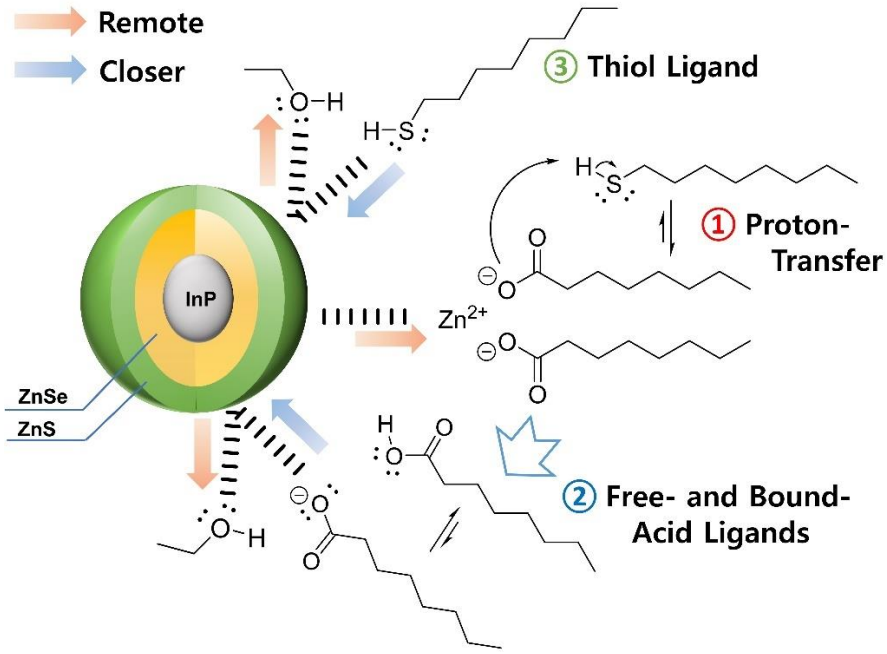

This section is based on published manuscript entitled "Ligand Effect in 1-Octanethiol Passivation of InP/ZnSe/ZnS Quantum Dots– Evidence of Incomplete Surface Passivation during Synthesis" (J. Kim et al., Small. 2022 Oct;18(40):2203093) to Small.

4.1. Introduction

In this work, the interaction between the QD surface and all ligands that are used in the synthesis of InP/ZnSe/ZnS QDs (zinc octanoate–ZnOA, 1-octanoate–OA, zinc stearate–ZnSA, 1-trioctylphosphine–TOP, acetone–AC, ethanol–EtOH) and the subsequent surface modification (1-octanethiol–OTT) are investigated in detail. Through surface analyses, such as ^{1}H-NMR spectroscopy and MS spectrometry, the amount of OTT on the QD surface not only affects the ratio to other ligands but also affects their binding energy to the QD surface. In addition, analysis of interparticle spacing (i.e., QD edge-to-QD edge distances) via transmission electron microscopy (TEM) indirectly provides evidence for incomplete surface passivation (i.e., the presence of surface vacancy sites) during synthesis. Initially, these vacancies are coordinated with EtOH and AC solvent ligands as evidenced by photoluminescence (PL), NMR spectroscopy, and thermogravimetric analysis–mass spectrometry (TGA–MS). Moreover, these experiments also show that OTT induces a surface passivation and ligand exchange on the QD surface via proton transfer with other ligands.

In prototype experiments, the data show that the incomplete surface passivation identified in this work are relevant to defect-related emission, current efficiency in EL devices, and UV stability of the QDs. As a result, this study shows the connectivity between the surface properties of the QDs and the resulting quantum dot light-emitting diodes (QD–LEDs).

4.2. Experimental Details

4.2.1. Materials

Indium acetate ($In(Ac)_3$, 99.99%), zinc acetate ($Zn(Ac)_2$, 99.99%) tri-n-octylphosphine (TOP, 97%), 1-octanoic acid (OA, ≥99%), 1-octadecene (ODE, 90%), zinc stearate (ZnSA, 10–12% Zn basis), 1-octanethiol (OTT, ≥98.5%), selenium (Se, 99.99%), sulfur (S, 99.98%), acetone (AC, ≥99.5%), toluene (anhydrous, 99.8%) and ethanol (EtOH, 96%), were purchase from Sigma-Aldrich Co. Tri(trimethylsilyl) phosphine (TMSP, 97.5%) was purchased from Vezerf Laborsynthesen GmbH. Zinc octanoate (ZnOA), tri-octylphosphine selenide (TOP–Se), and tri-octylphosphine sulfide (TOP–S) was prepared beforehand. For QD–LED fabrication, 4,4',4"–tris(carbazol–9–yl)triphenylamine (TCTA), molybdenum oxide (MoO_3, 99.99%), and silver (Ag) were purchased from Lumtec, Sigma Aldrich, and Umicore, respectively. All the chemicals were used without further purification.

(a) Preparation of ZnOA. $Zn(Ac)_2$ (3.70g, 20 mmol) and OA (6.40 ml, 40.4 mmol) were placed in a 100ml three-neck round bottom flask connected to a reflux condenser and equipped with rubber septa and thermocouple. The mixture was heated to 120°C and degassed under reduced pressure (<150 mTorr) for 10 h with vigorous stirring to remove water and acetic acid species. After backfilling the reactor with N_2 atmosphere, reaction flask cooled down to 80°C, the reaction mixture of which are poured into 250 ml of acetone for crystallization and filtered by Buchner funnel under low pressure to eliminate unreacted OA and acetone (<50 Torr). After filtration of mixture, ZnOA powder was dried at 80°C for 24 h.

(b) Preparation of 2M TOP–Se. Se powder (1.58 g, 20 mmol) and TOP (10 ml) were placed in 50ml two-neck round flask with rubber septa and thermocouple. The mixture was heated to 80°C for 2 h under reduced pressure (<150 mTorr). Se powder was dissolved in TOP and became a clear solution, 2M TOP–Se. After backfilling the reactor with N_2 atmosphere, the flask was cooled down to room temperature.

(c) Preparation of TOP–S. S powder (0.64 g, 20 mmol) and TOP (10 ml) were placed in 50ml two-neck round flask with rubber septa and thermocouple. The mixture was heated to 80°C for 2 h under reduced pressure (<150 mTorr). Se powder was dissolved in TOP and became a clear

solution, 2M TOP–S. After backfilling the reactor with N2 atmosphere, the flask was cooled down to room temperature.

4.2.2. Synthesis of InP QDs

$In(Ac)_3$ (584 mg, 2mmol), ZnSA (1.26 g, 2mmol), and 10ml of ODE were added into a 50ml three-neck round bottom flask connected to a reflux condenser and equipped with rubber septa and thermocouple. The mixture was heated to 150°C and degassed under reduced pressure (<150 mTorr) for 10 hours with vigorous stirring to remove water and oxygen species. After backfilling the reactor with N2 atmosphere, 1 mmol of 1M TMSP dissolved in ODE was rapidly injected into the flask at 150°C and the solution was heated up to 300°C (5 min / °C) for 3 min with vigorous stirring, and the growth solution cooled down to room temperature.

4.2.3. Synthesis of InP/ZnSe/ZnS QDs

All synthesis processes, including ZnSe and ZnS shelling on InP QDs, were continuously performed without purification. For ZnSe shelling on the surface of InP QD, ZnOA powder (2.11 g, 6 mmol) was introduced to the reaction flask, heated to 130°C, and degassed under reduced pressure (<150 mTorr) for 30 min with vigorous stirring to remove water and oxygen species. After backfilling the reactor with N2 atmosphere, the mixture was heated to 280°C and maintained for 10 min. 2M TOP–Se (3 ml, 6 mmol) was injected to reaction flask at 280°C and the injection temperature was maintained for 30 min. After the formation of ZnSe shell, the reaction mixture was cooled down to room temperature. For ZnS shelling on the surface of InP/ZnSe QDs, ZnOA powder (3.52 g, 5 mmol) was introduced to the reaction flask, heated to 130°C, and degassed under reduced pressure (<150 mTorr) for 30 min with vigorous stirring to remove water and oxygen species. After backfilling the reactor with N2 atmosphere, the mixture was heated to 300°C and maintained for 10 min. 2M TOP–S (5 ml, 10 mmol) was injected to reaction flask at 300°C for 1 h and cooled down to room temperature for surface modification.

4.2.4. Surface modification of InP/ZnSe/ZnS QDs

From QD1 to QD4, The surface modification by OTT was proceeded without purification of QDs. The as-synthesized InP/ZnSe/ZnS QDs were equally distributed into four 50ml three neck-round bottom flask and heated to 150°C. Then, 0 (QD1), 0.2 (QD2), 0.4 (QD3), and 0.6 ml (QD4) of OTT were each injected into four reaction flasks at 150°C and maintained for 10 min. Then, the whole reaction was terminated by cooling down to room temperature and adding an excess amount of toluene. The surface

modified InP/ZnSe/ZnS QDs were isolated by adding an excess amount of a solvent mixture (AC : EtOH = 3 : 1) and then purified by repeated two-times of precipitation/re-dispersion with a solvent mixture/toluene combination using centrifugation (5000 rpm, 20 min).

4.2.5. Inverted structure of QD–LED Fabrication

First, the indium tin oxide (ITO) substrates were cleaned by sequential ultra-sonication with AC and EtOH, and dried in an oven at 100°C for 3h, followed by oxygen plasma treatment. The following steps were performed in a glove box under nitrogen atmosphere. The ZnO nanoparticles for electron transport layer were prepared using procedures previously reported in the literature[191] and were spin-coated onto the as-prepared ITO substrates at 3000 rpm for 30 s, followed by drying at 180°C for 30 min. At QD1 to QD4, The 3 mg / mL of QD solutions were spin-coated onto the ZnO NP layer at 3000 rpm for 30 s without further thermal annealing. After the solution processes, TCTA (40 nm) and MoO_3/Ag (10 nm / 150 nm) were deposited by the thermal evaporation on the QD layer in a high-vacuum chamber as a hole transport layer and metallic anode, respectively.

4.2.6. Characterization

(a) **Optical spectra:** The absorption spectra of QDs dispersed in toluene were measured by UV-visible spectroscopy (UV-vis, Lambda 19 spectrometer, PerkinElmer), the results of which were obtained over a wavelength range of 250 to 800 nm. The optical density of the QD1, QD2, QD3, and QD4 samples in toluene was set to 0.1. The photoluminescence (PL) spectra and absolute photoluminescence quantum yields (PL QYs) of QDs in toluene were recorded using an integrating sphere with an absolute PL QY measurement system (C9920–02 system, Hamamatsu, Japan), including 150 W Xenon lamp, monochromator, and back-thinned CCD multichannel analyzer, with excitation wavelength of 350 nm for InP core, InP/ZnSe, InP/ZnSe/ZnS, and OTT–modified InP/ZnSe/ZnS QDs.

(b) **X-ray diffraction (XRD):** X-ray powder diffraction data were collected on a PANalytical Empyrean powder X-ray diffractometer in a Bragg–Brentano geometry. It was equipped with a PIXcel1D detector using Cu K_α radiation (λ= 1.5419 Å), operating at 40 kV and 40 mA. θ/θ scans were run in a 2θ range of 4-100° with a step size of 0.0131° and a sample rotation time of 1s. It was equipped with a programmable divergence, anti-scatter slit, and a large Ni-beta filter. The detector was set to continuous mode with an active length of 3.0061°. Each measurement was repeated five times, the results of which added up to a total spectrum. This resulted in a whole measurement time of 164 min.

(c) **Transmission Electron Microscopy (TEM):** The particle sizes and interparticle spacing, from QD1 to QD4, were determined using TEM (JEOL JEM–F200, Japan)

(d) **Nuclear magnetic resonance (NMR):** All NMR experiments were performed using a Unity INOVA 500 NMR spectrometer from Varian equipped with a (^{1}H-^{19}F) / (^{15}N-^{31}P) 5 mm switchable probe operating at 499.79 MHz (for the ^{1}H frequency). All samples, including QD1, QD2, QD3, and QD4, and reference chemicals were prepared with a concentration of 10 mg / ml in chloroform-d3. Besides ZnOA, all measurements were carried out at room temperature. In particular, ZnOA was measured in chloroform-d3 at 50°C due to its low solubility in chloroform.

(e) **Thermal Gravimetric Analysis with Mass Spectroscopy (TGA–MS**): The TGA/MS experiments were performed using a Mettler Toledo TGA2 LF/1100/885 (TGA) and Pfeiffer ThermoStar (MS). Under N_2 atmospheric conditions of 40 mL / min (20 mL / min balance purge + 20 mL / min sample), approximately 10 mg of each sample were stabilized at 30°C for 15 min and then heated up to 550°C (10 K / min). For MS analysis, the in-let and capillary temperatures are 120°C and 150°C, respectively. The scan modus is 10-199 amu at 200 ms / amu.

(f) **Thermal Gravimetric Analysis with Mass Spectroscopy (TGA–MS):** The TGA/MS experiments were performed using a Mettler Toledo TGA2 LF/1100/885 (TGA) and Pfeiffer ThermoStar (MS). Under N_2 atmospheric conditions of 40 mL / min (20 mL / min balance purge + 20 mL / min sample), approximately 10 mg of each sample were stabilized at 30°C for 15 min and then heated up to 550°C (10 K / min). For MS analysis, the in-let and capillary temperatures are 120°C and 150°C, respectively. The scan modus is 10-199 amu at 200 ms / amu.

(g) **Fourier Transform Infrared spectroscopy (FT–IR):** Fourier transform infrared spectroscopy (FT–IR) was measured by a Nicolet iS20 FT–IR Spectrometer (Thermo Scientific, USA) with an attenuated total reflection (ATR) hemisphere.

(h) **Time–resolved Photoluminescence spectroscopy (TR–PL):** Time-correlated single photon counting measurements were performed on a FLS920-stm fluorescence spectrometer (Edinburgh Instruments, UK). An EPLED-320 diode laser (Edinburgh Instruments, UK), with an emission wavelength of 405.6 nm (bandwidth = 12.2 nm), a pulse width of 628.3 ps, and a pulse period of 500 ns, was used as excitation source. Measurement points were collected on a 200 ns scale distributed over 512 channels until peak intensity reached 10,000 counts.

(i) **Photoelectron microscopy:** The ionization energy was measured by a photoelectron spectro-photometer (AC–2, Riken Keiki, Japan) under air in the incident energy range of 3.4 eV to 6.2 eV.

(j) **Characterization of QD–LED:** Current density–voltage–luminance (J–V–L) characteristics were measured with an experimental setup consisting of a source meter (Keithley SMU 236, voltage source range: ± 11.000 V, step size: 1 mV, accuracy: (0.033% + 2.4 mV)) with a current resolution of 100 nA) and spectroradiometer (CS–2000, Konica-Minolta, Japan) under ambient conditions. The spectro-radiometer was introduced to measure the EL spectrum in the range of wavelength from 380 nm to 780 nm with resolution of 0.9 nm/pixel, precision: ± 0.3 nm/luminance range: 0.075 to 125,000 cd/m^2 (measuring angle: 0.2°), accuracy: ± 2%.

4.3. Result and Discussion

4.3.1. Surface Passivation by 1-Octanethiol on InP QDs, and their Interparticle spacing

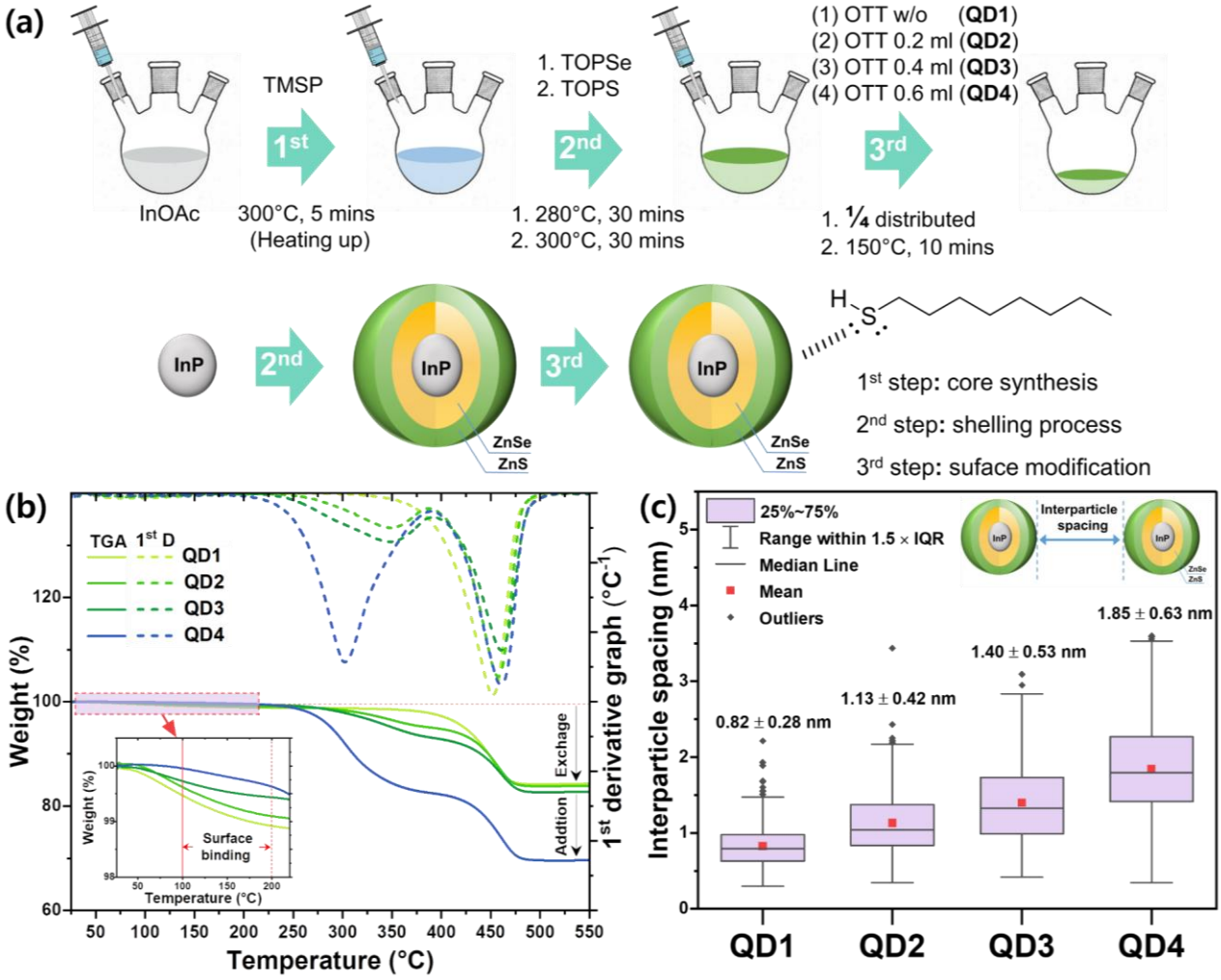

Figure 37. Synthesis of OTT–passivated InP/ZnSe/ZnS QDs in 1-octadecene. Abbreviations, experimental details, PL, PL–QY, UV spectra, and XRD patterns are shown in the Supporting Information (Figures S1, S2, and Table S1 and S2). (b) TGA data including 1st derivative curves (1st D) according to variation of OTT from QD1 to QD4, and (c) their box charts of interparticle spacing obtained from TEM images, where the statistical methods used to assess significant differences with sufficient detailed are described in the 8.2 Statistical Analysis in Supporting Information.

Figure 37a shows the synthetic process of InP/ZnSe/ZnS QDs, including the in-situ surface modification. After the synthesis of InP/ZnSe/ZnS QDs (end of 2nd step), the QD dispersion was split into four fractions without purification. To each of these flasks, a different amount of OTT was added (Figure 37a, 3rd step). After OTT addition, the QDs were purified using a mixture of AC and EtOH to remove residual 1-octadecene and free ligands.

Figure 37b shows the TGA curves from QD1 to QD4 when proportionally introducing OTTs on the QD surface. With increasing OTT content, the 1st derivative curve at around 350°C steadily intensified from QD1 to QD4, and it can be ascribed to the bound-OTT ligands present on the QD surface. Here, the total residual inorganic content is nearly the same from QD1 to QD3 (from 84.3 to 82.7%) but decreases significantly to 69.7% in QD4 (Figure 37b and Figure S4). These data therefore suggest that, from QD1 to QD3, mostly ligand exchange occurs, keeping the overall organic fraction roughly constant, while in QD4 shows significant ligand addition and a correspondingly smaller inorganic fraction (Figure 37b and Figure S4).

Figure 37c exhibits the average interparticle spacing of OTT–modified InP/ZnSe/ZnS QDs determined from over 200 particles, respectively, via TEM images (Figure S3). The resulting interparticle spacing represented an increasing trend from QD1 to QD4. In general, the increase of interparticle spacing is attributed to the increase in the number[192] (i.e., ligand amount or coverage on QD surface) and length[193-194] of ligands on the QD surface, inducing a stronger steric repulsion between surface ligands on neighboring QDs. This result suggests that the increase of OTT content changes the distance between neighboring QDs via ligand exchange or ligand addition. Particularly, in the TGA data (Figure 37b), the weight losses from QD1 to QD3 indicate that primarily ligand exchange occurred. Besides, the weight loss from QD3 to QD4 indicates significant ligand addition, described above. Thus, these data overall suggest that the increasing interparticle spacing at QD1 to QD3 is ascribed to the ligand exchange, related to the change of ligand length, by OTT. In contrast, the increase of the interparticle spacing at QD3 to QD4 is ascribed to the ligand addition, i.e., an addition of further OTT on the QD surface, by OTT

In general, the surface ligands with a more elongated alkyl chain tends to increase the interparticle spacing between neighboring QDs.[193-195] In particular, Oliveira et al. successfully demonstrated a linear correlation of the QD-to-QD distances with the length of various surface ligands.[193] With regards to our experiment, TOP, OA, and OTT all have a C–8 alkyl chain length, and the amount of 1-stearic acid (SA), applied during the InP core synthesis step, is relatively small content than OTT and equally applied from QD1 to QD4 (see the 4.2. Experimental Details in Supporting Information). Assuming that OTTs exchange SA ligands that are bound on the QD surface, a decrease of the interparticle spacing is more reasonable due to the longer chain length of SA (C–18) than that of OTT (C–8). However, the resulting interparticle spacing represents an increasing trend with increasing OTT content from QD1 to QD3; that is, it is experimentally not reasonable. Thus, it alludes that OTT ligands relate to the exchange of other ligands with a shorter carbon chain length (e.g., < C–

8) than OTT. Therefore, extensive investigations including solvent ligand such as EtOH and AC were required.

To elucidate this uncertain interpretation between interparticle spacing and TGA data, one must also consider the individual weight losses throughout the measurement of TGA. TGA data, Figure 37b, shows two different regimes: between 100 and 200°C, the TGA curves show that the weight loss in QD1 is the highest, followed by QD2, QD3, and finally QD4 which shows the lowest weight loss (inset graph of Figure 37b, and Figure S4). This trend is reversed between 200 and 550°C. Here, QD4 shows the highest mass losses, while QD1, QD2, and QD3 show significantly lower mass losses (Figure S4).

These observations can be explained for the weight losses between 50 to 200°C as follows: from QD1 to QD3, there are slightly higher fractions of loosely bound surface molecules, possibly compounds with a lower boiling point. This points to acetone (AC), ethanol (EtOH), and adsorbed water, whose boiling points are 59, 78.5, and 100°C, respectively, in bulk. If these compounds are bound to the QD surface, however, their evaporation may be shifted to higher temperatures. Indeed, TGA–MS data (see Figure 46) confirms the removal of these compounds starting from around 50°C and ending at around 200°C. In contrast, the weight losses between 200 and 550°C can be explained as follows: here, compounds with an even stronger attachment to the QD surface and with higher molecular weight and higher boiling points (bulk) desorb from the QD surface. These can include OTT (b.p. 199°C), TOP (b.p. 284–291°C) and 1-octanoic acid (HOA, b.p. 237°C). This effect is more pronounced between QD3 and QD4, which have been treated with the highest OTT fractions during the ligand modification process.

This may suggest that OTT is related to the displacement of solvent ligands such as EtOH and AC, and it can explain an increasing trend of interparticle spacing from QD1 to QD3 where ligand exchange is dominant (Figure 37b). This is because the carbon chain length of EtOH (C–2) and AC (C–3) is shorter than that of OTT (C–8). Thus, we could speculate that as-synthesized QD (i.e., QD1) has solvent ligands, such as EtOH and AC, that are bound on an incomplete surface generated during synthesis, resulting in the displacement of solvent ligands by OTTs.

4.3.2. TGA MS Analyses of QD surface

Prior to the mass spectral interpretation of the OTT–passivated QDs, the base peaks (i.e., the most intense or characteristic peak in the MS) of all ligands were investigated through the analyses of reference chemicals (OTT, HOA, ZnOA, TOP, AC, and EtOH) in bulk. The base peak of OTT represented M–34 (i.e., mass-to-charge ratio (m/z) = 112, M = molecular ion) as suitable fragment molecular ion peak, which arises from the elimination process of hydrogen sulfide (m/z = 34) of OTT

(Figures 38 and 39). HOA undergoes Mclaferrty rearrangement (γ–cleavage), and its base peak ion indicated the ion m/z = 60 (Figures S8 and S9). However, the base peak of ZnOA represented the ion m/z = 58, whose number is deducted as much as two protons compared to the base peak ion of HOA (m/z = 60) (Figures 40, 41 and 42). TOP is referred to as air-unstable and easily oxidized to the form of trioctylphosphine oxide (TOPO). Thus, the fragmentation patterns of TOP have similarity to that of TOPO, and its base peak represented the ion m/z = 112 at around 320°C (Figures 43 and 44). This base peak is the same as that of OTT, but the detection temperature of OTT is at 147°C which is much lower than that of TOP (315°C). In the case of solvent ligands, the base peaks of EtOH and AC are the ions m/z = 31 and 43, respectively (Figure 45).

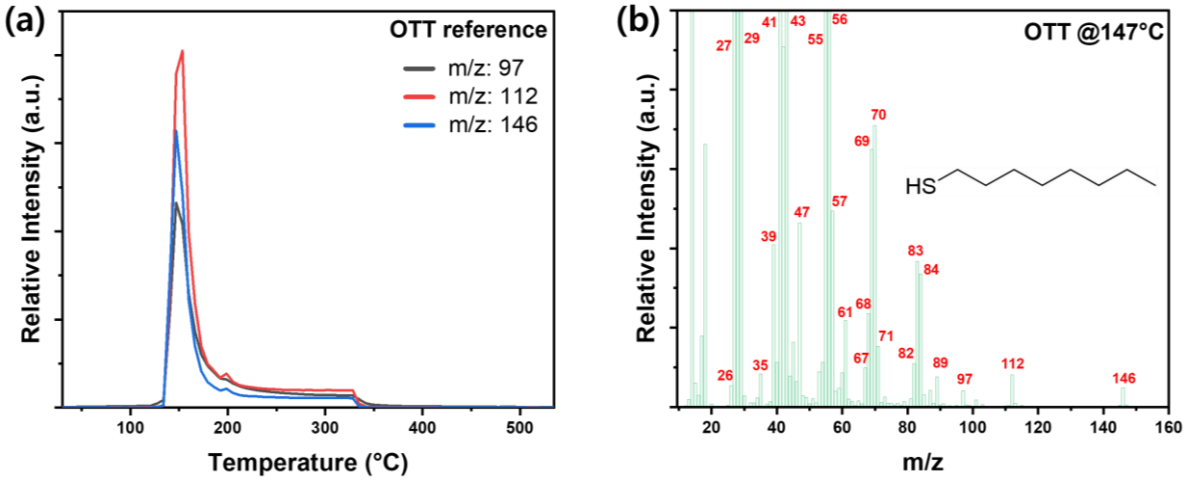

Figure 38. (a) The relative MS intensities of reference OTT and (b) its fragmentation pattern at 147°C.

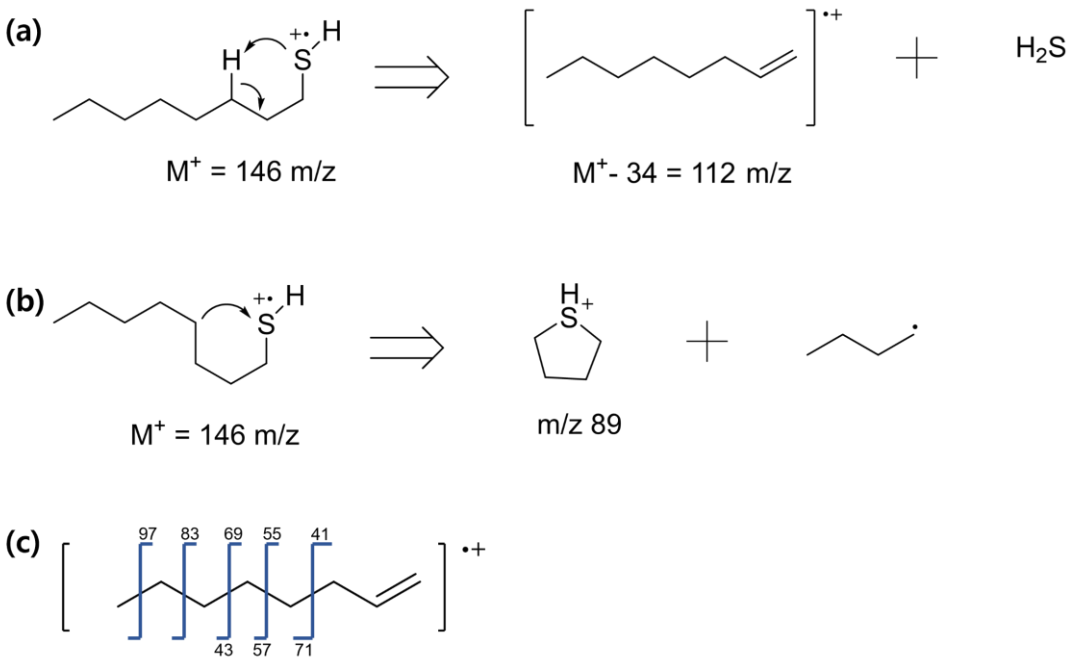

Figure 39. Schematic mechanism of ion fragmentation of reference OTT in MS[196]; (a) to lose the elements of H_2S (γ–cleavage), (b) ring-closing reaction (five–membered thiopenium), and (c) two peak series resulting from cleavages of C–C bonds. (a) the relative MS intensities of reference OTT and (b) its fragmentation pattern at 147°C.[197-198]

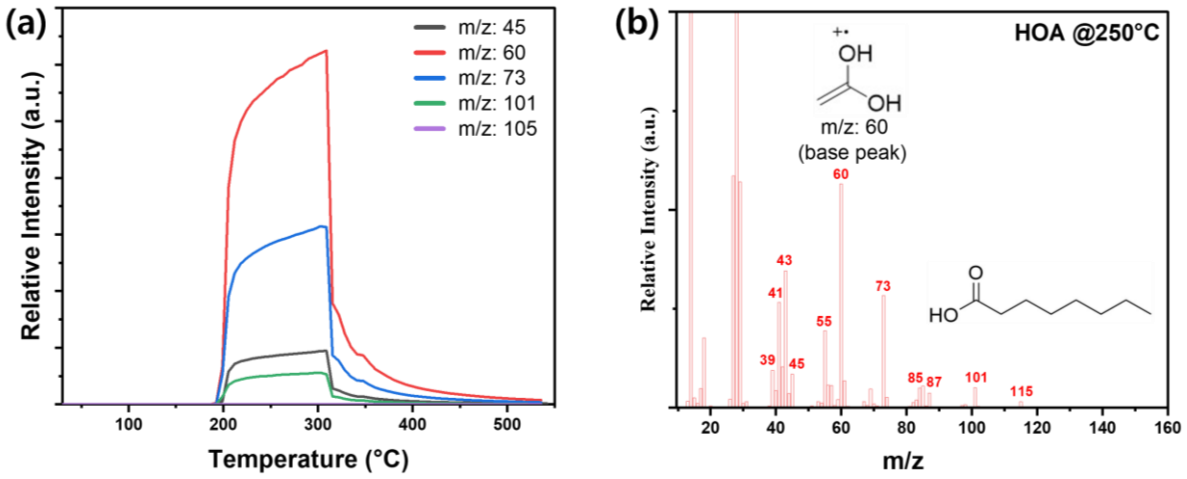

Figure 40. (a) The relative MS intensities of reference HOA and (b) its fragmentation pattern at 250°C

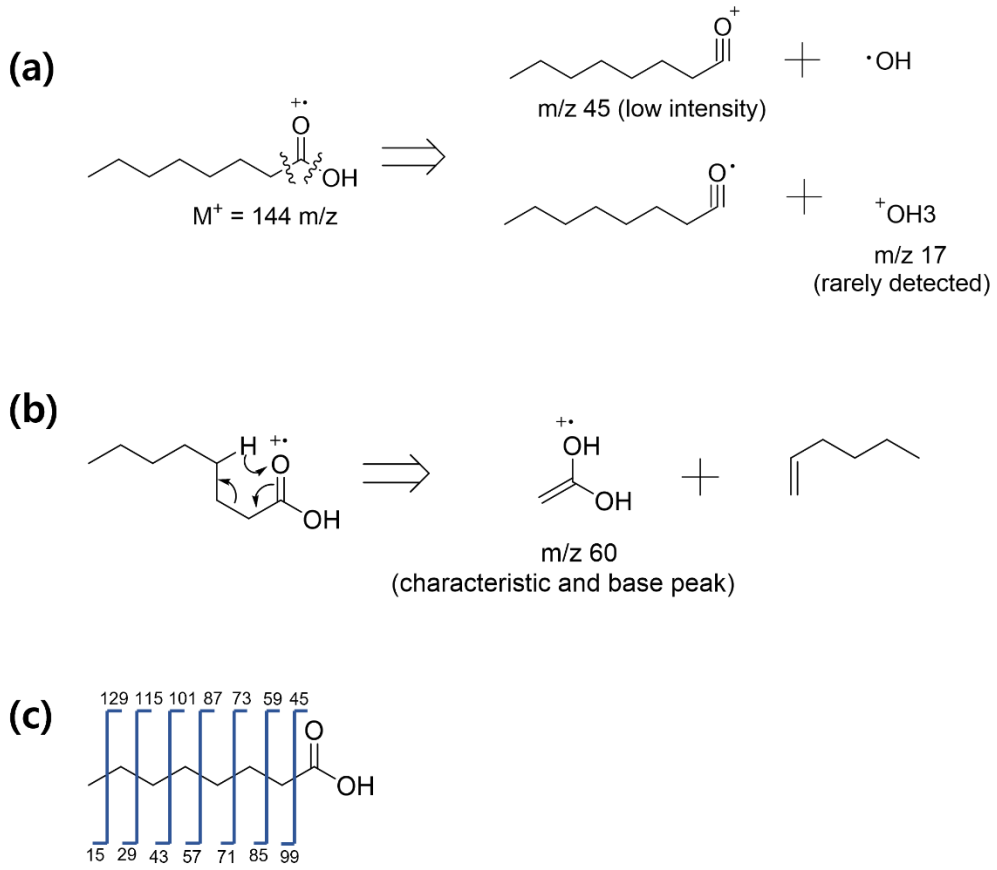

Figure 41. Schematic mechanism of ion fragmentation of reference HOA in MS[196, 198]; (a) α–cleavage, (b) Mclaferrty rearrangement (γ–cleavage), and (c) two peak series resulting from cleavages of C–C bonds.[198]

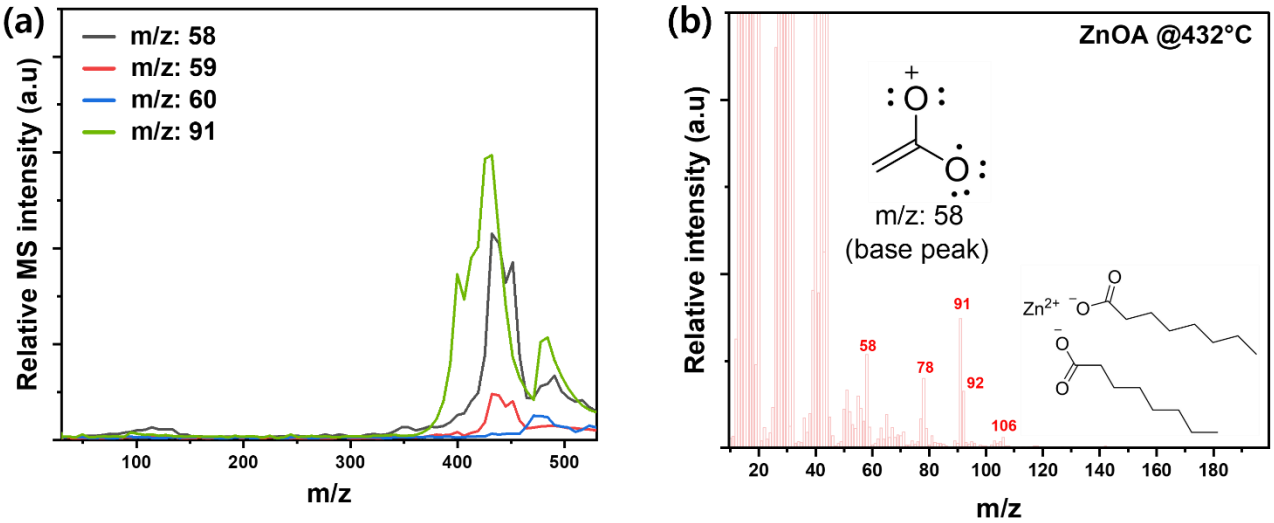

Figure 42. (a) the relative MS intensities of reference ZnOA and (b) its fragmentation pattern at 432°C.

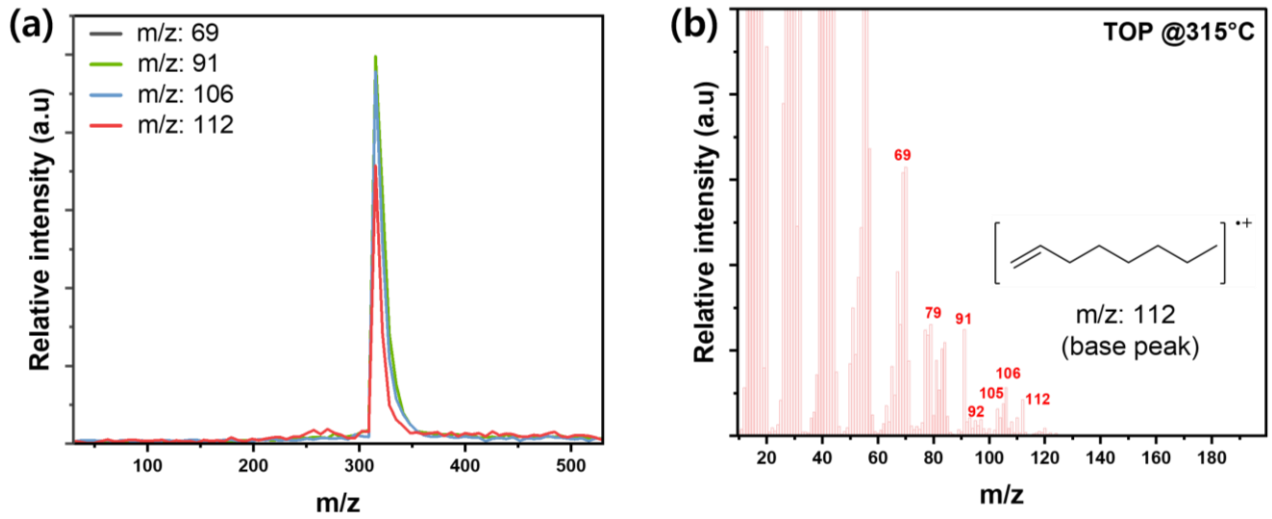

Figure 43. (a) The relative MS intensities of reference TOP and (b) its fragmentation pattern at 315°C.

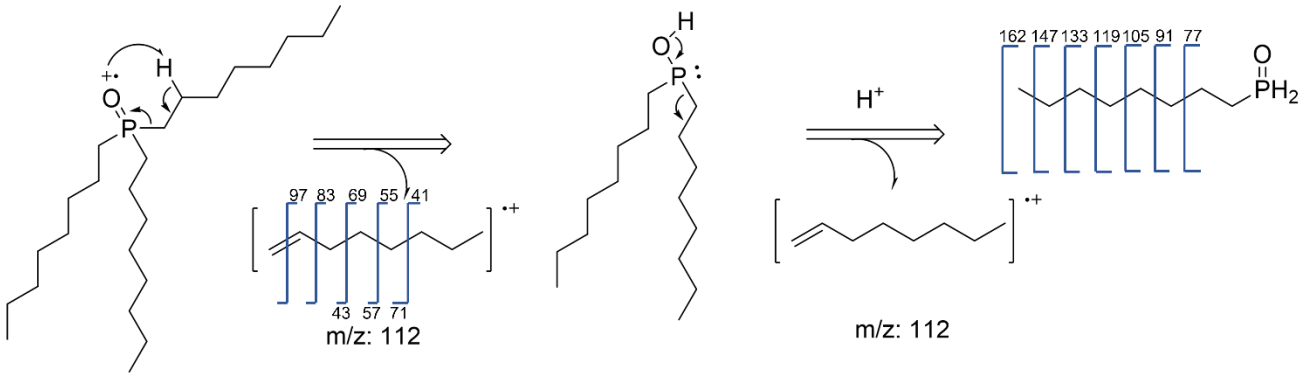

Figure 44. The mechanism of ion fragmentation of reference TOP in MS.[197-198]

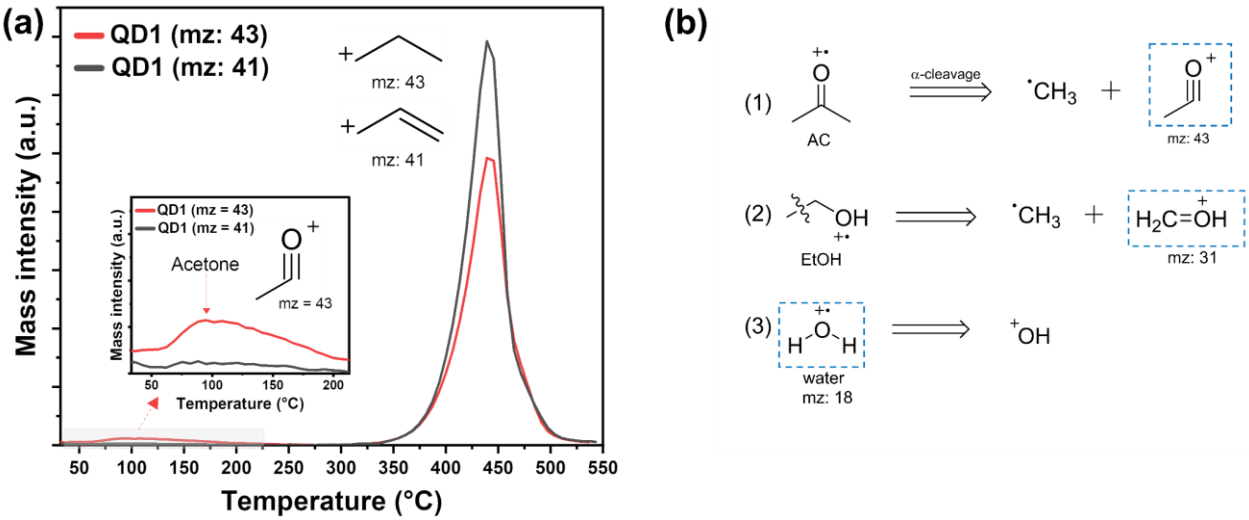

Figure 45. (a) Relative MS intensities of ions m/z = 43 and m/z = 41, and (b) the base peaks of AC, EtOH, and water in MS.[197-198]

In general, to MS analysis, the most stable fragment ion molecule, common to all ligands, is necessary to compare the overall MS peak intensities quantitatively and qualitatively. Generally, 1-propane carbocation ($CH2=CH–CH^{2+}$, m/z = 43) has been introduced to investigate MS peak intensities in an organic compound, for it is the most stable among n-alkyl carbocation substructures.[195] However, this 1-propane carbocation (m/z = 43) is not applied to EtOH and overlaid with fragment ion of acetone (Figures 45 and 49), so it was not suitable for the analysis of surface ligands except for solvent. All n-alkyl ligands (C–8), OTT, OA, and TOP, undergo either β– or γ–hydrogen elimination in the process of ionization of MS (Figure 39, 41, and 44), which induce a continuously ionized fragmentation up to relatively stable n-allylic carbocation substructures, 1-propene carbocation ($CH2=CH–CH^{2+}$, m/z = 41).

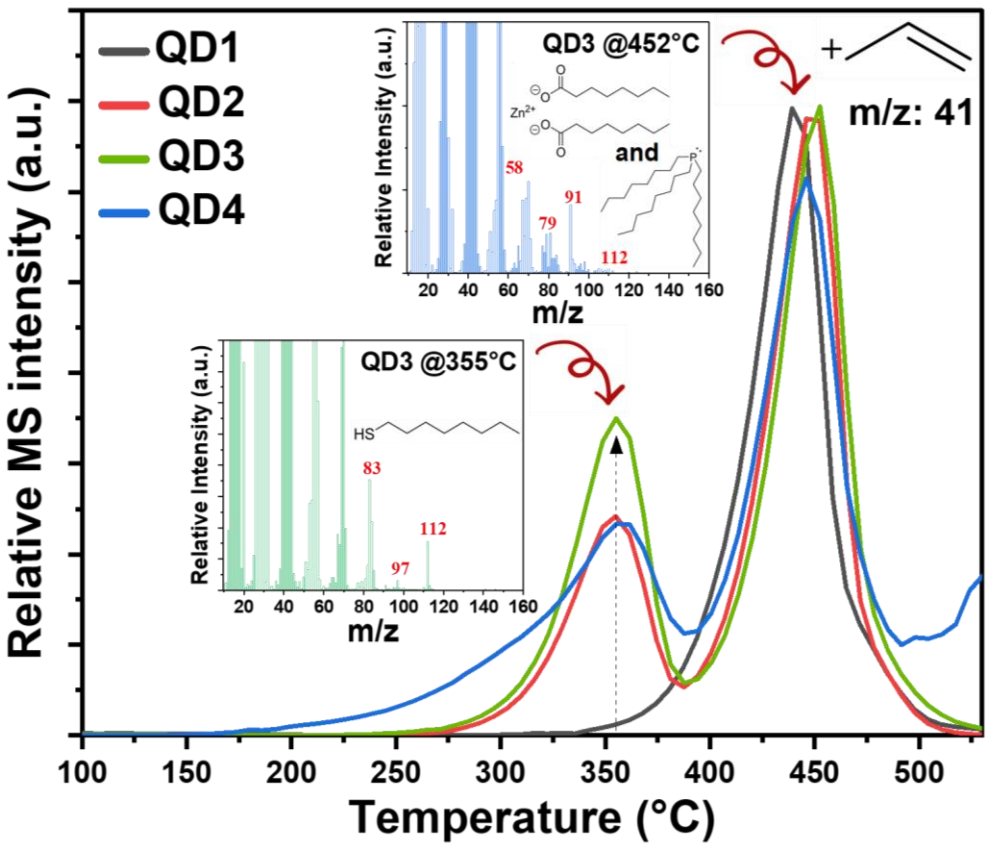

Figure 46. MS intensity of the ion m/z = 41 includes fragment ions of OTT, ZnOA, and TOP. The inset figures represent the fragmentation patterns of QD3 at 355°C and 452°C, respectively.

Figure 46 shows the MS intensities of 1-propene carbocation (m/z = 41) from QD1 to QD4 and the fragment patterns of QD3 at 355 and 452°C in TGA–MS data (Figure 46, inset). The peaks area at 355°C has increased with increasing OTT content from QD1 to QD4, and its fragmentation pattern apparently indicated M–34 (m/z = 112) of OTT. Thus, M–34 was not shown in the fragmentation pattern at 355°C of QD1 because OTT was not applied to QD1 as a surface ligand (Figures S5). In addition, this M–34, 1-octene, has a natural abundance of 0.2% of carbon isotopes (i.e., 13C), and the calculated number of carbons approximately indicated that of 1-octene (Tables 9 and 10). Considering all of these, MS intensity at 355°C represents that it originated from OTT.

The boiling point of OTT is 199°C in bulk, but its MS intensity was detected at 147°C due to its low vapor pressure (0.06 kPa at 25°C, Figure 38). However, from QD2 to QD4, the corresponding MS intensity of OTT emerged at 355°C. It means that OTTs are bound on the QD surface as a ligand, not free OTT, which also implies the increase of the surface binding energy. In addition, QD4 shows the peak broadening up to around 200°C, i.e., low temperature, which means that excess OTT ligands formed the weakly-bound status on the QD surface different from the relatively strongly bound-OTT ligand at 355°C.

The MS intensity at 452°C includes both ion fragmentation patterns of ZnOA and TOP (Figures S5, 42 and 44), where the fragmentation pattern of ZnOA, including the ion m/z = 58, has more intensely emerged than that of TOP, including the ion m/z = 112 (Figures 46, S5, and 47). However, these fragmentation patterns were not consistent with that of HOA (Figures S5, 40 and 41), suggesting that most OAs are present in the form of cationic ZnOA ligands rather than HOA or anionic OA ligands.

Table 9. The number of carbon atoms and the contents of 34S calculated from M–34 and M[a] in m/z intensities of reference OTT, based on relative abundance of carbon and sulfur isotopes.[197-198]

Isotopes	Relative abundance (%)	m/z intensities in OTT	Number of carbon atoms[b] in M–34	% of ^{34}S[c] in M
12C	98.89	1.57×10^{-5}	9.01	-
13C	1.11	1.47×10^{-5}		-
34S	94.81	4.87×10^{-4}	-	95.4
34S	4.4	2.33×10^{-5}	-	4.57

[a] M = molecular ion.

[b] Number of carbon atoms = [relative intensity of (M + 1) peak] / [0.0111 × relative intensity of M + (M + 1) peak]

[c] % of ^{34}S = [relative intensity of (M + 1) peak] / [relative intensity of M + (M + 2) peak]

Table 10. Relative abundance of carbon isotopes between 12C and 13C, and its number of carbon atoms calculated from the m/z intensity of 1-octene in QD3.[198]

Isotopes	^{12}C	^{13}C
Relative abundance (%)	98.89	1.11
m/z of 1-octene	112 (M)	113 (M+1)
m/z intensity of 1-octene	$1.571 \times 10^{-0.5}$	$1.467 \times 10^{-0.6}$
Number of carbon atoms[b]	7.69	

[a] M = molecular ion.

[b] Number of carbon atoms = [relative intensity of (M + 1) peak] / [0.0111 × relative intensity of M + (M + 1) peak]

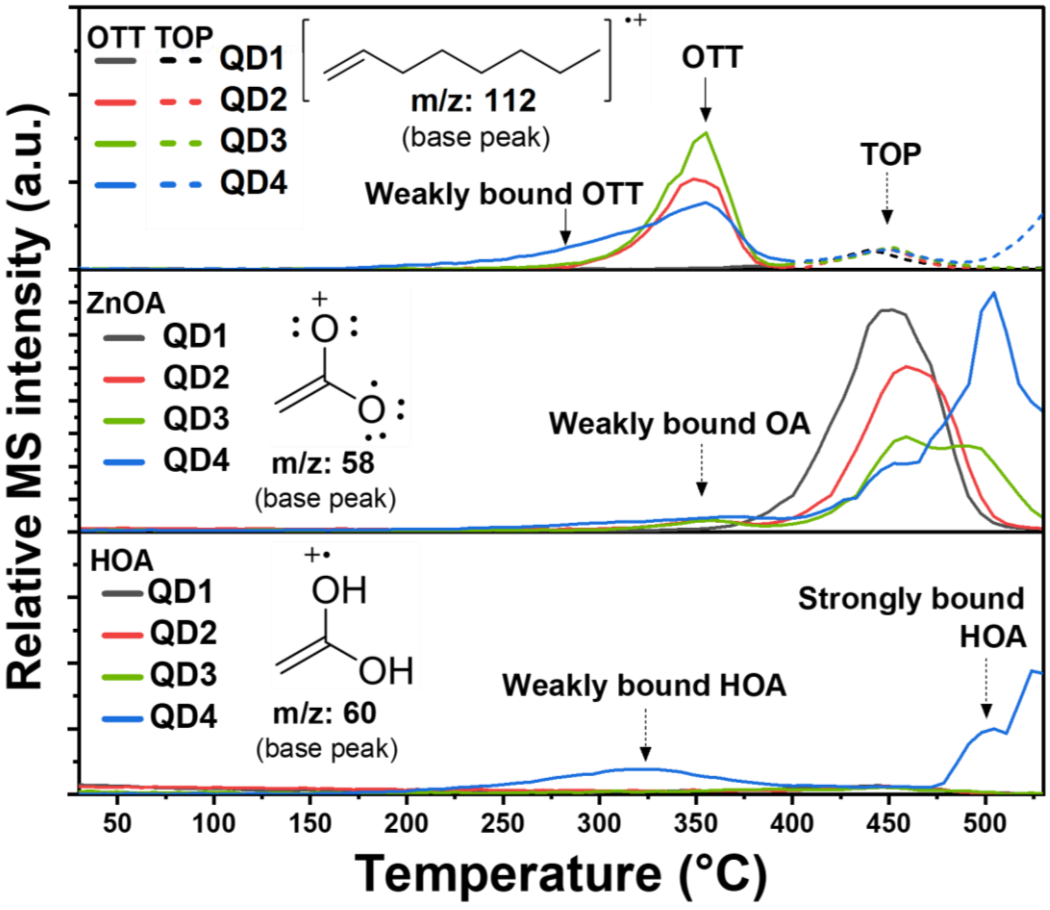

Figure 47. MS intensities of the base peaks of OTT (m/z = 112, from 200 to 400°C), TOP (m/z = 112, from 400 to 500°C) and ZnOA (m/z = 58), and OA (m/z = 60) from QD1 to QD4.

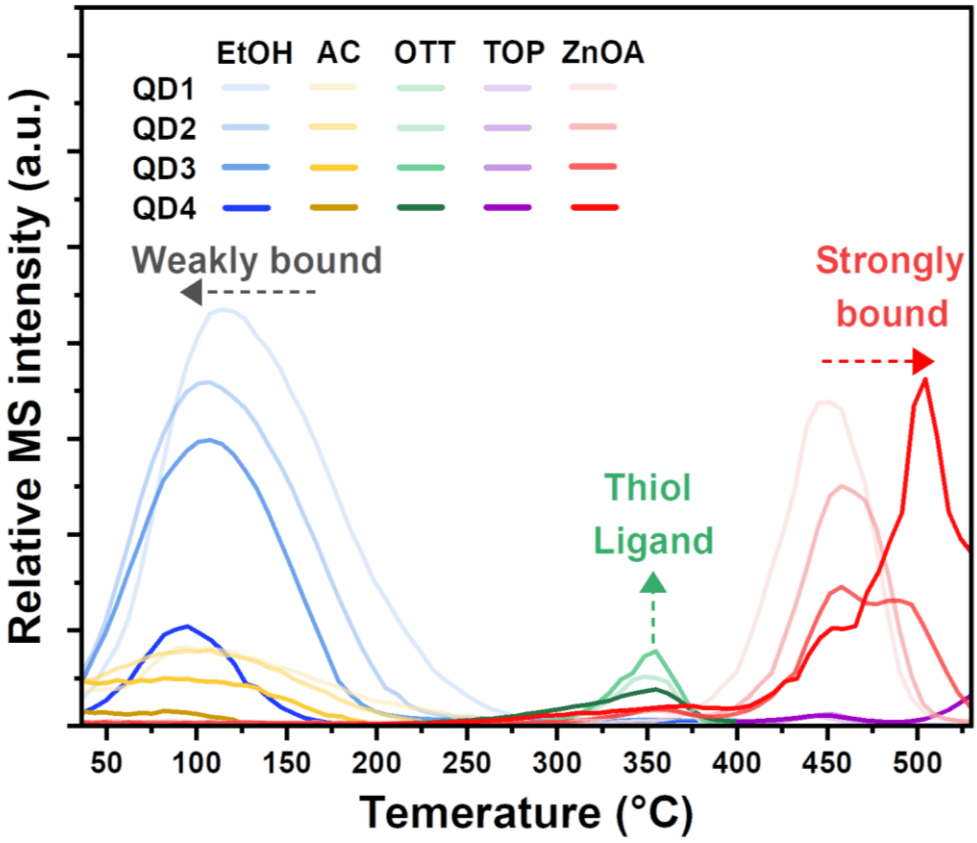

Figure 48. Overall relative MS intensities including OTT (m/z = 112, from 200 to 400°C), TOP (m/z = 112, from 400 to 500°C), ZnOA (m/z = 58), AC (m/z = 43) and EtOH (m/z = 31) from QD1 to QD4.

Figure 48 shows the MS intensities of base peaks including OTT, TOP, ZnOA, AC, and EtOH. The MS intensity of OTT (green lines) showed the same tendency with Figure 46. However, the MS intensity of ZnOA (red lines) was steadily shifted toward high temperature from QD1 to QD4, and its intensity decreased from QD1 to QD3 (Figure 47). In other words, the amount of ZnOA ligands decreased from QD1 to QD3, and it accompanied the increase of surface binding energy from QD1 to QD4. In particular, QD3 shows two-separate components in single MS intensity of ZnOA as if an intermediate state, and it advocates a specific structural transformation of ZnOA. At the same time, the weakly-bound peak of ZnOA and HOA has slightly emerged at 365°C and 325°C, respectively, from QD2 to QD4 (Figures 47 and 48). In other words, it means that OTT ligands induce the loss of OA anions of ZnOA ligands, resulting in weakly-bound ZnOA and HOA ligands on the QD surface. Therefore, we could speculate that OTT mediates proton transfer to OA anions of ZnOA ligands, resulting in OA or HOA ligands (Scheme 4). Mentioned above, the MS detection temperature of ZnOA ligands (red lines) gradually increased with increasing OTT content from QD1 to QD4. It suggests that OTTs not only generate HOA ligands via proton transfer with ZnOA but also derive anionic OA

ligands through acid dissociation of HOA ligands, leading to the strongly bound OA ligands more than ZnOA ligands (Scheme 4).

Scheme 4. Schematic motif of Z-type Ligand displacement via proton transfer by OTT ligands according to TGA-MS analysis

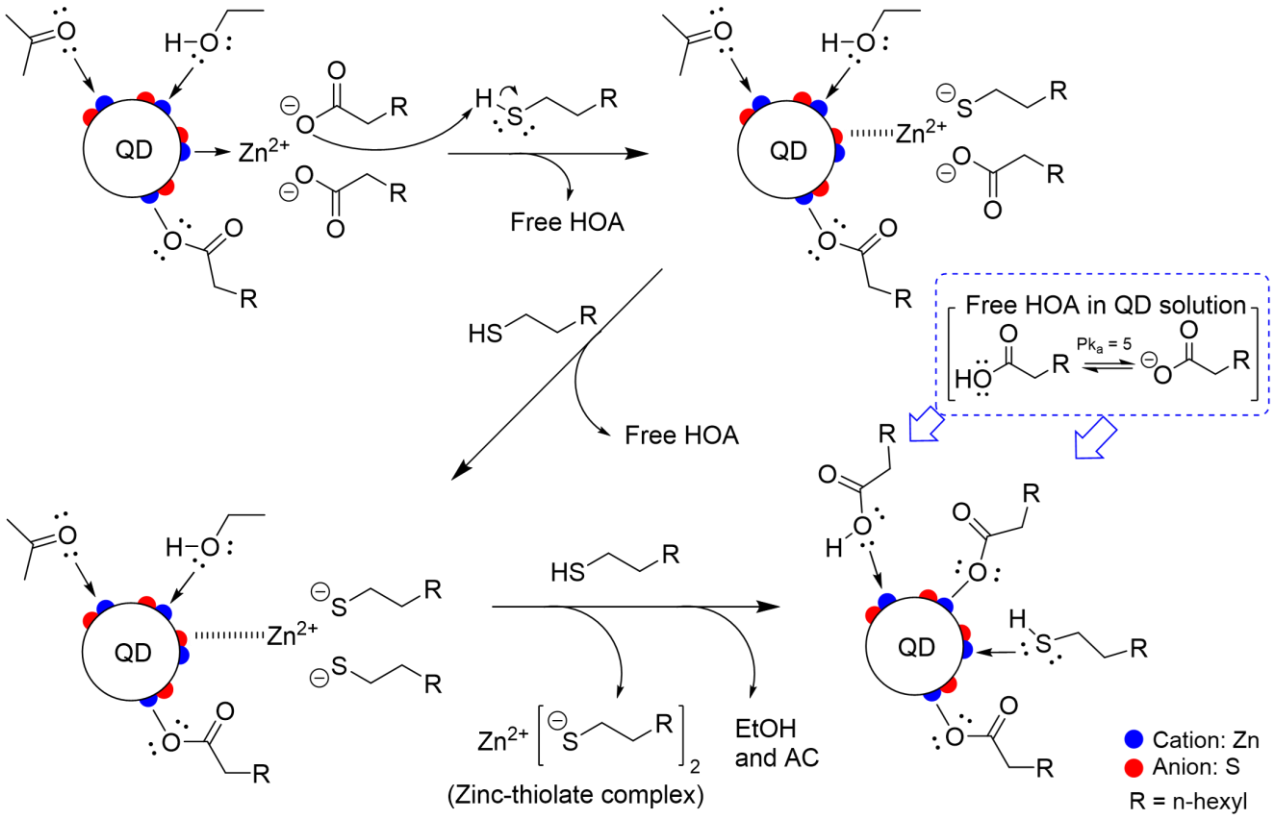

In addition, the weight losses of organic contents from QD1 to QD3 show a gradual increasing tendency (0, 3.8, and 6.4%) at 355°C and a decreasing tendency (14.6, 11.4, and 10.4%) at 452°C, respectively (Figures 37b and S4). In contrast to that, from QD3 to QD4, the weight loss of organic contents at 355°C has rapidly increased from 6.4 to 17.2%, and the weight loss of organic contents at 452°C has conversely even risen from 10.4 to 12.8%. In general, the ratio of surface ligands on QD surface follows Le Chatelier's principle, even though it is a Langmuir-like adsorption.[199] Given that OTTs were proportionally introduced from QD1 to QD4 (from 0 to 0.6 ml), this rapid increase of the organic content is not reasonable for Le Chatelier's principle. Therefore, It suggests that OA and HOA, generated from ZnOA ligands via proton transfer by OTT, re-attach to the QD surface as surface ligands, which can explain the conversely increased weight loss of organic contents at 452°C. Also, the generation of weakly-bound ZnOA and HOA ligands at QD4 can explain the rapidly increased weight loss of organic contents at 355°C (Figure 47 and 48).

In summary, OTTs generate OA and HOA ligands via proton transfer, so that they can re-attach as the form of free- or bound-ligands to the QD surface, not been eliminated out of the QD (Figure 47 and Scheme 4). In conclusion, the surface passivation by both OTT and OA (derived from ZnOA) ligands can explain the rapid increase of the organic content between QD3 and QD4. On the other hand, the MS intensity of TOP (purple lines, Figure 48) was nearly fixed at around 460°C regardless of the OTT content from QD1 to QD4, which alludes that OTT requires a protic ligand to displace other ligands through proton transfer.

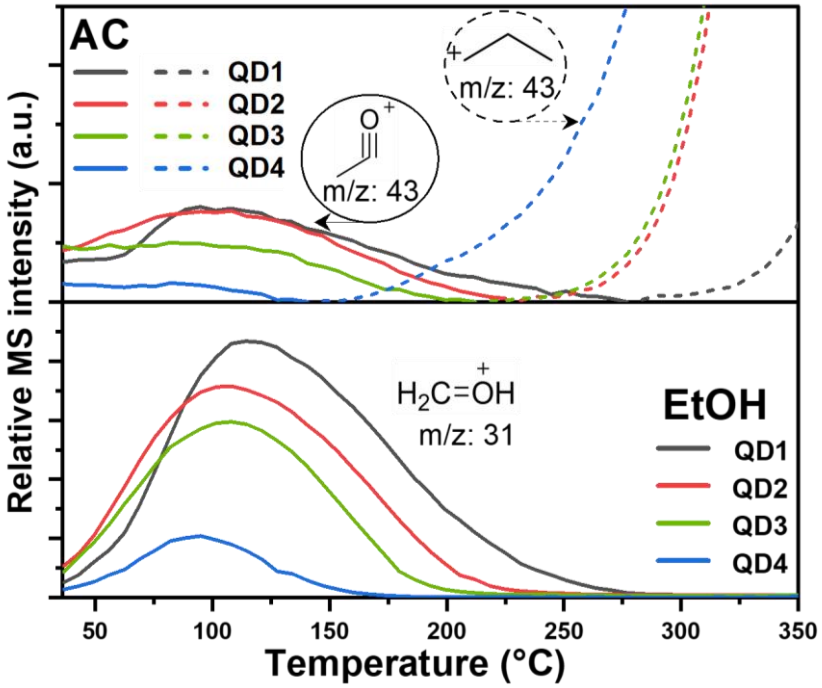

Figure 49. Relative MS intensities of AC (m/z = 43) and EtOH (m/z = 31) from QD1 to QD4.

About solvent ligands, the boiling points of AC and EtOH are 56°C and 78°C in bulk, and the corresponding MS detection signal intensities were detected at around 110°C (yellow lines) and 120°C (blue lines) at QD1, respectively (Figure 48). This result means that the solvent ligands coordinate with the QD surface, inducing an increase of surface binding energy. Meanwhile, with increasing OTT content from QD1 to QD4, the base peaks of AC (yellow lines) and EtOH (blue lines) were shifted from 110 and 120°C to 65 and 85°C, respectively, and their intensities are gradually weakened (Figure 48 and 49). In other words, OTT not only displaces the solvent ligands but also weaken the surface binding energy of them. Also, in QD4, the MS signal intensity of EtOH (blue lines) rapidly decreased when compared to the decreasing trend from QD1 to QD3. It means that OA and HOA ligands

generated from ZnOA take part in the displacement of solvent ligands as well as that by OTT ligands. In addition, the relatively higher MS intensities of solvent ligands allude to the incomplete surface passivation of as-synthesized QD that is not fully passivated by anionic OA ligands.

Scheme 5. Surface ligand binding models according to the covalent bond classification method.[1]

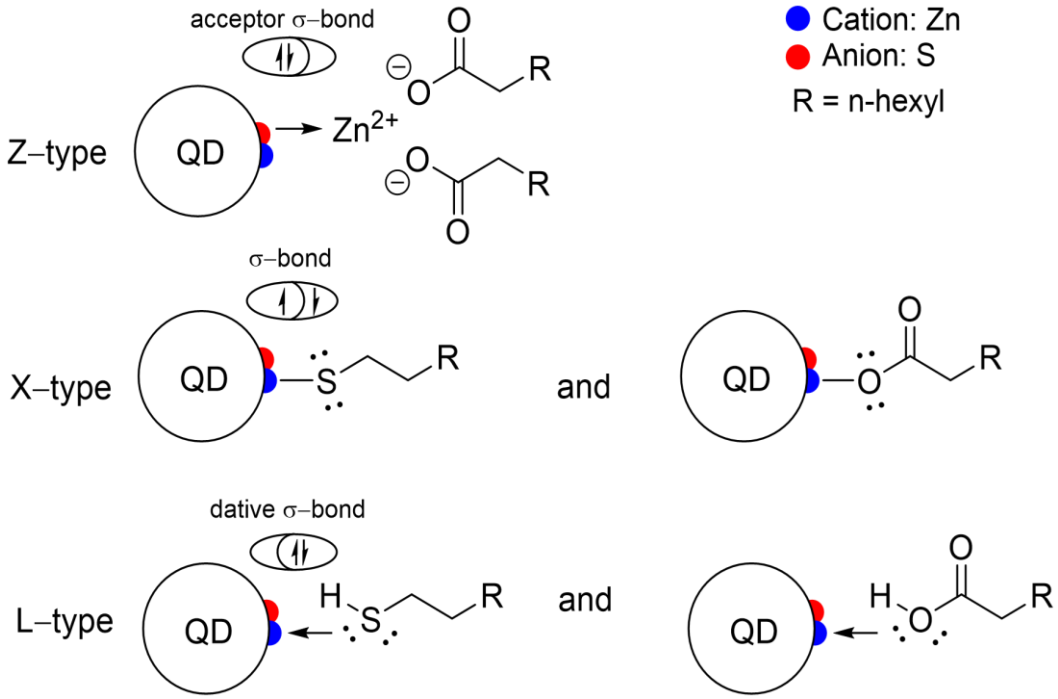

In principle, to form a chemical bond with QD surface, Z-type ZnOA ligand requires two electrons from QD surface, and OTT ligand donates two electrons to QD surface, according to Green's covalent bond classification method (Scheme 5).[45] Therefore, OTT binds to a cationic surface, and ZnOA ligands bind to an anionic surface. Taking this into account, we could not say that OTT ligands directly exchange ZnOA ligands. So, more acceptable is the perspective that ZnOA ligands were indirectly removed from the QD surface by proton transfer between OTT and the OA anion of ZnOA (Scheme 4).

4.3.3. NMR analyses of QDs

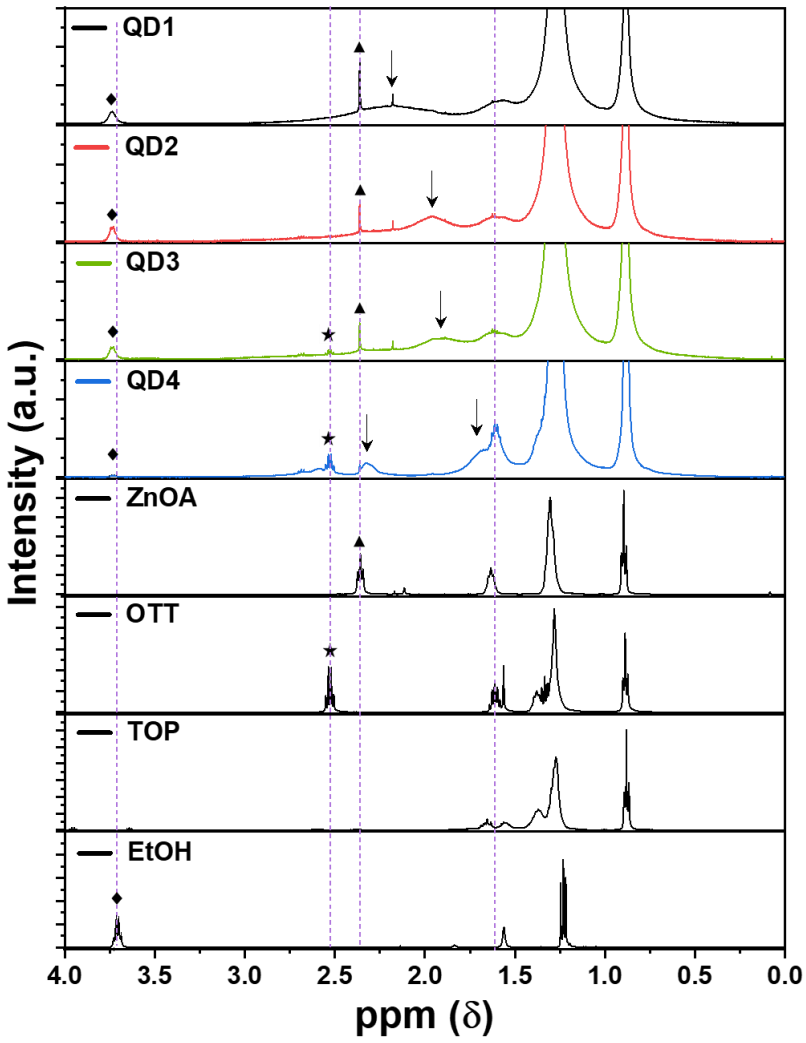

Figure 50. ^{1}H–NMR spectra from QD1 to QD4 including α–protons (αH) of ZnOA (▲), OA (↓), OTT(★), and EtOH(◆) in reference materials.

Figure 50 shows the overall chemical shifts in 1H–NMR spectra when OTTs were introduced onto InP/ZnSe/ZnS QDs. The ZnOA, OTT, EtOH, and TOP were also measured as reference chemicals, by which we have observed the significant changes such as αH (α–proton) chemical shifts and spin-spin coupling constant. The particle-size distributions at QD1 to QD4 are about 7 nm, i.e., a small size (Figure S3), so their ^{1}H-NMR signals usually undergo the peak broadening since protons of surface ligands have constrained highly close to the QD surface. Thus, accurate quantification of surface ligands through peak integration is quite restricted. However, the αH chemical shift of ligand protons makes it possible to indirectly distinguish how strongly specific ligands are bound on the QD surface. In particular, the α–protons of ZnOA undergo the peak broadening and the large up-field shift

(i.e., low chemical shift) from QD1 to QD4, which alludes that α–proton is confined close to the QD surface and shielded by electron charges. In detail, the magnetic field (B_{eff}) at the nucleus by induced field is as below.[197]

$$B_{eff} = B_0 - \sigma B_0 \quad (1)$$

In principle, B_{eff} at the specific proton is affected by the external field (B_0) and the dimensionless shielding constant σ. The larger a shielding constant σ is, the smaller B_{eff} is.[197] With increasing OTT ligands on the QD surface, the α–protons of ZnOA were steadily shifted toward up-field from QD1 to QD4 (Figure 50, ↓), which indicates that α–protons were further shielded by electron charges. In principle, a cationic Z-type ZnOA ligand requires two electrons from the anion (i.e., S^{2-}) of QD when it binds to the QD surface. Thus, the closer and stronger ZnOA ligand binds to the QD surface, the more the electrons get abundant, so that α–protons of ZnOA can be shielded by electron charges. However, in the TGA–MS result, we could confirm that OTT ligands induce the removal of ZnOA ligands via proton transfer with OA (Figure 50 and Scheme 4), which means that ZnOA ligands become far from the QD surface. Also, HOA and OA ligands derived from ZnOA ligands bind to the QD surface as either free- or bound ligands, inducing the increase of surface binding energy. Therefore, we could infer that this large up-field shift was ascribed to strongly bound OA ligands on the QD surface.

Scheme 6. Schematic motif of Z-type Ligand displacement via proton transfer by OTT ligands according to TGA–MS analysis.

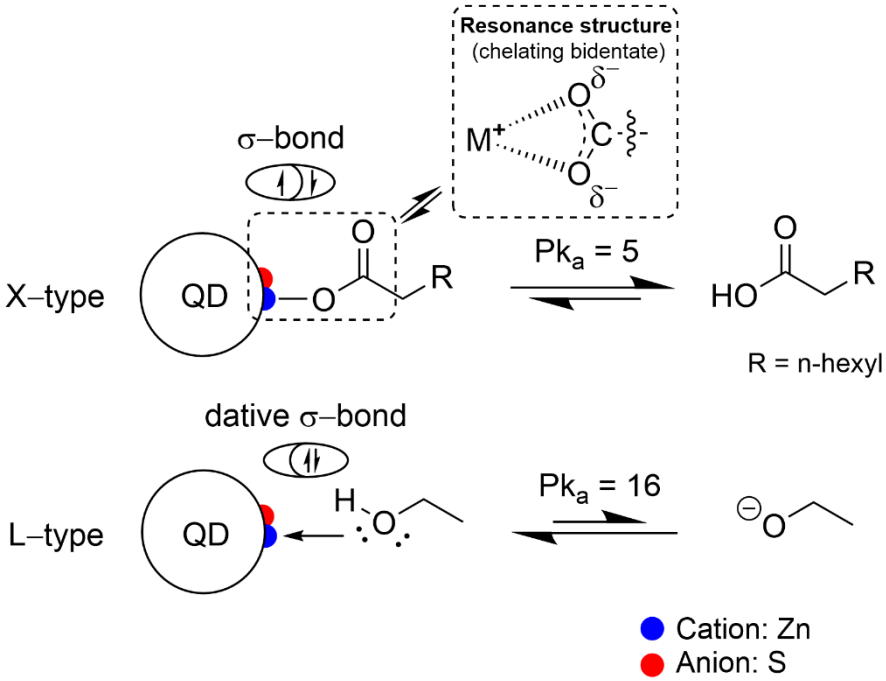

The ligating oxygen atom of OA ligand has a singly occupied orbital, which requires one electron from the cation (i.e., Zn^{2+}) on the QD surface (Scheme 6). As OA ligand closely binds to the QD surface, its carboxylate group, stabilized by resonance, becomes electronically abundant, so that the α–proton of bound-OA ligand becomes more shielded than free-OA. In other words, this large up-field shift (Figure 50, ↓) indicates that OA ligands (derived from ZnOA ligands) are strongly bound to the QD surface. In addition, the α–protons of OA ligands at QD4 exhibited one more peak appearing at 2.32 ppm, which is slightly shifted up-field (– 0.03 ppm) compared to the α–protons of ZnOA. This chemical shift can be also designated as a free-OA ligand derived from ZnOA ligand. Moreover, it is well-matched with the aforementioned TGA–MS data that the fragment ion peaks of weakly-bound HOA and OA ligands are more prominent in QD4 (Figures 47 and 48).

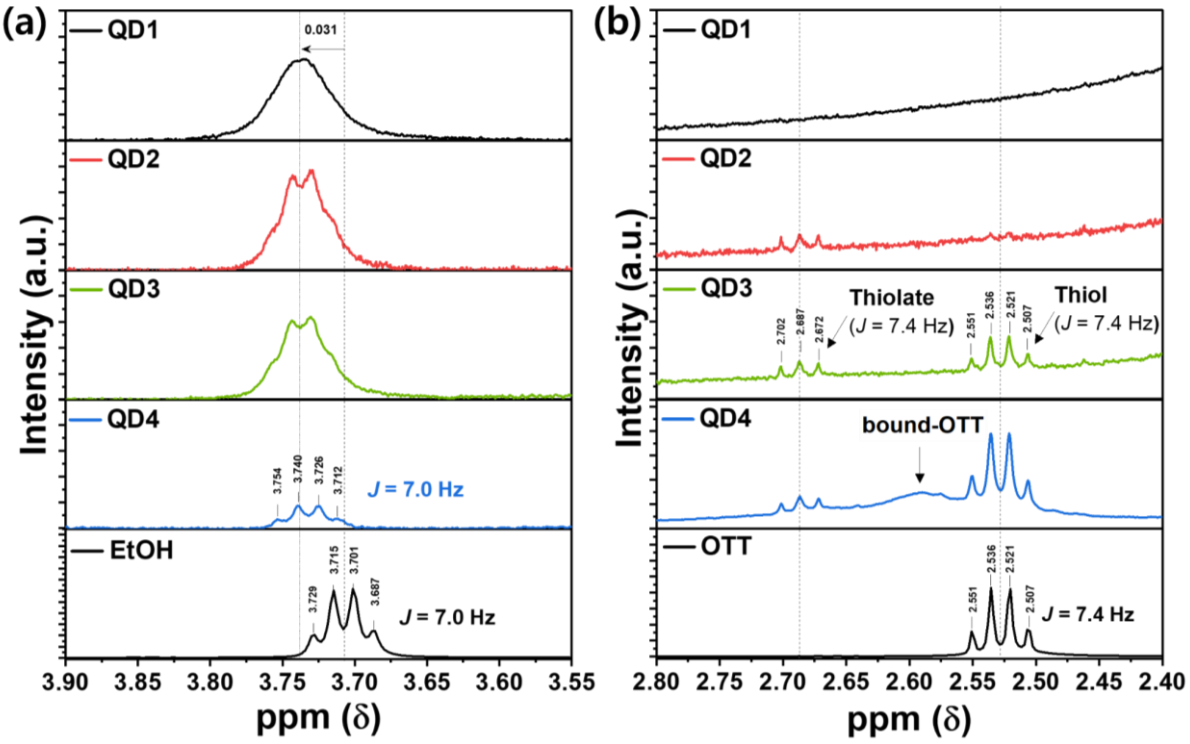

Figure 51. ^{1}H–NMR spectra of α–protons of a) EtOH and b) OTT from QD1–4, including coupling constants (J).

Figure 51a represents αH chemical shift of EtOH from QD1 to QD4. The α–protons of EtOH undergo the peak broadening and the down-field shifted αH resonance (i.e., high chemical shift) with decreasing OTT content from QD4 to QD1. In principle, EtOH as an electron donor pushes its lone-pair electrons to the QD surface (Scheme 6). Thus, the stronger EtOH binds to the QD surface, the lower the electron density of the hydroxyl group (–OH) is by donating its two electrons. In other words,

the α–protons of EtOH become deshielded as binding closely to the QD surface, resulting in the down-field shifted αH resonance. In other words, it means that EtOH ligands get far from the QD surface with increasing OTT contents, which is consistent with the aforementioned TGA–MS data that the surface binding energy of EtOH ligands gradually decreases with increasing OTT content. In addition, the spin–spin coupling is in principle independent of B_0 in [Eq. (1)]. The coupling constant (J) of EtOH at QD4 is consistent with that of reference EtOH, so that we could verify that the down-field shifted α–protons from QD4 to QD1 are originated from EtOH.

Figure 51b shows the αH chemical shifts of OTT ligands that indicate the thiolate and thiol groups of OTTs at 2.67 and 2.53 ppm, respectively.[200-201] Moreover, the α–protons of the thiolate group emerged earlier than those of its thiol form at QD2, which indicates that OTT initially undergoes a proton transfer process with ZnOA ligands before direct binding to the QD surface. Therefore, it supports the role of OTT that induces the formation of zinc thiolate complex via proton transfer with ZnOA (Scheme 5). In addition, the peak-broadened and down-field shifted α–protons of OTT showed up at 2.59 ppm in QD4. In other words, OTT ligands become binding closely to the QD surface with increasing OTT content, and it results in the peak broadening and the deshielding of its α–proton since OTT is a similar L-type ligand to EtOH (Scheme 5).

4.3.4. IR spectra of QDs

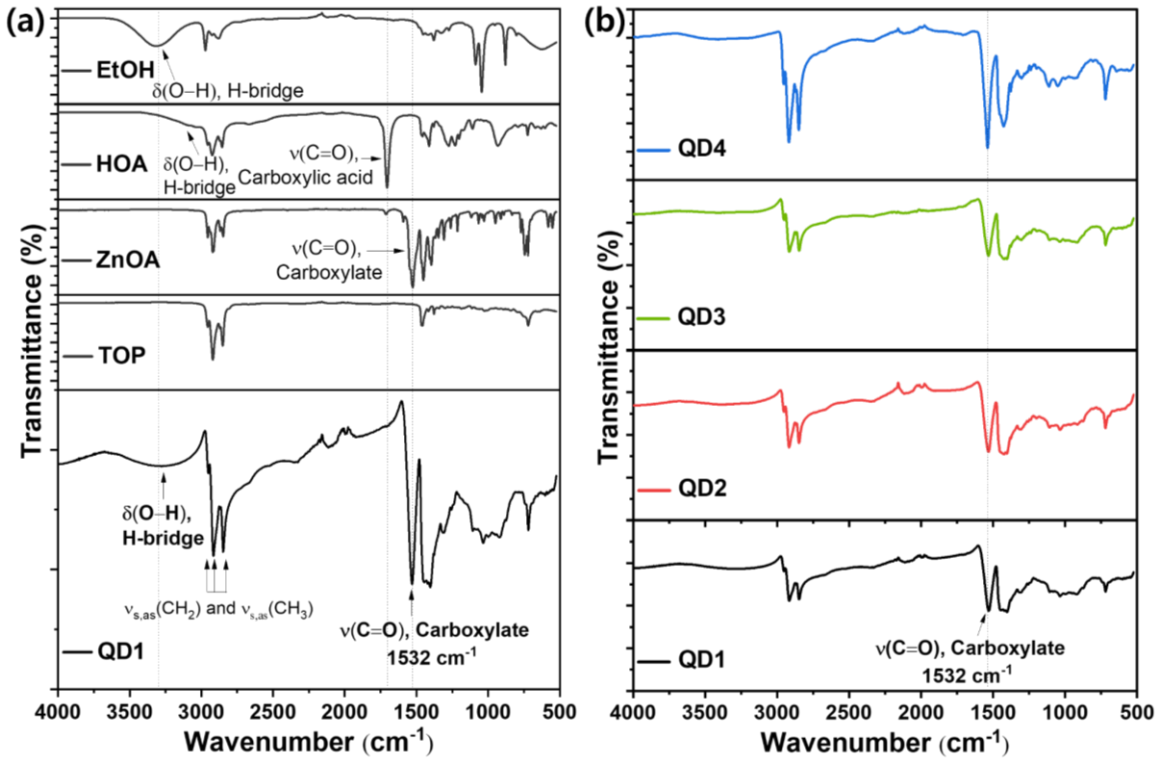

Figure 52. IR spectra of a) QD1 compared with reference chemicals and b) that from QD1 to QD4.

Figure 52a shows IR spectra of QD1 compared to the reference chemicals, including EtOH, ZnOA, TOP, OTT and etc. (Figure S7). In general, an absorption of ν(C=O) (i.e., stretching vibration) is detected between 1800 cm^{-1} and 1500 cm^{-1}, where carboxylic acid and carboxylate have a distinctive vibration at 1760 cm^{-1} and 1610–1550 cm^{-1}.[197] In particular, the absorption bands of QD1 clearly point to the functionality as a carboxylate group, not a carboxylic acid, and it is similar to the previous report that carboxylic acid ligands are almost all present as a carboxylate form on the QD surface.[54] In the range below 1500 cm^{-1} called as 'finger–print range', the assignment of specific bands is less straightforward because it contains a lot of bands that provoke overlaps and coupling with other vibrations.[197] Nevertheless, in the IR spectra of QD1, the weak trace of the hydrogen bridge, from 3000 cm^{-1} to 3500 cm^{-1}, supports the presence of EtOH on the QD surface.

In Figure 52b, the ν(C=O) intensity of carboxylate group at around 1532 cm^{-1} was mostly maintained even though the increase of OTT content from QD1 to QD4. It supports the aforementioned TGA–MS data that OA ligands, dissociated from ZnOA ligands via proton transfer by OTT, re-attach to the QD surface as anionic X-type ligand, not been removed out of QD. Also, the absorption band of the carboxylic acid at around 1760 cm^{-1} was barely detected relative to that of carboxylate group in

QD4, which is consistent with the aforementioned TGA–MS data that most OA ligands are present on the QD surface, not HOA ligands. Meanwhile, the IR spectrum of OTT was not utilized as a comparison group from QD1 to QD4 due to its extremely low absorption intensity of ν(S–H) (Figure S6).

4.3.5. TR PL decay spectra of QD films

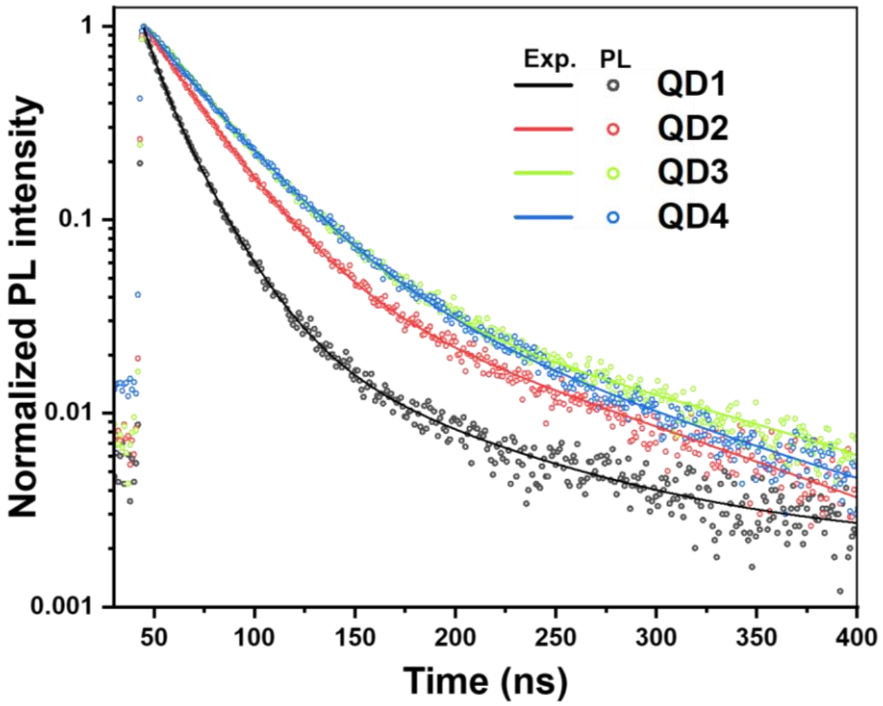

Figure 53. Time–resolved photoluminescence (TR–PL) decay spectra of QD films, including bi-exponential fitting lines.

Table 11. Summary of the parameters from fitting to the TR–PL decay of QD film.

QD	A_1	τ_1 (ns)	A_2	τ_2 (ns)	τ_{ave} (ns)
QD1	0.993	15.64	0.106	71.72	16.02
QD2	0.982	27.10	0.017	126.98	28.86
QD3	0.977	33.29	0.023	142.25	35.81
QD4	0.972	33.30	0.028	129.17	35.97

Figure 53 reveals the normalized PL decay curves of InP/ZnSe/ZnS QD films with increasing OTT content on the QD surface. The curves are fitted with double exponentials having amplitudes (A_1, A_2) and lifetimes τ_1, τ_2), and the results are summarized in Table 11 (see the 8.3. Determination of carrier lifetime in TR PL curve in Supporting Information). The exciton lifetimes of InP/ZnSe/ZnS QDs having nearly unity quantum yield are assessed to be 30–40 ns.[41] In contrast to QD3 and QD4, QD1 and QD2 have average lifetimes (τ_{ave}) below 30 ns, which is attributed to the contribution of defect-mediated transitions from incomplete surface passivation. In particular, the fast decay components (τ_1) of QD1 and QD2 are 15.64 and 27.10 ns with 0.99 and 0.98 contributions, respectively, to the total lifetime, which is known to predominantly result from recombination at unpassivated surface trap states in InP[202], InP/ZnSe[203], or InP/ZnS[204] QDs. Therefore, the incomplete passivation of QDs by solvent ligands, not passivated by anionic OA ligands, is likely the main origin of electron traps in the band gap of QD (Figure 54), resulting in the faster decay components (τ_1) in QD1 and QD2. Passivating the QD surface by OTT induced more strongly bound anionic OA ligands via proton transfer as well as surface-bound OTT ligands. As a result, the longer lifetimes (τ_1) are observed for QD3 to QD4 than for QD1 and QD2 due to passivation of surface traps.

4.3.6. Stability of QDs and QD films

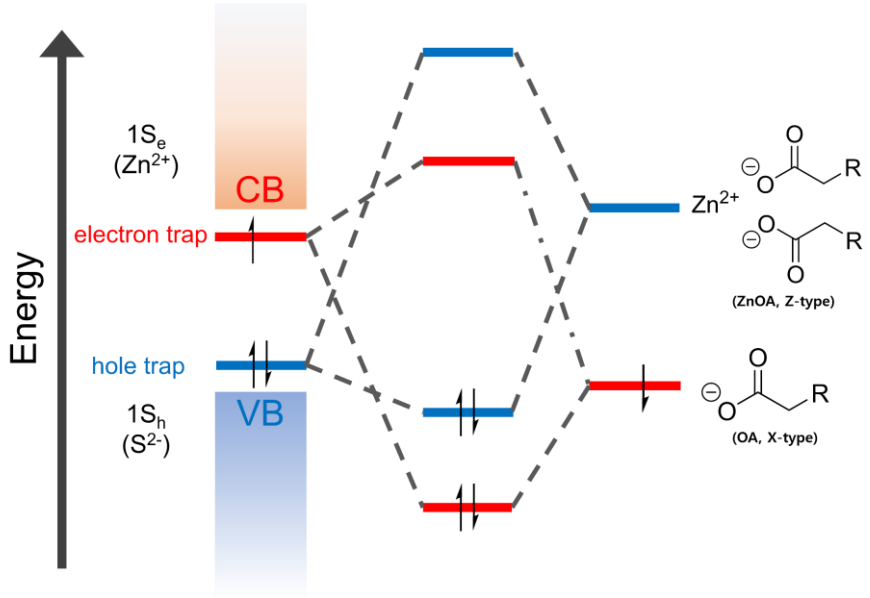

Figure 54. Schematic illustration of electron and hole traps in II–VI ZnS outmost shell and different type of chemical bonds between under-coordinated surface atoms and ZnOA ligand (Z-type) or anionic OA ligand (X-type).[66, 200]

Figure 54 shows the surface passivation of electron and hole traps with X-type and Z-type ligands in metal chalcogenide QDs like ZnS.[66, 205] In this point of view, as-synthesized QD (i.e., QD1) has a lot of electron trap states present on the cationic surface (i.e., Zn^{2+}) where is not fully passivated during the synthesis. In other words, X-type anionic OA ligands are significantly deficient on the QD surface during the synthesis, resulting in the incomplete surface passivation. Additionally, τ_2 values from QD3 to QD4 decreased from 142.25 to 129.17 ns, which is different from an increasing tendency from QD1 to QD3 (Table 11). It alludes to a generation of hole trap states interfering with the excitonic transition. That is, cationic ZnOA ligands convert to anionic OA ligands via proton transfer by OTT (Scheme 4), so it can give rise to a relative lack of cationic Z-type ZnOA ligands on the QD surface, resulting in the hole traps on the anionic surface (i.e., S^{2-}).

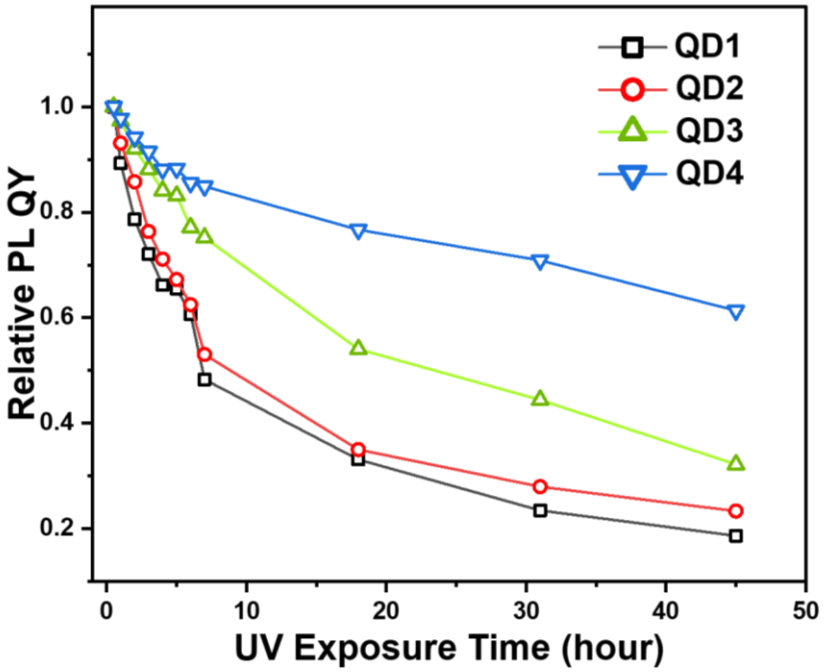

Figure 55. Photostability of QD films at UV light (8 W) from QD1 to QD4.

Also, the UV stability of QDs enhanced with increasing OTT content (Figure 55). This trend has a similarity with an increasing trend of τ_{ave} from QD1 to QD4 (Table 11). It means that the presence of electron and hole traps on the QD surface gives rise to surface degradation, and it results in a low PL QY. As shown in the results of TGA–MS and 1H–NMR analyses mentioned above, it represents that the passivation of an incomplete surface by OTT, HOA, and OA ligands is effective to enhance the stability of QDs. Therefore, it means that a modulation of surface ligands not only induces

neutralization of dangling bonds exposed on the QD surface but also can relate to an electronic and excitonic process of QD bandgap in optical devices.[205]

4.3.7. QD–LEDS fabricated from surface-passivated InP QDs

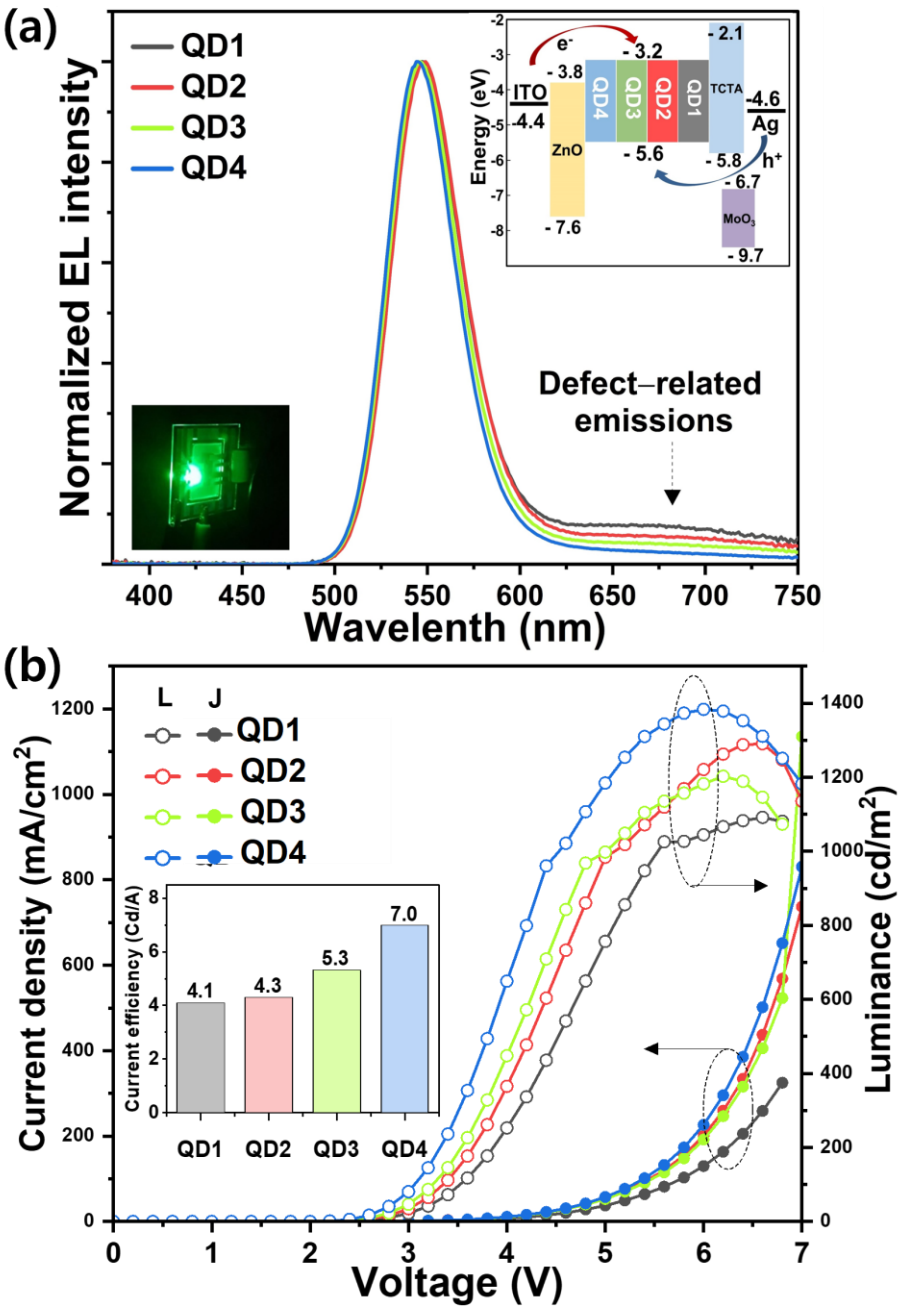

Figure 56. a) the normalized EL intensities and b) the current density– voltage–luminance (J–V–L) curves in inverted structure QD–LEDs from QD1 to QD4.

Figures 56a and b show the normalized EL intensities and their J–V–L curves in QD–LEDs, where QDs were fabricated into inverted structure EL devices (See the 4.2.5. Inverted structure of QD–LED Fabrication). In Figure 56a, the defect-related emissions at around 670 nm decreased with increasing OTT content on the QD surface. In other words, OA (derived from ZnOA) and OTT ligands effectively stabilize the incomplete QD surface, which is consistent with TR–PL, TGA–MS, and ^{1}H–NMR analyses mentioned above. In addition, all QDs have the equal energy level of valence band obtained from AC-2 measurement (Figure S8). So, the change of dipole moment by OTT passivation has a negligible effect on the band gap of QDs, thus it is not a crucial factor in our result of QD–LEDs. In Figure 8b, the resulting current efficiency of QD–LEDs shows the gradual improvement from QD1 to QD4. This is reasonable when considering the defect passivation of the QD surface (Figure 48, 50, and 53) and enhanced stability (Figure 55) from QD1 to QD4.

Meanwhile, the TGA curve of QD4 showed the increase of organic content compared to QD1 to QD3, which all had similar organic content (Figure 37b). This may result from the ligand addition of weakly bound OTT as excess ligands detected in TGA–MS and ^{1}H–NMR (Figures 48 and 50). In general, organic ligands can act as an insulator in QD–LEDs, which may negatively affect charge transport and injection in the QD layer. Nevertheless, in this work, Figures 56a and b showed that the current density of the QD–LED fabricated from QD4 materials is significantly higher than those fabricated from QD1 to QD3. This therefore results in the highest current efficiency among QD1 to QD4. Thus, the data imply that excess OTT ligands dominantly act as a surface passivation rather than an insulator in QD devices. In principle, the surface defects of the QDs induce a generation of electronic states within the QD band gap, which consequently result in the negative effect to charge transporting properties in QD–LEDs.[72] A decreasing trend of defect-related emissions from QD1 to QD4 and the alleviation of the faster decaying components (τ_1) at QD3 and 4 improves the charge transport properties by reducing non-radiative transition into surface trap states in QD layer of QD–LEDs (Figure 56a and Table 11). Nevertheless, these results may include the complex interactions inside QD–LEDs since, for example, the charge transport in QD film is affected by defect sites, interparticle spacing with neighboring QDs, and electrode surface.[206] Thus, the optimization of QD devices is still challenging, and it requires a detailed further investigation from QD–LEDs standpoints about which positive effects, such as defect passivation and enhanced stability, play a prominent role in increasing the current efficiency.

4.4. Conclusion

This research proposed the TGA–MS analytic method through fragmentation patterns of surface ligands and their surface binding affinity analysis to understand surface chemistry in detail. Also, it was supported through TEM, ^{1}H–NMR, FT–IR, and TR–PL. Thus, we could confirm that paves the way in revealing a relatively ambiguous analytical area of QD surface than its bulk counterpart.

To conclude, we proved that OTT passivation onto the QD surface undergoes the proton transfer process with cationic Z-type ZnOA ligands, inducing strongly-bound anionic X-type OA ligand derived from ZnOA ligand. This new proton transfer model between ZnOA and OTT ligands elucidates the role of OTT as a proton donor as well as a surface ligand on the QD surface. In other words, these systematic investigations directly show the interrelation of surface ligands. Toward advanced research, an analysis of two-dimensional nuclear magnetic resonance spectroscopy (2D NMR), such as DOSY and NOESY, will be necessary to explore and understand the further deep insight into the interrelation of QD surface and ligands.

In addition, we suggested the connectivity between surface modification and EL device. As a result, OA (derived from ZnOA) and OTT ligands stabilize the incomplete QD surface and enhance the UV stability of QDs, leading to the high current efficiency of QD–LEDs.

5. STABILITY OF INP/ZNSE/ZNS QUANTUM DOTS IN LIGHT-EMITTING DIODES: ROLE OF SHELL THICKNESS AND SURFACE CHEMISTRY

This section is based on the accepted "conference paper" in 2022 IEEE–NAP (manuscript entitled "Stability of InP/ZnSe/ZnS Quantum Dots in Light-Emitting Diodes: Role of Shell Thickness and Surface Chemistry")

5.1. Introduction

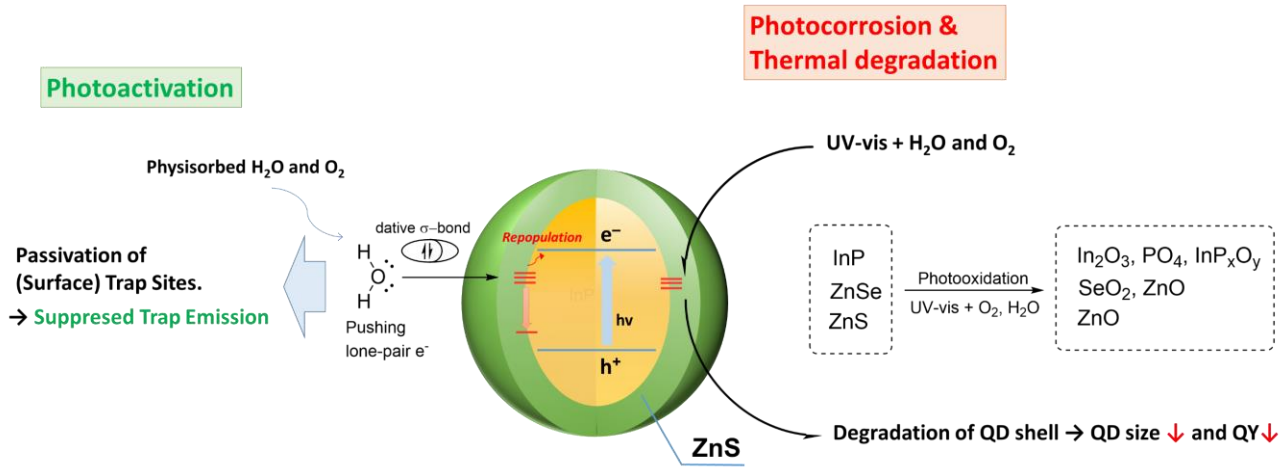

Figure 57. Schematic illustration of degradation of QD. Reproduced from the previous report.[71]

QDs are basically nano-hybrid materials and are stabilized by surface ligands. These surface ligands are classified according to the coordination chemistry concept.[45] In principle, ligands coordination on the QD surface are classified as X–ligands (anionic, one-electron donor), L–ligands (neutral Lewis bases, two-electron donor), and Z–ligands (Lewis acid, two-electron acceptor).[45, 47] In other words, cationic and anionic QD surfaces are charge-compensated by ligand coordinating, leading to the enhancement of QD stability. Among surface ligands, alkylthiol is one of the strongest surface binding species; thus, it offers better thermal stability than other ligands, such as carboxylic acid and tertiary alkylamine. For example, T. Kim et al. demonstrated that CdSe/ZnS QDs passivated by 1-dodecanethiol ligands enhance thermal stability compared to that passivated by oleic acid ligands (Figure 57).[83] However, the role of alkylthiol still remains controversial due to its concentration- and PH-dependencies. It has been reported that a high concentration of OTTs provokes low PL QY by hole trapping, which is known to be ascribed to a thiolate form of alkylthiols.[84-85] Furthermore, alkylthiols have other roles as sulfur donors to form sulfide compound with cationic metal ions, such as Zn and Pb, when reaction temperature reaches around 200°C, where the thermal decomposition of thiol groups is usually taking place. However, the role of not only a surface ligand but also a sulfur donor obstructs

observing the ligand effect caused by alkylthiols, so that needs elaborate temperature control, maintaining a low temperature under 150°C to independently investigate the ligand effect.[207]

For a definite validation of surface ligand on QD surface, spectroscopic methods of organic chemistry usually suggest at least two analytic combinations for precise interpretation among Nuclear magnetic resonance (NMR), Infrared (IR), ultraviolet-visible (UV-vis) spectroscopy, and mass spectrometry (MS). In particular, MS and NMR are the most common techniques in metabolomics studies, and their analytic results complement each other's strengths and weak points.[197] NMR spectroscopy is quantitative and not targeted for analysis; that is, the magnetic resonance signals of ^{1}H, ^{31}P, and ^{13}C are obtained throughout all molecules in a sample. Unlike NMR spectroscopy, MS-based metabolomics provides the highest level of sensitivity and selectively targeted analyses through ion fragmentation patterns of molecules.[208]

In this study, InP/ZnSe/ZnS QDs with thick or thin ZnS shells were synthesized, where 1-octanethiol (OTT) was introduced as a sulfur source to form ZnS thicker shell on the surface of InP/ZnSe/ZnS QDs, and then equally modified the QD surface using OTT in the thick and the thin ZnS shelled QDs. As for these QDs, optical properties, such as PL QY and UV spectra, and photostability, were investigated in detail, where the thicker ZnS shelled QDs show better PL QY but low stability rather than the thin-shelled QDs. In addition, we confirmed that OTT in the process of the ZnS shelling has the role not only as a sulfur donor for ZnS layer but also as a surface ligand through MS and NMR spectroscopy. In other words, OTT affects other ligands via proton transfer in the ZnS shelling process even though the reaction temperature is high enough, over 250°C, to form a ZnS shell. Thus, we compare this ZnS shelling process by OTT with that by S-TOP (trioctylphosphine sulfide) and discuss why the sulfur precursors, OTT and S–TOP, make a difference in surface passivation based on their reaction mechanism.

With the analyses of ligand effect by OTT, we fabricated QD–LEDs using OTT–modified InP/ZnSe/ZnS QDs with thick or thin ZnS shell. As for the results, a trend of lifetimes in devices was not following the photostability of QDs, where the QD–LED fabricated with thicker ZnS shelled QDs was more stable than that fabricated with thin shell QDs. Herein, we discuss which factors dominantly affect the stability of QDs and QD–LEDs based on their degradation mechanism from chemical and physical perspectives.

5.2. Experimental Details

5.2.1. Materials

Indium acetate ($In(Ac)_3$, 99.99%), zinc acetate (Zn(Ac)2, 99.99%) tri-n-octylphosphine (TOP, 97%), 1-octanoic acid (OA, >99%), 1-octadecene (ODE, 90%), zinc stearate (ZnSA, 10–12% Zn basis), 1-octanethiol (OTT, >98.5%), selenium (Se, 99.99%), sulfur (S, 99.98%), acetone (AC, >99.5%), toluene (anhydrous, 99.8%) and ethanol (EtOH, 96%), were purchase from Sigma-Aldrich. Tri(trimethylsilyl) phosphine (TMSP, 97.5%) was purchased from Vezerf Laborsynthesen GmbH. Zinc octanoate (ZnOA), tri-octylphosphine selenide (TOP–Se), and tri-octylphosphine sulfide (TOP–S) was prepared beforehand. For QD–LED fabrication, 4,4',4"–tris(carbazol–9–yl) triphenylamine (TCTA, 99%), molybdenum oxide (MoO_3, 99.99%), and silver (Ag, >99.9%) were purchased from Lumtec, Sigma Aldrich, and Umicore, respectively.

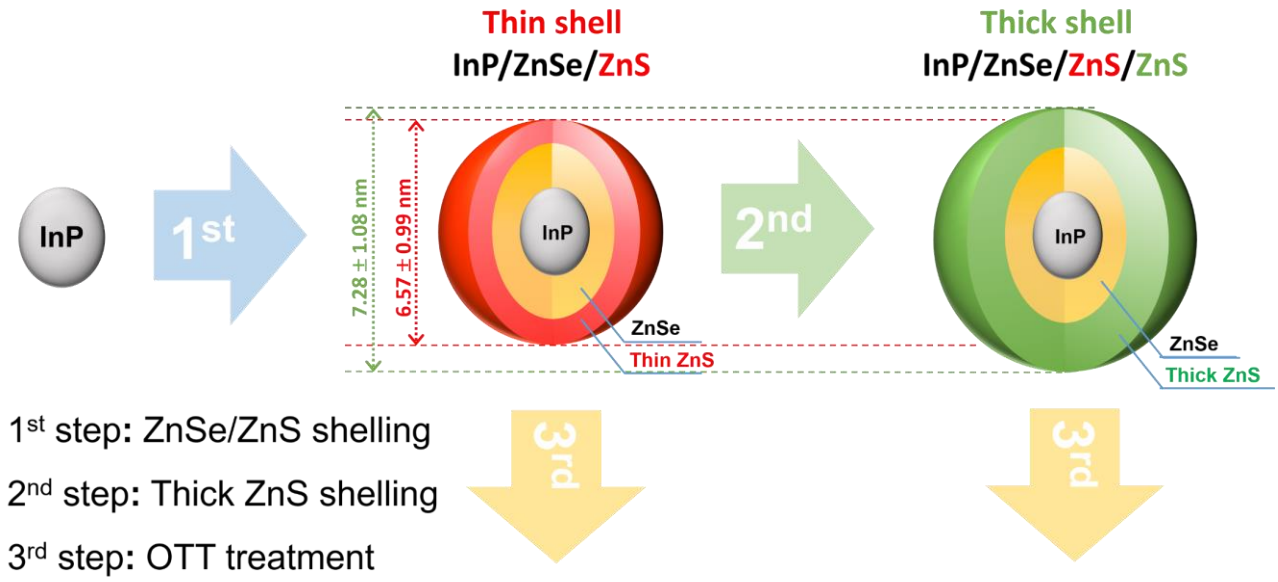

Figure 58. Illustrated synthesis process of surface modified InP/ZnSe/ZnS QDs with thick or thin ZnS shell.

5.2.2. Synthesis of InP/ZnSe/ZnS QDs (thin ZnS shell)

$In(Ac)_3$ (292 mg, 1mmol), ZnSA (1.26 g, 2mmol), and 10ml of ODE were introduced into a 50ml three-neck round bottom flask equipped with rubber septa and thermocouple. The mixture was heated to 150°C and degassed under reduced pressure (<150 mTorr) for 2 hours with vigorous stirring to remove water and oxygen species. After backfilling the reactor with N2 atmosphere, 1 mmol of 1M TMSP dissolved in ODE was rapidly injected into the flask at 150°C, and the solution was heated up to 310°C within 10 min with vigorous stirring, maintained 10 min for core growth, and cooled down to room temperature. For ZnSe shelling on the surface of InP QD, ZnOA powder (1.06 g, 3 mmol) was

added to the reaction flask, heated to 130°C, and degassed under reduced pressure (<150 mTorr) for 30 min to remove water and oxygen species. After backfilling the reactor with N_2 atmosphere, the mixture was heated to 280°C and maintained for 10 min. 2M TOP–Se (1.5 ml, 3 mmol) was injected to the reaction flask at 280°C, maintained for 30 min, and cooled down to room temperature. For ZnS shelling on the surface of InP/ZnSe QDs, ZnOA powder (3.52 g, 5 mmol) was introduced to the reaction flask, heated to 130°C, and degassed under reduced pressure (<150 mTorr) for 30 min. After backfilling the reactor with N_2 atmosphere, the mixture was heated to 300°C and maintained for 10 min. 2M TOP–S (2.5 ml, 5 mmol) was injected into the reaction flask at 300°C for 1 h and cooled down to room temperature for surface modification.

5.2.3. Synthesis of InP/ZnSe/ZnS QDs (thick ZnS shell)

All synthesis processes were continuously performed without purification. 2 ml of OTT was introduced into the reaction flask having as-synthesized InP/ZnSe/ZnS QDs, heated up to 280°C under N_2 atmosphere for 20 min, and maintained for 2.5 hours to form ZnS thick shell. Then, all reaction process was terminated by cooling down to room temperature and adding an excess amount of toluene.

5.2.4. Surface modification of InP/ZnSe/ZnS QDs

The surface modification was also performed without the purification of QDs. The as-synthesized InP/ZnSe/ZnS QDs with thick or thin ZnS shell were equally distributed into two round bottom flasks. Then, 2 ml of OTT were each rapidly introduced into two reaction flasks at 150°C, and maintained for 15 min.

5.2.5. Purification of surface-modified InP/ZnSe/ZnS QDs

The surface modified InP/ZnSe/ZnS QDs with thick or thin ZnS shells were isolated by adding an excess amount of a solvent mixture (AC : EtOH = 3 : 1) and then purified by repeated two-times of precipitation/re-dispersion with a solvent mixture/toluene combination using centrifugation (7000 rpm, 25 min).

5.2.6. Inverted structure of QD–LED Fabrication.

First, the indium tin oxide (ITO) substrates were cleaned by sequential ultra-sonication with AC, isopropyl alcohol, and EtOH, and dried in an oven at 100°C for 3h, followed by oxygen plasma treatment. The following steps were performed in a glove box under a nitrogen atmosphere. The ZnO nanoparticles for the electron transport layer were prepared using procedures previously reported in

the literature[191] and were spin-coated onto the as-prepared ITO substrates at 3000 rpm for 30 s, followed by drying at 180°C for 30 min. The 9 mg / mL of QD solutions were spin-coated onto the ZnO nanoparticle layer at 3000 rpm for 30 s without further thermal annealing. After the solution processes, TCTA (40 nm) and MoO_3/Ag (10 nm / 150 nm) were deposited by the thermal evaporation on the QD layer in a high-vacuum chamber as a hole transport layer and metallic anode, respectively.

5.3. Result and Discussion

5.3.1. PL and UV spectra

As for inorganic materials to enable epitaxial growth as an outmost shell on the surface of InP QDs, an inorganic ZnS shell is one of the most stable compounds to provide chemical stability versus ZnSe and GaP shells.[191]

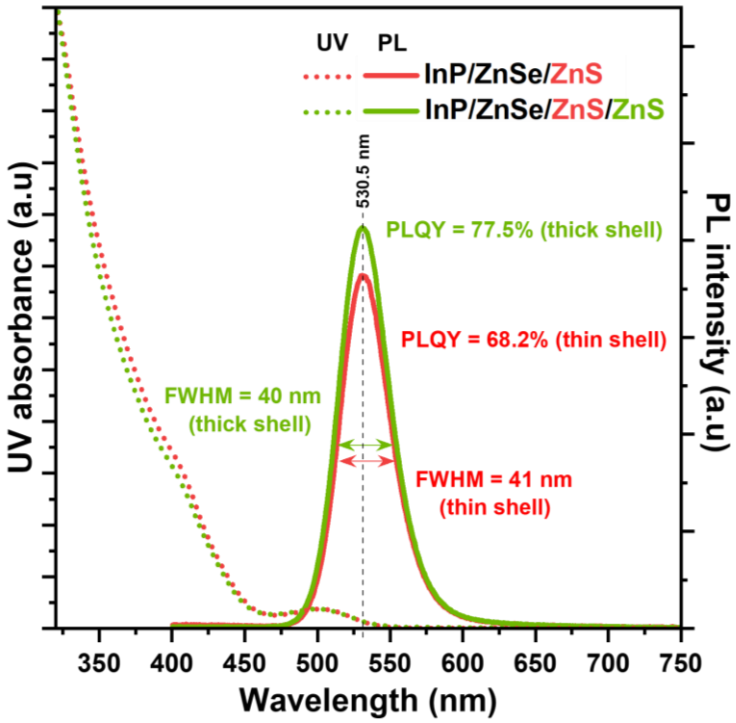

Figure 59. PL and UV spectra of OTT–modified InP/ZnSe/ZnS QDs with thick or thin ZnS shell.

Figure 59 represents PL QY, FWHM, and UV absorbance obtained from optical measurements of the OTT–modified InP/ZnSe/ZnS QDs with thick or thin ZnS shells. Similar to the previous reports, the thicker ZnS shelled QDs show higher PL QY than that with a thin ZnS shell. Before and after ZnS overshelling on top of InP/ZnSe/ZnS QDs, PL wavelength (WL) and FWHM are maintained at 530.5 nm and 40–41 nm, respectively, and it means the ZnS overshelling is constrained

from ZnSe to ZnS shells, not the InP core. In addition, it also shows that an additional ZnS layer has epitaxially grown upon the thin ZnS shelled QDs without interfacial lattice mismatch.

5.3.2. Particle size distribution of QDs and their elemental compositions

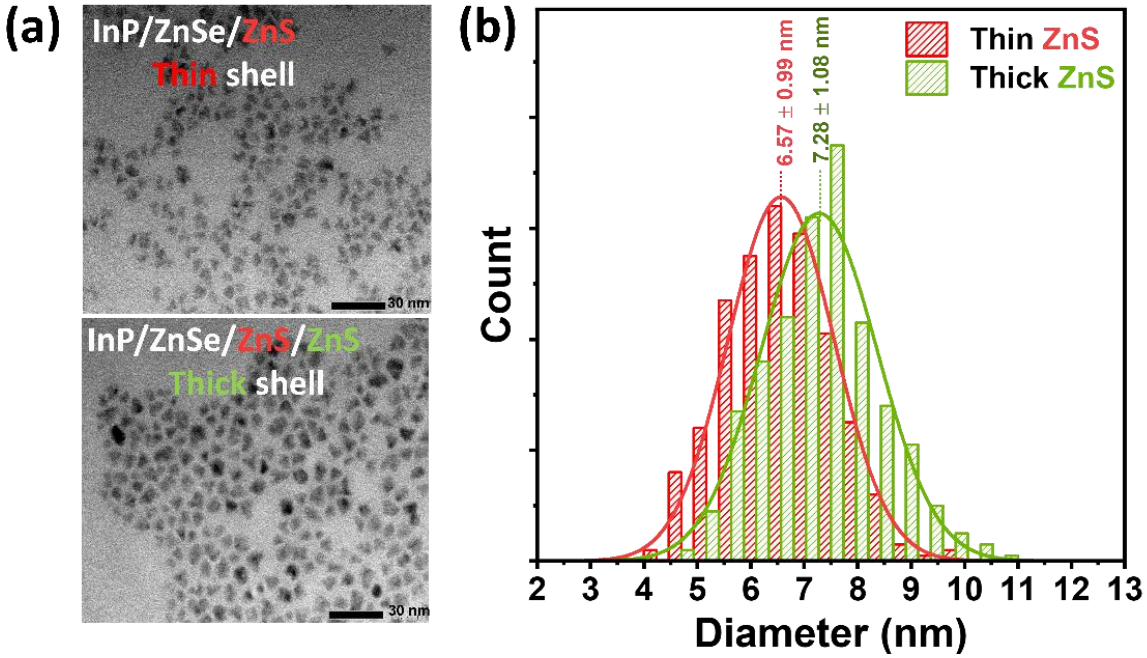

Figure 60. (a) TEM images of OTT–modified InP/ZnSe/ZnS QDs with a thick and a thin shell and corresponding histograms of particle size distribution.

Figures 60a and b show the particle size distribution obtained from TEM images before and after the additional ZnS shelling process on top of the thin ZnS shelled QDs. Herein, we could confirm that the shell thickness of QDs increased uniformly after the ZnS shelling process using OTTs at 280°C, whose trend corresponds to the FWHM of QDs that were maintained before and after ZnS shelling. Therefore, the improvement of PL QY in the thick ZnS shelled QDs can be explained as a result of the increased ZnS shell thickness, not the ligand effect by OTT.

However, as shown in Figure 61, the actual S content of QDs increased with increasing ZnS shell thickness, but the actual Se content decreased oppositely. It means that OTTs as a sulfur source induces a somewhat surface etching process when forming a ZnS shell. In core/shell heterostructured QDs, an inorganic shell absorbs UV light into their excited states. Basically, The band gap of ZnSe nanoparticles is reported on a wide range between 2.25 eV[209] and 3.23 eV[210], and its absorption peak emerges at about 370 nm;[211] that is, UV absorption at around 370 nm indicates mainly the absorbed

light by ZnSe mid-shell. Therefore, in Fig. 3, the slightly reduced absorptivity at around 370 nm after the additional ZnS shelling can imply the decrease of ZnSe shell thickness.

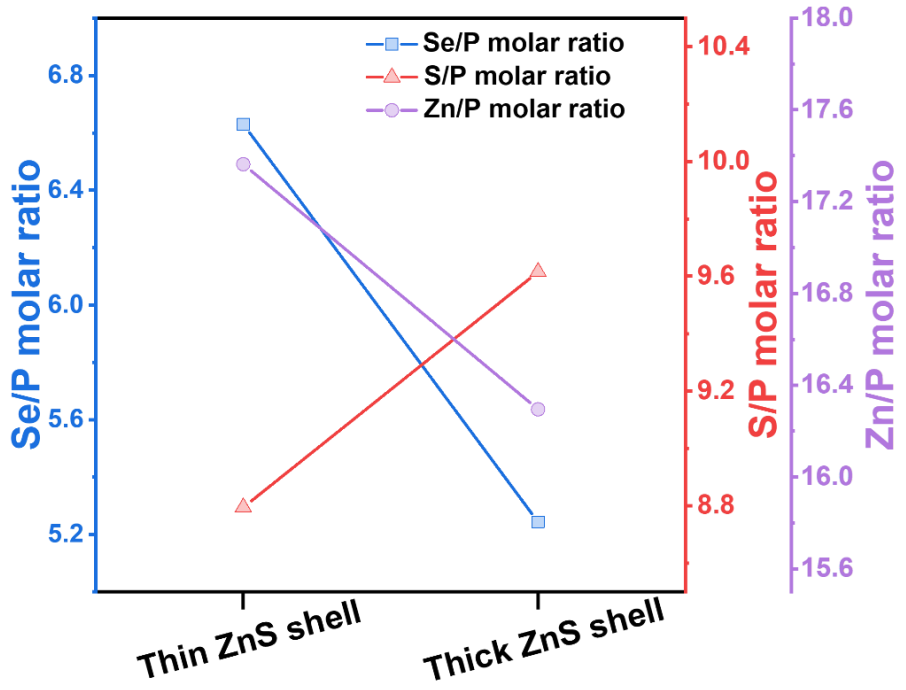

Figure 61. Inductively Coupled Plasma optical emission spectroscopy (ICP OES)–based on actual elemental compositions of Se/P, S/P, and Zn/P between the thick and the thin ZnS shelled QDs.

In addition, the reduced actual Zn content after the additional ZnS shelling is not easy to interpret in terms of inorganic core/shell QD structure. This is because the increase of ZnS shell thickness is significantly definite when considering the particle size distribution and optical properties, including PL and UV spectra. Thus, we can infer it originated from the consumption of cationic Z–type zinc carboxylate ligands in forming the ZnS shell.

Both OTT and TOP–S as sulfur sources consume zinc cations to form ZnS shell in wet chemical synthesis of QDs, where most zinc cations are present as the formation of Z–type zinc carboxylate ligands. In principle, the smaller the size of QDs is, the higher the ratio of surface-to-volume is. Thus, increasing shell thickness can accompany a decrease in surface area compared to smaller QDs. Taken together, the decrease of actual Zn content after thick ZnS shelling can be explained by both the consumed Zn cations and reduced surface area.

5.3.3. Photo-stability of QDs and their causes

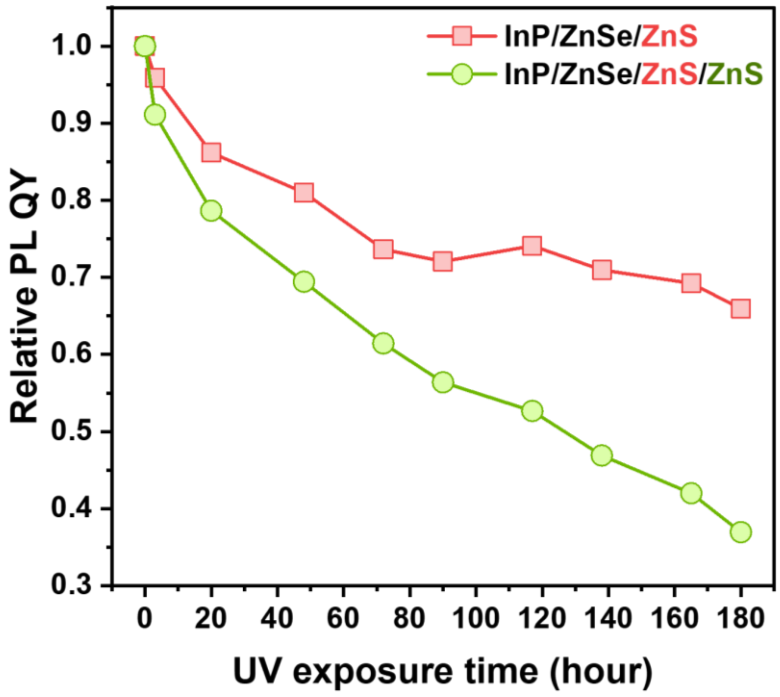

Figure 62. Photo-stability of OTT–modified InP/ZnSe/ZnS QDs with a thick and a thin shell exposured to UV light (8W)

Figure 62 shows the photostability of InP/ZnSe/ZnS QDs before and after thick ZnS shelling, where the thin ZnS shelled QDs showed relatively high stability to the thicker shelled QDs. This result is not coincident with previous reports that thicker ZnS shelled QDs are more stable than thinner ZnS shelled QDs.[78-79] Considering optical properties, such as high PL QY and well-maintained FWHM after thicker ZnS shelling, the generation of interfacial lattice strain in the inorganic lattice matrix is not reasonable, and we could speculate this originated from surface degradation by defect sites.

In the ZnS shelling process, including thin or thick shell, of core/shell/shell InP/ZnSe/ZnS QDs, TOP–S was applied as a sulfur source until the thin ZnS shelled QDs, but OTT was additionally used as a sulfur source for thicker ZnS shelling. As shown in Scheme 7, OTT can induce proton transfer with carboxylate or zinc carboxylate ligands, by which it can produce protonated carboxylic acid ligand as a byproduct. However, TOP–S does not have a proton source to induce proton transfer with other ligands, producing carboxylate ions as a byproduct, not carboxylic acids. In general, it is known that most carboxylic acid ligands are present as a form of anionic carboxylate ligand on the QD surface.[54] Thus, the generation of carboxylic acid ligands can give rise to a form of weakly bound surface ligands. However, to clear the ligand effects giving rise to the surface degradation between InP/ZnSe/ZnS QDs with a thick and a thin shell, the temperature-dependent mass spectral

investigation, such as TGA–MS, is necessary to observe an interplay between surface ligands and QD surface due to its target analysis rather than NMR spectroscopy.

Scheme 7. Illustrated schematic reaction motif of ZnS using (a) OTT and (b) TOP–S on the QD surface.

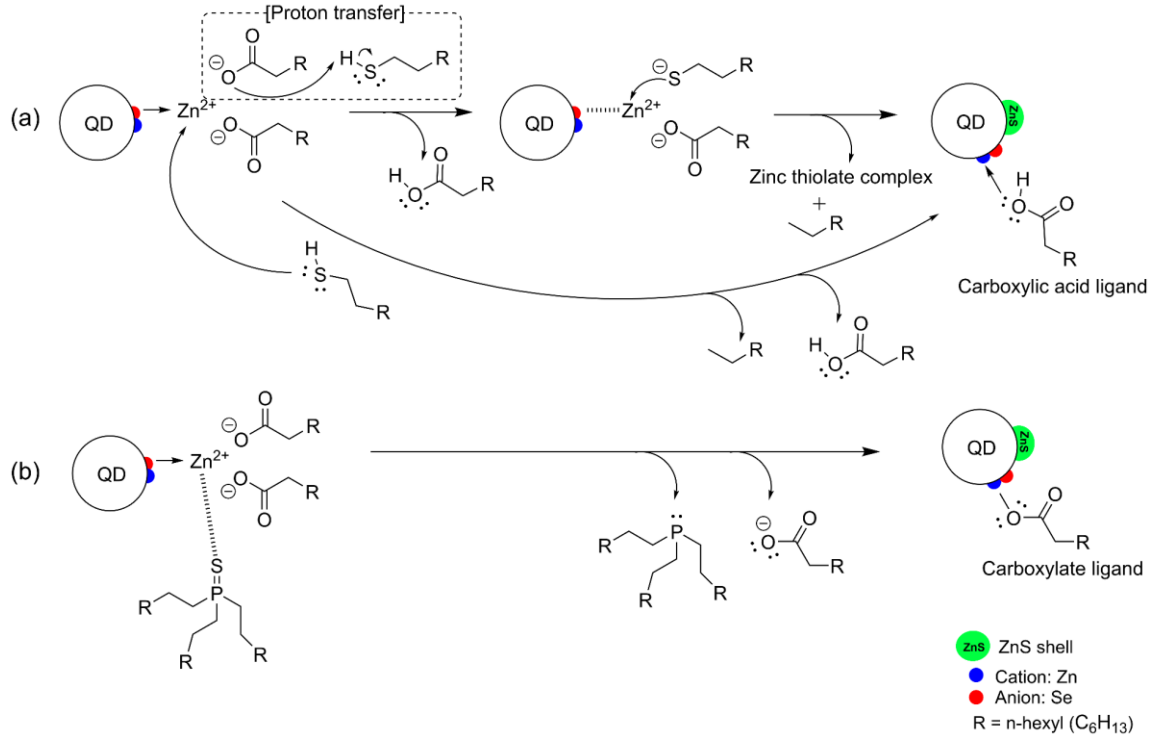

Prior to the interpretation of mass spectral signals, the base peaks (i.e., the most stable or characteristic peak) of reference chemicals, OTT and ZnOA, were investigated. The base peak of OTT and ZnOA represented the ions m/z = 112 and 58, respectively, the former one being resulted from the elimination of hydrogen sulfide (m/z = 24) in OTT, the latter one being resulted from the elimination of two protons in the base peak (m/z = 60) of 1-octanoic acid (HOA).

5.3.4. Surface analyses of MS and ^{1}H-NMR spectroscopy

Fig. 63 shows MS peak signals of the base peaks of OTT and ZnOA; corresponding base peaks are ions m/z = 112 and 58, respectively, as mentioned above. Both the QDs with a thick and a thin ZnS shell were surface-modified by OTTs after synthesis. Thus, the nearly equal signals of ions m/z = 112 emerged at around 355°C in the QDs with a thick and thin ZnS shell, indicating the equal amount of OTTs bound on the QD surface. However, a weak and broad MS signal was detected from 150 to 350°C in the thick ZnS shelled QDs, which indicates the weakly bound OTT ligands since a detection temperature is involved with a surface binding energy of ligands to the QD surface. On the other hand, at around 460°C, the signal of ions m/z = 112 was more intensified after thicker ZnS shelling. In

general, both TOP and OTT undergo the β– and γ–hydrogen elimination in the ionization of MS. Therefore, the signal of ion m/z = 112 at around 460°C is mainly ascribed to TOP ligands on the QD surface, but the same amount of TOP precursors was introduced in the thick and the thin ZnS shelled QDs. This may be originated from thiolate ions binding to zinc cations in the process of proton transfer with 1-octanoate (OA) anions (Scheme 7). Thus, it supports that alkylthiols undergo proton transfer with OA anions in the process of ZnS forming. Also, a weak and broad signal of ions m/z =58 in the range from 100 to 350°C was detected in the thick ZnS shelled QDs, not in the thin ZnS shelled QDs. This also indicates the weakly bound ZnOA or HOA ligands arising from proton transfer with OTT.

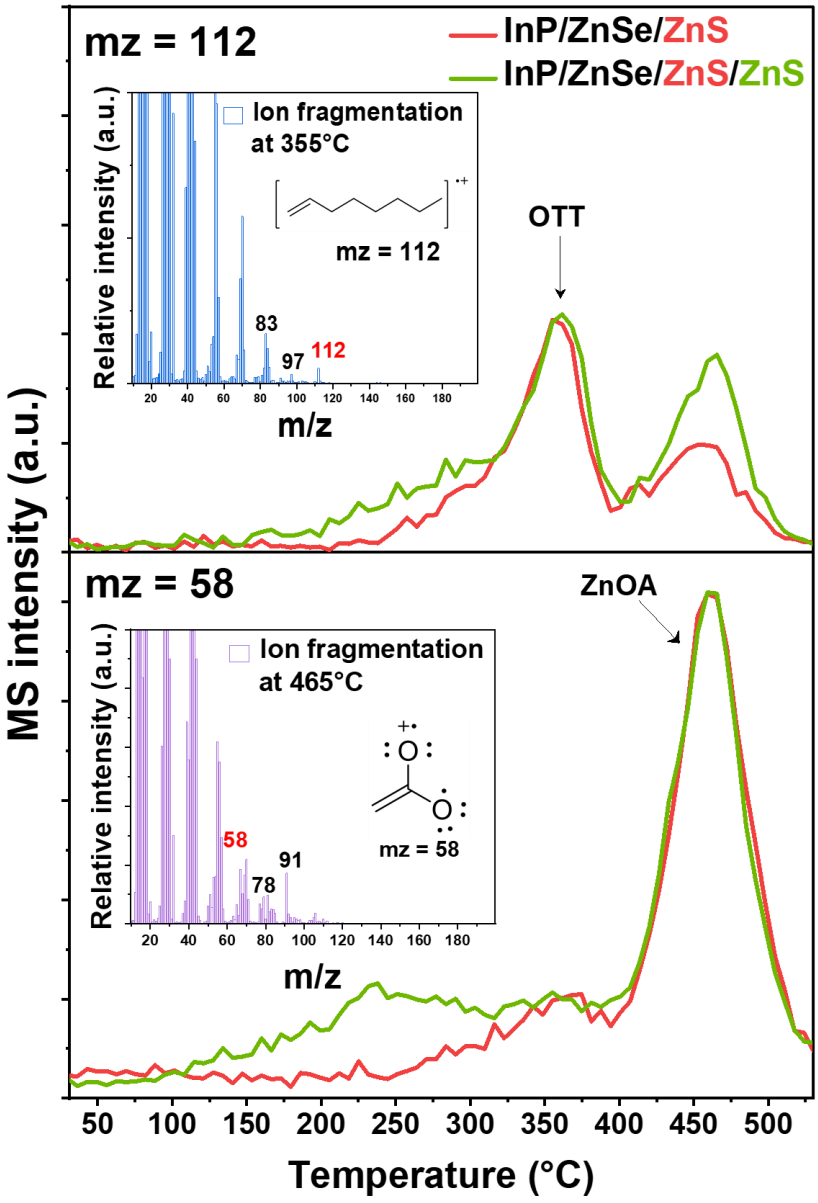

Figure 63. MS intensities of the base peaks of OTT (m/z = 112) and ZnOA (m/z = 58).

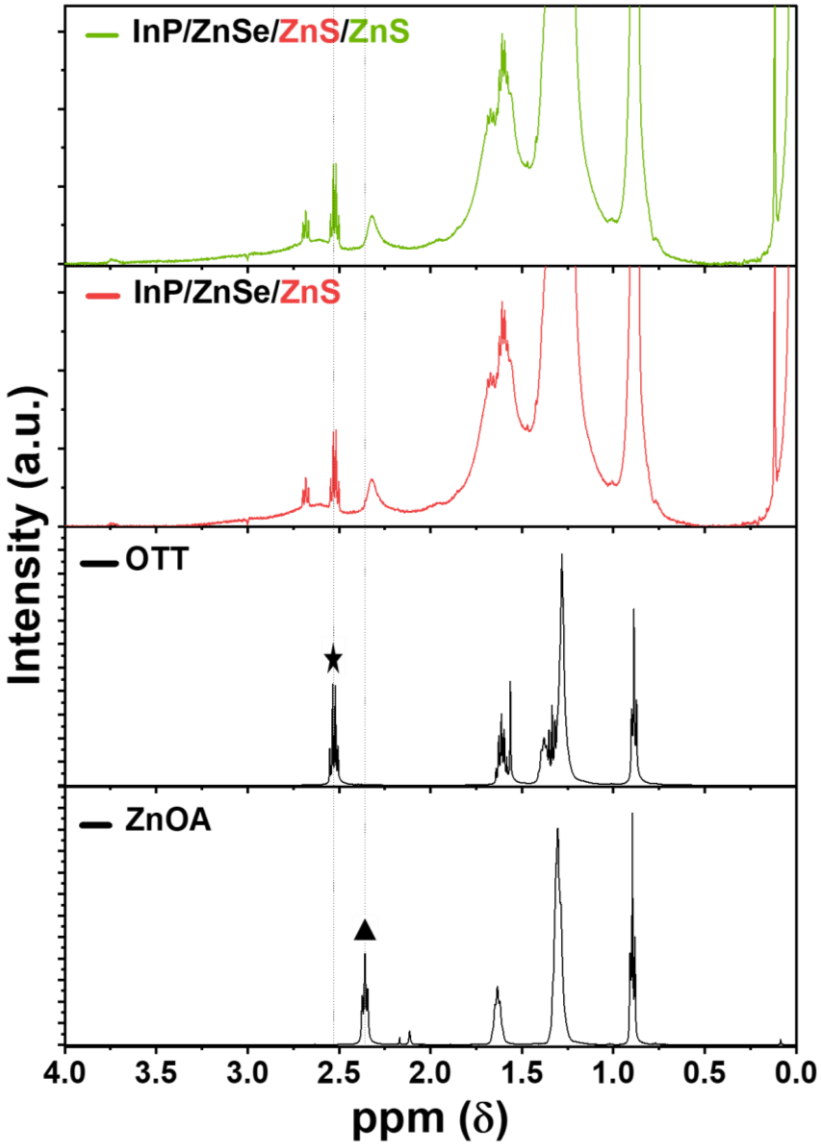

Figure 64. ^{1}H–NMR spectra of OTT–modified InP/ZnSe/ZnS QDs with a thick and a thin ZnS shell compared to the reference chemicals including α–protons of OTT(★) and ZnOA(▲).

On the other hand, the thin ZnS shelled QDs do not show the MS signals of weakly bound ZnOA and OTT ligands in the range from 100 to 350°C. In the synthesis process of the thin ZnS shelled QDs, TOP–S was applied as a sulfur source for ZnS shelling, different from the thick ZnS shelled QDs where OTTs were used as a sulfur source. As shown in Scheme 7 and Fig. 63, OTT produces HOA as a byproduct via proton transfer with OA anion of ZnOA, but TOP–S only produces OA as a byproduct since it does not have a proton source (Scheme 7). Comparing anionic OA ligand to HOA ligands, anionic X–type OA ligand (i.e., σ–bond) binds strongly to the QD surface compared to L–type HOA ligand (i.e., dative σ–bond due to a donation of lone pair electron).[45, 47] Therefore, the broad peaks

from 100 to 350°C can be designated as the weakly bound ZnOA and OTT ligands produced in ZnS shelling.

Fig. 64 shows ^{1}H–NMR spectra of the thick and the thin ZnS shelled QDs compared to the reference chemicals, OTT and ZnOA, where surface ligands are closely constrained to the QD surface, resulting in peak broadening and chemical shift of α–protons. So, α–proton of ZnOA was slightly shifted towards up-field from 2.36 to 2.32 ppm, indicating a strongly bound OA anion to QD surface compared to that of ZnOA in bulk.

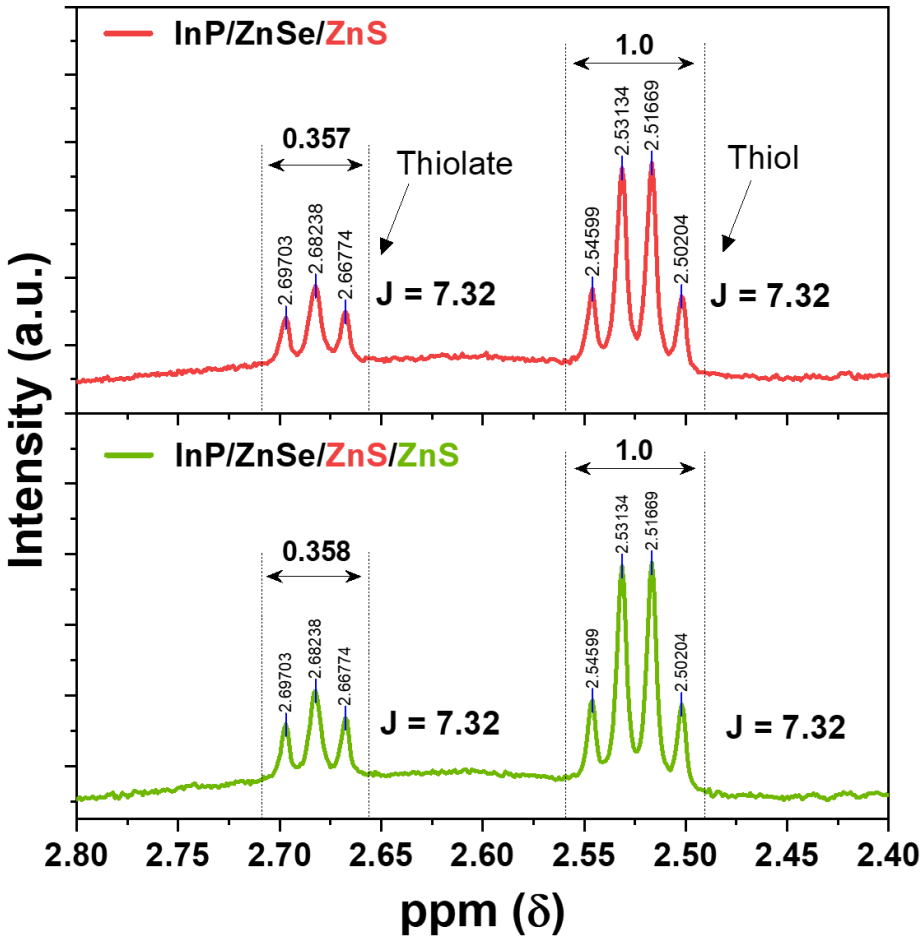

Figure 65. ^{1}H–NMR spectra of α–protons and peak integrations of OTT from OTT–modified InP/ZnSe/ZnS QDs with thick and thin ZnS shells.

Table 12. Pros and cons of ^{1}H–NMR spectroscopy and MS as an analytical tool for organic chemical[26]

	Analytical tool	
	^{1}H–NMR	MS
Sensitivity	Generally low, and especially need a high concentration in C-NMR	High, and the range of detection levels are from picomole to femtomole
Selectivity	Nonselective analysis in general	Both selective and nonselective analyses
Sample preparation	Required a minimum NMR concentration level to be able to be detected	Need different columns and ionization techniques as a preprocessing
Sample recovery	Nondestructive	Destructive
Target analysis	Not relevant for targeted analysis	Superior for targeted analysis

Figure 65 revealed two chemical shifts of α–protons at 2.68 and 2.52 ppm, corresponding to thiolate and thiol forms of OTT ligands, respectively. This also advocates the proton transfer of OTT with ZnOA above mentioned (Scheme 7 and Figure 63). In principle, the coupling constant (J) is independent of the external magnetic field in NMR spectroscopy; that is, the same J values between thiolate and thiol peaks can be considered to originate from OTT molecules. Also, the ratio of peak integration between thiolate and thiol peaks is 0.36 to 1, respectively, which indicates the deprotonation of OTT ligands is prominent if considering the pKa of OTT molecule is at around 5 in bulk. Assuming the pKa of OTT is 5 in bulk, the ratio of thiolate to thiol peaks should be around 0.003 to 1.

However, ^{1}H–NMR spectra of the thick and the thin ZnS shelled QDs are nearly the same, and it is different from MS data that shows the weakly bound ZnOA and OTT ligands in low temperature. This is attributed to a relatively low detection range of ^{1}H–NMR spectroscopy compared to the sensitivity of MS that generally cover from picomole to femtomole (Table 12). That is why we strongly suggest MS analysis to observe the QD surface relative to NMR spectroscopy accurately.

5.3.5. Lifetimes of QD–LEDs and electron overcharge

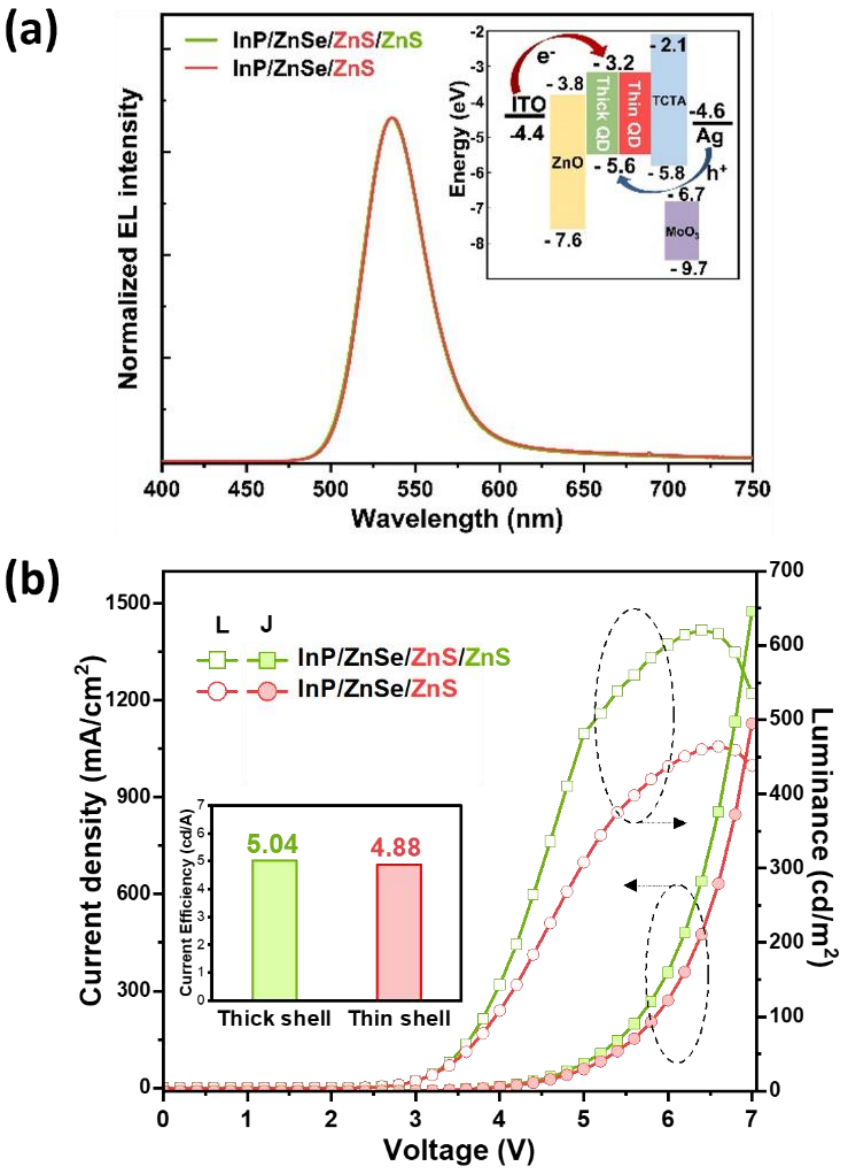

Figure 66. (a) the normalized EL intensities and (b) the current density–voltage–luminance (J–V–L) curves in inverted structure QD–LEDs from OTT–modified InP/ZnSe/ZnS QDs with a thick and a thin ZnS shell.

Figure 66 represents the normalized EL intensities and their J–V–L curves in inverted QD–LEDs fabricated from the thick and the thin ZnS shelled QDs. The EL intensities undergo red-shifted PL wavelength maximum from 531 nm to 537 nm due to the closely packed QDs with neighboring particles in the solid QD layer of QD–LEDs. Also, the intensities of defected-related emissions at around 700 nm were nearly similar between the thick and the thin ZnS shelled QDs, indirectly indicating that a surface defect level is negligible at making a difference in the current efficiency of EL devices. The current efficiency and maximum luminance in QD–LEDs improved after thicker ZnS

shelling, and it may be attributed to the higher PL QY of QDs with a thick ZnS shell compared to that with a thin shell.

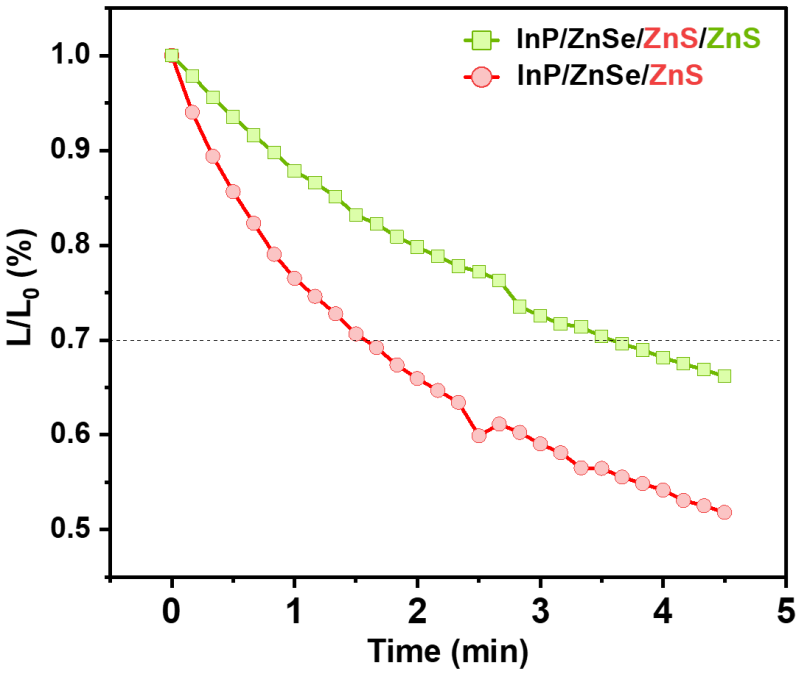

Figure 67. Lifetimes of the QD–LEDs fabricated from OTT–modified InP/ZnSe/ZnS QDs with a thick and a thin ZnS shell.

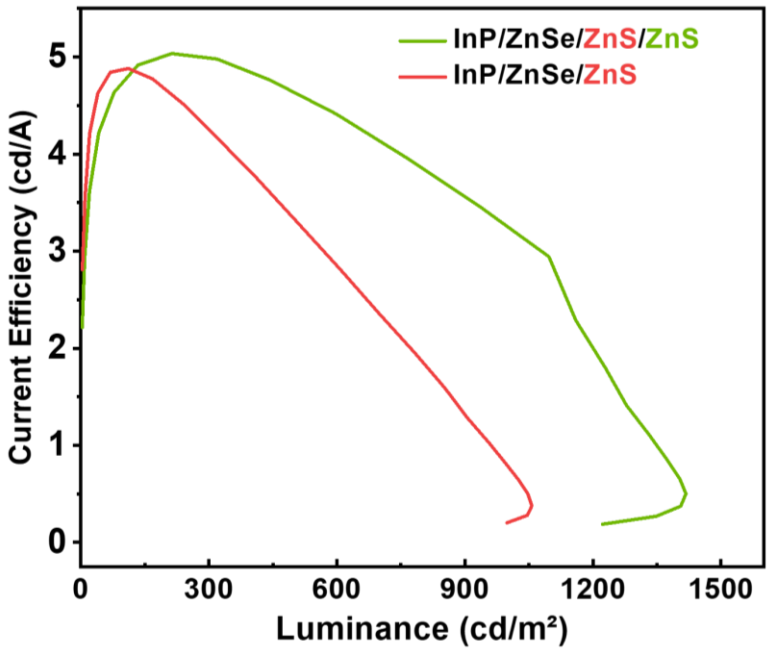

Figure 68. The current efficiency as a function of the luminance in the QD–LEDs fabricated from OTT–modified InP/ZnSe/ZnS QDs with a thick and a thin ZnS shell.

However, the lifetimes of QD–LEDs with the thick and the thin ZnS shelled QDs show opposite results from the photo-stability of QDs at UV light, where the QD–LEDs with thick ZnS shelled QDs maintained their high luminance longer time than that with thin ZnS shelled QDs (Figure 67). Therefore, it means that the degradation mechanisms between the QD–LEDs and the QDs operate differently, and the main factors and degradation conditions should be considered differently. In this point of view, the QD–LEDs were fabricated under the inert condition of a glove box and encapsulated by a cover glass, so the surface degradation of QDs by water and oxygen in EL devices is relatively suppressed when compared to that of the solution-based QDs. So, the unbalanced charges and (negatively) overcharging can be inferred it mainly dominant in terms of stability in QD–LEDs.

Figure 68 shows the current efficiency curves of the QD–LEDs with a thick and a thin ZnS shell QDs according to their luminance. The maximum luminance of thin ZnS shelled QDs (red line) was relatively low compared to the thick ZnS shelled QDs (green line) despite the similarity of their maximum efficiencies. Furthermore, the luminance of thin ZnS shelled QDs rapidly decreased with increasing the current efficiency relative to that of thick ZnS shelled QDs. This may advocate an electron overcharging of the QD layer in QD–LEDs, corresponding to the previous reports that thicker shelled QDs suppress a nonradiative Auger recombination process which induces luminance quenching of QDs.[72, 80] As a result, improving the stability of QD–LEDs depends on how to control a charge imbalance giving rise to degradation of HTL and QD layers, and the material stability of QDs is mostly involved with a modification of surface defect sites. Therefore, inserting an electron blocking layer between ETL and QD layers can be suggested for enhanced stability and high current efficiency via controlling an exciton decay process.[49]

5.4. Conclusion

OTT–modified InP/ZnSe/ZnS QDs with thick or thin ZnS shells were synthesized and fabricated for the QD–LEDs. As a result, a trend of material stability did not correspond to that of device stability, thus we discussed which factor accelerates and dominates the degradation of QDs and QD–LEDs as a driving force. In many cases, researchers expect device stability to depend on the corresponding material stability, but here we suggested an appropriate example to explain why device stability should be considered independently from material stability.

Moreover, this research presented a limitation of ^{1}H–NMR spectroscopy in observing a ligand effect on the QD surface as compared to the results of MS analysis. Thus, significantly important is the fact that NMR spectroscopy and MS should be combined to investigate an interplay of ligands on the QD surface. We believe this better understanding of the relation between QD materials and QD–LEDs leads to a bright future for QD display.

6. InP/GaP/ZnSeS QUANTUM DOTS IN ELECTROHYDRODYNAMIC JET PRINTING FOR ELECTROLUMINESCENCE DEVICES.

This section is based on the accepted "conference paper" in 2022 Eurodisplay (manuscript entitled "Application of InP/GaP/ZnSeS Quantum Dots in Electrohydrodynamic Jet Printing for Electroluminescence Devices.")

6.1. Introduction

Colloidal quantum dots (QDs) have shown great potential in diverse fields of photovoltaic,[212] transistor,[213] and display[41] due to their tunable emission color, high color saturation, narrow full width at half maximum (FWHM) by varying the size of QDs.[214] Also, remarkably advanced and elaborate wet chemical synthesis of InP QDs has led to the level of commercial application, such as QD liquid crystal display (QD–LCD) as a green or red emitter on top of blue backlight units and QD light-emitting diodes (QD–LEDs) as a self-emitting layer.[61]

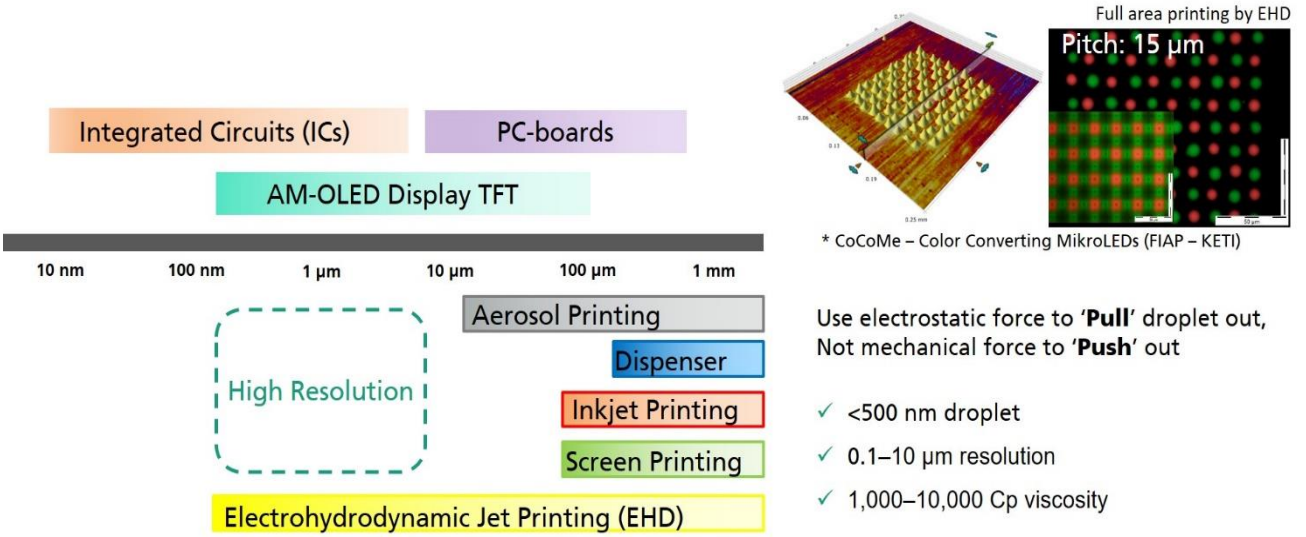

Figure 69. Resolution range and pixel size according to printing methods.

Different from organic emitting light-emitting diodes (OLEDs) fabricated by thermal vapor deposition process to make high-resolution patterns,[72] colloidal QDs having an inorganic core and organic ligand shell are well-soluble in organic solvents and relatively stable to organic counterparts in OLEDs under ambient conditions, so that it makes possible all solution process which is suitable for spin-coating or ink jet printing.[215-216] However, with increasing higher demands for small and compact mobile phones rather than personal computers having a relatively large screen in display market, high-resolution pixels over 300 pixels per in. (PPI) became necessary to realize compactable

small-size display panels (Figure 69). Thus, traditional inkjet printing with about 100 PPI is quite limited to following current market flow and demand.

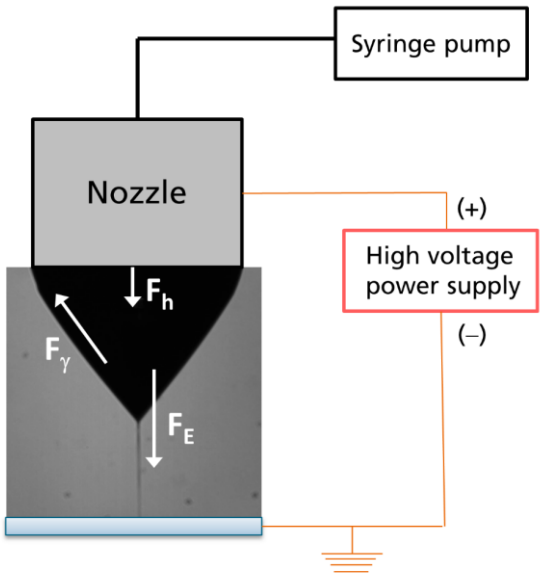

Figure 70. Schematic diagram of EHD printing device and forces acting on the fluid surface in cone jet formation. Reproduced and modified from ref.[149]

Electrohydrodynamic (EHD) printing is one of the powerful tools compared to traditional inkjet printing, because it realizes high-resolution pixelated patterning for QD–LED fabrication. In principle, with high voltage between nozzle and substrate, the fluid meniscus is polarized and pulled out under the electric field, so the conical meniscus is formed and maintained over a certain critical limit of electric potential. In this point, the fluid meniscus undergoes three kinds of forces: the hydrodynamic force (F_h), the capillary force (F_γ), and the electrostatic force (F_E) shown in Figure 70.

In addition, the surface charge of fluid undergoes the process of charge conduction and convection, where the variables include an electric field, the distance between nozzle tip and substrate, the permittivity and conductivity indicating the charge amount of ink, and the physical properties of ink (viscosity, density, and surface tension) when a supplied flow rate and an applied voltage are fixed.[149] In general, QD–LEDs require an extremely thin QD emitting layer on the level of a monolayer to implement high current efficiency, so the ratio of QD content to QD ink formulation is very low under 1 wt.% (see 6.2. Experimental details). Therefore, when a supplied flow rate is fixed, the charge amount of QD ink often becomes one of the most significant factors that can adjust and determine the cone-jet forming voltage. This is because the physical properties of ink such as viscosity and surface tension mainly are governed by the casting solvent that accounts for most of the QD ink formulation.

Herein, InP/GaP/ZnSeS core/shell/shell QDs were synthesized by varying the amount of Ga precursors, gallium (III) chloride, and measured indirectly their surface charge of QDs via zeta potential analysis which influences the cone jet forming voltage. In addition, this research confirmed these QDs not only reduce cone-jet forming voltage in EHD printing system but also improve the current efficiency in QD–LEDs.

6.2. Experimental details

6.2.1. Materials

Indium acetate ($In(Ac)_3$, 99.99%), zinc acetate ($Zn(Ac)_2$, 99.99%) tri-n-octylphosphine (TOP, 97%), gallium chloride ($GaCl_3$, >99.99%) 1-oleic acid (OA, technical grade, 90%), 1-octadecene (ODE, 90%), zinc stearate (ZnSA, 10–12% Zn basis), selenium (Se, 99.99%), sulfur (S, 99.98%), acetone (AC, >99.5%), toluene (anhydrous, 99.8%) and ethanol (EtOH, 96%), were purchase from Sigma-Aldrich. Tri(trimethylsilyl) phosphine (TMSP, 97.5%) was purchased from Vezerf Laborsynthesen GmbH. 1M Gallium oleate (Ga(OA)3), 2M tri-octylphosphine selenide (TOP–Se), and 2M tri-octylphosphine sulfide (TOP–S) was prepared beforehand. For QD–LED fabrication, 4,4',4"–tris(carbazol–9–yl)triphenylamine(TCTA), molybdenum oxide (MoO_3, 99.99%), and silver (Ag) were purchased from Lumtec, Sigma Aldrich, and Umicore, respectively.

6.2.2. Synthesis of InP/GaP/ZnSeS QDs

$In(Ac)_3$ (292 mg, 1mmol), ZnSA (1.26 g, 2mmol), and 10ml of ODE were introduced into a 50ml three-neck round bottom flask equipped with rubber septa and thermocouple. The mixture was heated to 150°C and degassed under reduced pressure (<150 mTorr) for 2 hours with vigorous stirring to remove water and oxygen species. After backfilling the reactor with N_2 atmosphere, 1 mmol of 1M TMSP dissolved in ODE was rapidly injected into the flask at 150°C and the solution was heated up to 310°C within 10 min with vigorous stirring, maintained 10 min for core growth, and cooled down to room temperature. For GaP shelling on the InP core, 0 to 1ml of 1M $Ga(OA)_3$ was slowly introduced into a reaction flask at 200°C and maintained for 1.5 hours. For ZnSeS shelling on the surface of InP QD, ZnSA powder (5.06 g, 8 mmol) was added into the reaction flask, heated to 130 °C, and degassed under reduced pressure (<150 mTorr) for 30 min to remove water and oxygen species. After backfilling the reactor with N_2 atmosphere, the mixture was heated to 280 °C and maintained for 10 min. 2M TOP–Se (1.5 ml, 3 mmol) was injected to reaction flask at 280°C, maintained for 30 min, heated up to 300°C. 2M TOP–S (2.5 ml, 5 mmol) was rapidly injected at 300°C, maintained reaction flask at 300°C

for 1 h. Then, all reaction process was terminated by cooling down to room temperature and adding an excess amount of toluene.

6.2.3. Fabrication of QD–LEDs

First, the indium tin oxide (ITO) substrates were cleaned by sequential ultra-sonication with AC, isopropyl alcohol and EtOH, and dried in an oven at 100°C for 3h, followed by oxygen plasma treatment. The following steps were performed in a glove box under nitrogen atmosphere. The ZnO nanoparticles for electron transport layer were prepared using procedures previously reported in the literature[209] and were spin-coated onto the as-prepared ITO substrates at 3000 rpm for 30 s, followed by drying at 180°C for 30 min. The 9 mg / mL of QD solutions were spin-coated onto the ZnO nanoparticle layer at 3000 rpm for 30 s without further thermal annealing. After the solution processes, TCTA (40 nm) and MoO_3/Ag (10 nm / 150 nm) were deposited by the thermal evaporation on the QD layer in a high-vacuum chamber as a hole transport layer and metallic anode, respectively.

6.3. Result and Discussion

6.3.1. Optical properties of InP/GaP/ZnSeS QDs

To enhance photoluminescence quantum yields (PL QYs) of type-I core/shell heterostructured InP/ZnS QD, a formation of the intermediate shell, such as ZnSe and GaP, between InP core and ZnS outmost shell has been suggested to alleviate their lattice mismatch and interfacial traps for industrially feasible applications, QD–LCD and QD–LEDs. In particular, the insertion of GaP mid-shell between InP and ZnS not only led to high PL QY of over 80% but also enhance the thermal stability of QDs.[75-76] In general, forming the GaP shell onto InP core is known to require high reactive precursors such as $GaCl_3$ and GaI_3. As for this synthetic process, Ga cation usually often induces the cation exchange with Zn when a small amount of Ga precursors is injected, but an excess amount of Ga precursors leads to not only improvement of PL QYs but also red-shifted PL peak wavelength.[118]

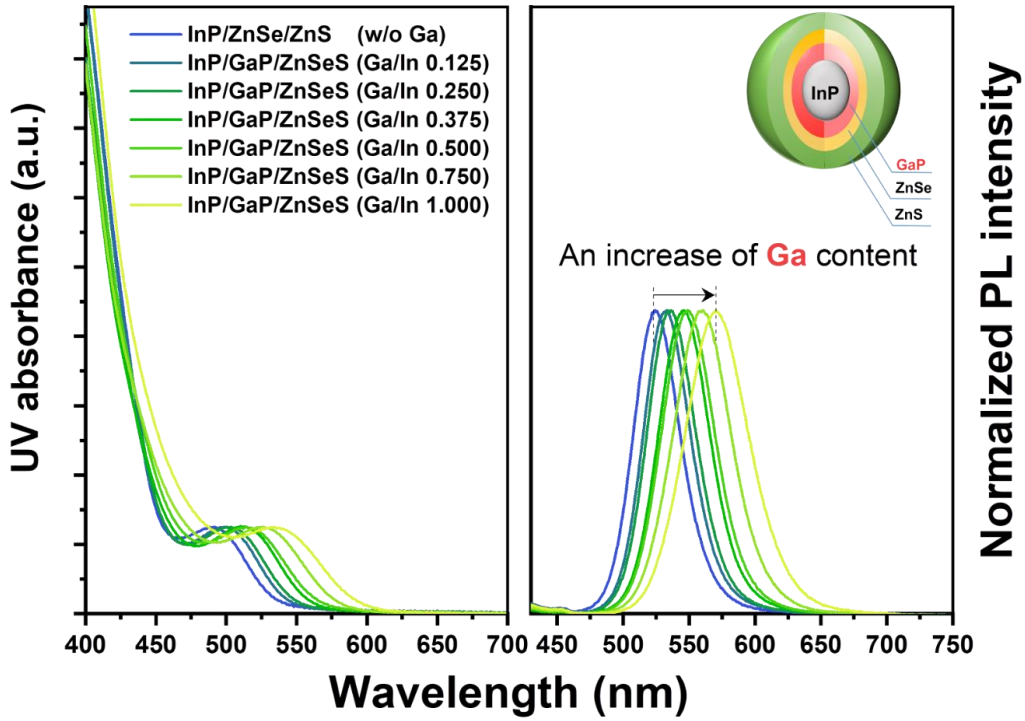

Figure 71. PL and UV spectra of InP/GaP/ZnSeS QDs obtained by varying the Ga/In mole ratio from 0 to 1.

Table 13. Optical properties of InP/GaP/ZnSeS QDs by varying the Ga/In mole ratio from 0 to 1.

Ga/In mole ratio	Structure		
	InP/ZnSe/ZnS		
	Peak WL (nm)	PL QYs (%)	FWHM (nm)
0.000	524.2	55.5	41.2
0.125	533.2	64.5	41.4
0.250	536.2	66.4	43.0
0.375	545.9	65.8	45.7
0.500	548.9	67.7	47.6
0.750	560.8	66.7	51.7
1.000	570.5	58.6	56.9

Figure 71 and Table 13 show the resulting optical properties of as-synthesized InP/GaP/ZnSeS QDs, where PL peak wavelength (WL) was red-shifted with increasing the ratio of Ga to In contents, corresponding to the previous report that a formation of GaP mid-shell induces the red-shifted peak

WLs.[118] In principle, the energy level of the valence band of InP is relatively similar to GaP compared to ZnSe or ZnS in type-I core/shell/shell InP/GaP/ZnSeS QDs; thus, the hole is confined to the InP core and the electron is delocalized throughout valence band from InP to GaP.[217] It supports also that GaP shell was formed well on the surface of InP core.

6.3.2. Analysis of Inductively Coupled Plasma optical emission spectroscopy (ICP–OES)

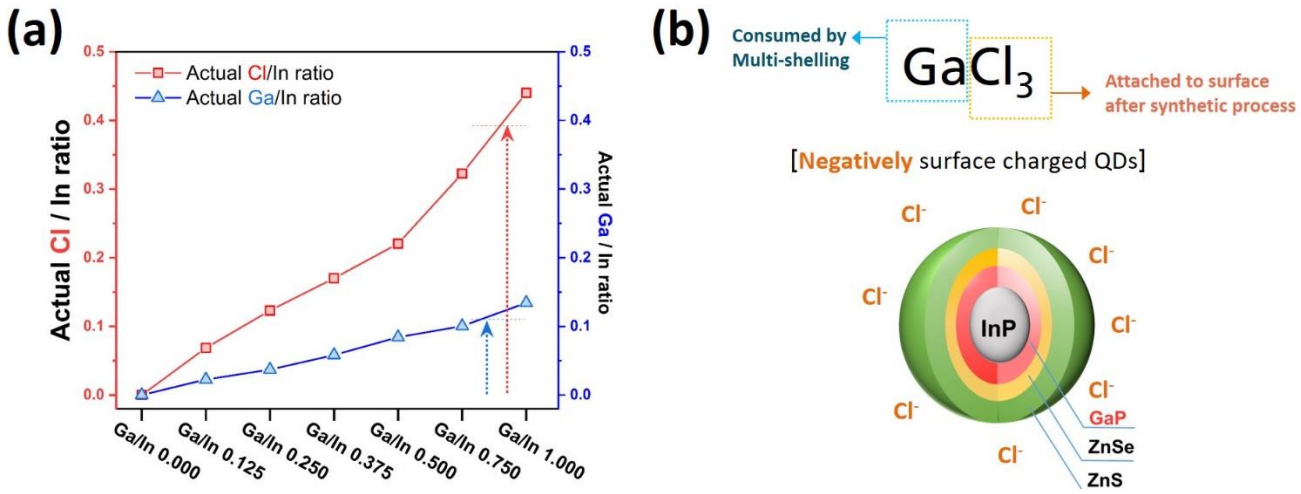

Figure 72. Inductively Coupled Plasma optical emission spectroscopy (ICP–OES) based actual elemental compositions of Ga/In and Cl/In in InP/GaP/ZnSeS QDs by varying Ga content, and the illustrated surface binding motif of $GaCl_3$ precursor.

In Figure 72a, Inductively Coupled Plasma optical emission spectroscopy (ICP–OES) proves a formation of GaP shell within InP/GaP/ZnSeS QDs. Comparing the ratio of Ga and Cl to In contents, the increase of Cl content is nearly three times bigger than Ga content, which alludes that unreacted Cl anions are remained on the QD surface. Basically, Ga cation induces cation exchange with Zn cation in In(Zn)P core or reacts with unreacted P precursors in the 1:1 stoichiometric ratio, so Cl anions can be considered to be eliminated from QDs after the purification step since it does not form any inorganic compounds. Also, Cl anion is one of the strongly bound ligands on QD surface, even its surface-binding affinity is much stronger than generally applied carboxylic acid ligands. Therefore, we could infer strongly that Cl anions can remain on the QD surface after the purification, not being eliminated out of QDs (Figure 72b).

6.3.3. Zeta potential measurement of InP/GaP/ZnSeS QDs, and their Surface Charge

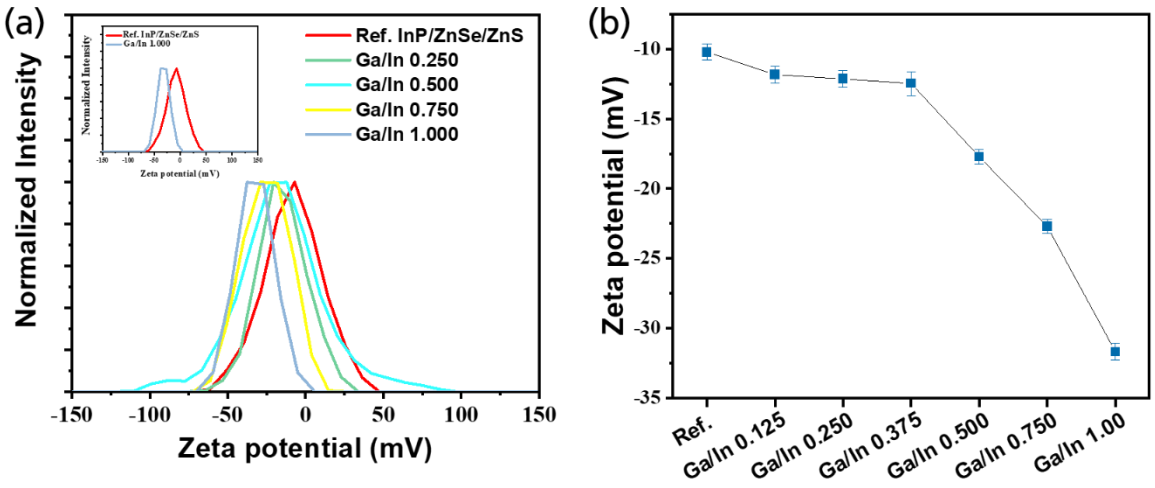

Figure 73. Zeta potential as a function of introduced Ga content in synthesis process of InP/GaP/ZnSeS QDs.

Figures 73a and b show the results of zeta potential of InP/GaP/ZnSeS QDs with increasing Ga content to form GaP mid-shell. Increasing Ga content in the synthesis process induces negative zeta potential, which moves toward more negative with increasing Ga content. In principle, negative zeta potential means that the net charge of dispersed particles in the suspension is negative, and it strongly advocates that Cl anions are bound to the QD surface, not has been removed out of QD.

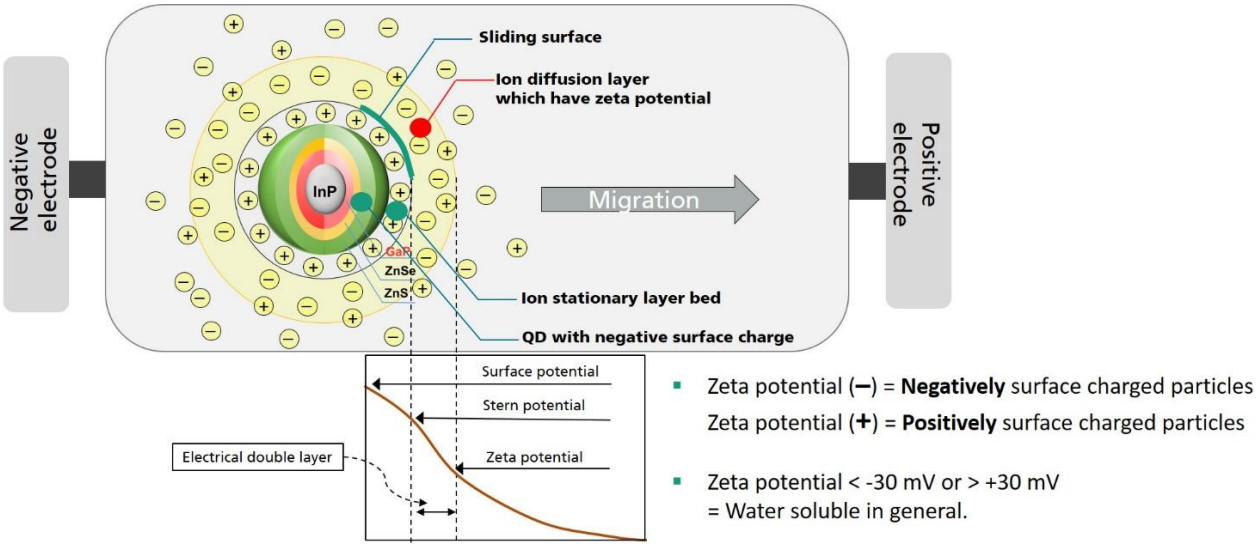

Figure 74. Zeta potential of a negatively charged colloidal QDs. Reproduced from ref.[218]

Zeta potential is a parameter that contains the electrical equilibrium between particle and liquid phase (solvent) with various application throughout medicine, chemical industry, mineral processing, and soil treatment.[219-220] In principle, the ionization of surface chemical groups, or absorption of suspended ions, increases or decreases the surface charge, so zeta potential is one of the most accessible analytical techniques to indirectly show the surface net charge..[221] Figure 74 shows the zeta potential of a negatively charged colloidal QDs, where surface charge and zeta potential are situated independent relation. Surface charge indicates the charge density on the surface of a particle, and zeta potential means the strength parameter of a shear plane during electrophoresis that expresses the movement of electric field and separation of charged ions.[221] Basically, the resultant mobility of the materials (e.g., ions on the QD surface) in zeta potential can be attributed to the dielectric constant of materials, the viscosity of the suspended liquid, and the electrical potential at the slipping plane, as shown in Figure 68.[218] Simply, we can confirm the surface charge of particles using zeta potential as an indicator, where positive and negative values, obtained from zeta potential, indicate positive and negative charged particles, respectively.

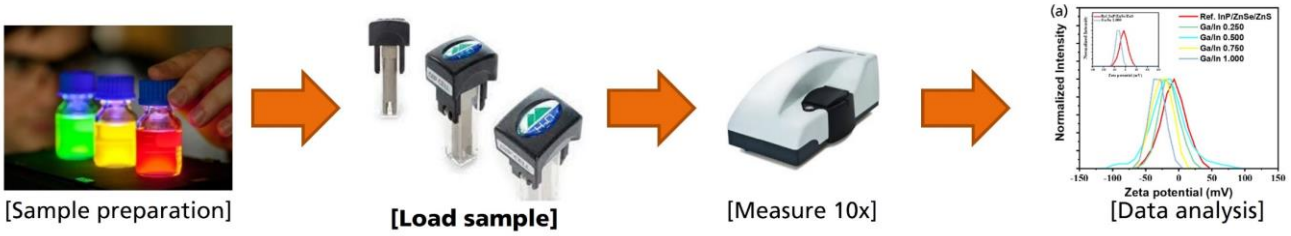

Figure 75. Schematic representation of the zeta potential measurement workflow using colloidal QDs.

Table 14. Physical properties of chlorobenzene compared to toluene.

	Dielectric constant	Dipole moment	Vapor pressure	Zeta potential	EHD jet printing
Toluene	2.4	0.375 D	22 mmHg	Low signal	No
Chlorobenzene	5.62	1.55 D	11 mmHg	High signal	Acceptable

Figure 75 shows the schematic workflow of the zeta potential when a colloidal QD solution was applied. The measuring solution usually requires a minimum degree of conductivity to maintain a constant voltage and avoid induced electrode polarization.[221] In particular, colloidal QDs, which are usually employed in display industry, has hydrophobic property, so these generally dissolve in organic non-polar solvents, such as toluene and hexane. Thus, for measuring zeta potential in a non-polar organic solvent, a universal dip cell that can generate a high field strength at a lower voltage is necessary. Despite using this universal dip cell in toluene solvent, the signal of zeta potential was too low to obtain trustable data. Therefore, we investigated the physical properties of non-polar organic solvents within the range that colloidal InP QDs can dissolve well. Consequently, we could confirm that chlorobenzene solvent, which has a slightly higher dielectric constant than toluene, is appropriate for not only dissolving colloidal QDs well but also obtaining the correct value of zeta potential (Table 14).

6.3.4. Electrohydrodynamic (EHD) Jet Printing of InP/GaP/ZnSeS QDs

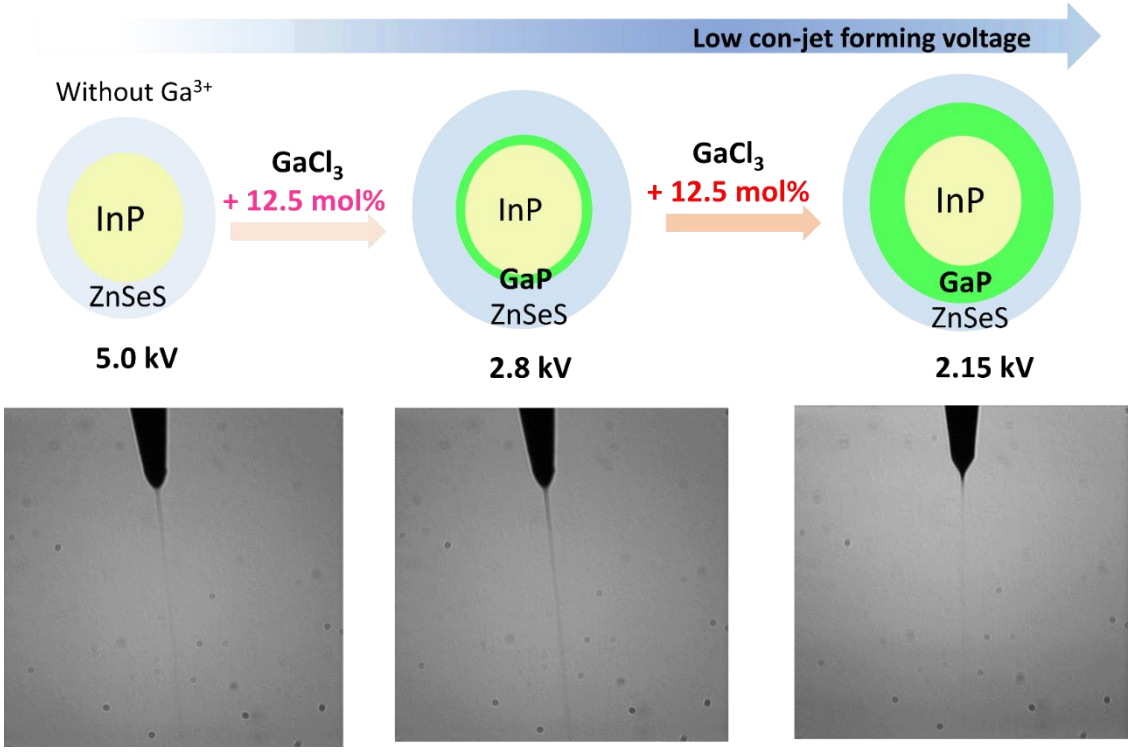

Figure 76. Change of cone-jet forming voltage when using InP/GaP/ZnSeS QDs in EHD jet printing.

As a result, we applied these negatively charged QDs to EHD jet printing and observed the cone-jet forming voltage in Figure 76. With increasing $GaCl_3$ precursors in QDs, definitely revealed was the result that the cone-jet forming voltage decreased rapidly. This is likely attributed to the negative charged InP QD due to surface bound Cl anion ligands. Theoretically, an increasing trend of

surface charge induces the reduced cone-jet forming voltage, which is well matched with this experimental result that the amount of GaC_3 precursors has a linear correlation with the negative value of zeta potential (Figure 73). EHD printing has unique merit in realizing nanoscale printing, but its experimental process is still challenging to control due to its high working voltage over generally 5 kV. Thus, a decrease of cone-jet forming and working voltage is beneficial to the industrially feasible printed pattering display.

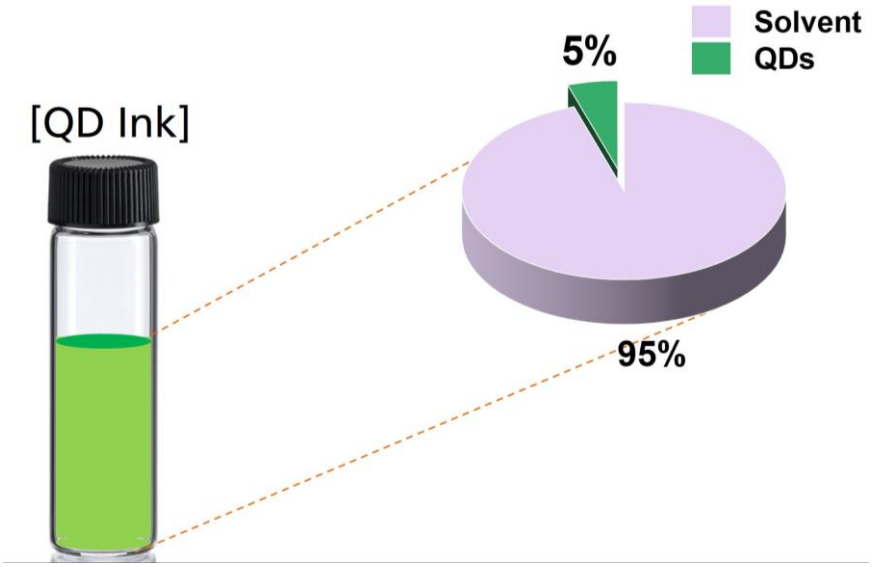

Figure 77. QD ink formulation for EHD jet printing

Different from QD film application as a PL device, QD–LEDs as an EL device do not require a large amount of QD concentration because one or two monolayers emit by an injected hole and electron via ETL and HTL. Also, the excess QD layer of over three monolayers disturbs charge transporting that pass through the whole device, giving rise to a decrease in current efficiency. Thus, only 3–5 wt% of QD solid content is usually acceptable for the fabrication of EL devices, which limits the modification of the QD ink formulation for QD–LEDs. Considering this low concentration of QD solid content in ink formulation, a rapid decrease of cone-jet forming voltage with increasing negative charged particles suggests a promising possibility that a subtle change of precursors can result in the largely reduced EHD operating voltage.

6.3.5. TR PL decay curves of InP/GaP/ZnSeS QDs, and their Current Efficiency of EL Devices

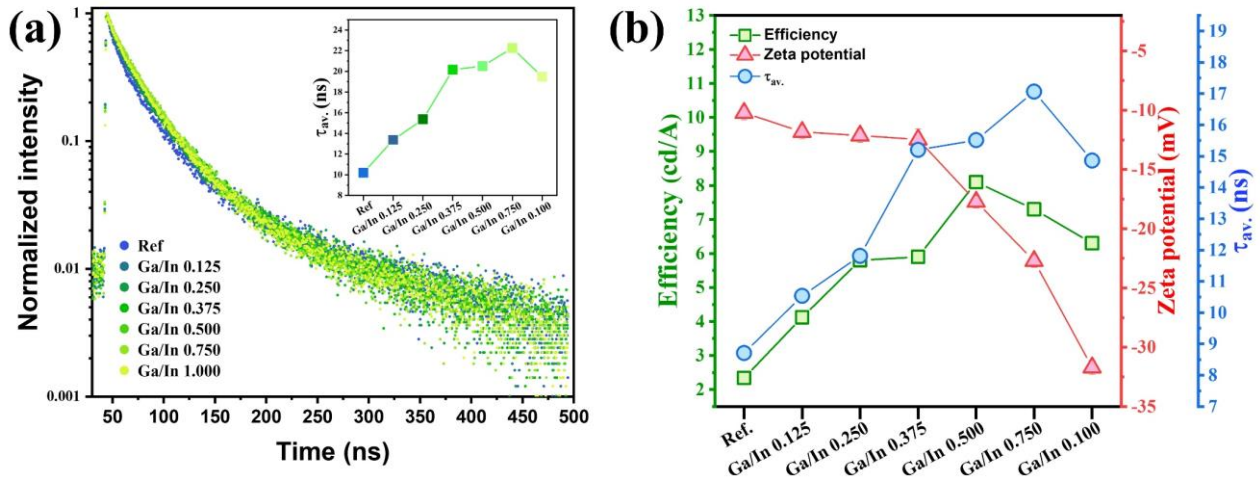

Figure 78. (a) decay curve of time resolved PL (TR PL) at the emission peak, and (b) the comparison of their current efficiency, zeta potential, and calculated tau (τ) average values.

In addition, the inverted QD–LEDs were fabricated using the synthesized InP/GaP/ZnSeS QDs, where the calculated τ average values from TR–PL and current efficiencies were obtained (Figure 78). In particular, the calculated τ average values show an increasing trend with increasing Ga content, which has similar tendency with their current efficiencies in the inverted QD–LEDs. However, with rapidly increasing negative zeta potential from 0.375 to 1.000 molar ratio in Ga/In, the corresponding current efficiencies reversely represent a decreasing trend which is opposite from one that applied the small amount of Ga content from 0.125 to 0.250 molar ratio in Ga/In. This result may originate from the electron overcharging of the QD layer in QD–LEDs due to excess Cl anions bound to the QD surface. As a result, an appropriate adjustment of surface charge on the QD surface is one of the critical points to realizing both high efficiency in QD–LEDs and a low voltage-operating EHD printing system.

6.4. Conclusion

This brief report proposed zeta potential analysis as a convenient way to measure the surface charge of QDs. Also, we confirmed this result obtained from zeta potential is related to the determination of cone-jet forming voltage in the EHD jet printing system. Also, this zeta potential measurement technique strengthens ICP–OES data of QDs to reveal the charge amount on the QD surface rather than the total ratio of elements. In addition, we fabricated the inverted QD–LEDs using these negatively charged QDs and investigated the optimized ratio of Ga and Cl contents to be able to realize both high-quality QD–LEDs and well-operating EHD jet printing conditions at the lower range under 3 kV. As a result, we believe this promising data can help implement an industrially applicable patterned display in the near future.

7. SUMMARY

Had all studies been organized in this doctoral thesis briefly, this research tried to show a direct comparison with experimental results for better connectivity with QD materials and QD devices. However, from the chemist's point of view, the structure of QD material and its modification of surface status is mainly focused on and conducted via practical experiments based on wet chemical synthesis to explore a difference in the corresponding QD devices. Nevertheless, it still had a specific limitation in interpreting the result of QD devices from physical standpoints in detail, so further research, such as simulated interpretation according to quantum mechanics and LED device mechanism analysis, should be followed up in the future.

In recent industry trends, the pioneering material patents about new structures and material components have been recognized as a powerful weapon without bullets for future benefit in the industry. Thus, the new structural InP:Cu/ZCIS/ZnS QD in Chapter 3 was registered as an international patent with publication as a research article, which ensures sustainable research in Fraunhofer IAP and the related internal industry. In addition, despite an intrinsically large Stokes shift of transition metal doped QDs, CIS (copper indium sulfide) type QDs have played a significant role as a crucial material in LSC fabrication for the past twenty years due to their highest level of PL QY of over 90% and moderate broad Stokes shift. Herein, we suggested the new structural Cu-doped InP QDs with the highest PL QY of over 80% as a promising material to replace CIS QDs and utilize for LSCs. Furthermore, the possibility of LSC fabrication using Cu-doped InP QDs could be expected to bring about a significant ripple effect via steady research in the future.

In response to demands from the modern display industry that requires high resolution and efficiency, display materials throughout organic and inorganic compounds have been developed toward high stability, high color purity, color-tunability, and various versatility in liquid or solid matrix structures, such as resin and solvent. Herein, this doctoral thesis suggested that the surface chemistry of QDs affects the material and its corresponding device stability and efficiency, which could be one of the promising solutions that can realize industrially feasible QD-LEDs. More detailed, breaking away from the limitations of the previous mechanism that thiol ligands are solely bound to the QD surface without proton transfer with other ligands, this research revealed that thiol ligands manipulate Zn carboxylate ligands via proton transfer and are favorable to surface passivation. Also, this fact is strongly related to the stability and efficiency of the corresponding QD devices fabricated from the surface-treated QDs. Consequently, this study systematically demonstrated that the degradation mechanism by organic ligands in surface chemistry is as vital as the morphology and structural stability of inorganic core/shell heterostructure QDs.

On the other hand, conventional inkjet printing systems faced a limitation that should overcome the big huddles of high resolution on the sub-micro scale. Thus, this study suggested the EHD jet printing system combined with QD material, which is more advanced than the conventional inkjet printing system. However, the operating voltage was still high at over 5kV in implementing an industrially friendly process. This experimental weakness could be solved using negatively charged InP QDs instead of as-synthesized InP QDs with neutral surface charge. In addition, the zeta potential, an industrially convenient analysis, was employed away from the existing complicated method and interpretation of measuring surface charge.

As a result, QD materials have endless possibilities beyond InP QD materials that are applied in the display field. For example, intrinsically more stable boron nitride and carbon dots more than InP QDs have risen as candidates for LED devices, which can also implement to the narrow FWHM as blue, green, and red emitters. Therefore, further research for post-InP materials should proceed proactively to lead the future industry, including academic territories. Additionally, InP QD materials still have fundamental and theoretical huddles about their relatively lower blue light absorptivity than Cd-type QDs, which is based on the absence of an inorganic mid-shell to be able to absorb blue light from LED light sources. This is one of the crucial issues in overcoming the power consumption rate in all LED-related devices, including EL and PL applications, toward advanced micro-LEDs that can realize wearable and transparent future displays. Of course, my research showed a lot of effort to be able to overcome the color purities of InP QDs, the realization of LSC devices in Cu-doped InP QDs, and the feasibility of the EHD printing process. Nevertheless, it is impossible for us to conclude that all these reported studies are the final solution. Still, hopefully, this effort can contribute to developing the display industry toward the highest level of display material and devices.

8. SUPPORTING INFORMATION

8.1. Determination of carrier lifetime in TR PL curve

The PL decay curves from QD1 to QD4 were fitted by the following bi-exponential equation.

$$y = y_0 + A_1\exp(-x/\tau_1) + A_2\exp(-x/\tau_2) \quad (1)$$

Here, y_0, A, and τ_1 are transient light intensity (i.e., an offset), pre-exponential constant and lifetime of each component, respectively. As using these fitting components, the average lifetime, i.e., mean value, was calculated as follow.

$$A_1\,(\%) = A_1 / (A_1 + A_2) \times 100 \quad (2)$$

$$A_2\,(\%) = A_2 / (A_1 + A_2) \times 100 \quad (3)$$

The average lifetime was obtained from equations (1), (2) and (3) as following:

$$\text{Average lifetime (ps)} = (A_1\tau_1^2 + A_2\tau_2^2) / (A_2\tau_1 + A_2\tau_2) \quad (4)$$

8.2. Statistical Analysis

First, for the pre-processing of data for statistical analysis, we calculate the median value to replace the missing values with the median values. For the statistical analysis of interparticle spacing (Figure 37c), we have conducted 1) One-way ANOVA and 2) Tukey's honestly significantly differenced (HSD) tests for statistical methods to assess differences in four sample sets (QD1, QD2, QD3, QD4, n = 362). The P value calculated by One-way ANOVA was smaller than 0.001 (2.85e-149), which indicates the statistically significant difference among the four sample sets. Sequentially, for the pair-wise comparison between samples, P values were additionally calculated by Tukey's HSD test to complement the One-way ANOVA test, where every P values were smaller than 0.001, indicating that an increasing trend of the mean value in the interparticle spacing from QD1 to QD4 is statistically significant and reasonable. This process was performed using python 3.7.13, package of pandas, scipy, and bioinfokit. In addition, in the box chart in Figure 37c, the Interquartile range (IQR) is the box plot showing the middle of scores, which was set as 1.5 indicating 25th percentile. As for the whisker, a factor of n was adjusted to expand the whisker length, and the default Coef value of 1.5 was applied as a n value. Data presentation of the average QD-to-QD distance distributions in the interparticle spacing was represented as a mean ± SD (standard deviation). This process was performed using Origin 2021 software.

For the statistical analysis of particle size (Figure S3), we have conducted One-way ANOVA, and the P value was calculated as 0.8 from four sample sets (QD1, QD2, QD3, QD4, n = 358), which indicates there is no statistically significant difference between the four samples in terms of particle size. This process was performed using python 3.7.13, package of pandas, scipy, and bioinfokit. For the particle size distributions of QDs obtained from TEM images (Figure S3, inset), the Bin size at x-axis was fixed at 0.9 nm throughout all data from QD1 to QD4. Data presentation of the average particle size distributions was represented as a mean ± SD (standard deviation). This process was performed using Origin 2021 software.

In addition, the normalization was proceeded for scaling individual samples, where the PL emission of QDs and the EL emission of QD-LEDs were normalized with respect to the PL peak wavelength of QD emissions. This process was performed using Origin 2021 software.

8.3. Supplementary Analytical Data

Table S1. Variations of PL peak wavelength (PL WL), FWHM, and PL QYs in the synthetic process of InP/ZnSe/ZnS QDs.

QD	PL WL (nm)	FWHM (nm)	PL QY (%)
InP	475.8	44.6	0.4
InP/ZnSe	541.4	43.6	55.4
InP/ZnSe/ZnS	536.3	43.0	73.5

Table S2. Variations of PL WL, FWHM, and PL QYs of a series of InP/ZnSe/ZnS QDs according to amount of OTT treated.

QD	PL WL (nm)	FWHM (nm)	PL QY (%)
QD1	536.3	43.0	73.5
QD2	537.0	42.9	72.4
QD3	537.8	42.9	71.0
QD4	537.8	42.9	72.7

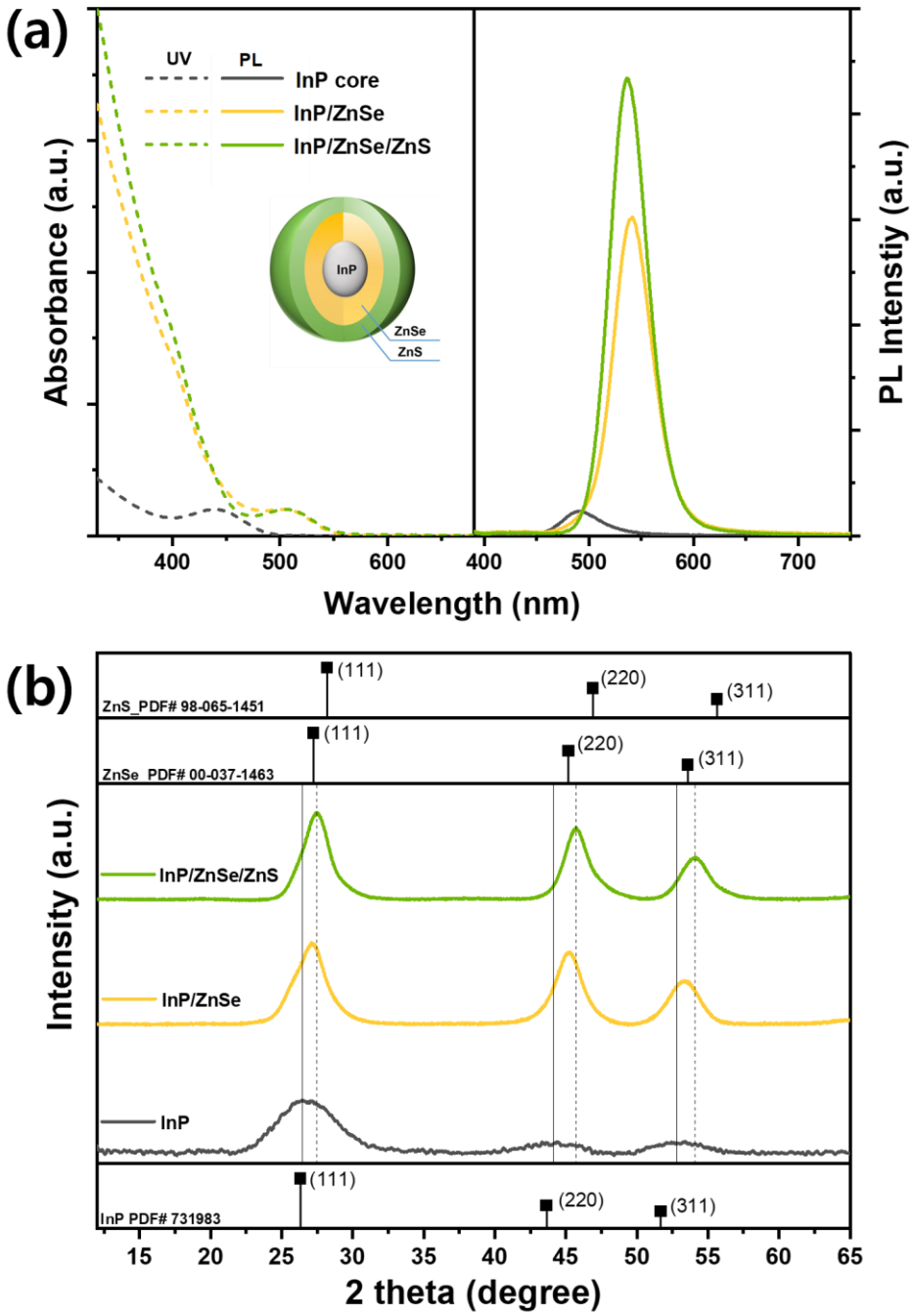

Figure S1. (a) PL and UV spectra in synthetic process of InP/ZnSe/ZnS QD and (b) corresponding XRD patterns

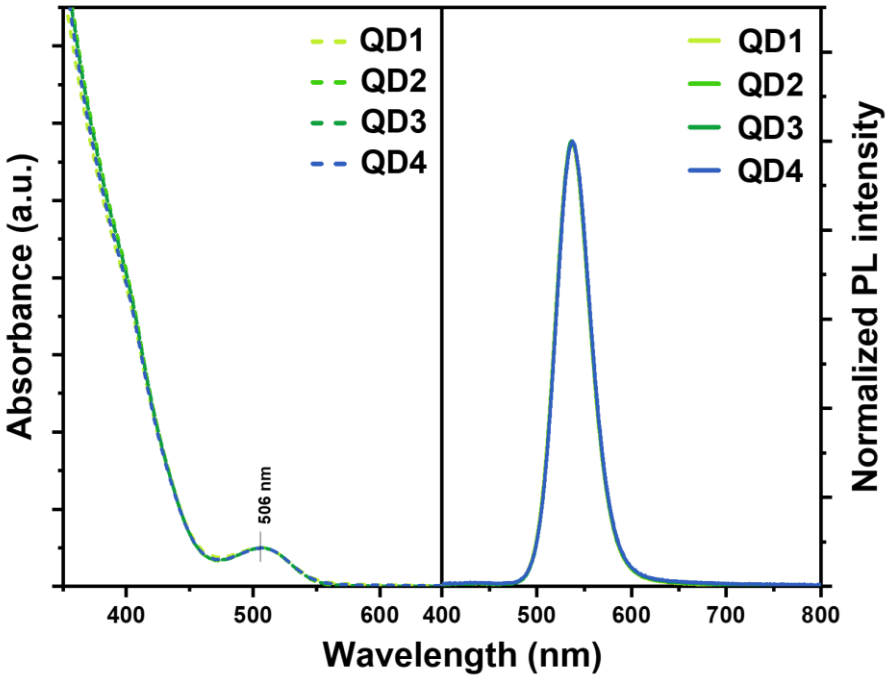

Figure S2. (a) PL and UV spectra from QD1 to QD4.

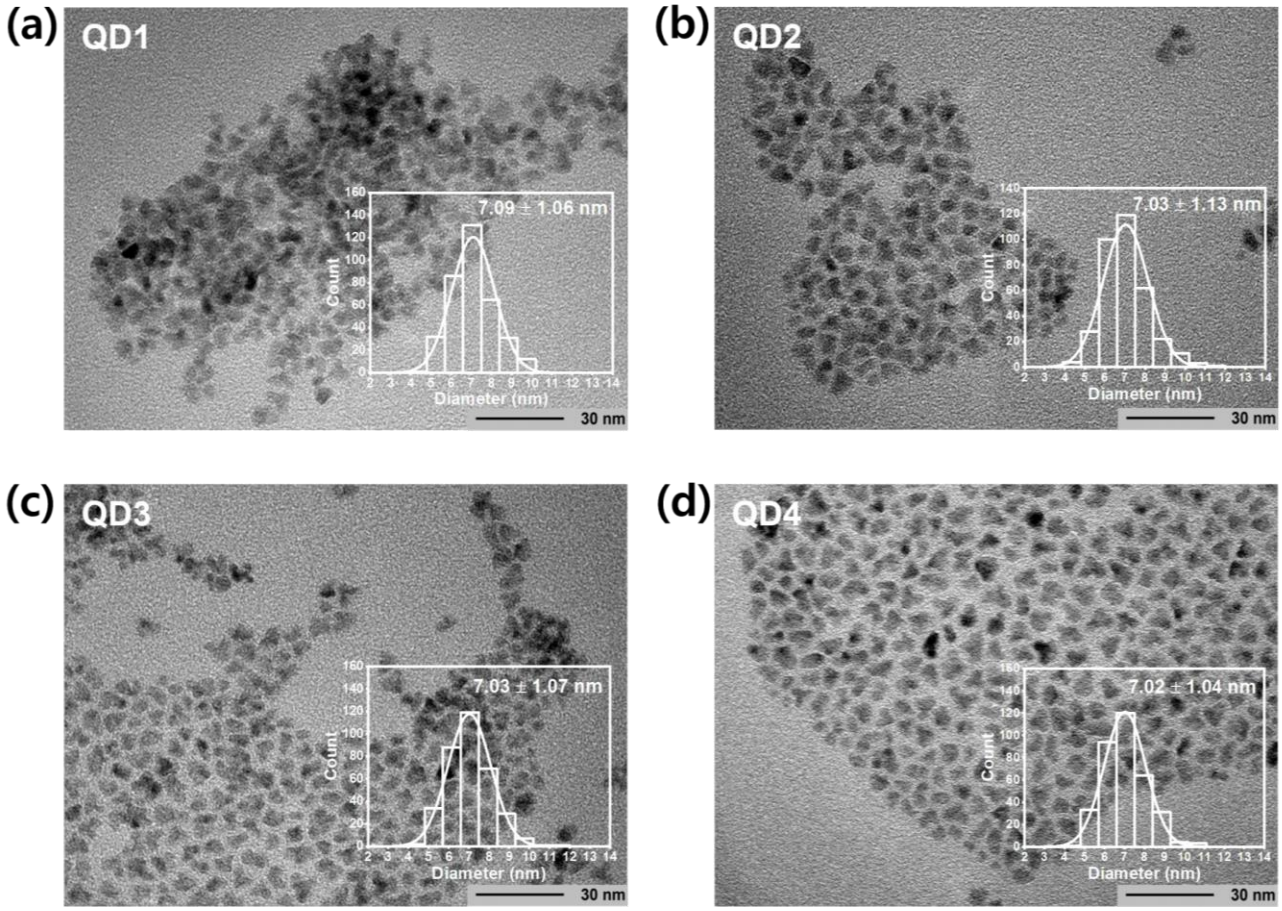

Figure S3. TEM images and their particle size distributions from QD1 to QD4. The statistical methods used to assess significant differences with sufficient detailed are described in the 2.7 Statistical Analysis in Supporting Information.

OTT has another role as a sulfur donor to be able to form sulfide compound, such as ZnS shelling on InP/ZnSe QD, when the reaction temperature rises to over 200°C where the thermal decomposition of thiol groups is usually taking place.[86] Thus, we have selected the surface modification temperature at 150°C for 10 min, i.e., extremely short time, to prevent further formation of ZnS shell derived from OTT. Even though this elaborate controlling of reaction temperature, additional TEM measurements of over 300 particles have been performed to examine whether further growth was formed or not. From QD1 to QD4, the corresponding average diameters were almost similar, not increased, where it even decreases as much as 0.07 nm (Figure S3). This result alludes that polarity variation of surface ligands by OTT on the QD surface can provoke a particle size fractionation process in purification step.[222]

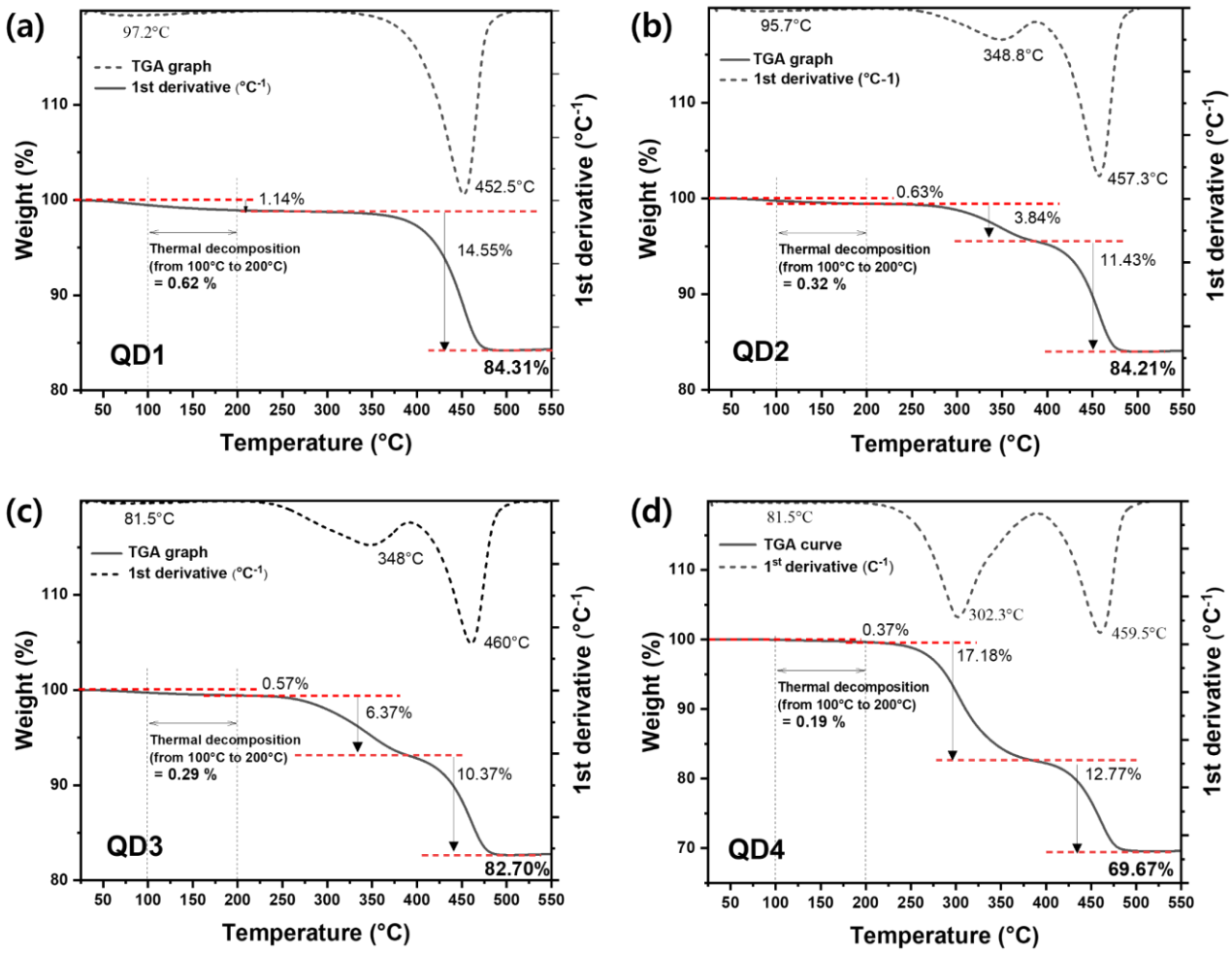

Figure S4. TGA analyses and 1st derivative curves from QD1 to QD4.

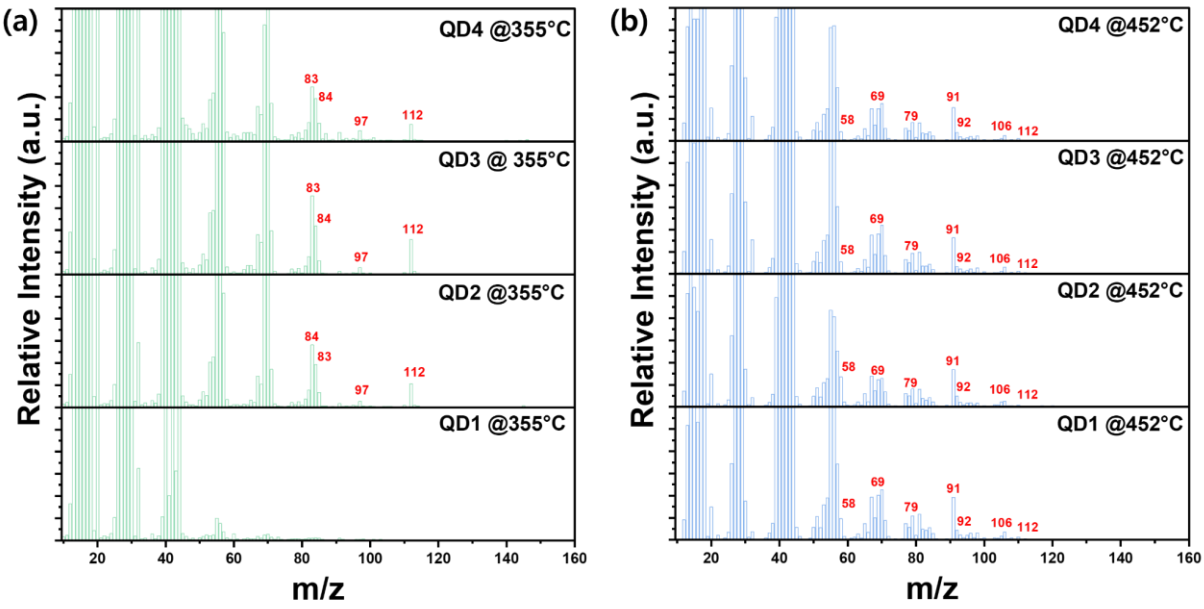

Figure S5. Evolutions of relative MS intensities according to thermal deposition temperatures at (a) 355°C and (b) 452°C from QD1 to QD4.

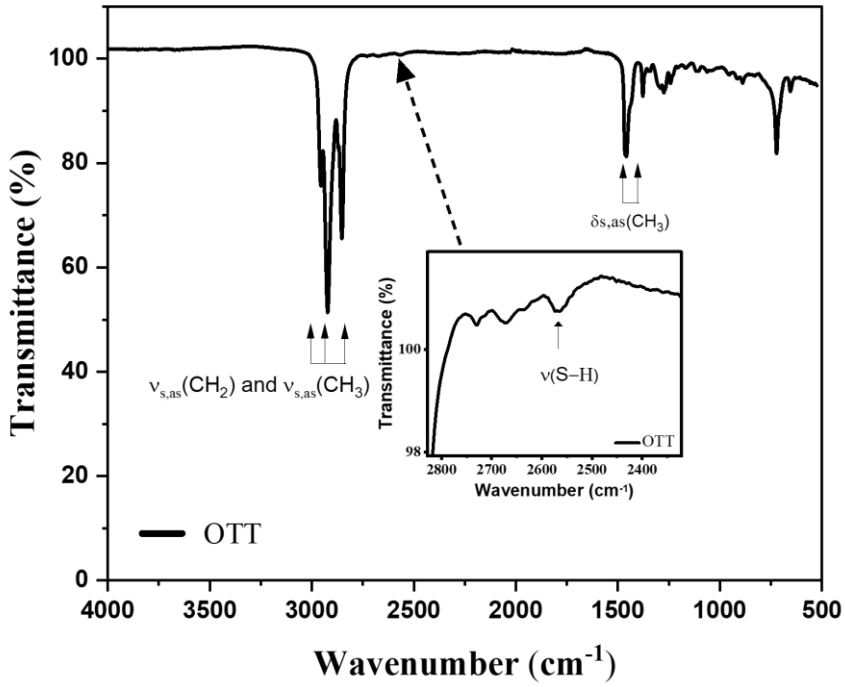

Figure S6. (a) The IR spectra of OTT including ν(S–H) peak of insert graph, and (b) the evolution of IR spectra from QD1 to QD4.[197]

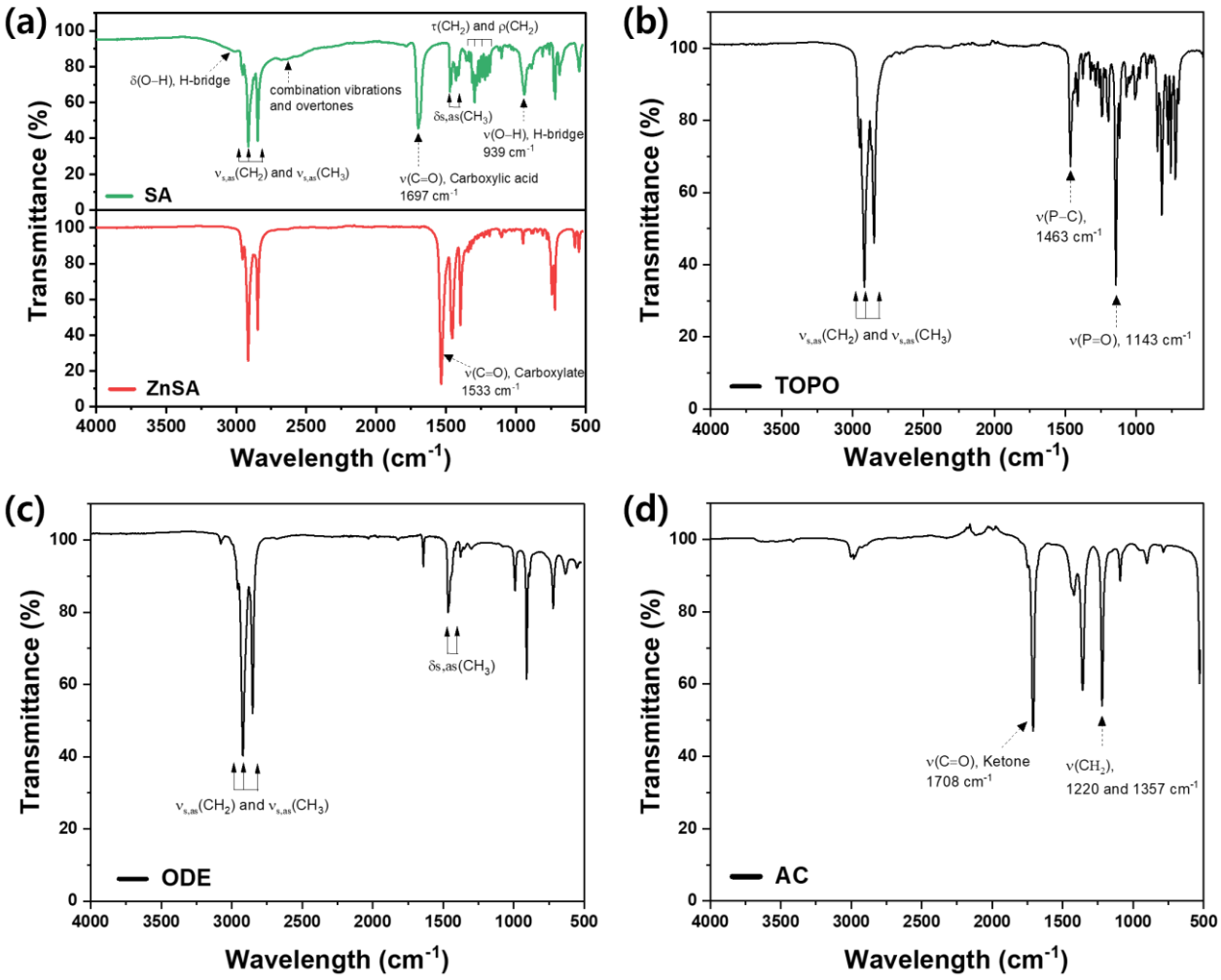

Figure S7. The IR spectra of (a) SA and ZnSA, (b) TOPO, (c) ODE, and (d) AC.[197]

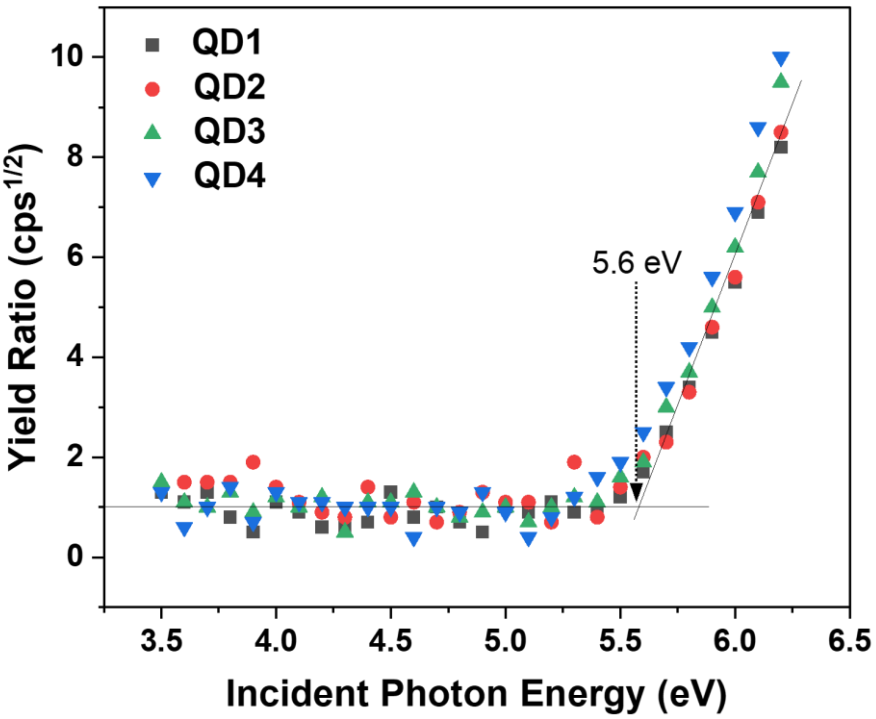

Figure S8. AC–2 measurements from QD1 to QD4.

9. SELBSTSTÄNDIGKEITSERKLÄRUNG

Hiermit versichere ich, dass ich die vorliegende Arbeit ohne Hilfe Dritter und ohne Zuhilfenahme anderer als der angegebenen Quellen und Hilfsmittel angefertigt habe. Die den benutzten Quellen wörtlich oder inhaltlich entnommenen Stellen sind als solche kenntlich gemacht.

Die „Richtlinie zur Sicherung guter wissenschaftlicher Praxis für Studierende an der Universität Potsdam (Plagiatsrichtlinie) - Vom 20. Oktober 2010“, im Internet unter http://uni-potsdam.de/ambek/ambek2011/1/Seite7.pdf, habe ich zur Kenntnis genommen.

_____ _____

Ort, Datum Unterschrift

10. REFERENCE

1. Service, R. F., Is nanotechnology dangerous? American Association for the Advancement of Science: 2000.
2. Parak, W. J.; Manna, L.; Simmel, F. C.; Gerion, D.; Alivisatos, P., Quantum dots. *Nanoparticles: from theory to application* **2003**, 4-49.
3. Schmid, G., *Nanoparticles: from theory to application*. John Wiley & Sons: 2011.
4. Baker, G., Book review: Polymer Films with Embedded Metal Nanoparticles. By Andreas Heilmann. Wiley Online Library: 2004.
5. Yoffe, A. D., Semiconductor quantum dots and related systems: electronic, optical, luminescence and related properties of low dimensional systems. *Advances in physics* **2001,** *50* (1), 1-208.
6. Alivisatos, A. P., Nanocrystals: building blocks for modern materials design. *Endeavour* **1997,** *21* (2), 56-60.
7. Jaeckel, G., Some modern absorption glasses. *Z. Tech Phys* **1926,** *7*, 301-304.
8. Brus, L. E., Electron–electron and electron-hole interactions in small semiconductor crystallites: The size dependence of the lowest excited electronic state. *The Journal of chemical physics* **1984,** *80* (9), 4403-4409.
9. Rossetti, R.; Nakahara, S.; Brus, L. E., Quantum size effects in the redox potentials, resonance Raman spectra, and electronic spectra of CdS crystallites in aqueous solution. *The Journal of Chemical Physics* **1983,** *79* (2), 1086-1088.
10. Gaponenko, S. V., *Optical properties of semiconductor nanocrystals*. Cambridge university press: 1998.
11. Bawendi, M. G.; Steigerwald, M. L.; Brus, L. E., The quantum mechanics of larger semiconductor clusters ("quantum dots"). *Annu. Rev. Phys. Chem* **1990,** *41* (1), 477-496.
12. Onyia, A.; Ikeri, H.; Nwobodo, A., Theoretical study of the quantum confinement effects on quantum dots using particle in a box model. *Journal of Ovonic Research* **2018,** *14* (1), 49-54.
13. keri, H.; Onyia, A.; Vwavware, O., The Dependence of Confinement Energy on the Size of Quantum Dots. *Intl. Jol. of scientific research in Physics and Applied Science* **2019,** *7* (2), 12-16.
14. livisatos, A. P., Semiconductor clusters, nanocrystals, and quantum dots. *science* **1996,** *271* (5251), 933-937.
15. adelung, O., Semiconductors-Physics of II-VI and I-VII Compounds, Semi-magnetic Semiconductors. *Landolt-Bornstein-Numerical Data and Fundamental Relationships in Science and Technology* **1982,** *17*, 255.
16. dachi, S., *Electronic, Transport, Optical and Other Properties: Supplement to Vols. III/17a, 22a (print Version); Revised and Updated Edition of Vols. III/17a, 22a (CD-ROM)*. Springer: 2002.
17. radhan, N.; Peng, X., Efficient and color-tunable Mn-doped ZnSe nanocrystal emitters: control of optical performance via greener synthetic chemistry. *Journal of the American Chemical Society* **2007,** *129* (11), 3339-3347.
18. Pradhan, N.; Goorskey, D.; Thessing, J.; Peng, X., An alternative of CdSe nanocrystal emitters: pure and tunable impurity emissions in ZnSe nanocrystals. *Journal of the American Chemical Society* **2005,** *127* (50), 17586-17587.

19. Xie, R.; Rutherford, M.; Peng, X., Formation of high-quality I− III− VI semiconductor nanocrystals by tuning relative reactivity of cationic precursors. *Journal of the American Chemical Society* **2009,** *131* (15), 5691-5697.
20. Jana, S.; Srivastava, B. B.; Acharya, S.; Santra, P. K.; Jana, N. R.; Sarma, D.; Pradhan, N., Prevention of photooxidation in blue–green emitting Cu doped ZnSe nanocrystals. *Chemical Communications* **2010,** *46* (16), 2853-2855.
21. Bol, A. A.; Ferwerda, J.; Bergwerff, J. A.; Meijerink, A., Luminescence of nanocrystalline ZnS: Cu2+. *Journal of Luminescence* **2002,** *99* (4), 325-334.
22. Beaulac, R.; Archer, P. I.; Ochsenbein, S. T.; Gamelin, D. R., Mn2+-doped CdSe quantum dots: new inorganic materials for spin-electronics and spin-photonics. *Advanced Functional Materials* **2008,** *18* (24), 3873-3891.
23. Zhong, H.; Bai, Z.; Zou, B., Tuning the luminescence properties of colloidal I–III–VI semiconductor nanocrystals for optoelectronics and biotechnology applications. *The journal of physical chemistry letters* **2012,** *3* (21), 3167-3175.
24. Song, W.-S.; Yang, H., Efficient White-Light-Emitting Diodes Fabricated from Highly Fluorescent Copper Indium Sulfide Core/Shell Quantum Dots. *Chemistry of Materials* **2012,** *24* (10), 1961-1967.
25. Chen, Y.; Li, S.; Huang, L.; Pan, D., Green and Facile Synthesis of Water-Soluble Cu–In–S/ZnS Core/Shell Quantum Dots. *Inorganic Chemistry* **2013,** *52* (14), 7819-7821.
26. Yoon, S.-Y.; Kim, J.-H.; Jang, E.-P.; Lee, S.-H.; Jo, D.-Y.; Kim, Y.; Do, Y. R.; Yang, H., Systematic and extensive emission tuning of highly efficient Cu–In–S-based quantum dots from visible to near infrared. *Chemistry of Materials* **2019,** *31* (7), 2627-2634.
27. Zang, H.; Li, H.; Makarov, N. S.; Velizhanin, K. A.; Wu, K.; Park, Y.-S.; Klimov, V. I., Thick-shell CuInS2/ZnS quantum dots with suppressed “blinking” and narrow single-particle emission line widths. *Nano letters* **2017,** *17* (3), 1787-1795.
28. Meinardi, F.; McDaniel, H.; Carulli, F.; Colombo, A.; Velizhanin, K. A.; Makarov, N. S.; Simonutti, R.; Klimov, V. I.; Brovelli, S., Highly efficient large-area colourless luminescent solar concentrators using heavy-metal-free colloidal quantum dots. *Nat Nanotechnol* **2015,** *10* (10), 878-85.
29. Li, H.; Wu, K.; Lim, J.; Song, H.-J.; Klimov, V. I., Doctor-blade deposition of quantum dots onto standard window glass for low-loss large-area luminescent solar concentrators. *Nature Energy* **2016,** *1*.
30. Huang, W.-T.; Yoon, S.-Y.; Wu, B.-H.; Lu, K.-M.; Lin, C.-M.; Yang, H.; Liu, R.-S., Ultra-broadband near-infrared emission CuInS2/ZnS quantum dots with high power efficiency and stability for the theranostic applications of mini light-emitting diodes. *Chemical Communications* **2020,** *56* (59), 8285-8288.
31. Fuhr, A.; Yun, H. J.; Crooker, S. A.; Klimov, V. I., Spectroscopic and Magneto-Optical Signatures of Cu1+ and Cu2+ Defects in Copper Indium Sulfide Quantum Dots. *ACS nano* **2020**.
32. Shen, H.; Wang, H.; Li, X.; Niu, J. Z.; Wang, H.; Chen, X.; Li, L. S., Phosphine-free synthesis of high quality ZnSe, ZnSe/ZnS, and Cu-, Mn-doped ZnSe nanocrystals. *Dalton Transactions* **2009,** (47), 10534-10540.
33. Gul, S.; Cooper, J. K.; Corrado, C.; Vollbrecht, B.; Bridges, F.; Guo, J.; Zhang, J. Z., Synthesis, optical and structural properties, and charge carrier dynamics of Cu-doped ZnSe nanocrystals. *The Journal of Physical Chemistry C* **2011,** *115* (43), 20864-20875.

34. Zhang, Y.; Shen, Y.; Wang, X.; Zhu, L.; Han, B.; Ge, L.; Tao, Y.; Xie, A., Enhancement of blue fluorescence on the ZnSe quantum dots doped with transition metal ions. *Materials Letters* **2012,** *78*, 35-38.
35. Kumar, R. A.; Prasad, M. S.; Kumar, G. K.; Venkateswarlu, M.; Rajesh, C., Tuning of emission from copper-doped ZnSe quantum dots. *Physica Scripta* **2019,** *94* (11), 115806.
36. Xie, R.; Li, Z.; Peng, X., Nucleation kinetics vs chemical kinetics in the initial formation of semiconductor nanocrystals. *Journal of the American Chemical Society* **2009,** *131* (42), 15457-15466.
37. Lim, M.; Lee, W.; Bang, G.; Lee, W. J.; Park, Y.; Kwon, Y.; Jung, Y.; Kim, S.; Bang, J., Synthesis of far-red-and near-infrared-emitting Cu-doped InP/ZnS (core/shell) quantum dots with controlled doping steps and their surface functionalization for bioconjugation. *Nanoscale* **2019,** *11* (21), 10463-10471.
38. Mei, S.; Wei, X.; Yang, D.; Su, D.; Yang, W.; Zhang, G.; Hu, Z.; Yang, B.; Dai, H.; Xie, F., Color-tunable optical properties of cadmium-free transition metal ions doped InP/ZnS quantum dots. *Journal of Luminescence* **2019**.
39. Kim, H.-J.; Jo, J.-H.; Yoon, S.-Y.; Jo, D.-Y.; Kim, H.-S.; Park, B.; Yang, H., Emission Enhancement of Cu-Doped InP Quantum Dots through Double Shelling Scheme. *Materials* **2019,** *12* (14), 2267.
40. Li, Y.; Hou, X.; Dai, X.; Yao, Z.; Lv, L.; Jin, Y.; Peng, X., Stoichiometry-controlled InP-based quantum dots: synthesis, photoluminescence, and electroluminescence. *Journal of the American Chemical Society* **2019**.
41. Kim, Y.; Ham, S.; Jang, H.; Min, J. H.; Chung, H.; Lee, J.; Kim, D.; Jang, E., Bright and Uniform Green Light Emitting InP/ZnSe/ZnS Quantum Dots for Wide Color Gamut Displays. *ACS Applied Nano Materials* **2019,** *2* (3), 1496-1504.
42. Xie, R.; Peng, X., Synthesis of Cu-doped InP nanocrystals (d-dots) with ZnSe diffusion barrier as efficient and color-tunable NIR emitters. *Journal of the American Chemical Society* **2009,** *131* (30), 10645-10651.
43. Railsback, L. B., Patterns in the compositions of oxysalt and sulfosalt minerals, and the paradoxical nature of quartz. *American Mineralogist* **2007,** *92* (2-3), 356-369.
44. Ip, A. H.; Thon, S. M.; Hoogland, S.; Voznyy, O.; Zhitomirsky, D.; Debnath, R.; Levina, L.; Rollny, L. R.; Carey, G. H.; Fischer, A.; Kemp, K. W.; Kramer, I. J.; Ning, Z.; Labelle, A. J.; Chou, K. W.; Amassian, A.; Sargent, E. H., Hybrid passivated colloidal quantum dot solids. *Nat Nanotechnol* **2012,** *7* (9), 577-82.
45. Green, M., A new approach to the formal classification of covalent compounds of the elements. *Journal of Organometallic Chemistry* **1995,** *500* (1-2), 127-148.
46. De Roo, J.; Van den Broeck, F.; De Keukeleere, K.; Martins, J. C.; Van Driessche, I.; Hens, Z., Unravelling the surface chemistry of metal oxide nanocrystals, the role of acids and bases. *Journal of the American Chemical Society* **2014,** *136* (27), 9650-9657.
47. Anderson, N. C.; Hendricks, M. P.; Choi, J. J.; Owen, J. S., Ligand exchange and the stoichiometry of metal chalcogenide nanocrystals: spectroscopic observation of facile metal-carboxylate displacement and binding. *J Am Chem Soc* **2013,** *135* (49), 18536-48.
48. Owen, J., The coordination chemistry of nanocrystal surfaces. *Science* **2015,** *347* (6222), 615-616.
49. Choi, H.-S.; Janietz, S.; Roddatis, V.; Geßner, A.; Wedel, A.; Kim, J.; Kim, Y., Enhanced Electroluminescence via a Nanohybrid Material Consisting of Aromatic Ligand-Modified InP

Quantum Dots and an Electron-Blocking Polymer as the Single Active Layer in Quantum Dot–LEDs. *Nanomaterials* **2022,** *12* (3), 408.
50. Hughes, B. K.; Ruddy, D. A.; Blackburn, J. L.; Smith, D. K.; Bergren, M. R.; Nozik, A. J.; Johnson, J. C.; Beard, M. C., Control of PbSe quantum dot surface chemistry and photophysics using an alkylselenide ligand. *Acs Nano* **2012,** *6* (6), 5498-5506.
51. Dai, Q.; Wang, Y.; Li, X.; Zhang, Y.; Pellegrino, D. J.; Zhao, M.; Zou, B.; Seo, J.; Wang, Y.; Yu, W. W., Size-dependent composition and molar extinction coefficient of PbSe semiconductor nanocrystals. *ACS nano* **2009,** *3* (6), 1518-1524.
52. Hassinen, A.; Moreels, I.; De Nolf, K.; Smet, P. F.; Martins, J. C.; Hens, Z., Short-chain alcohols strip X-type ligands and quench the luminescence of PbSe and CdSe quantum dots, acetonitrile does not. *Journal of the American Chemical Society* **2012,** *134* (51), 20705-20712.
53. Gomes, R.; Hassinen, A.; Szczygiel, A.; Zhao, Q.; Vantomme, A.; Martins, J. C.; Hens, Z., Binding of phosphonic acids to CdSe quantum dots: a solution NMR study. *The Journal of Physical Chemistry Letters* **2011,** *2* (3), 145-152.
54. Fritzinger, B.; Capek, R. K.; Lambert, K.; Martins, J. C.; Hens, Z., Utilizing self-exchange to address the binding of carboxylic acid ligands to CdSe quantum dots. *Journal of the American Chemical Society* **2010,** *132* (29), 10195-10201.
55. Owen, J. S.; Park, J.; Trudeau, P.-E.; Alivisatos, A. P., Reaction chemistry and ligand exchange at cadmium− selenide nanocrystal surfaces. *Journal of the American Chemical Society* **2008,** *130* (37), 12279-12281.
56. Moon, H.; Chae, H., Efficiency Enhancement of All-Solution-Processed Inverted-Structure Green Quantum Dot Light-Emitting Diodes Via Partial Ligand Exchange with Thiophenol Derivatives Having Negative Dipole Moment. *Advanced Optical Materials* **2020,** *8* (1), 1901314.
57. Harris, R. D.; Bettis Homan, S.; Kodaimati, M.; He, C.; Nepomnyashchii, A. B.; Swenson, N. K.; Lian, S.; Calzada, R.; Weiss, E. A., Electronic Processes within Quantum Dot-Molecule Complexes. *Chem Rev* **2016,** *116* (21), 12865-12919.
58. Yang, Y.; Qin, H.; Jiang, M.; Lin, L.; Fu, T.; Dai, X.; Zhang, Z.; Niu, Y.; Cao, H.; Jin, Y., Entropic ligands for nanocrystals: from unexpected solution properties to outstanding processability. *Nano letters* **2016,** *16* (4), 2133-2138.
59. Kim, D.; Fu, Y.; Kim, J.; Lee, K.-h.; Kim, H.; Yang, H.; Chae, H., Improved electroluminescence of quantum dot light-emitting diodes enabled by a partial ligand exchange with benzenethiol. *Nanotechnology* **2016,** *27* (24), 245203.
60. Lim, S.-R.; Schoenung, J. M., Human health and ecological toxicity potentials due to heavy metal content in waste electronic devices with flat panel displays. *Journal of Hazardous Materials* **2010,** *177* (1-3), 251-259.
61. Won, Y.-H.; Cho, O.; Kim, T.; Chung, D.-Y.; Kim, T.; Chung, H.; Jang, H.; Lee, J.; Kim, D.; Jang, E., Highly efficient and stable InP/ZnSe/ZnS quantum dot light-emitting diodes. *Nature* **2019,** *575* (7784), 634-638.
62. Kang, H.; Kim, S.; Oh, J. H.; Yoon, H. C.; Jo, J. H.; Yang, H.; Do, Y. R., Color-by-Blue QD-Emissive LCD Enabled by Replacing RGB Color Filters with Narrow-Band GR InP/ZnSeS/ZnS QD Films. *Advanced Optical Materials* **2018,** *6* (11), 1701239.
63. Hahm, D.; Park, J.; Jeong, I.; Rhee, S.; Lee, T.-S.; Lee, C.; Chung, S.; Bae, W. K.; Lee, S., Surface Engineered Colloidal Quantum Dots Toward Complete Green Process. *ACS Applied Materials & Interfaces* **2020**.

64. Tomaselli, M.; Yarger, J.; Bruchez Jr, M.; Havlin, R.; DeGraw, D.; Pines, A.; Alivisatos, A., NMR study of InP quantum dots: Surface structure and size effects. *The Journal of chemical physics* **1999,** *110* (18), 8861-8864.
65. Moreels, I.; Martins, J. C.; Hens, Z., Solution NMR techniques for investigating colloidal nanocrystal ligands: a case study on trioctylphosphine oxide at InP quantum dots. *Sensors and Actuators B: Chemical* **2007,** *126* (1), 283-288.
66. Houtepen, A. J.; Hens, Z.; Owen, J. S.; Infante, I., On the origin of surface traps in colloidal II–VI semiconductor nanocrystals. *Chemistry of Materials* **2017,** *29* (2), 752-761.
67. Hassinen, A.; Moreels, I.; de Mello Donegá, C.; Martins, J. C.; Hens, Z., Nuclear magnetic resonance spectroscopy demonstrating dynamic stabilization of CdSe quantum dots by alkylamines. *The Journal of Physical Chemistry Letters* **2010,** *1* (17), 2577-2581.
68. Hens, Z.; Martins, J. C., A Solution NMR Toolbox for Characterizing the Surface Chemistry of Colloidal Nanocrystals. *Chemistry of Materials* **2013,** *25* (8), 1211-1221.
69. Bonilla, C. A. M.; Flórez, M.-H. T.; Velasco, D. R. M.; Kouznetsov, V. V., Surface characterization of thiol ligands on CdTe quantum dots: analysis by 1 H NMR and DOSY. *New Journal of Chemistry* **2019,** *43* (22), 8452-8458.
70. Jasinski, J.; Leppert, V.; Lam, S.-T.; Gibson, G.; Nauka, K.; Yang, C.; Zhou, Z.-L., Rapid oxidation of InP nanoparticles in air. *Solid state communications* **2007,** *141* (11), 624-627.
71. Moon, H.; Lee, C.; Lee, W.; Kim, J.; Chae, H., Stability of quantum dots, quantum dot films, and quantum dot light-emitting diodes for display applications. *Advanced Materials* **2019,** *31* (34), 1804294.
72. Gomes, R.; Hassinen, A.; Szczygiel, A.; Zhao, Q.; Vantomme, A.; Martins, J. C.; Hens, Z., Binding of phosphonic acids to CdSe quantum dots: a solution NMR study. *The Journal of Physical Chemistry Letters* **2011,** *2* (3), 145-152.
73. Lee, C.; Nam, E.; Lee, W.; Chae, H., Hydrosilylation of Reactive Quantum Dots and Siloxanes for Stable Quantum Dot Films. *Polymers* **2019,** *11* (5), 905.
74. Jun, S.; Jang, E., Bright and stable alloy core/multishell quantum dots. *Angewandte Chemie* **2013,** *125* (2), 707-710.
75. Wang, H. C.; Zhang, H.; Chen, H. Y.; Yeh, H. C.; Tseng, M. R.; Chung, R. J.; Chen, S.; Liu, R. S., Cadmium-Free InP/ZnSeS/ZnS Heterostructure-Based Quantum Dot Light-Emitting Diodes with a ZnMgO Electron Transport Layer and a Brightness of Over 10 000 cd m− 2. *Small* **2017,** *13* (13), 1603962.
76. Kim, S.; Kim, T.; Kang, M.; Kwak, S. K.; Yoo, T. W.; Park, L. S.; Yang, I.; Hwang, S.; Lee, J. E.; Kim, S. K., Highly luminescent InP/GaP/ZnS nanocrystals and their application to white light-emitting diodes. *Journal of the American Chemical Society* **2012,** *134* (8), 3804-3809.
77. Lim, J.; Jun, S.; Jang, E.; Baik, H.; Kim, H.; Cho, J., Preparation of highly luminescent nanocrystals and their application to light-emitting diodes. *Advanced Materials* **2007,** *19* (15), 1927-1932.
78. Fu, Y.; Kim, D.; Jiang, W.; Yin, W.; Ahn, T. K.; Chae, H., Excellent stability of thicker shell CdSe@ ZnS/ZnS quantum dots. *RSC advances* **2017,** *7* (65), 40866-40872.
79. Zhang, H.; Hu, N.; Zeng, Z.; Lin, Q.; Zhang, F.; Tang, A.; Jia, Y.; Li, L. S.; Shen, H.; Teng, F., High-efficiency green InP quantum dot-based electroluminescent device comprising thick-shell quantum dots. *Advanced Optical Materials* **2019,** *7* (7), 1801602.

80. Yang, Y.; Zheng, Y.; Cao, W.; Titov, A.; Hyvonen, J.; Manders, J. R.; Xue, J.; Holloway, P. H.; Qian, L., High-efficiency light-emitting devices based on quantum dots with tailored nanostructures. *Nature Photonics* **2015,** *9* (4), 259-266.
81. Shen, H.; Lin, Q.; Cao, W.; Yang, C.; Shewmon, N. T.; Wang, H.; Niu, J.; Li, L. S.; Xue, J., Efficient and long-lifetime full-color light-emitting diodes using high luminescence quantum yield thick-shell quantum dots. *Nanoscale* **2017,** *9* (36), 13583-13591.
82. Lim, J.; Jeong, B. G.; Park, M.; Kim, J. K.; Pietryga, J. M.; Park, Y. S.; Klimov, V. I.; Lee, C.; Lee, D. C.; Bae, W. K., Influence of shell thickness on the performance of light-emitting devices based on CdSe/Zn1-XCdXS core/shell heterostructured quantum dots. *Advanced Materials* **2014,** *26* (47), 8034-8040.
83. Kim, T.; Yoon, C.; Song, Y.-G.; Kim, Y.-J.; Lee, K., Thermal stabilities of cadmium selenide and cadmium-free quantum dots in quantum dot–silicone nanocomposites. *Journal of Luminescence* **2016,** *177*, 54-58.
84. Jeong, S.; Achermann, M.; Nanda, J.; Ivanov, S.; Klimov, V. I.; Hollingsworth, J. A., Effect of the thiol− thiolate equilibrium on the photophysical properties of aqueous CdSe/ZnS nanocrystal quantum dots. *Journal of the American Chemical Society* **2005,** *127* (29), 10126-10127.
85. Lystrom, L.; Roberts, A.; Dandu, N.; Kilina, S., Surface-induced deprotonation of thiol ligands impacts the optical response of CdS quantum dots. *Chemistry of Materials* **2021,** *33* (3), 892-901.
86. Kim, J.; Choi, H.-S.; Wedel, A.; Yoon, S.-Y.; Jo, J.-H.; Kim, H.-M.; jong Han, C.; Song, H.-J.; Yi, J.-M.; Jang, J.-S., Highly luminescent near-infrared Cu-doped InP quantum dots with Zn-Cu-In-S/ZnS double shell scheme. *Journal of Materials Chemistry C* **2021**.
87. Boles, M. A.; Ling, D.; Hyeon, T.; Talapin, D. V., Erratum: The surface science of nanocrystals. *Nat Mater* **2016,** *15* (3), 364.
88. Li, L.-s.; Hu, J.; Yang, W.; Alivisatos, A. P., Band gap variation of size-and shape-controlled colloidal CdSe quantum rods. *Nano letters* **2001,** *1* (7), 349-351.
89. Murray, C.; Norris, D. J.; Bawendi, M. G., Synthesis and characterization of nearly monodisperse CdE (E= sulfur, selenium, tellurium) semiconductor nanocrystallites. *Journal of the American Chemical Society* **1993,** *115* (19), 8706-8715.
90. Heath, J. R., Covalency in semiconductor quantum dots. *Chemical Society Reviews* **1998,** *27* (1), 65-71.
91. Wells, R. L.; Aubuchon, S. R.; Kher, S. S.; Lube, M. S.; White, P. S., Synthesis of nanocrystalline indium arsenide and indium phosphide from indium (III) halides and tris (trimethylsilyl) pnicogens. Synthesis, characterization, and decomposition behavior of I3In. cntdot. P (SiMe3) 3. *Chemistry of materials* **1995,** *7* (4), 793-800.
92. Tamang, S.; Lincheneau, C.; Hermans, Y.; Jeong, S.; Reiss, P., Chemistry of InP nanocrystal syntheses. *Chemistry of Materials* **2016,** *28* (8), 2491-2506.
93. Healy, M. D.; Laibinis, P. E.; Stupik, P. D.; Barron, A. R., The reaction of indium (III) chloride with tris (trimethylsilyl) phosphine: a novel route to indium phosphide. *Journal of the Chemical Society, Chemical Communications* **1989,** (6), 359-360.
94. Wells, R. L.; Pitt, C. G.; McPhail, A. T.; Purdy, A. P.; Shafieezad, S.; Hallock, R. B., The use of tris (trimethylsilyl) arsine to prepare gallium arsenide and indium arsenide. *Chemistry of Materials* **1989,** *1* (1), 4-6.
95. Allen, P. M.; Walker, B. J.; Bawendi, M. G., Mechanistic insights into the formation of InP quantum dots. *Angewandte Chemie International Edition* **2010,** *49* (4), 760-762.

96. Liu, Z.; Kumbhar, A.; Xu, D.; Zhang, J.; Sun, Z.; Fang, J., Coreduction colloidal synthesis of III–V nanocrystals: the case of InP. *Angewandte Chemie International Edition* **2008,** *47* (19), 3540-3542.
97. Jun, K.-W.; Khanna, P.; Hong, K.-B.; Baeg, J.-O.; Suh, Y.-D., Synthesis of InP nanocrystals from indium chloride and sodium phosphide by solution route. *Materials chemistry and physics* **2006,** *96* (2-3), 494-497.
98. Li, L.; Protière, M.; Reiss, P., Economic synthesis of high quality InP nanocrystals using calcium phosphide as the phosphorus precursor. *Chemistry of Materials* **2008,** *20* (8), 2621-2623.
99. Green, M.; O'Brien, P., A novel metalorganic route for the direct and rapid synthesis of monodispersed quantum dots of indium phosphide. *Chemical Communications* **1998,** (22), 2459-2460.
100. van Embden, J.; Chesman, A. S. R.; Jasieniak, J. J., The Heat-Up Synthesis of Colloidal Nanocrystals. *Chemistry of Materials* **2015,** *27* (7), 2246-2285.
101. Van Embden, J.; Mulvaney, P., Nucleation and growth of CdSe nanocrystals in a binary ligand system. *Langmuir* **2005,** *21* (22), 10226-10233.
102. Clark, M. D.; Kumar, S. K.; Owen, J. S.; Chan, E. M., Focusing nanocrystal size distributions via production control. *Nano letters* **2011,** *11* (5), 1976-1980.
103. Battaglia, D.; Peng, X., Formation of high quality InP and InAs nanocrystals in a noncoordinating solvent. *Nano Letters* **2002,** *2* (9), 1027-1030.
104. Xu, S.; Ziegler, J.; Nann, T., Rapid synthesis of highly luminescent InP and InP/ZnS nanocrystals. *Journal of Materials Chemistry* **2008,** *18* (23), 2653-2656.
105. Micic, O. I.; Curtis, C. J.; Jones, K. M.; Sprague, J. R.; Nozik, A. J., Synthesis and characterization of InP quantum dots. *The Journal of Physical Chemistry* **1994,** *98* (19), 4966-4969.
106. Gary, D. C.; Terban, M. W.; Billinge, S. J.; Cossairt, B. M., Two-step nucleation and growth of InP quantum dots via magic-sized cluster intermediates. *Chemistry of Materials* **2015,** *27* (4), 1432-1441.
107. Kim, K.; Suh, Y.-H.; Kim, D.; Choi, Y.; Bang, E.; Kim, B. H.; Park, J., Zinc Oxo Clusters Improve the Optoelectronic Properties on Indium Phosphide Quantum Dots. *Chemistry of Materials* **2020,** *32* (7), 2795-2802.
108. Beberwyck, B. J.; Alivisatos, A. P., Ion exchange synthesis of III–V nanocrystals. *Journal of the American Chemical Society* **2012,** *134* (49), 19977-19980.
109. Reiss, P.; Protiere, M.; Li, L., Core/shell semiconductor nanocrystals. *small* **2009,** *5* (2), 154-168.
110. Hines, M. A.; Guyot-Sionnest, P., Synthesis and characterization of strongly luminescing ZnS-capped CdSe nanocrystals. *The Journal of Physical Chemistry* **1996,** *100* (2), 468-471.
111. Ippen, C.; Greco, T.; Wedel, A., InP/ZnSe/ZnS: A Novel Multishell System for InP Quantum Dots for Improved Luminescence Efficiency and Its application in a Light-Emitting Device. *Journal of Information Display* **2012,** *13* (2), 91-95.
112. Haubold, S.; Haase, M.; Kornowski, A.; Weller, H., Strongly luminescent InP/ZnS core–shell nanoparticles. *ChemPhysChem* **2001,** *2* (5), 331-334.
113. Talapin, D. V.; Rogach, A. L.; Kornowski, A.; Haase, M.; Weller, H., Highly luminescent monodisperse CdSe and CdSe/ZnS nanocrystals synthesized in a hexadecylamine− trioctylphosphine oxide− trioctylphospine mixture. *Nano letters* **2001,** *1* (4), 207-211.
114. Cros-Gagneux, A.; Delpech, F.; Nayral, C.; Cornejo, A.; Coppel, Y.; Chaudret, B., Surface chemistry of InP quantum dots: a comprehensive study. *Journal of the American Chemical Society* **2010,** *132* (51), 18147-18157.

115. Virieux, H.; Le Troedec, M.; Cros-Gagneux, A.; Ojo, W.-S.; Delpech, F.; Nayral, C.; Martinez, H.; Chaudret, B., InP/ZnS nanocrystals: coupling NMR and XPS for fine surface and interface description. *Journal of the American Chemical Society* **2012,** *134* (48), 19701-19708.
116. Lim, J.; Bae, W. K.; Lee, D.; Nam, M. K.; Jung, J.; Lee, C.; Char, K.; Lee, S., InP@ZnSeS, Core@Composition Gradient Shell Quantum Dots with Enhanced Stability. *Chemistry of Materials* **2011,** *23* (20), 4459-4463.
117. Lim, J.; Park, M.; Bae, W. K.; Lee, D.; Lee, S.; Lee, C.; Char, K., Highly efficient cadmium-free quantum dot light-emitting diodes enabled by the direct formation of excitons within InP@ ZnSeS quantum dots. *ACS nano* **2013,** *7* (10), 9019-9026.
118. Pietra, F.; Kirkwood, N.; De Trizio, L.; Hoekstra, A. W.; Kleibergen, L.; Renaud, N.; Koole, R.; Baesjou, P.; Manna, L.; Houtepen, A. J., Ga for Zn Cation Exchange Allows for Highly Luminescent and Photostable InZnP-Based Quantum Dots. *Chem Mater* **2017,** *29* (12), 5192-5199.
119. Sowers, K. L.; Swartz, B.; Krauss, T. D., Chemical mechanisms of semiconductor nanocrystal synthesis. *Chemistry of Materials* **2013,** *25* (8), 1351-1362.
120. Kloper, V.; Osovsky, R.; Kolny-Olesiak, J.; Sashchiuk, A.; Lifshitz, E., The growth of colloidal cadmium telluride nanocrystal quantum dots in the presence of Cd0 nanoparticles. *The Journal of Physical Chemistry C* **2007,** *111* (28), 10336-10341.
121. Liu, H.; Owen, J. S.; Alivisatos, A. P., Mechanistic study of precursor evolution in colloidal group II− VI semiconductor nanocrystal synthesis. *Journal of the American Chemical Society* **2007,** *129* (2), 305-312.
122. Hines, M. A.; Scholes, G. D., Colloidal PbS nanocrystals with size-tunable near-infrared emission: observation of post-synthesis self-narrowing of the particle size distribution. *Advanced Materials* **2003,** *15* (21), 1844-1849.
123. Du, H.; Chen, C.; Krishnan, R.; Krauss, T. D.; Harbold, J. M.; Wise, F. W.; Thomas, M. G.; Silcox, J., Optical properties of colloidal PbSe nanocrystals. *Nano letters* **2002,** *2* (11), 1321-1324.
124. Steckel, J. S.; Yen, B. K.; Oertel, D. C.; Bawendi, M. G., On the mechanism of lead chalcogenide nanocrystal formation. *Journal of the American Chemical Society* **2006,** *128* (40), 13032-13033.
125. Ruberu, T. P. A.; Albright, H. R.; Callis, B.; Ward, B.; Cisneros, J.; Fan, H.-J.; Vela, J., Molecular control of the nanoscale: effect of phosphine–chalcogenide reactivity on CdS–CdSe nanocrystal composition and morphology. *ACS nano* **2012,** *6* (6), 5348-5359.
126. Owen, J. S.; Chan, E. M.; Liu, H.; Alivisatos, A. P., Precursor conversion kinetics and the nucleation of cadmium selenide nanocrystals. *Journal of the American Chemical Society* **2010,** *132* (51), 18206-18213.
127. García-Rodríguez, R. l.; Liu, H., Mechanistic study of the synthesis of CdSe nanocrystals: release of selenium. *Journal of the American Chemical Society* **2012,** *134* (3), 1400-1403.
128. Moon, H.; Lee, W.; Chae, H., Energy-Band Alignment and Charge Balance of Electron Transport Layer With Quinary Zn–Mg–Ga–Cl–O Nanoparticles in InP-Based Quantum Dot Light Emitting Diodes. *IEEE Electron Device Letters* **2019,** *40* (11), 1872-1875.
129. Bozyigit, D.; Yarema, O.; Wood, V., Origins of low quantum efficiencies in quantum dot LEDs. *Advanced Functional Materials* **2013,** *23* (24), 3024-3029.
130. Bae, W. K.; Park, Y.-S.; Lim, J.; Lee, D.; Padilha, L. A.; McDaniel, H.; Robel, I.; Lee, C.; Pietryga, J. M.; Klimov, V. I., Controlling the influence of Auger recombination on the performance of quantum-dot light-emitting diodes. *Nature communications* **2013,** *4* (1), 1-8.

131. Dai, X.; Zhang, Z.; Jin, Y.; Niu, Y.; Cao, H.; Liang, X.; Chen, L.; Wang, J.; Peng, X., Solution-processed, high-performance light-emitting diodes based on quantum dots. *Nature* **2014,** *515* (7525), 96-99.
132. Juang, F.-S.; Lee, C.-C.; Chen, J.-Y.; Lin, Y.-H.; Zhang, D.-W. In *Lifetime study for solution processed organic light emitting diodes*, IOP Conference Series: Materials Science and Engineering, IOP Publishing: 2019; p 012018.
133. Wu, Z.; Liu, P.; Qu, X.; Ma, J.; Liu, W.; Xu, B.; Wang, K.; Sun, X. W., Identifying the Surface Charges and their Impact on Carrier Dynamics in Quantum-Dot Light-Emitting Diodes by Impedance Spectroscopy. *Advanced Optical Materials* **2021**, 2100389.
134. Ikai, M.; Tokito, S.; Sakamoto, Y.; Suzuki, T.; Taga, Y., Highly efficient phosphorescence from organic light-emitting devices with an exciton-block layer. *Applied Physics Letters* **2001,** *79* (2), 156-158.
135. Debije, M. G.; Verbunt, P. P. C., Thirty Years of Luminescent Solar Concentrator Research: Solar Energy for the Built Environment. *Advanced Energy Materials* **2012,** *2* (1), 12-35.
136. Bornstein, J. G. In *Luminescent solar concentrator daylighting*, Optical Materials Technology for Energy Efficiency and Solar Energy Conversion III, SPIE: 1984; pp 138-145.
137. Earp, A. A.; Smith, G. B.; Franklin, J.; Swift, P., Optimisation of a three-colour luminescent solar concentrator daylighting system. *Solar Energy Materials and Solar Cells* **2004,** *84* (1-4), 411-426.
138. Bradshaw, L. R.; Knowles, K. E.; McDowall, S.; Gamelin, D. R., Nanocrystals for luminescent solar concentrators. *Nano letters* **2015,** *15* (2), 1315-1323.
139. Batchelder, J.; Zewai, A.; Cole, T., Luminescent solar concentrators. 1: Theory of operation and techniques for performance evaluation. *Applied Optics* **1979,** *18* (18), 3090-3110.
140. Currie, M. J.; Mapel, J. K.; Heidel, T. D.; Goffri, S.; Baldo, M. A., High-efficiency organic solar concentrators for photovoltaics. *Science* **2008,** *321* (5886), 226-228.
141. Wilson, L. R. Luminescent solar concentrators: a study of optical properties, re-absorption and device optimisation. Heriot-Watt University Edinburgh, 2010.
142. Bomm, J.; Büchtemann, A.; Chatten, A. J.; Bose, R.; Farrell, D. J.; Chan, N. L.; Xiao, Y.; Slooff, L. H.; Meyer, T.; Meyer, A., Fabrication and full characterization of state-of-the-art quantum dot luminescent solar concentrators. *Solar Energy Materials and Solar Cells* **2011,** *95* (8), 2087-2094.
143. Inman, R.; Shcherbatyuk, G.; Medvedko, D.; Gopinathan, A.; Ghosh, S., Cylindrical luminescent solar concentrators with near-infrared quantum dots. *Optics express* **2011,** *19* (24), 24308-24313.
144. Purcell-Milton, F.; Gun'ko, Y. K., Quantum dots for luminescent solar concentrators. *Journal of Materials Chemistry* **2012,** *22* (33), 16687-16697.
145. Krumer, Z.; Pera, S. J.; van Dijk-Moes, R. J.; Zhao, Y.; de Brouwer, A. F.; Groeneveld, E.; van Sark, W. G.; Schropp, R. E.; de Mello Donegá, C., Tackling self-absorption in luminescent solar concentrators with type-II colloidal quantum dots. *Solar energy materials and solar cells* **2013,** *111*, 57-65.
146. Meinardi, F.; Colombo, A.; Velizhanin, K. A.; Simonutti, R.; Lorenzon, M.; Beverina, L.; Viswanatha, R.; Klimov, V. I.; Brovelli, S., Large-area luminescent solar concentrators based on 'Stokes-shift-engineered'nanocrystals in a mass-polymerized PMMA matrix. *Nature Photonics* **2014,** *8* (5), 392.
147. Coropceanu, I.; Bawendi, M. G., Core/shell quantum dot based luminescent solar concentrators with reduced reabsorption and enhanced efficiency. *Nano letters* **2014,** *14* (7), 4097-4101.

148. Erickson, C. S.; Bradshaw, L. R.; McDowall, S.; Gilbertson, J. D.; Gamelin, D. R.; Patrick, D. L., Zero-reabsorption doped-nanocrystal luminescent solar concentrators. *ACS nano* **2014,** *8* (4), 3461-3467.
149. Lee, A.; Jin, H.; Dang, H.-W.; Choi, K.-H.; Ahn, K. H., Optimization of experimental parameters to determine the jetting regimes in electrohydrodynamic printing. *Langmuir* **2013,** *29* (44), 13630-13639.
150. Li, J., On the meniscus deformation when the pulsed voltage is applied. *Journal of electrostatics* **2006,** *64* (1), 44-52.
151. Yudistira, H. T.; Nguyen, V. D.; Dutta, P.; Byun, D., Flight behavior of charged droplets in electrohydrodynamic inkjet printing. *Applied physics letters* **2010,** *96* (2), 023503.
152. Lee, A.; Sudau, K.; Ahn, K. H.; Lee, S. J.; Willenbacher, N., Optimization of experimental parameters to suppress nozzle clogging in inkjet printing. *Industrial & engineering chemistry research* **2012,** *51* (40), 13195-13204.
153. Korkut, S.; Saville, D. A.; Aksay, I. A., Collodial cluster arrays by electrohydrodynamic printing. *Langmuir* **2008,** *24* (21), 12196-12201.
154. Muhammad, N. M.; Sundharam, S.; Dang, H.-W.; Lee, A.; Ryu, B.-H.; Choi, K.-H., CIS layer deposition through electrospray process for solar cell fabrication. *Current Applied Physics* **2011,** *11* (1), S68-S75.
155. Park, S.-E.; Hwang, J.-Y.; Kim, K.; Jung, B.; Kim, W.; Hwang, J., Spray deposition of electrohydrodynamically atomized polymer mixture for active layer fabrication in organic photovoltaics. *Solar energy materials and solar cells* **2011,** *95* (1), 352-356.
156. Jang, K.-I.; Hong, E.; Kim, J. H., Improved electrochemical performance of dye-sensitized solar cell via surface modifications of the working electrode by electrodeposition. *Korean Journal of Chemical Engineering* **2013,** *30* (3), 620-625.
157. Park, J.-U.; Hardy, M.; Kang, S. J.; Barton, K.; Adair, K.; Lee, C. Y.; Strano, M. S.; Alleyne, A. G.; Georgiadis, J. G.; Ferreira, P. M., High-resolution electrohydrodynamic jet printing. *Nature materials* **2007,** *6* (10), 782-789.
158. Gómez-Estaca, J.; Balaguer, M. P.; Gavara, R.; Hernandez-Munoz, P., Formation of zein nanoparticles by electrohydrodynamic atomization: Effect of the main processing variables and suitability for encapsulating the food coloring and active ingredient curcumin. *Food Hydrocolloids* **2012,** *28* (1), 82-91.
159. Luo, C.; Loh, S.; Stride, E.; Edirisinghe, M., Electrospraying and electrospinning of chocolate suspensions. *Food and Bioprocess Technology* **2012,** *5* (6), 2285-2300.
160. Park, J.-U.; Lee, J. H.; Paik, U.; Lu, Y.; Rogers, J. A., Nanoscale patterns of oligonucleotides formed by electrohydrodynamic jet printing with applications in biosensing and nanomaterials assembly. *Nano letters* **2008,** *8* (12), 4210-4216.
161. Ekemen, Z.; Ahmad, Z.; Stride, E.; Kaplan, D.; Edirisinghe, M., Electrohydrodynamic bubbling: an alternative route to fabricate porous structures of silk fibroin based materials. *Biomacromolecules* **2013,** *14* (5), 1412-1422.
162. Hashimdeen, S.; Miodownik, M.; Edirisinghe, M., Print head design and control for electrohydrodynamic printing of silk fibroin. *Materials Science and Engineering: C* **2013,** *33* (6), 3309-3318.
163. Zeleny, J., The electrical discharge from liquid points, and a hydrostatic method of measuring the electric intensity at their surfaces. *Physical Review* **1914,** *3* (2), 69.

164. Zeleny, J., Instability of electrified liquid surfaces. *Physical review* **1917,** *10* (1), 1.
165. Taylor, G. I., Disintegration of water drops in an electric field. *Proceedings of the Royal Society of London. Series A. Mathematical and Physical Sciences* **1964,** *280* (1382), 383-397.
166. Jayasinghe, S.; Edirisinghe, M., Effect of viscosity on the size of relics produced by electrostatic atomization. *Journal of Aerosol Science* **2002,** *33* (10), 1379-1388.
167. Chen, D.-R.; Pui, D. Y., Experimental investigation of scaling laws for electrospraying: dielectric constant effect. *Aerosol science and technology* **1997,** *27* (3), 367-380.
168. Grigoriev, D.; Edirisinghe, M.; Bao, X., Deposition of fine silicon carbide relics by electrostatic atomization of a polymeric precursor. *Journal of materials research* **2002,** *17* (2), 487-491.
169. Edirisinghe, M.; Jayasinghe, S., Electrohydrodynamic Atomization of a Concentrated Nano-Suspension. *International Journal of Applied Ceramic Technology* **2004,** *1* (2), 140-145.
170. Yoon, H.; Woo, J. H.; Ra, Y. M.; Yoon, S. S.; Kim, H. Y.; Ahn, S.; Yun, J. H.; Gwak, J.; Yoon, K.; James, S. C., Electrostatic spray deposition of copper–indium thin films. *Aerosol Science and Technology* **2011,** *45* (12), 1448-1455.
171. Kolny-Olesiak, J.; Weller, H., Synthesis and application of colloidal CuInS2 semiconductor nanocrystals. *ACS applied materials & interfaces* **2013,** *5* (23), 12221-12237.
172. Knowles, K. E.; Hartstein, K. H.; Kilburn, T. B.; Marchioro, A.; Nelson, H. D.; Whitham, P. J.; Gamelin, D. R., Luminescent colloidal semiconductor nanocrystals containing copper: synthesis, photophysics, and applications. *Chemical reviews* **2016,** *116* (18), 10820-10851.
173. Kim, J.-H.; Kim, K.-H.; Yoon, S.-Y.; Kim, Y.; Lee, S.-H.; Kim, H.-S.; Yang, H., Tunable emission of bluish Zn–Cu–Ga–S quantum dots by Mn doping and their electroluminescence. *ACS applied materials & interfaces* **2019,** *11* (8), 8250-8257.
174. Skolnick, M.; Dean, P.; Pitt, A.; Uihlein, C.; Krath, H.; Deveaud, B.; Foulkes, E., Optical properties of copper-related centres in InP. *Journal of Physics C: Solid State Physics* **1983,** *16* (10), 1967.
175. Pal, D.; Bose, D., Photoconductivity and photoluminescence studies in copper diffused InP. *Journal of electronic materials* **1996,** *25* (5), 677-684.
176. Knowles, K. E.; Nelson, H. D.; Kilburn, T. B.; Gamelin, D. R., Singlet–triplet splittings in the luminescent excited states of colloidal Cu+: CdSe, Cu+: InP, and CuInS2 nanocrystals: charge-transfer configurations and self-trapped excitons. *Journal of the American Chemical Society* **2015,** *137* (40), 13138-13147.
177. Whitham, P. J.; Knowles, K. E.; Reid, P. J.; Gamelin, D. R., Photoluminescence Blinking and Reversible Electron Trapping in Copper-Doped CdSe Nanocrystals. *Nano Lett* **2015,** *15* (6), 4045-51.
178. Brovelli, S.; Galland, C.; Viswanatha, R.; Klimov, V. I., Tuning radiative recombination in Cu-doped nanocrystals via electrochemical control of surface trapping. *Nano Lett* **2012,** *12* (8), 4372-9.
179. Viswanatha, R.; Brovelli, S.; Pandey, A.; Crooker, S. A.; Klimov, V. I., Copper-doped inverted core/shell nanocrystals with "permanent" optically active holes. *Nano letters* **2011,** *11* (11), 4753-4758.
180. Chen, D.; Viswanatha, R.; Ong, G. L.; Xie, R.; Balasubramaninan, M.; Peng, X., Temperature dependence of "elementary processes" in doping semiconductor nanocrystals. *Journal of the American Chemical Society* **2009,** *131* (26), 9333-9339.
181. Erwin, S. C.; Zu, L.; Haftel, M. I.; Efros, A. L.; Kennedy, T. A.; Norris, D. J., Doping semiconductor nanocrystals. *Nature* **2005,** *436* (7047), 91.

182. Ozanyan, K.; Parbrook, P.; Hopkinson, M.; Whitehouse, C.; Sobiesierski, Z.; Westwood, D. I., In situ monitoring of the surface reconstructions on InP (001) prepared by molecular beam epitaxy. *Journal of applied physics* **1997,** *82* (1), 474-476.
183. Boles, M. A.; Ling, D.; Hyeon, T.; Talapin, D. V., The surface science of nanocrystals. *Nature materials* **2016,** *15* (2), 141-153.
184. Wuister, S. F.; de Mello Donega, C.; Meijerink, A., Influence of thiol capping on the exciton luminescence and decay kinetics of CdTe and CdSe quantum dots. *The Journal of Physical Chemistry B* **2004,** *108* (45), 17393-17397.
185. Kane, E. O., Band structure of indium antimonide. *Journal of Physics and Chemistry of Solids* **1957,** *1* (4), 249-261.
186. Van Bree, J.; Silov, A. Y.; Koenraad, P.; Flatté, M.; Pryor, C., g factors and diamagnetic coefficients of electrons, holes, and excitons in InAs/InP quantum dots. *Physical Review B* **2012,** *85* (16), 165323.
187. Park, J.; Kim, S.-W., CuInS2/ZnS core/shell quantum dots by cation exchange and their blue-shifted photoluminescence. *Journal of Materials Chemistry* **2011,** *21* (11).
188. De Trizio, L.; Prato, M.; Genovese, A.; Casu, A.; Povia, M.; Simonutti, R.; Alcocer, M. J. P.; D'Andrea, C.; Tassone, F.; Manna, L., Strongly Fluorescent Quaternary Cu–In–Zn–S Nanocrystals Prepared from Cu1-xInS2 Nanocrystals by Partial Cation Exchange. *Chemistry of Materials* **2012,** *24* (12), 2400-2406.
189. Jiang, T.; Song, J.; Wang, H.; Ye, X.; Wang, H.; Zhang, W.; Yang, M.; Xia, R.; Zhu, L.; Xu, X., Aqueous synthesis of color tunable Cu doped Zn–In–S/ZnS nanoparticles in the whole visible region for cellular imaging. *Journal of Materials Chemistry B* **2015,** *3* (11), 2402-2410.
190. Chen, Y.; Li, S.; Huang, L.; Pan, D., Low-cost and gram-scale synthesis of water-soluble Cu–In–S/ZnS core/shell quantum dots in an electric pressure cooker. *Nanoscale* **2014,** *6* (3), 1295-1298.
191. Mashford, B. S.; Stevenson, M.; Popovic, Z.; Hamilton, C.; Zhou, Z.; Breen, C.; Steckel, J.; Bulovic, V.; Bawendi, M.; Coe-Sullivan, S., High-efficiency quantum-dot light-emitting devices with enhanced charge injection. *Nature photonics* **2013,** *7* (5), 407-412.
192. Liu, X.; Lu, P.; Zhai, H., Ligand coverage dependence of structural stability and interparticle spacing of gold supracrystals. *Journal of Applied Physics* **2018,** *123* (4), 045101.
193. Oliveira, J. P.; Prado, A. R.; Keijok, W. J.; Valotto, R. S.; Silva, A. R.; Guimarães, M. C., Quantification of Inter-particle Spacing Caused by Thiol Self-Assembled Monolayers Using Transmission Electron Microscopy. *Plasmonics* **2019,** *14* (3), 743-753.
194. Weidman, M. C.; Nguyen, Q.; Smilgies, D.-M.; Tisdale, W. A., Impact of size dispersity, ligand coverage, and ligand length on the structure of PbS nanocrystal superlattices. *Chemistry of Materials* **2018,** *30* (3), 807-816.
195. Pang, Z.; Zhang, J.; Cao, W.; Kong, X.; Peng, X., Partitioning surface ligands on nanocrystals for maximal solubility. *Nature communications* **2019,** *10* (1), 1-8.
196. McLafferty, F. W.; Tureček, F.; Turecek, F., *Interpretation of mass spectra*. University science books: 1993.
197. Knill, C.; Kennedy, J., Spectroscopic Methods in Organic Chemistry; M. Hesse, H. Meier, B. Zeeh (Translated by A. Linden and M. Murray); George Thieme Verlag, Stuttgart, 1997, viii+ 365 pages, ISBN 3-13-106061-1, DM 168.00. *Book reviews* **2000,** *41*, 219-221.

198. Nibbering, N. M., Interpretation of Mass Spectra: Fred W. McLafferty and František Tureček University Science Books, 20 Edgehill Road, Mill Valley, CA 94941 [Fax:(415) 383-3167], 371 pp., ISBN# 0-935702-25-3, 1993, $27.00. No longer published by Elsevier: 1994.
199. Anderson, N. C.; Owen, J. S., Soluble, chloride-terminated CdSe nanocrystals: ligand exchange monitored by 1H and 31P NMR spectroscopy. *Chemistry of Materials* **2013,** *25* (1), 69-76.
200. Hasan, M.; Bethell, D.; Brust, M., The fate of sulfur-bound hydrogen on formation of self-assembled thiol monolayers on gold: 1H NMR spectroscopic evidence from solutions of gold clusters. *Journal of the American Chemical Society* **2002,** *124* (7), 1132-1133.
201. Jadhav, S. A.; Maccagno, M., Identification of thiol from 11-(9-carbazolyl)-1-undecyl disulfide by NMR spectroscopy and single step coating of gold nanoparticles. *Journal of Sulfur Chemistry* **2014,** *35* (6), 587-595.
202. Kim, T.-G.; Zherebetskyy, D.; Bekenstein, Y.; Oh, M. H.; Wang, L.-W.; Jang, E.; Alivisatos, A. P., Trap passivation in indium-based quantum dots through surface fluorination: mechanism and applications. *ACS nano* **2018,** *12* (11), 11529-11540.
203. Reid, K. R.; McBride, J. R.; Freymeyer, N. J.; Thal, L. B.; Rosenthal, S. J., Chemical structure, ensemble and single-particle spectroscopy of thick-shell InP–ZnSe quantum dots. *Nano letters* **2018,** *18* (2), 709-716.
204. Thuy, U. T. D.; Reiss, P.; Liem, N. Q., Luminescence properties of In (Zn) P alloy core/ZnS shell quantum dots. *Applied Physics Letters* **2010,** *97* (19), 193104.
205. Kagan, C. R.; Lifshitz, E.; Sargent, E. H.; Talapin, D. V., Building devices from colloidal quantum dots. *Science* **2016,** *353* (6302), aac5523.
206. Brawand, N. P.; Goldey, M. B.; Voros, M.; Galli, G., Defect states and charge transport in quantum dot solids. *Chemistry of Materials* **2017,** *29* (3), 1255-1262.
207. Kim, J.; Choi, H. S.; Wedel, A.; Yoon, S.-Y.; Jo, J.-H.; Kim, H.-M.; Han, C.-J.; Song, H.-J.; Yi, J.-M.; Jang, J.-S., Highly luminescent near-infrared Cu-doped InP quantum dots with a Zn–Cu–In–S/ZnS double shell scheme. *Journal of Materials Chemistry C* **2021,** *9* (12), 4330-4337.
208. Emwas, A.-H. M., The strengths and weaknesses of NMR spectroscopy and mass spectrometry with particular focus on metabolomics research. In *Metabonomics*, Springer: 2015; pp 161-193.
209. Alghamdi, Y., Composition and band Gap controlled AACVD of ZnSe and ZnS x Se 1-x thin films using novel single Source precursors. *Materials Sciences and Applications* **2017,** *8* (10), 726.
210. Pavesi, L.; Piazza, F.; Rudra, A.; Carlin, J. F.; Ilegems, M., Temperature dependence of the InP band gap from a photoluminescence study. *Physical Review B* **1991,** *44* (16), 9052-9055.
211. Senthilkumar, K.; Kalaivani, T.; Kanagesan, S.; Balasubramanian, V., Synthesis and characterization studies of ZnSe quantum dots. *Journal of Materials Science: Materials in Electronics* **2012,** *23* (11), 2048-2052.
212. Duan, L.; Hu, L.; Guan, X.; Lin, C. H.; Chu, D.; Huang, S.; Liu, X.; Yuan, J.; Wu, T., Quantum dots for photovoltaics: a tale of two materials. *Advanced Energy Materials* **2021,** *11* (20), 2100354.
213. Kahmann, S.; Shulga, A.; Loi, M. A., Quantum Dot Light-Emitting Transistors—Powerful Research Tools and Their Future Applications. *Advanced Functional Materials* **2020,** *30* (20), 1904174.
214. Kim, J. Y.; Voznyy, O.; Zhitomirsky, D.; Sargent, E. H., 25th anniversary article: colloidal quantum dot materials and devices: a quarter-century of advances. *Advanced Materials* **2013,** *25* (36), 4986-5010.

215. Li, H.; Duan, Y.; Shao, Z.; Zhang, G.; Li, H.; Huang, Y.; Yin, Z., High-Resolution Pixelated Light Emitting Diodes Based on Electrohydrodynamic Printing and Coffee-Ring-Free Quantum Dot Film. *Advanced Materials Technologies* **2020,** *5* (10), 2000401.
216. Liu, Y.; Jiang, C.; Song, C.; Wang, J.; Mu, L.; He, Z.; Zhong, Z.; Cun, Y.; Mai, C.; Wang, J., Highly efficient all-solution processed inverted quantum dots based light emitting diodes. *ACS nano* **2018,** *12* (2), 1564-1570.
217. Peng, X.; Schlamp, M. C.; Kadavanich, A. V.; Alivisatos, A. P., Epitaxial growth of highly luminescent CdSe/CdS core/shell nanocrystals with photostability and electronic accessibility. *Journal of the American Chemical Society* **1997,** *119* (30), 7019-7029.
218. Ohshima, H.; Makino, K., *Colloid and interface science in pharmaceutical research and development*. Elsevier: 2014.
219. Honary, S.; Zahir, F., Effect of zeta potential on the properties of nano-drug delivery systems-a review (Part 2). *Tropical journal of pharmaceutical research* **2013,** *12* (2), 265-273.
220. Levin, A.; Alenichev, M.; Masalov, V.; Sukhinina, N.; Emelchenko, G., Developing of standard reference materials of the electrokinetic (Zeta) potential of nanoparticles. *Nanotechnologies in Russia* **2018,** *13* (1), 90-95.
221. Lunardi, C. N.; Gomes, A. J.; Rocha, F. S.; De Tommaso, J.; Patience, G. S., Experimental methods in chemical engineering: Zeta potential. *The Canadian Journal of Chemical Engineering* **2021,** *99* (3), 627-639.
222. Jo, J.-H.; Jo, D.-Y.; Lee, S.-H.; Yoon, S.-Y.; Lim, H.-B.; Lee, B.-J.; Do, Y. R.; Yang, H., InP-based quantum dots having an InP core, composition-gradient ZnSeS inner shell, and ZnS outer shell with sharp, bright emissivity, and blue absorptivity for display devices. *ACS Applied Nano Materials* **2020,** *3* (2), 1972-1980.